MICROSTRUCTURE AND MECHANICAL BEHAVIOUR OF P/M SUPERALLOYS BASED ON ZhS6-K
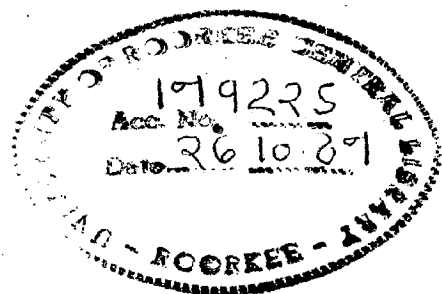
A THESIS

Submitted in fulfilment of the
requirements for the award of the degree
of
DOCTOR OF PHILOSOPHY
in
METALLURGICAL ENGINEERING

By

K. K. SHARMA

DEPARTMENT OF METALLURGICAL ENGINEERING
UNIVERSITY OF ROORKEE
ROORKEE-247 667 (INDIA)

MAY, 1986

CANDIDATE'S DECLARATION

I hereby certify that the work which is being presented in the thesis entitled "Microstructure and Mechanical Behaviour of the P M Superalloys Based on Zhs6-K" in fulfilment of the requirement for the award of the Degree of Doctor of Philosophy, submitted in the Department of Metallurgical Engineering of University of Roorkee, is an authentic record of my own work carried out during the period from November, 1979 to March, 1986 under the supervision of Dr. S.N. Tewari and Dr. N.C. Birla of Defence Metallurgical Research Laboratory, Hyderabad and Dr. P.S. Misra, Reader in Department of Metallurgical Engineering at University of Roorkee.

The matter embodied in this thesis has not been submitted by me for the award of any other degree.
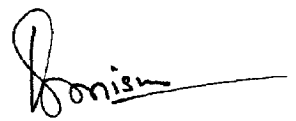
(K.K. SHARMA)

This is to certify that the above statement made by the candidate is correct to the best of my knowledge.

(S.N. TEWARI)

4873, Columbia Rd #91
N. OLMSTED
OHIO - 44070

(N.C. BIRLA)

Dy Director
Defence Metall. Res. Lab.
P-O Kanchanbagh
Hyderabad-500258

(P.S. MISRA)

Reader
Dept of Metall. Eng
Univ- of Roorkee
Roorkee - 247667

C O N T E N T S

ACKNOWLEDGEMENTS

I am grateful to Dr. S.N.Tewari of Defence Metallurgical Research Laboratory, Hyderabad, who is presently on leave at NASA-Lewis Centre, Cleveland, USA, for suggesting the problem of this work and in providing invaluable guidance at various stages. I am extremely thankful to Dr. N.C.Birla of DMRL for further guidance and several useful discussions. I express my deep sense of gratitude to Dr. P.Rama Rao, Director, DMRL for his keen interest, constant encouragement and support provided during the course of this work. I am also grateful to Dr. V.S.Arunachalam, formerly Director, DMRL and presently Director General, Defence Research and Development Organisation for his permission to carry out this work and continued encouragement.

I am indebted to Dr. P.S.Misra, Reader at the Department of Metallurgical Engineering, University of Roorkee for his illuminating guidance throughout my work. I am also thankful to Professor D.B.Goel, Head, Department of Metallurgical Engineering, University of Roorkee and Professor M.L.Mehta for their keen interest in this work.

I am greatly indebted to Dr. E.S.Bhagiradha Rao of DMRL for evincing keen interest in this work and many fruitful discussions. I am also thankful to Dr. M.L.Bhatia and Dr.A.M.Srirammurthy of DMRL for their advice and many useful discussions. I am indebted to Mr Mahendra Kumar of DMRL for making the powders and Dr. T.L.Prakash also of DMRL for performing the hot isostatic pressing experiments. It would not have been possible to carry out this work without their support.

ABSTRACT

The present work is aimed at studying the metallurgical behaviour of P/M superalloys which are low in cobalt and are comparatively richer in refractory elements such as tungsten, molybdenum, niobium etc. Chemistry of a high performance Soviet cast superalloy ZhS6-K (Ni-10Cr-5W-5Al-4.5Co-4Mo-2.5Ti-0.15C-0.02B) has been modified by slight reductions in carbon, titanium and aluminium and by minor additions of boron, niobium and hafnium. These chemistry variants of the P/M alloys designated as DMP-1 (with 0.7% Hf and 0.02% B), DMP-2 (with 0.7% Hf and 0.085% B) and DMP-3 (sigma-prone composition but without Hf) have been prepared by argon atomization. Followed by characterization, the powders have been hot isostatically pressed at different temperatures below and above the γ' solvus. It has been observed that unlike carbon, increase in boron does not promote the continuous precipitation at the prior particle boundaries. However, boron beyond 0.02% does narrow down the consolidation temperature range and changes the morphology of γ' particles from cuboidal to dendritic. The precipitation of eutectic $\gamma + \gamma'$ structure and boride films at the grain boundaries have been shown to adversely affect the mechanical properties of the high-boron alloy pressed at temperature a little above the γ' solvus. These borides have been analysed to contain tungsten, molybdenum, niobium and chromium but no titanium. Addition of hafnium has also been found to decrease the alloy solidus reflected by the precipitation of eutectic $\gamma + \gamma'$ structure and formation of hafnium-rich phase at the triple point boundaries. In contrast, the addition of hafnium has been observed to reduce the activity of sulphur. However, the hafnium-free alloy has been found to be relatively less prone to the development of eutectic $\gamma + \gamma'$ structure.

The consolidation of the three alloys at temperatures very close to their γ' solvus has produced significant property improvement. Out of these alloys, sigma-prone Hf-free alloy has been found to offer the best combination of tensile and stress-rupture properties after a suitable heat treatment. Additions of boron and hafnium have been found to restrict the use of solutioning temperatures above the γ' solvus of the alloys thereby demanding not only a control on the consolidation temperature but also on the solutioning temperatures.

SYNOPSIS

MICROSTRUCTURE AND MECHANICAL BEHAVIOUR OF P/M SUPERALLOYS BASED ON Zhs6-K

Last decade has seen significant scientific and technological advances in the field of powder metallurgy (PM) of nickel base superalloys to meet the evergrowing demand of gas turbine disc materials[1-3]. Due to the absence of macrosegregation, PM superalloys offer a better combination of elevated temperature strength, hot workability and structural homogeneity. A review of the current literature shows that further improvement in their mechanical properties and structural stability can be achieved by making some minor chemistry variations and changes in the processing conditions[4-6].

The present work is aimed at having further understanding of the effects of minor variations in chemical composition and processing parameters on the structural and mechanical behaviour of PM alloys which are comparatively richer in refractory elements such as tungsten, molybdenum, niobium etc., but have lower proportion of cobalt. A Soviet cast nickel base superalloy, ZhS6-K[7] having the composition Ni-11Cr-5W-5Al-4.5Co-4Mo-2.5Ti-0.15C-0.02B, is considered to be a good representative of such alloys since its properties are also found comparable with the American cast alloy IN-100 (Ni-15Co-10Cr-5.5Al-4.5Ti-3Mo-1V-0.18C-0.06Zr-0.01B) which has already been processed by PM route.

Three chemistry variants of ZhS6-K, designated as DMP I, DMP II and DMP III (Table I) were considered for examining their potential as the alternate turbine disc alloys. Carbon was restricted to the maximum level of 0.025 wt% to reduce the tendency of undesirable carbides precipitation at the prior particle boundaries (PPBs). Titanium and aluminium contents were slightly lowered in both DMP I and DMP II to make way for the additions of niobium and hafnium, which are reported to strengthen the intermetallic coherent phase, $\gamma'(Ni_3(TiAl))$ and minimize carbide precipitation at PPBs[6-8]. In DMP II,

boron was increased to 0.1 wt% as compared to 0.02% of DMP I. Fixation of 0.1% boron for this modification is based on a recent investigation on the investment cast ZhS6-K^9. In the case of DMP III, marginal increases in the levels of Cr, Co, W, Ti, Al and Nb were made to make the alloy prone to the precipitation of deleterious topologically close-packed (TCP) phases such as Sigma, Mu, Laves etc[10]. All the three alloys were critically examined to optimize their hot isostatic pressing parameters and to establish correlation between their microstructures and resulting properties.

The alloys prepared by vacuum induction melting were heat treated at 1123 K for 300 hours and microstructurally examined to detect the precipitation of TCP phases. Each machined ingot weighing about 15 Kg was argon atomised and the powders thus produced were cooled in argon atmosphere, sieved to obtain various size fractions and tested for physical properties and chemical composition. Optical and scanning microscopy and Auger electron spectroscopy techniques were also employed to characterize the powders. Some of the powder characteristics are listed in Table II.

The alloy powders of <150 μm size filled into stainless steel cans were evacuated to 1.3 x 10^{-3} Pa, outgassed at 1073 K for 12 hours and then vacuum sealed. Consolidation of the encapsulated powders was carried out in an ASEA QUINTUS QIH-32 Hot Isostatic Press (HIP) at a pressure of 120 MPa for three hours under argon atmosphere at three different temperatures of 1448 K, 1473 K and 1498 K. Detailed microstructural investigation including electron microscopy and electron probe microanalysis techniques was conducted on each consolidated alloy before and after several heat treatments. Tensile and stress rupture properties of as - HIPed and heat treated alloys were evaluated at different temperatures. Fracture surfaces of the tensile tested specimens were examined using optical and scanning electron microscopy.

Metallographic examination of the three alloys DMP I, DMP II and DMP III in as - cast condition showed that alloys have approximately 50% volume fraction of the hardening phase γ' with varying propor-

tions of eutectic γ-γ'. In addition, DMP II also contained large boride precipitates at the grain boundaries. Appearance of Wirdmanstatten type of structure in DMP III after heat treatment at 1073 K/300 h, confirmed this alloy to be sigma prone.

It was observed that increase in the consolidation temperature from 1448 K to 1498 K in both DMP I and DMP II produced major structural changes. On HIPing at 1448 K the alloys showed the presence of dendritic structure and bimodal distribution of γ'. Besides increasing the grain size, HIPing at 1498 K, which is well above the γ' solvus temperature of both the alloys (γ' solvus for DMP I and DMP II is in the range of 1463 to 1483 K) also resulted in the formation of eutectic γ-γ' structure. In addition DMP II also showed the presence of massive grain boundary precipitates (5 to 10 μm in size) which were found to be oxyborides of W, Mo, Cr and Nb.

HIPing of DMP II at the intermediate temperature 1473 K inhibited the formation of boride films and produced a random distribution of inter-and intra-granular cuboid shaped borides of 2 to 5 μm size. Eutectic γ-γ' structure accompanied with some grain growth was however, observed in both DMP I and DMP II. It was also observed that besides enhancing the volume fraction of eutectic γ-γ' structure, increase in boron produced noticeable changes in the morphology of γ' precipitates, as is evident from the electron micrographs of the three alloys HIPed at 1448 K (Fig.1). Dendritic configuration of γ' precipitates was attributed to low mismatch between γ and γ' based on X-ray and electron diffraction studies.

In case of DMP III, which has γ' solvus between 1473 and 1483K, microstructural changes caused by the increase in HIPing temperature were found to be less pronounced. Consolidation of the alloy in the intermediate temperature regime of 1473 K produced a discrete grain boundary precipitation of globular carbides and coarse γ' and randomly dispersed intragranular plate shaped carbides, which were of M_6C type and rich in W, Mo and Nb. Increase in the HIPing temperature to 1498 K resulted in appreciable grain growth and finer distribution of γ', whereas lowering of the HIPing temperature left some of the

powder particles with their original dendritic structure intact. This study indicated that consolidation needs to be done at temperature close to or slightly above the γ' solvus of each alloy.

An examination of the ambient and elevated temperature tensile properties of these alloys HIPed at the three temperatures (Table III) further indicated that the consolidation temperature of 1448 K was not adequate. A marked reduction in the 0.2% YS, UTS and elongation of the 1498 K HIPed DMP II was attributed to the precipitation of boride films on the grain boundaries and large grain size. Room temperature tensile properties of DMP I showed an upward trend with the increase in HIPing temperature but a significant drop in 1033 K tensile properties of the 1498 K HIPed alloy was probably due to the precipitation of a considerable amount of eutectic γ-γ'. In the case of DMP III, room temperature yield strength improved with the increase in HIPing temperature but UTS and ductility experienced drastic drop when the alloy was HIPed at 1498 K. Fractographic examination of the tensile tested specimens confirmed that 1473 K is the most optimum consolidation temperature.

It was observed that out of several heat treatments examined, H_2 (1353 K/8h, rapid air cool + 923 K/24h, air cool + 1033 K/16h, air cool) offered the best combination of tensile and stress rupture properties on account of finely distributed carbide precipitates engloved by coarse γ' precipitates (2 to 5 μm in size) at the grain boundaries and bimodal distribution of fine to medium coarse γ' precipitates (<0.5 to 2 μm) within the grains. The heat treatment H_1 (1493 K/2h, rapid air cool + 1323 K/8h, air cool + 1123 K/16h, air cool) appeared to agglomerate carbides on the grain boundaries, which during deformation, possibly acted as stress raisers prompting the initiation of cracks. Microstructures obtained by these two heat treatments and microanalysis of grain boundary carbides in case of DMP II are illustrated in Fig.2.

Fig.3 shows a comparison of some of the tensile and stress rupture properties due to the two heat treatments H_1 and H_2 on DMP III HIPed at 1473 K. A substantial drop in the alloy strength after the heat treatment H_1 is a manifestation of the adverse effects

of carbides agglomeration at the grain boundaries and rafted morphology of γ'. Fractographic examination conducted on the tensile and stress rupture tested specimens further confirmed the evidence of this behaviour.

The following conclusions have been drawn from this research:

1. Increase in the boron content narrows down the sintering temperature range and drastically affects the morphology of γ' precipitates.

2. Hot isostatic pressing of boron containing superalloys should be carried out at temperatures close to the γ' solvus and below the boride solvus to prevent the formation of boride films and also to minimize the precipitation of eutectic $\gamma-\gamma'$ structure.

3. Boride films when present makes the alloy highly sensitive to rapid cooling solution treatments inducing quench cracks even in small samples.

4. M_6C of carbides formed at the grain boundaries are rich in W and Mo and do not degenerate even after long exposures at high temperatures. Absence of depleted zone around carbides and precipitation of coarse γ' at the grain boundaries further contribute to the high elevated temperature strength.

5. Reduction of cobalt in the alloys examined does not produce any adverse effects on the elevated temperature properties of superalloys which contain high proportions of refractory elements.

6. DMP III offers a good combination of tensile and stress rupture properties as compared with several existing PM superalloys.

REFERENCES

1. C.T. Sims & WC Hagel, "The Superalloys", John Willey & Sons, New York, 1972, 612.

2. G.H. Gessinger & M.J. Bomford, Int. Met. Rev., 1974 Vol 19, pp 55-76.

3. R.D. Eng and D.J. Evans, Superalloys 1980, Tien et al Ed., ASM Metals Park, Ohio, Sept.1980, pp 493-500.

4. J.P. Immargion ' W. Wallace, Metal Powder Report, Oct.1983, pp 537-544.

5. M.J.Blackburn & R.A.Sprague, Met. Tech., 1977, Vol 4 (8), pp 388-395.

6. J.H. Davidson & C. Aubin, Proceedings on 2nd International Conference on 'High Temperature Alloys for Gas Turbine', Liege, Belgium, 1982, pp 853-886.

7. F.F. Khimushin, High Temperature Steels & Alloys, Part II, Foreign Technology Division, WP-AFB, Ohio, USA, April 1971.

8. R.Thamburaj, W. Wallace, Y.N. Chari and T.L.Prakash, Powder Metallurgy, 1984, Vol.27, No. 3, pp 169-180.

9. S.N. Tewari & M.Hema Reddy, Journal of Mat. Sc., 1983, Vol.18(3), pp 1155-1163.

10. J.R. Mihilsin, C.G.Bieber and R.T. Grant, Trans. AIME, 1968, Vol. 242, No. 12, pp 2399-2414.

TABLE I : CHEMICAL COMPOSITIONS OF ZhS6-K AND
ITS MODIFICATIONS IN AS-CAST CONDITION (Wt%)

Element	ZhS6-K	DMP-I	DMP-II	DMP-III
C	0.15-0.20	0.016	0.018	0.028
Cr	9.5-12.0	10.0	9.90	11.20
Co	4.0-5.0	4.40	4.60	5.4
W	4.5-5.5	4.35	4.20	5.2
Mo	3.5-4.8	3.235	3.40	3.2
Ti	2.5-3.2	2.10	1.95	3.0
Al	4.5-5.5	4.60	4.45	4.8
Nb	-	0.92	0.90	1.35
Hf	-	0.71	0.72	0.07
Zr	-	0.07	0.08	0.065
B	0.02 Max	0.018	0.085	0.023
Ce	0.015	-	-	-
Fe	2.0 Max	0.52	0.50	0.65
Ni	Balance	Balance	Balance	Balance

TABLE II : CHARACTERISTICS OF – 100 MESH (<150 μm) ARGON ATOMIZED SUPERALLOY POWDERS

Nomencla-ture	Mesh Size Distribution		Apparent Density (% theoretical)*	Tap Density (% theoretical)*	Flow Rate (gm/Sec)	Oxygen (ppm)	Argon (ppm)
	Mesh size	Weight%					
DMP I	-100 + 150	45	50.6	57.5	3.54	95	1.7
	-150 + 325	33					
	-325	22					
DMP II	-100 + 150	42	51.7	58.4	3.70	73	1.4
	-150 + 325	34					
	-325	24					
DMP III	-100 + 150	43	53.4	60.7	3.72	81	1.6
	-150 + 325	32					
	-325	25					

DMP – 1 8.9, DMP II – 8.9, DMP III – 8.8 (gm/cc)

TABLE III : TENSILE PROPERTIES OF AS-HIPED NICKEL BASE PM SUPERALLOYS

Alloy	HIP Temperature (K)	300 K				1033 K			
		YS (MPa)	UTS (MPa)	El (%)	RA (%)	YS (MPa)	UTS (MPa)	El (%)	RA (%)
DMP-1	1448	791	1065	7	8	815	985	7	7
	1473	844	1325	14	16	802	976	15	18
	1498	825	1054	8	9	768	889	6	8
DMP II	1448	855	963	4.5	6	908	953	7	8
	1473	846	1138	15	16	789	986	15	18
	1498	858	1038	5	7	749	959	3.5	5
DMP III	1448	844	1159	8	9	898	981	5	5
	1473	952	1349	15	16	975	1019	7	10
	1498	974	1200	7.5	10	950	1000	4	4
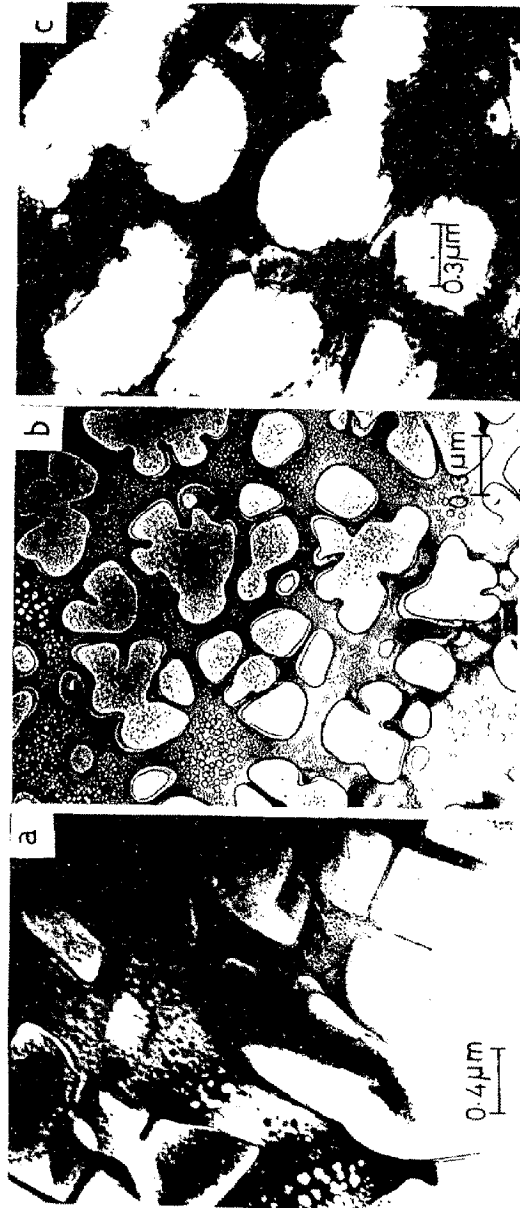
Fig.1 Microstructures of Alloys Hiped at 1448 K/120 MPa/3H (a) DMP I
(b) DMP II (c) DMP III
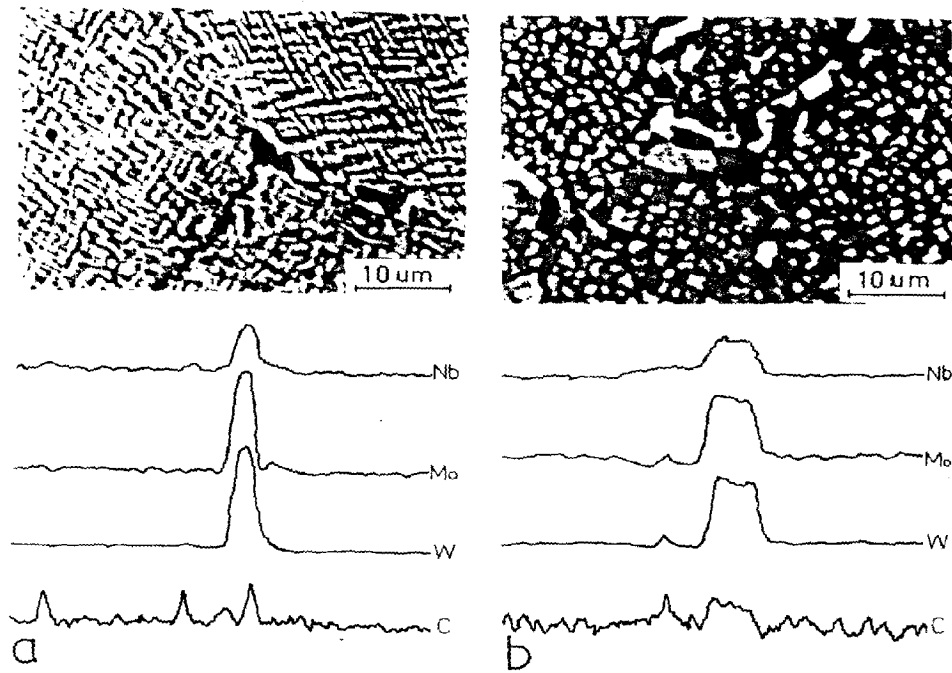
Fig.2 Effect of Heat Treatment on Microstructures
of DMP III HIPed at 1473 K
(a) 1493K/2H, RAC + 1323 K/8H, AC + 1123 K/16H,AC
(b) 1353 K/8H, RAC + 923K/24H, AC + 1033 K/16H,AC

STRESS (MPa)

TENSILE PROPERTIES

UTS

0.2% YS

El, %

RUPTURE LIFE (h)

S-R PROPERTIES

RED. IN AREA

FIG.3 EFFECT OF HEAT TREATMENT ON TENSILE AND STRESS-RUPTURE PROPERTIES OF
DMP III ALLOY HIPED AT 1473K.
H$_1$- 1493K/2H,RAC + 1323K/8H,AC + 1123K/16H,AC
H$_2$- 1353K/8H,RAC + 923K/24H,AC + 1033K/16H,AC

xvi

LIST OF FIGURES

LIST OF TABLES

LIST OF SYMBOLS

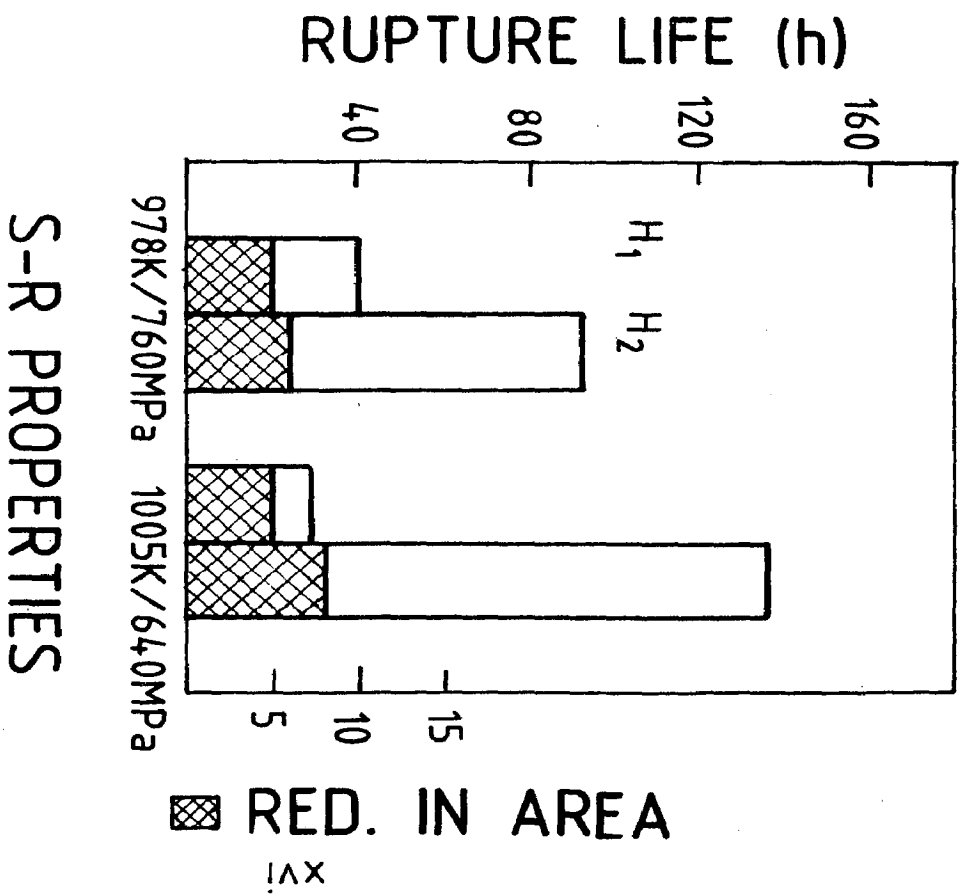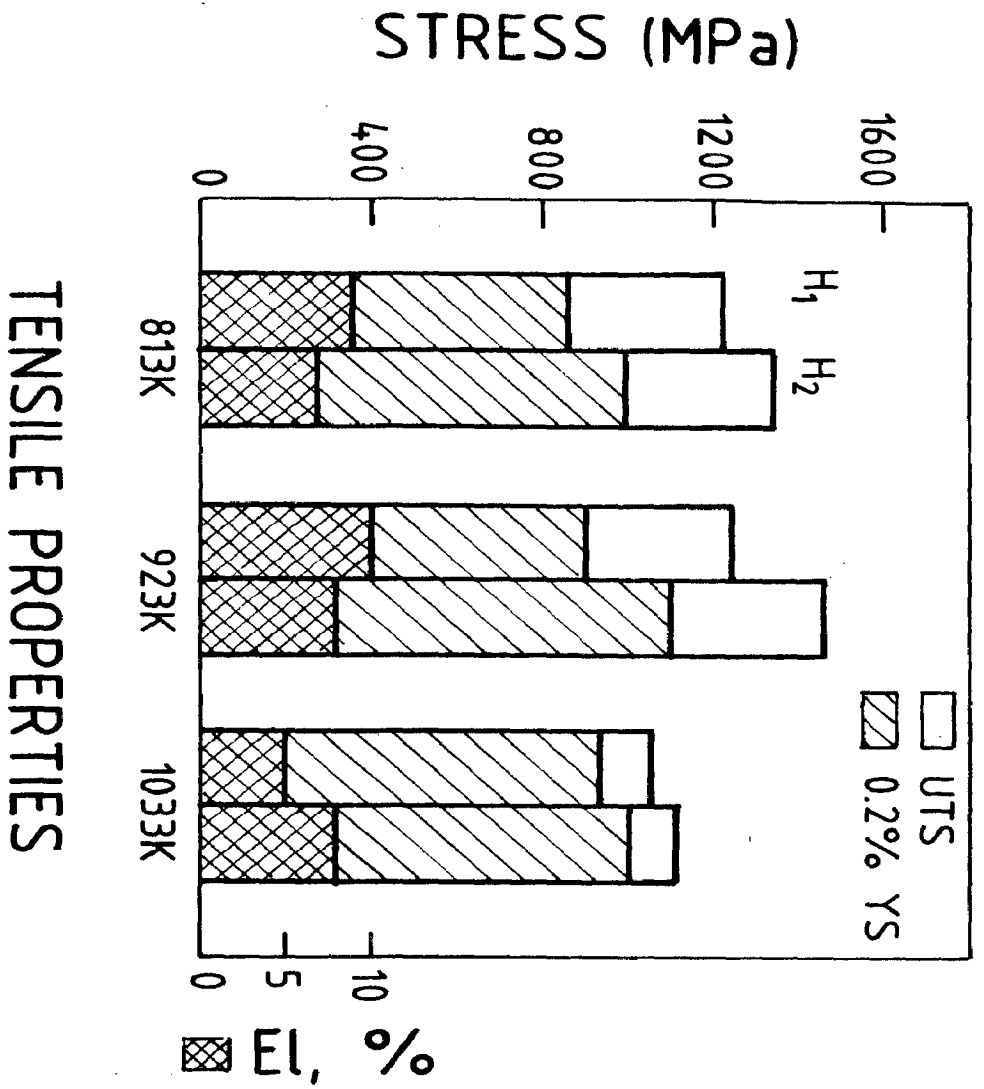|		
γ	–	Gamma matrix
γ'	–	Intermetallic Coherent gamma prime precipitate
σ	–	Topologically close-packed sigma phase
TCP	–	Topologically close-packed phase
τ_c	–	Critical resolved shear stress
γ_o	–	Anti-phase boundary energy
r_o	–	Radius of the solute precipitate
b	–	Burger's vector
T	–	Dislocation line tension
τ'_o	–	Lattice friction stress of the matrix
α_p	–	Lattice friction stress of the particle
	–	Misfit parameter
a_p	–	Lattice parameter of solute precipitate
a_m	–	Lattice parameter of matrix
$\bar{a}$	–	Average lattice parameter
Pa	–	Surface energy
R	–	Radius of the powder particle
P_{eff}	–	Effective stress
D	–	Theoretical Density
P_a	–	Applied Pressure
$\dot{\varepsilon}$	–	Tensile Strain rate
θ	–	Average Porosity
τ	–	Applied Shear Stress
G	–	Shear modulus
R	–	Gas Constant

T	–	Absolute temperature in Kelvin
Qi	–	Activation energy for creep
A°	–	Angstrom unit (= 10^{-9} m)
mA	–	Milli amperes
kV	–	Kilo volts
nm	–	Nano meter
μm	–	Micro meter
K	–	Kelvin

CHAPTER 1

AIM AND SCOPE OF THE WORK

1.1 INTRODUCTION

The quest for stronger and more reliable materials to meet the increasing requirements of higher thrust and higher thermal efficiency of gas turbine aeroengines has led to the development of a spectrum of new alloys and materials of which nickel-base superalloys occupy a prominent position. The nickel-base superalloys possess outstanding strength, resistance to surface degradation and structural stability — all these over a wide temperature range of 800 to 1300 K. They owe their high temperature strength primarily to the precipitation of gamma prime (γ') — a finely distributed, ordered, intermetallic phase $Ni_3(Al, Ti)$ — and also a variety of carbides in a solid solution strengthened fcc matrix. The size, distribution and morphology of γ' as well as carbide particles have a marked influence on the mechanical properties of superalloys [1-3]. Fig. 1.1 illustrates a panorama of microstructural features in nickel base superalloys [3].

One critical area of gas turbine materials, which has received wide attention in the last two decades is the gas turbine disc superalloys, which demand high tensile strengths in the hub region (operating temperatures upto 800 K), high
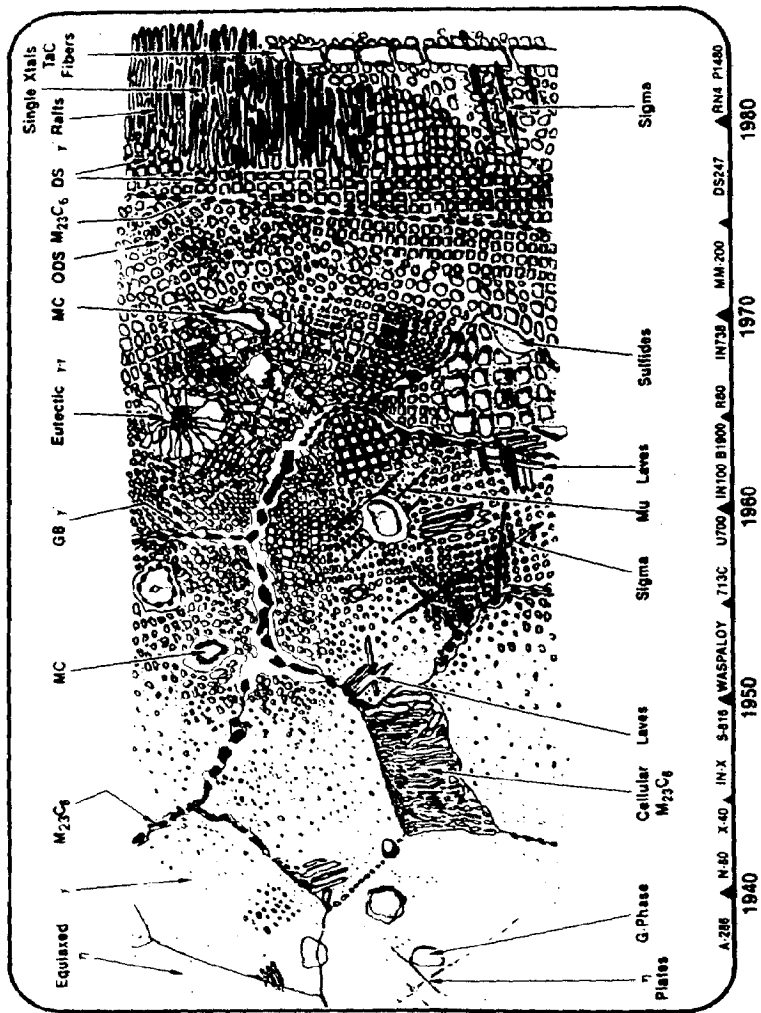
1.1 Panorama of microstructural features in nickel base superalloys [3].

..pture strengths in the rim portion (operating temperatures upto 1000 K), good low cycle fatigue properties and freedom from metallurgical defects. Thus the advanced disc alloys have a comparatively high volume fraction of the hardening γ ' phase, but such highly alloyed compositions when produced through conventional ingot metallurgy route, will have poor forgeability due to severe interdendritic segregation and un-acceptable mechanical property scatter and microstructural inhomogeneities in the as-cast condition. With the emergence of economically viable large scale processes such as inert gas atomization for powder making and hot isostatic pressing (HIP) or hot extrusion for powder consolidation, several highly alloyed compositions which were mainly developed for cast turbine blade4, are now processed through powder metallurgy (P/M) route for disc applications [3,7]. Segregational effects are virtually absent in a gas atomized superalloy powder particle because of the high solidification rates involved, while HIP or extrusion consolidates the powders to theoretical density levels with comparatively refined and fine-grained microstructures. Con-sequently, a powder billet becomes highly workable by forging and other standard hot working techniques. Table 1.1 is an illustrative list of the chemical compositions of some current disc superalloys and Fig. 1.2 shows their strength trends [5].

Although P/M processing produces fine-grained homoge-neous microstructures resulting in vastly improved hot workability and higher strength levels at moderate temperature , it introduces certain problems such as the need for utmost care in powder

Table 1.1

Nominal Composition of Disc Superalloys, wt%

Alloy	C	Co	Cr	Al	Ti	Mo	W	Nb	Hf	V	B	Zr	Ni
Waspaloy	0.08	13.5	19.5	1.3	3.0	4.3	-	-	-	-	0.01	0.06	balance
Udimet 700	0.07	18.5	15.0	4.4	3.5	5.0	-	-	-	-	0.025	-	balance
PM Rene'95	0.05	8.0	14.0	3.5	2.5	3.5	3.5	3.3	-	-	0.01	0.05	balance
P/M LC Astroloy	0.03	17.0	15.0	4.0	3.5	5.0	-	-	-	-	0.02	-	balance
P/M IN-100	0.07	15.0	12.0	5.5	4.5	3.2	-	-	-	0.8	0.01	0.05	balance
P/M AF-115	0.05	15.0	10.7	3.8	3.9	2.8	5.9	1.7	-	2.0	0.02	0.05	balance
MERL 76 (modified IN-100)	0.025	18.0	12.5	5.0	4.3	3.2	-	-	0.4	-	0.02	0.06	balance

UTS. AT 923K , MPa
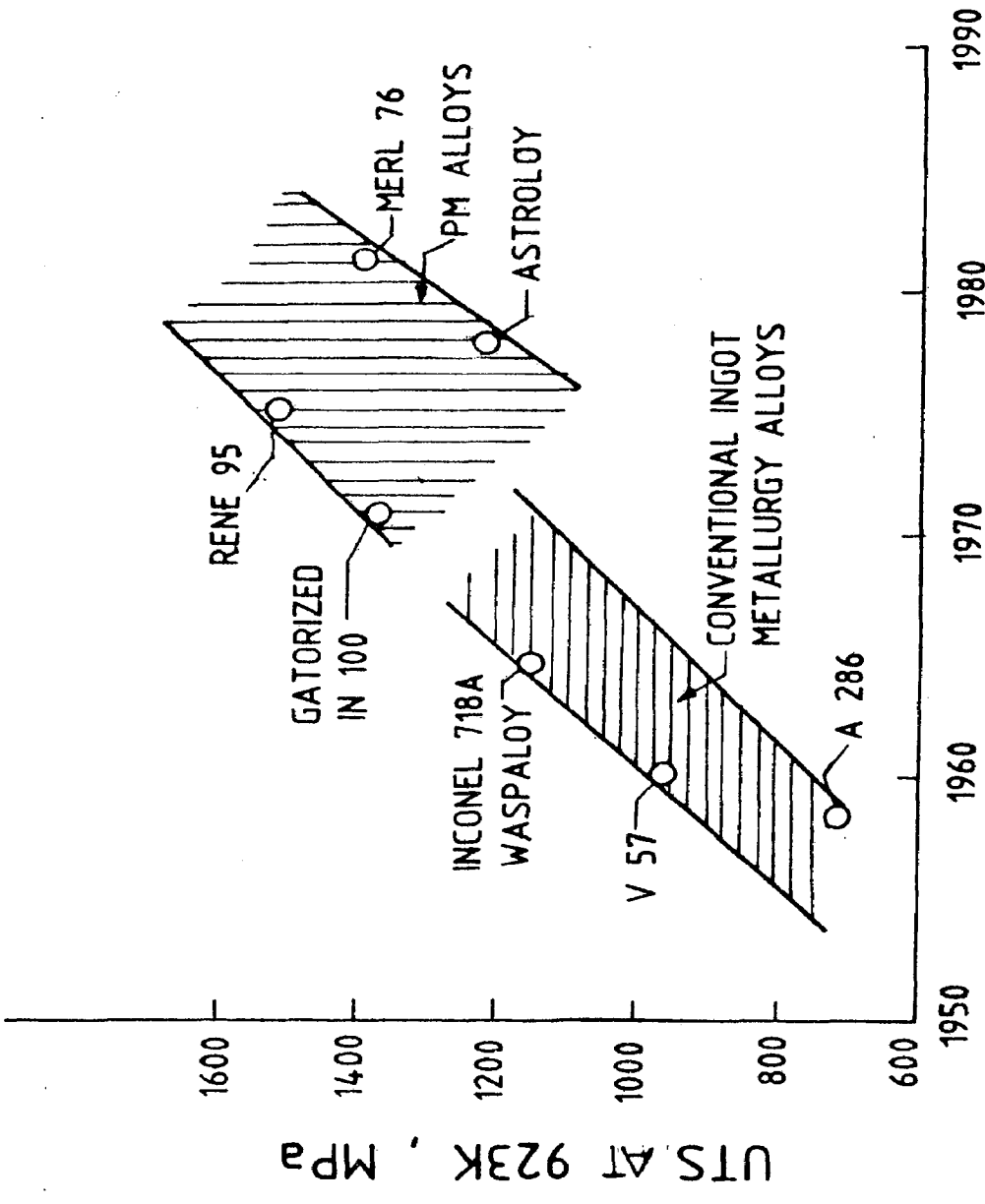
APPROXIMATE YEAR OF
INTRODUCTION IN AIRCRAFT

1.2   Strength trends in turbine disc materials [5].

handling, gas porosity, ceramic inclusions and prior particle boundary (PPB) carbide precipitates. The presence of a fine oxide layer at the nascent powder particle surface is believed to provide preferred sites for the undesirable PPB precipitation during HIP consolidation and the PPB precipitates are usually identified to be oxycarbides [8]. A review of the current literature shows that some thermo-mechanical measures, subtle chemistry variations such as reduction of carbon to a level below 200 ppm and minor additions of tantalum, niobium, hafnium, zirconium or boron can supress the tendency of PPB precipitation in P/M superalloys [9-16]. While these additions improve the temperature capability of the alloys by raising the γ' solvus, they also lower the solidus of the alloys [13, 16], thereby narrowing down the consolidation and hot forging temperature ranges of P/M superalloys. As such, a precise control of the consolidation and hot forging temperatures becomes essential to avoid problems such as incipient melting.

1.2 AIM OF THE WORK

Although extensive studies have been carried out to understand the role of minor additions such as boron, hafnium, niobium, zirconium etc., on numerous cast and wrought nickel base superalloys, there is considerable scope for the optimization of P/M superalloys through a greater insight into their structural and mechanical behaviour in response to compositional modifications. For instance, the worldwide crisis of cobalt scarcity in the late 1970s provoked several alloy modification programmes to reduce the concentration of cobalt in conventional

superalloys [17]. Although the cobalt scarcity has come out of crisis proportions the need for cobalt conservation cannot be overemphasised. However, the current P/M superalloys do contain rather high proportions of cobalt. It is thus felt that a superalloy chemistry which is not only low in cobalt but which can also inhibit or retard the tendency for the precipitation of TiC type of PPB carbides should be investigated as it offers potential as a prospective P/M disc material. A Soviet cast nickel base blading superalloy, ZhS6-K [22], with the nominal composition of Ni-11Cr-5W-5Al-4.5Co-4Mo-2.5Ti-0.15C-0.02B has been chosen to be investigated for P/M modification. This alloy is closely akin to the Western grade IN-100. Three chemistry variants of the P/M alloys designated as DMP-1 (with hafnium and low boron), DMP-2 (with hafnium and high boron) and DMP-3 (sigma prone composition with low boron and without hafnium) have been critically examined to bring out the effects of boron and hafnium on the powder consolidation behaviour, microstructure and mechanical properties.

1.3   SCOPE OF THE WORK

Chapter 2 traces the history of the development of superalloys in general and P/M nickel base superalloys in particular. A review of the alloying behaviour and developments in the powder production and processing techniques is followed by microstructural and analytical observations on the subject compositions - the loose powders as well as consolidated alloys. Effects of microstructure on mechanical properties are then discussed with particular reference to P/M superalloys.

In Chapter-3, details of the experiments conducted to prepare the alloys are presented. After a brief discussion on the vacuum induction melting and inert gas atomization experiments, the powder characteristics are examined. Details of the various experiments performed to chracterize the consolidated alloys are also presented.

Chapter-4 begins with an evaluation of the as-cast alloys in terms of microstructure and mechanical properties. This is followed by the results on the powder characterization which includes Auger electron spectroscopic (AES) studies on the alloy powders to show the effects of boron and hafnium on the composition of the powder surface.

Chapter-5 presents the studies carried out to optimize the consolidation parameters of each alloy. Effects of variations in consolidation temperature on microstructure and mechanical properties are discussed in relation to the levels of boron and hafnium. Scanning Auger microprobe analysis of the in-situ fracture surface of these alloys is presented, which indicates the significant influence of hafnium on the activity of sulphur. Results of the phase identification studies by X-ray and electron diffraction are also presented.

In Chapter-6, the effects of heat treatment variations on the microstructure and mechanical properties of the three alloys are presented and discussed. A heat treatment schedule having a solutionizing temperature below the γ' solvus is found to be optimum for these alloys. Limited forging experiments carried out on the as-HIP σ-prone alloy are also included

in this chapter.

The results of the work are summarized in Chapter-7 which also lists the main conclusions drawn from the research work as well as the suggestions for further work.

CHAPTER 2

POWDER METALLURGY PROCESSING OF NICKEL BASE SUPERALLOYS

2.1   INTRODUCTION

Ever since the introduction of Nimonic range of alloys in the early 1940s [1], nickel base superalloys have been at the forefront of gas turbine materials technology. Intensive efforts to increase the temperature capability of these alloys have resulted in the development of highly complex compositions, the processing of which has not only led to several technological breakthroughs but has also generated tremendous scientific interest the world over. Though based on the empirical approach of the early days of alloy development, the present scientific understanding of the metallurgy of nickel base superalloys has reached a high level of sophistication. The effects of various alloying elements on the microstructure and mechanical properties of superalloys and the underlying strengthening mechanisms now appear to be well understood [1 - 3]. The present chapter briefly describes the alloying behaviour of nickel base superalloys and the limitations in the working of advanced superalloys which led to their processing by P/M route. Current powder making and consolidation techniques, with emphasis on hot isostatic pressing (HIP) technique have also been discussed. Problems of P/M superalloy technology particularly with reference to surface composition and structure of the powder particles and their effects on the HIP consolidation behaviour have been

highlighted. Available literature on the influence of HIP parameters and minor chemistry variations on the structural and mechanical behaviour of P/M superalloys is briefly surveyed bringing out the aspects of further work that merit attention.

2.2   METALLURGICAL BEHAVIOUR OF NICKEL BASE SUPERALLOYS

2.2.1   Effects of Alloying Elements

Table 2.1 presents the effects of alloying elements in nickel base superalloys. Almost, all nickel base super-alloys contain 10 to 20% chromium and 6 to 10% aluminium and titanium. As chromium and aluminium form adherent, protective oxide scales, they confer oxidation and hot corrosion resistance to the alloy at high temperatures. Whereas chromium mainly partitions to the matrix (γ) forming solid solution with nickel and other constituents, aluminium and titanium primarily form the hardening precipitate γ', Ni_3 (Al, Ti). Titanium also forms primary MC carbides. Most of the advanced superalloys contain 12 to 20% cobalt. Increase in Co is reported to raise the γ' solvus thereby improving the temperature capability of the alloy. Heslop [18] in a study on Nimonic 80A and Nimonic 90 (the former has no cobalt and the later has 18% cobalt) showed that the Ni-Cr-Co matrix has lower solubility for Al and Ti than the Ni-Cr matrix implying that the volume fraction of γ' would be more in the superalloys containing cobalt. In a study on Waspaloy, Maurer et al [19] showed that although there is little effect of cobalt on the elevated temperature tensile properties, the stress rupture life of the alloy at 1005 K and 552 MPa

TABLE 2.1   EFFECTS OF ALLOYING ELEMENTS IN NICKEL-BASE SUPERALLOYS

ELEMENT	EFFECT
Chromium	Mainly provides oxidation and hot corrosion resistance, also strengthens the matrix.
Cobalt	Goes into solid solution (matrix) and also raises γ' solvus by decreasing the solubility of matrix for the hardening phase γ'.
Molybdenum and tungsten	Considerably enhance the strength of the matrix and promote the formation of M_6C carbides when more than 6 at%.
Aluminium and titanium	Form the hardening precipitate γ', $Ni_3(Al\ Ti)$. Al also increases oxidation resistance and Ti forms MC carbides.
Niobium	Forms γ'', Ni_3Nb which enriches γ'. Also forms orthorhombic Ni_3Nb and MC carbides.
Tantalum	Strengthens solid solution and also forms MC carbides.
Hafnium	Forms MC carbides and also promotes eutectic $\gamma + \gamma'$ formation in cast alloys. Raises γ' solvus but decreases alloy solidus.
Boron and zirconium	Improve rupture life by precipitating at grain boundaries. In addition, Zr acts as scavenger of sulphur and B forms borides.
Carbon	Forms a series of carbides such as MC, M_7C_3, $M_{23}C_6$ and M_6C depending upon the concentrations of other elements.

decreases considerably with decrease in cobalt content from 13.5% to zero. In a comprehensive study on Udimet 700 (Ni-17Co-15Cr-5Mo-4Al-3.5Ti-0.06C-0.025B), Jarrett and Tien [21] found that creep resistance at 1033 K remained unaffected when the cobalt level was decreased from 17 to 8%. Marginal decrease in YS and UTS was attributed to the reduction in the volume fraction of fine γ ' (total content of γ ' remaining the same). Increase in the aging temperature, however, helped in producing more fine γ ' precipitates implying that reduction in cobalt makes the alloy highly temperature sensitive [21]. However, in a Soviet study [20], the addition of 10 to 12% cobalt to a nickel base alloy containing a fairly high proportion of W and Mo did not improve the creep properties ; apparently, lower content of cobalt is not in a position to influence the properties of superalloys high in refractory elements. The underlying mechanism is suggested to be the effect of these refractory elements in decreasing the solubility of the matrix for Al and Ti [17]. Advanced Soviet cast/wrought superalloys [22] thus contain large amounts of W and Mo and relatively less Co but possess strength levels comparable to their Western counterparts as has also been demonstrated in recent studies on the Soviet wrought superalloy EI-929 [23] and cast alloy ZhS6-K [24]. Except for the popular disc alloy Rene'95, which has 8% Co, most P/M superalloys contain 15 to 18% Co; apparently, there appears to be further scope for processing low cobalt high performance superalloys by P/M route.

Solid solution strengthening provided by the "big four", i.e., W, Mo, Ta and Nb is attributed to their large atomic size difference in relation to nickel (Fig. 2.1). In addition, when W and Mo are in a proportion exceeding 6 atomic %, precipitation of M_6C carbides is favoured [25]. M_6C carbides are more stable at elevated temperatures than MC or $M_{23}C_6$ carbides [26]. In contrast, niobium stabilizes primary MC carbides. Niobium, being the most electropositive element of the refractory metals, has a strong affinity for the formation of Ni_3Nb phase [27]. Nb, therefore, increases the volume fraction and solvus temperature of γ' phase. Guo and Ma [28] have shown that with increase in Nb from 0 to 2.5%, the amount of γ' increases by 3.7%. They have also suggested that niobium increases the resistance of γ' to dislocation cutting, thereby increasing the high temperature strength of the alloy. Addition of hafnium has received wide attention in recent years because of its effect on the refinement of carbides and improvement of casting characteristics [29, 30]. Since hafnium has approximately 7% solubility in γ' [29] as compared to 1% in nickel [30], increase in hafnium will result in higher volume fraction and solvus temperature of γ' leading to improved temperature capability, as demonstrated by Miner [13]. Refinement of carbides is not only helpful for increasing the ductility of cast alloys but also improves the forgeability of wrought superalloys. However, a precise control is essential to avoid the occurrence of incipient melting during hot working of wrought superalloys because hafnium also lowers the solidus [13, 15].

II A	III A	IV B					PERCENT DIFFERENCE IN ATOMIC DIAMETER FROM NICKEL

The figure shows a partial periodic table:

II A	III A	IV B
· ··	-21 B	-27 C
+29 Mg	+6 Al	

		IV A	V A	VI A	VII A	VIII A		
		+9 Ti 6.66	+5 V 5.66	+3 Cr 4.66		+3 Fe 2.66	+1 Co 1.71	0 Ni 0.66
		+28 Zr	+18 Nb 5.66	+12 Mo				
			+18 Ta 5.66	+13 W 4.66				

Legend:
- ☐ ELEMENT PARTITIONS TO γ
- ▨ (dotted) ELEMENT PARTITIONS TO γ'
- ▨ (hatched) ELEMENT PARTITIONS TO GRAIN BOUNDARY

Nv label points to Fe.
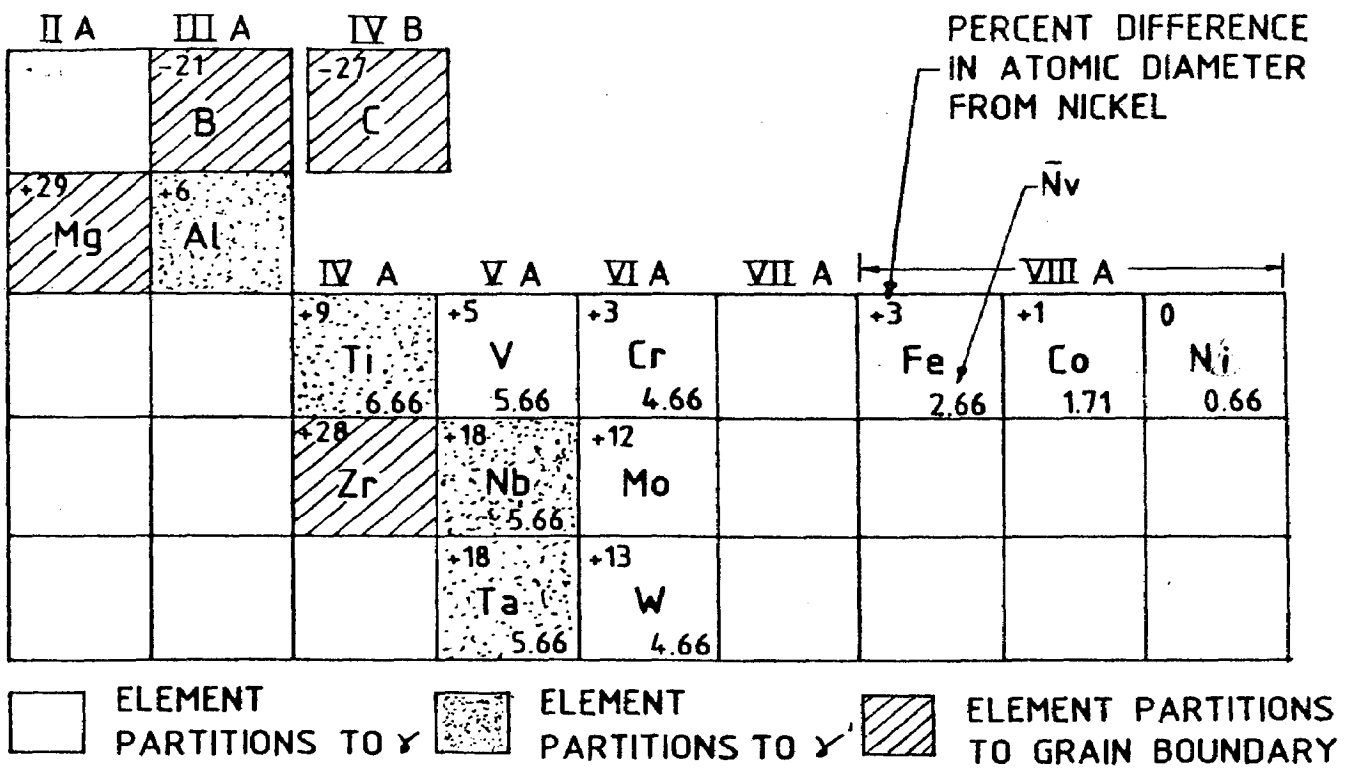
2.1   Elements important in the constitution of nickel base alloys[1].

The most remarkable effects in superalloys are due to minor additions of boron and zirconium. Although it is well known that creep properties of nickel base superalloys improve when boron and zirconium are added in trace amounts [33], the underlying mechanisms are not fully understood. However, it is generally agreed that on account of their odd atomic size mismatch i.e., -21% for B and + 28% for Zr (Fig.2.1), and low solubilities in γ as well as γ ', boron and zirconium segregate to grain boundaries [15, 16]. Boron is also reported [16] to reduce secondary carbide precipitation at grain boundaries by forcing retention of carbon in solution and form borides, which are more amenable to heat treatments. Boron is thus believed to supress the tendency of the precipitation of such undesirable phases at the grain boundaries as would normally be prompted by the presence of carbides [16]. Zirconium mainly acts as a scavenger of sulphur [16]. Calcium, magnesium, rhenium and cerium (when added in minute proportions) improve workability and oxidation resistance [16].

Because of their complex and highly alloyed compositions, advanced nickel base superalloys are susceptible to the formation of plate-like, topologically close-packed (TCP) phases, such as sigma, Laves, Mu etc. (Fig.1.1), which are detrimental to elevated temperature mechanical properties, particularly the long-term stress-rupture life and tensile ductility [2, 34, 35] A careful compositional balance is, therefore, necessary not only to achieve the desired properties but also to prevent the formation of these TCP phases [34, 35]. Such a balance

can be obtained by using PHACOMP technique, which has proved to be very useful in the development of high performance super-alloys [36]. The technique makes use of the electron hole theory to determine the mean electron hole number of the matrix after the composition of secondary phases formed is discarded from the whole alloy [35, 36].

2.2.2   Strengthening Phases

Austenitic Matrix:-   As already indicated, nickel base super-alloys have fcc matrix phase and it contains several solid solution strengtheners such as Cr, W, Mo and Ta whose strengthen-ing effects are proportional to the difference in atomic size between the matrix and the solute atom.

Gamma Prime Precipitates :- γ' is a coherent, ordered, inter-metallic compound mainly based on the Ni_3Al composition. The lattice structure of γ' is also fcc with nickel atoms at face centres and aluminium atoms at cube corners. The γ' precipitates strengthen the alloy by various mechanisms described in detail by Decker [2]. In simple terms, coherency strains hinder the movement of dislocations to penetrate the precipitates. However, with increasing stress, these dislocations do penetrate by cutting or looping depending upon the size of γ' precipitates, once the antiphase boundary (APB) energy barrier of the ordered structure of γ' has been overcome. Copley and Kear [37, 38] have shown that dislocation penetration of γ' particles is the major strengthening mechanism in nickel base superalloys having large volume fraction of the hardening phase γ'.

They have demonstrated that the strength of these alloys is governed by an equation:

$$\tau_c = \frac{\gamma_0'}{2b} - \frac{T}{b\gamma_0''} + \frac{1}{2}\left(\tau_0 + \tau_p\right)$$

where τ_c is the critical resolved shear stress,

γ_0' is the APB energy,

γ_0'' is the radius of γ' precipitate,

b is the Burger's Vector,

T is the dislocation line tension,

τ_0 is the lattice friction stress of the matrix and

τ_p is the lattice friction stress of the particle.

The γ' phase has high temperature stability. In fact, its strength increases with increase in temperature upto approximately 1200 K depending upon the alloy composition [39]. The morphology and structural stability of γ' depend on the misfit parameter, δ, which is given by

$$\delta = \frac{a_p - a_m}{\bar{a}}$$

where a_p is the lattice parameter of γ' precipitate,

a_m is the lattice parameter of matrix and

$\bar{a}$ is the average lattice parameter.

When the size of γ' or misfit parameter is small, the γ' particles tend to acquire a spherical shape [40]. For alloys having large misfit parameters, γ' precipitates are cuboidal with their faces parallel to $\{100\}$ matrix planes. Since $\{100\}$ planes are "soft", elastic deformation is most easily

accommodated when these planes are the matching planes. The misfit parameter depends on composition and heat treatment. Elements such as niobium and titanium tend to increase it [41]. The misfit parameter can also be altered by an appropriate aging treatment. When the misfit is large, deformation tends to occur by the well known mechanism of Orowan dislocation looping of the precipitates, leading to work hardening. In contrast, when the misfit is small, particle shearing can occur [41].

Carbides:- Most common types of carbides which precipitate in nickel base superalloys are MC, M_6C and $M_{23}C_6$.

(i) MC carbides are fcc in nature, generally assume a blocky or script like morphology and are believed to form below the *liquidus* temperature. They tend to degenerate with increasing temperature, unless the alloys are high in niobium, tantalum and hafnium — these elements have a stabilizing influence on MC carbides. According to Zheng and Cai [42] formation of these carbides follows the order of preference as:

$$HfC \longrightarrow NbC \longrightarrow TaC \longrightarrow TiC$$

which is in contrast to that proposed by Sims and Hagel [1], i.e.,

$$TaC \longrightarrow NbC \longrightarrow TiC \longrightarrow VC$$
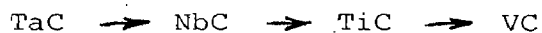
Although MC carbides have a very high solvus temperature almost *exceeding* the solidus of the alloy, they are unstable at intermediate temperatures, decomposing to $M_{23}C_6$ at temperatures in the range of 1023 to 1143 K or possibly degenerating to

M_6C at temperatures of 1223 to 1323 K provided the alloy has a sufficiently large Mo + W content. Pigrova and Levin [43] have demonstrated that in the case of Soviet superalloys containing high proportions of W and Mo, carbides decompose according to the reaction:

$$MC \longrightarrow M_{23}C_6 \longrightarrow M_6C$$
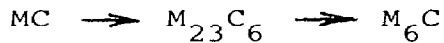
as aging temperature and time increase.

(ii) M_6C carbides which have a complex cubic crystal structure generally precipitate at the grain boundaries and possess a higher temperature stability in comparison with the $M_{23}C_6$ carbides. Thus, M_6C carbides are more beneficial for wrought superalloys in controlling the grain size. They mostly assume blocky and spheroidal morphologies but needle-shaped (Widmanstatten type) M_6C precipitates have also been reported in some alloys [1,2]. According to Pigrova and Levin [43] who conducted a phase analysis study on several Soviet superalloys, M_6C is difficult to distinguish from $M_{23}C_6$ and likely to have the formula $(Ni\ Co\ Cr)_4(Mo\ W)_2C$. Other elements such as Si are also likely to enter. [44].

(iii) $M_{23}C_6$ carbides are prominent in alloys containing high chromium content. They have a complex cubic structure, mostly form along the grain boundaries and are stable at intermediate temperatures between 1143 and 1253 K. Depending upon the composition, M is likely to vary. For example, when W and Mo are present, the composition of the carbide may be $Cr_{21}(MoW)_2C_6$ [1]. Nickel and cobalt can also substitute for chromium.

Because these carbides mostly precipitate at grain boundaries, they provide creep strength by increasing resistance to grain boundary sliding at elevated temperatures. The deformation is accommodated either by cracking of these carbides or by interfacial decohesion leading to intergranular fracture. Carbides are frequently the initiation sites for high temperature creep failure. Cellular morphology of carbides in nickel base superalloys is found to be detrimental to the mechanical properties. Another effect produced by grain boundary $M_{23}C_6$ carbide precipitation is the formation of a precipitate-free zone (PFZ) which has significant effect on the rupture life of nickel base alloys. If the PFZ becomes wider or much weaker than the matrix, deformation would concentrate there, leading to a premature failure [45].

Borides:- Boron, as mentioned earlier segregates to grain boundaries in elemental form. In addition to occupying vacancies and lowering diffusion rates in the boundaries, boron also forms borides primarily of the M_3B_2 type, largely seen at grain boundary sites. These borides being hard, refractory precipitates, tend to compensate the effects of PFZ and also delay the onset of grain boundary tearing thus increasing the creep resistance of the alloy.

2.2.3   Effect of Heat Treatment

An optimum combination of mechanical properties in nickel base superalloys, which are strengthened by the precipitation of γ' and carbides, is achievable only by an appropriately

tailored heat treatment schedule. The selection of a heat treatment mainly depends upon the composition, i.e., the volume fraction of γ' in a particular alloy. In practice, the heat treatment of superalloys consists of two major sequences:

(i) Solution annealing at a high enough temperature to completely dissolve γ' precipitates and $M_{23}C_6$ type of carbide precipitates. This would facilitate the homogeneization of the microstructure. The γ phase (matrix) can then be retained in a supersaturated state, if the cooling is carried out at a sufficiently fast rate; air or oil quenching is the common practice . The annealing temperatures vary from 1273 to 1500 K depending upon the amounts of γ' forming elements in the alloy. Some grain growth is usually unavoidable in this heat treatment.

(ii) Annealing at temperatures in the heterogeneous $\gamma+\gamma'$ region mainly with the objective of controlling grain size and volume fraction, morphology and size distribution of precipitates. Various parameters which influence these structural features are temperature, holding time, cooling rate and number of heat treatment stages.

Fig.2.2 shows the scheme for heat treatment of γ'-hardened superalloys [46]. Depending upon the volume fraction of γ', the heat treatment would consist of several stages. A four stage heat treatment generally used for alloys containing a γ' fraction of 40 to 45% volume, such as Udimet 700, is given below [46]

VOL. % γ'

20 35 45 60

1 : SOLUTION TREATMENT

234 : AGEING TREATMENT
(No.OF STAGES)

SOLUTION
TEMPERATURE
FOR γ'

--- 1140-1170 °C

--- 1070-1110 °C

--- 980-1020 °C

γ $\gamma + \gamma'$ γ'

TEMPERATURE

SUM OF γ'-FORMING ELEMENTS
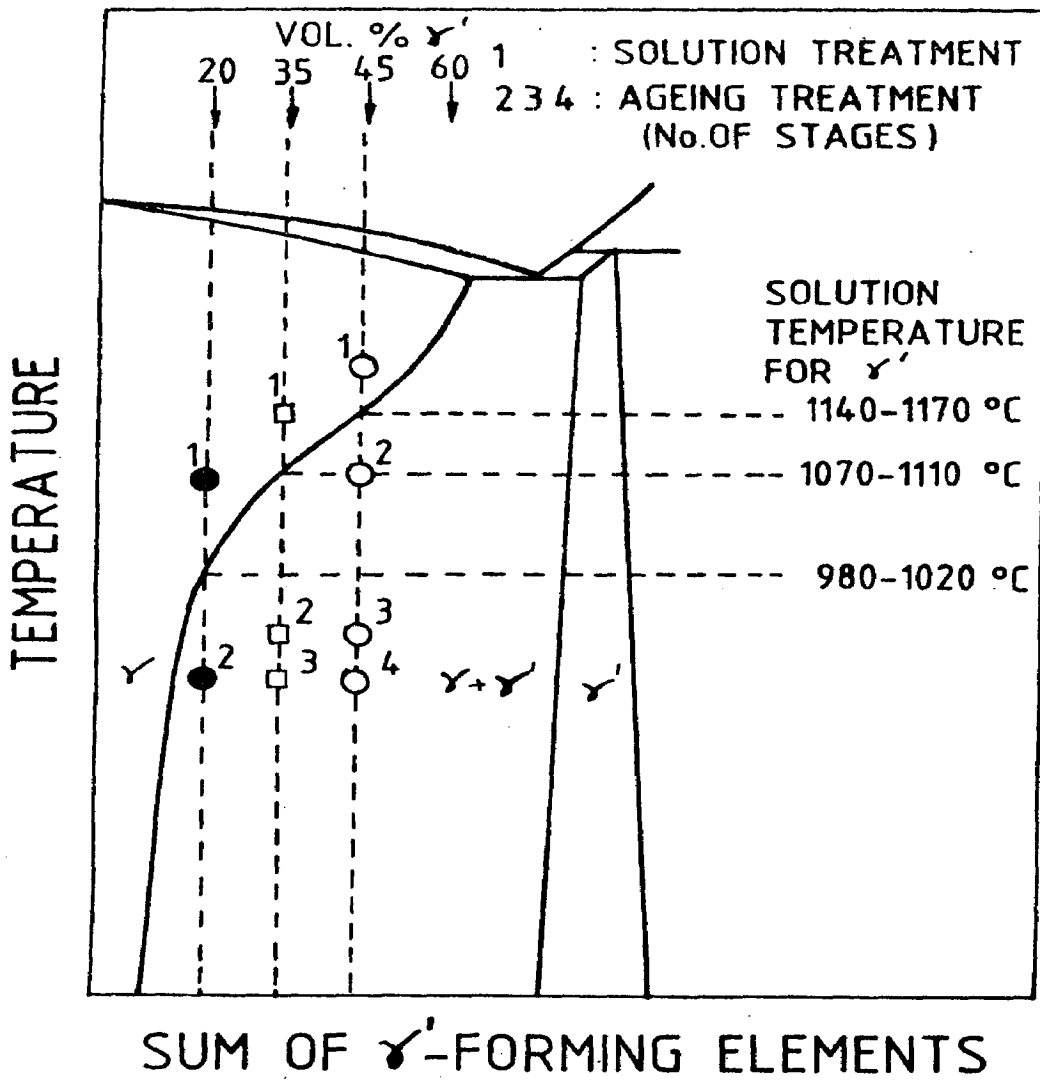
2.2   Scheme for heat treatment of γ'-hardened nickel base superalloys [46].

(a)   solution annealing at a temperature above 1373 K,

(b)   first aging at a temperature between 1323 and 1353 K

(c)   second aging at about 1153 K for stabilizing γ' precipi-
        tates formed during stage (ii) and also to nucleate
        and grow additional fine γ' precipitates; carbides
        are also precipitated,

(d)   third aging at about 973 to 1023 K to increase the amount
        of fine γ' precipitates.

In the case of alloys containing less than 30% volume
fraction of γ', two- or three-stage heat treatments are used.
P/M superalloys acquire an optimal combination of properties
usually after 3-stage heat treatments and occasionally 4-stage
treatments. Typically, aging temperatures are low in P/M alloys.

2.3   **ADVANTAGES OP P/M PROCESSING**

With increase in the solute content of nickel base
superalloys, although the high temperature capability of the
alloy would increase by virtue of the increase in volume fraction
and solvus of γ', the solidus decreases. Consequently, hot
working temperature range of these alloys would drastically
narrow down. More significantly, increased chemical segregation
and susceptibility to the formation of undesirable TCP phases
make these highly alloyed compositions unsuitable for wrought
applications, chiefly the turbine discs of aeroengines which
demand high tensile strength (for protection against overspeed
burst), good low cycle fatigue (LCF) strength (to resist LCF
conditions arising out of engine start-run-stop cycles) and
moderately high creep strength in the intermediate temperature

range of 800 to 1000 K. The use of powder metallurgy route has greatly facilitated the achievement of these property goals in highly alloyed compositions by producing a segregation-free, homogeneous and fine-grained material [47], leading to the establishment of industrial scale powder-making and consolidation technologies for their processing. Major advantages of P/M route for the processing of superalloys may be summarised as follows:

(i) Compositional segregation is reduced to the scale of the powder particle size and may even be fully eliminated if particles are solidified sufficiently rapidly. The product obtained after consolidation, therefore, possesses a homogeneous microstructure leading to significant improvement in mechanical properties such as ductility and fatigue strength [48]. Reduced segregation also results in higher incipient melting temperatures thereby broadening to some extent, the otherwise narrow hot working range [49].

(ii) Increased amounts of solute elements can be added in P/M alloys. The newly emerging rapid solidification processing (RSP) technology heavily depends upon this advantage to produce microcrystalline alloys [50]. Mechanical alloying [51] is another important P/M technique which has resulted in the development of a new class of materials, viz., the oxide dispersion strengthened (ODS) superalloys [52,53].

(iii) Preforms obtained from the P/M route offer better workability as compared to a cast billet [54]. Several innovative

techniques such as isothermal forging to near-net shape [55] and Gatorizing [56] through superplastic forming have been the outcome of P/M approach.

(iv) P/M route possesses direct shape-making capabilities with the advent of several new consolidation methods such as hot isostatic pressing (HIP) [57], cold isostatic pressing followed by sintering [4] and consolidation at atmospheric pressure (CAP) [58].

(v) The macrosegregation-free, fine-grained microstructure of a P/M product facilitates better ultrasonic detection ability for minute flaws [6,59].

(vi) Although TCP phases may form in some advanced P/M super-alloys, they are not likely to assume the harmful needle-shaped morphology because of the nearly absent segregation and low volume fraction of carbides.

Use of P/M technology has thus facilitated the processing of several highly alloyed superalloy compositions which were otherwise not considered feasible for turbine disc applications and current P/M nickel base superalloys are much stronger than the conventional wrought superalloys as shown in Fig. 2.3. Tensile and stress-rupture properties of a few important current P/M superalloys are listed in Tables 2.2 and 2.3.

2.4 SUPERALLOY POWDER PRODUCTION

Several processes such as argon atomization process [4,67,69], rotating electrode process (REP) [4,68], soluble
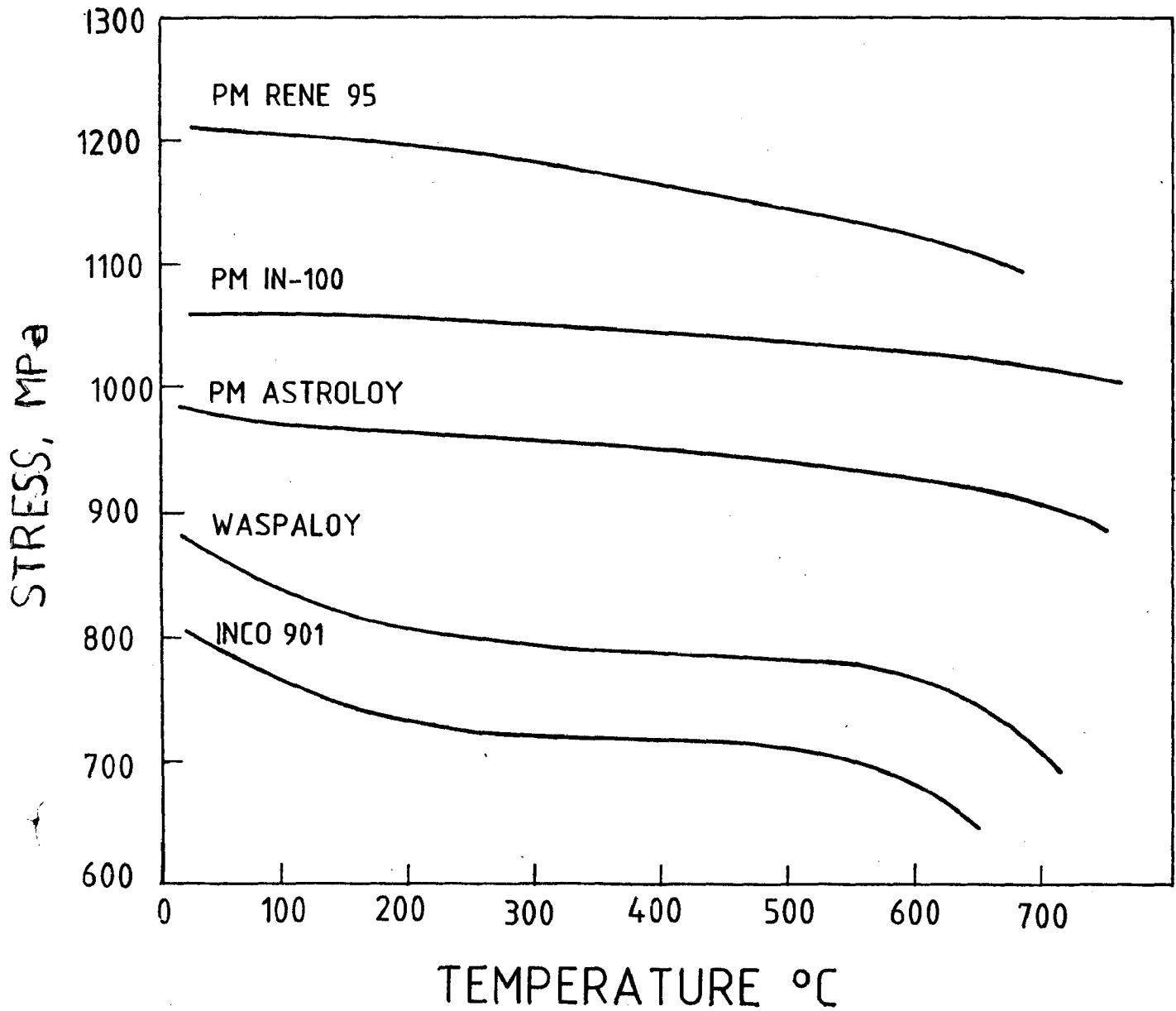
2.3   Comparison of 0.1% proof stress of some current disc super-
alloys [5].

Table 2.2 Tensile properties of current P/M disc superalloys

S.No	Alloy Grade	Condition	298 K				Elevated temperature				References
			0.2%YS MPa	UTS MPa	El %	RA %	0.2%YS MPa	UTS MPa	El %	RA %	
1	IN-100[1]	As - HIP	1048	1491	10	-	1008	$\frac{978K}{1176}$	9	-	56,61,62
		HIP and gatorized	1120	1610	26	28	2054	1263 923K	21	25	
2	RENE-95[2]	As - HIP	1257	1671	20	20	1096	1497	15	17	63,64,65
		HIP and isoforged	1268	1657	20	22	1147	1453 1033K	19	20	
3	Astroloy[3]	As - HIP	826	1241	15	11	955	1080 978K	27	40	9,61
4	MERL 76[4]	As - HIP	1034	1482	15	15	1014	1482	15	15	
		HIP and isoforged	1175	1666	15	18	1131	1439 1033K	18	18	
5	AF 115	As - HIP	1100	1510	16	17	855	1310	8	10	66

1 Heat treated - 1393K/2hr/OQ + 1144K/40 min AC + 923K/24hr/AC + 1033K/4hr/AC

2. Heat treated - 1393K/2hr/OQ + 1144K/1hr/AC + 923K/24hr/AC

3 Heat treated - 1393K/4hr/OQ + 1144K/8hr/AC + 1255K/4hr/AC + 955K/24hr/AC + 1033K/8hr/AC

4 Heat treated - 1536K/2hr/OQ + 1163K/40 min AC + 1253K/45 min/AC + 923K/24hr/AC + 1033K/16hr/AC

Table 2.3 Stress-rupture properties of current P/M disc superalloy

S.No	Alloy Grade	Condition	Temperature/ (K)	Stress MPa	Time to rupture Hours	Elonga-tion %	Reference
1	IN-100[1]	HIP and gatorized	1005	748	35	12	56,61,62
2	RENE-95[2]	As - HIP	923	1034	29.5	5.5	63,64,65
		HIP and isoforged	923	1034	45.0	5.0	
3	Astroloy[3]	As - HIP	1033	590	36	13	9,61
4	MERL 76[4]	As - HIP	1005	1050	23.0	5.0	7
5	AF 115	As - HIP	1033	59	15.0	-	66

1. Heat treated - 1393 K/ 2hr/ OQ + 1144K/ 40 min/ AC + 923K/ 24hr/ AC + 1033K/ 4hr/ AC

2. Heat treated - 1393K/ 2hr/ OQ + 1144K/ 1hr/ AC + 923K/ 24hr/ AC

3. Heat treated - 1393K/ 4hr/ OQ + 1144K/ 8hr/ AC + 1255K/ 4hr/ AC + 955K/ 24hr/ AC + 1033K/ 24hr/ AC

4. Heat treated - 1536K/ 2hr/ OQ + 1163K/ 40 min/ AC + 1253K/ 45 min/ AC + 923K/ 24hr/ AC + 1033K/ 16hr/ AC

gas process [4] and rotating disc process also known as centri-
fugal atomization [4,69] have been developed during the last
fifteen years and most of them have become commercial practice.
The basic principle is the same, i.e., all these processes
are invariably performed in an inert atmosphere or vacuum to
overcome the problem of irreducible oxide formation by the
reactive elements such as Cr, Ti and Al present in all the
P/M superalloys. Among all the available processes, argon
gas atomization is the most economical and widely used process
for the manufacture of a variety of superalloy powders. Being
the process employed in this research work, it is described
in some detail here.

2.4.1   Argon Atomization Process

The process consists of remelting a superalloy ingot
in a vacuum induction melting furnace and allowing the molten
metal to pass through an orifice in a tundish as a vertically
downward straight stream into the atomizer. High velocity
jets of argon gas from the atomizer nozzle impinge on the molten
metal stream which is disintegrated into a multitude of droplets.
These droplets solidify into spherical particles during their
free fall in an argon filled chamber. Control of various process-
ing parameters such as argon gas pressure, gas velocity, the
melt superheat and the atomizer nozzle design is essential
in obtaining a high yield [69]. The coarse fraction of the
powder particles are prone to the development of entrapped
gas pores and the very fine fraction have higher oxygen contents

INERT GAS ATOMIZATION PLANT

VACUUM MELTING

ARGON GAS

T.V. CAMERA

CYCLONE SEPARATOR

ROOTS PUMP

POWDER COLLECTION
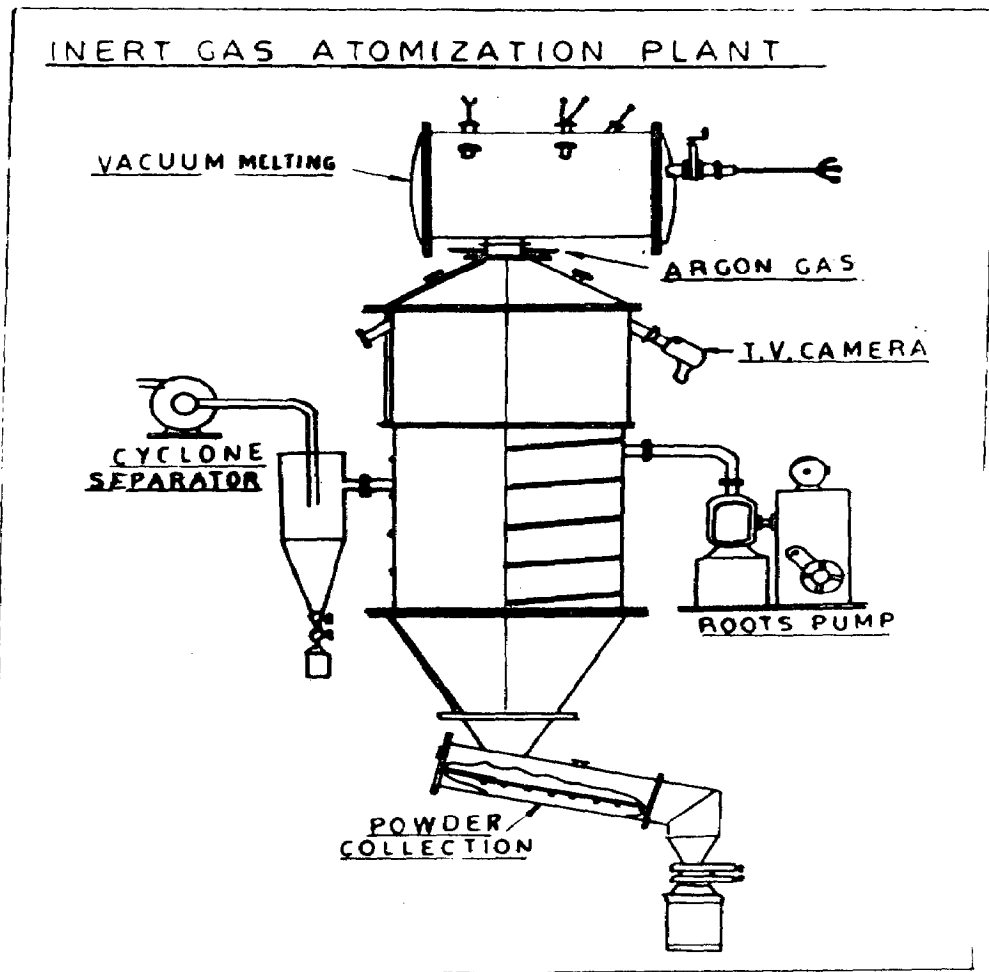
2.4   Schematic of argon-atomization facility at Defence Metallurgical Research Laboratory, Hyderabad [7].

thus compelling the screening of the coarsest (+36 to + 80 mesh) and the finest (< -325 mesh) fraction. Yet, the flexibility and the economical advantages offered by this process make it by far the most attractive. M/s. Crucible Inc., M/s. Special Metals, M/s. Kelsey Heyes (all in USA) and M/s. Henry Wiggin (UK) are some of the leading producers of the argon atomized superalloy powders. In India, only Defence Metallurgical Research Laboratory, Hyderabad [70] has set up an argon atomization facility of 50 kg melt capacity; the superalloy powders used in the present work were produced in this plant (Fig. 2.4). Important processing parameters used for the atomization of powders are described in Section 3.2.

2.5   POWDER CONSOLIDATION

Superalloy powders can be consolidated by forging, extrusion or hot isostatic pressing. Conventional P/M approach involving cold compaction followed by sintering in vacuum or inert atmosphere is not suitable for superalloy powders because of their poor cold compactibility arising out of their spherical morphology and high yield strength. When heat and pressure are simultaneously applied - as in pressure sintering - the powder consolidates to full density without residual porosity. When this pressure is isostatic - as in HIP - the densification will be truly uniform and isotropic. HIP is thus the most popular consolidation process for superalloys [71] and is also the method chosen in the present study.

2.5.1 HIP Consolidation of Powders

Hot isostatic pressing involves simultaneous application of temperature and isostatic gas pressure and is the most cost-effective process — particularly for producing near-net shapes [55 - 57]. A unique feature of this process is its ability to produce 100% density of the powder material.

The process requires canning or encapsulation as the first step : the powder is filled in a metallic, ceramic or glass container of the desired shape followed by evacuation and prolonged outgassing in vacuum at moderate temperatures to remove any adsorbed gases or moisture from the powder mass. The degassed capsule is then sealed in vacuum by crimp-sealing the evacuation tube connected to the body of the capsule. The capsule is then charged in the HIP autoclave and isostatically pressed under argon pressure at the desired temperature. Integrity of the capsule has significant bearing on the success of consolidation because any minute leak in the sealed capsule will result in incomplete consolidation. Effects of other processing parameters such as pressure, time and temperature also influence consolidation and are discussed in some detail in Section 2.7.

Two types of hot isostatic presses are in vogue, hot-loading type and cold-loading type. In the hot-loading type, the charge is preheated externally in a separate furnace and then transferred to the HIP autoclave. Hot-loading variety is preferred for production purposes in view of time saving.

In the cold-loading HIP, the charging is done in cold condition and the temperature and pressure are gradually raised to the desired level. The latter type of press is available at DMRL, Hyderabad and the present work has made use of this press according to parameters given in Section 3.3.

2.5.2 Mechanism of HIP Densification

One of the main differences between HIP and other consolidation techniques such as forging or extrusion is the degree of material flow. Whereas material flow and material transport are the greatest in extrusion, these are the least in HIP. The deformation in extrusion or forging breaks the oxide layers present on the powder particle surface and hence the PPB networks, if any, are broken up. Although gross particle deformation is virtually absent in HIP, several other mechanisms contribute to densification of the particles in HIP consolidation. These mechanisms may or may not involve material transport. For example, adhesion does not involve material transport [72]. Examples of processes involving both material flow as well as material transport are vaporisation and condensation of vacancies [73], surface lattice and grain boundary diffusion [74], plastic flow and grain boundary sliding [75]. Additionally, small distance flow processes such as recovery and recrystallization may also be important in HIP. All these processes are activated by the externally applied isostatic pressure and surface tension forces. Several models have been proposed to describe sintering process during hot pressing and the most

important ones are briefly described below:

(i)   Diffusion Model

Coble [76] has developed models for the first and final stages of hot pressing including both the applied pressure and the surface energy as the driving forces. The lattice diffusion and grain boundary models have been shown to follow the same time-dependent and particle size effects for neck growth and shrinkage as the earlier sintering models. Coble proposed that only driving force would be expanded as:

$$\text{D.F.} = \gamma + P_a \frac{R}{\pi}$$

where γ is the surface energy,

P_a is the applied pressure and

R is the radius of the powder particle.

For the intermediate stage of the hot isostatic process, Coble proposed an expansion to the Nebarro-Herring creep equation by incorporating the effect of surface energy as well as applied pressure. It is assumed that this adaptation can only provide an approximate densification rate because of differences in areas and path lengths for diffusion between the models and the actual case. It is further assumed that the effective stress on grain boundaries will not include a stress concentration factor due to porosity. As a result, the effective stress σ_{eff} for the later stage of the process will be $\sigma_{eff} = \frac{P_a}{D}$ where D is the theoretical density.

For the final stage of hot isostatic pressing, it is hypothesised that the driving force due to surface energy becomes

infinite as the pore size approaches zero at theoretical density. Therefore, for the final stage of hot pressing, the model involves the steady state diffusive flow of material between concentric spherical shells. The driving force is expressed in terms of the applied pressure and pressure difference across the pore surface and is given by

$$D.F. = \frac{2\gamma}{\gamma} + \frac{P_a}{D}$$

where γ is the surface energy,

γ is the pore radius, when the pore is approximated as cylinder,

P_a is the applied pressure and

D is the theoretical density.

This equation predicts that the densification rate is finite at theoretical density and matches well with a few experiments.

(ii)   **Power Law Creep Model**

Wilkinson and Ashby [77] proposed that the densification rate is related to the applied pressure and the constants "A" and "n" in the power law creep equation for the dense solid,

i.e. $\dot{\varepsilon} = A\sigma^{-n}$

where $\dot{\varepsilon}$ is the tensile strain rate and

σ is the tensile stress.

It is assumed that the first stage of consolidation occurs by neck formation between particles and the applied pressure forces the particles to deform their neighbours.

During the second stage in which the interconnected pores exist, the process is assumed to be similar to the creep of a thick-walled cylindrical shell. In the final stage, the process can be assumed to be almost like the pressure induced creep collapse of a spherical shell having isolated pores. The main drawback of this model is that particle sliding has been neglected.

(iii) **Generalised Model**

A generalised model involving effective pressure as the driving force and based on probability terms has recently been developed by Bhatt and Arunachalam [78,79] to describe the densification kinetics during hot isostsatic pressing. Effective pressure for pore closure is given by

$$P_{eff} = \left\{ \frac{P}{1-\theta} \right\} \theta$$

where P is the external pressure and

θ is the average porosity.

In the conventional approach, the effective pressure has been assumed to be equal to the external pressure. With the help of finite element analysis of the consolidation process and assuming power law creep under conditions of quasi-steady state creep, the average shear stress at the enveloping surface was shown to closely correspond to P_{eff} [79]. These shear stresses generated due to the unbalanced forces at the pore surface cause material flow into the pores. The densification rate at quasi-steady state is given by

$$\dot{\theta} = \sum_{i=1}^{m} 3 \dot{\varepsilon}_i (1-\theta)$$

where m is the number of independent mechanisms leading to compaction and

$\dot{\varepsilon}_i$ is the steady state creep rate in the ith mechanism.

For example, for the power law creep equation

$$\dot{\varepsilon}_i = A_i \left(\frac{\tau}{G}\right)^{n_i} exp \left(-\frac{Q_i}{RT}\right)$$

where A_i is a constant depending upon the mechanism, the microstructure and the physical properties of the material,

τ is the applied shear stress,

G is the shear modulus,

Q_i is the activation energy for creep by the particular mechanism,

n_i is a constant,

R is the gas constant and

T is the absolute temperature.

This model can be applied to calculate the contribution to the densification from the diffusion creep, dislocation creep, particle-sliding and grain boundary sliding mechanisms. It also facilitates the preparation of densification maps (HIP diagrams) for any set of processing and material parameters.

2.6   LIMITATIONS OF P/M PROCESSING

The progress of P/M superalloy technology got a set-back in 1980 with the crash of F-100 aircraft flying with an as-HIP superalloy disc [4]. Although this incident could not be conclusively

linked with any basic problem of P/M technology, the fact remains that the technology involves the handling of fine powders and greater demands are being placed on a precise control of a large number of processing parameters right from the ingot preparation stage. It is, therefore, appropriate to discuss the salient problems inherent in the existing powder-making and consolidation techniques.

2.6.1 Powder Cleanliness

Larson [80] carried out a series of experiments to determine the oxygen pick-up in argon-atomized IN-100 powder exposed under different conditions and concluded that the all-inert handling practice is unnecessary. However, it is essential to take utmost precautions during the handling of superalloy powders to avoid contamination from moisture, foreign material etc. It is also important that the pre-alloyed ingot should be free from surface defects, refractory inclusions etc., and must be extremely low in gas content. Slag or refractory inclusions introduced during ingot preparation or atomization stage are reported to influence the stress-rupture and low-cycle fatigue (LCF) properties if their size exceeds 100 μm [81-83]. Even the present non-destructive testing methods cannot reliably detect such small inclusions [110]. The problem can be solved by a judicious use of nozzle and tundish refractories and by avoiding the entrapment of slag during melting stage. A cut-off size for the use of coarse fraction is also helpful in screening out the coarse ceramic inclusions.

2.6.2   Porosity and Gas Content

Powders produced by REP process are generally free from internal gas porosity and ceramic inclusions and also contain much lower oxygen contents as compared to the powders produced by argon atomization process. Argon present as bubbles entrapped within the powder particles or as solid solution is more harmful than in the adsorbed state. Adsorbed argon can be removed by hot dynamic vacuum outgassing technique commonly employed before the HIP consolidation. Although occluded gas bubbles within powder particles get closed during consolidation they again open up during subsequent elevated temperature exposure [84,85]. This problem, known as thermally induced porosity (TIP), can be solved by using powders of size below 150 μm as entrapped gas porosity is usually found in size fraction above 150 μm. However, the most dangerous gas porosities are those situated between powder particles or at the triple point particle boundaries. These are attributed to the incomplete sintering or leaks developed during consolidation or to insufficient outgassing before densification. Studies carried out on low-carbon P/M Astroloy have shown the adverse effects of porosity on the tensile strength and ductility and also the creep-rupture properties [85]. Davidson and Aubin [86] have also reported the effect of varying amounts of inter-particle porosity on impact strength and tensile ductility of partially consolidated low - C Astroloy.

2.6.3 Chemical Homogeneity

The superalloy powder produced by REP process is bound to suffer from some chemical inhomogeneity because of segregation in the starting material i.e., the as-cast electrode. Larger powder particles originating at the centre of the electrode are solute-rich but the finer powder fraction coming from the edge of the electrode is poorer in solute content. Obviously, the REP powder will have a lower incipient melting temperature which will result in a narrower consolidation temperature range. In contrast, the argon-atomized powder offers a higher degree of homogeneity and freedom from macro - segregation. Rotating disc and soluble gas processes, by virtue of higher solidification rates attained, ensure much better chemical homogeneity and extremely low segregation.

2.6.4 Formation of PPB Networks

The problem of carbide precipitation at the prior particle boundaries (PPBs) is marked in HIP consolidated material. Several process variables and chemistry modifications which influence P P B-precipitation have recently been reviewed by Thamburaj et al [9]. While investigating the nature and origin of PPB-precipitation in low - C P/M Astroloy, Ingesten et al [87] surveyed similar work done in last ten years and concluded that an oxidised layer enriched in aluminium and chromium is formed on the surface of the particle as it is solidified from liquid. This film remains intact even during compaction and provides preferred sites for secondary carbide precipitation.

Using Auger electron spectroscopy (AES) Aubin et al [88] showed that the degree of PPB precipitation depends on the amount of adsorbed carbon and oxygen. Similar AES studies on several other alloys have also indicated the surface enrichment of titanium [8,88,89] and sulphur [88,89]. Nitrogen was not detectable by AES [93] but Davidson et al [86] have confirmed the presence of nitrogen on the powder surface using secondary ion mass spectrometry. Presence of boron at the powder surface has not been confirmed.

The PPB network provides an easy path for a crack to propagate thus adversely affecting the tensile properties particularly the ductility. Although the reasons for the PPB precipitation are not fully understood, it is generally agreed that PPB-precipitation can be minimized by reducing the total content of carbon and oxygen in the powder [87]. Reduction in carbon below 100 ppm has been found to virtually eliminate the formation of PPB-networks and produce significant improvement in tensile ductility [10]. However, control of carbon to such a low level is not only difficult in actual practice but the elevated temperture properties of such a low - C P/M superalloy are likely to suffer due to reduced grain boundary strength.

The PPB precipitation can also be minimized by making some minor additions. Additions of tantalum [12], niobium [12] and hafnium [13] have been shown to reduce the tendency of PPB precipitation. It is suggested that the presence of these stable carbide forming elements deplete the amount of dissolved

carbon in the matrix, thereby minimizing the PPB precipitation tendency. Role of these elements in P/M superalloys has been discussed in detail in Section 2.7.2.

The consolidation temperature has a significant influence on the formation of PPB networks. Although a controversy exists as to whether consolidation at temperature below the γ' solvus or above the γ' solvus should be used for minimizing PPB precipitation, some recent studies on Nimonic AP-1 have shown that a consolidation temperature above the γ' solvus is definitely beneficial in reducing the precipitation at PPBs [47,62,90,91].

The fact that the precipitation of carbides at PPBs is strongly temperature dependent has also led to several studies involving the heat treatment of the powder mass before consolidation or pre-consolidation intermediate temperature heat treatments. Dahlen et al [92] observed that the melt-formed MC type carbides are dissolved and substituted by $M_{23}C_6$ on heating an argon atomized low-carbon Astroloy powder at temperatures between 1223 and 1373 K but at higher temperatures MC carbides are prominent. Dahlen also observed that the mating surfaces between two or more particles are more susceptible to the nucleation of PPB precipitation than the free particle surfaces. Similar surfaces are likely to form during HIP consolidation. This study, therefore, suggested that suitable pre-heat treatment of the powder may homogeneously precipitate stable carbides inside the powder particles thus leaving little carbon available for redistribution during densification. This in fact became

the basis for two-stage consolidation technique. Although detailed information is not available on the aplicability of this technique but a recent study on Nimonic AP-1 [93] has conclusively illustrated the beneficial effect of the introduction of primary consolidation step at 1223 K before final consolidation at a temperature slightly below γ' solvus. This consolidation treatment not only produces a microstructure free from PPBs, but also ensures fine grain size [9,94].

Some thermo-mechanical measures ,such as the strain energizing process [95], in which the powder is subjected to heavy plastic deformation by cold rolling before HIP densification and critical straining of the as-HIP material followed by annealing at higher temperatures ,   have also been reported to minimize the tendency of PPB-precipitation.

2.7   STRUCTURAL AND MECHANICAL BEHAVIOUR OF P/M SUPERALLOYS

Mechanical properties of P/M superalloys are strongly dependent on their microstructures which are sensitive to changes in processing conditions. Minor elemental additions also affect the processing parameters which in turn greatly influence the microstructure and mechanical properties of P/M superalloys. The effects of these variables are briefly reviewed in the present section.

2.7.1   Effects of HIP Parameters

In a comprehensive study on low-carbon P/M Astroloy, Price et al [96] showed that consolidation must be carried out at a pressure above 15,000 psi (approximately 100 MPa)

for about 3 hours to achieve complete densification. For other P/M superalloys also these pressure and time conditions have been found to be adequate [13,47,61,63].

Variations in consolidation temperature considerably affect the microstructure and mechanical properties of the as-HIP material [7,9,61,93,96,97]. This behaviour is in fact dictated by the γ' solvus and solidus temperatures of the alloys. When consolidation is performed above γ' solvus, dissolution of γ' takes place. During cooling, reprecipitation of γ' occurs with coarser γ' particles precipitating at the grain boundaries and finer particles within the grains [9]. Due to the presence of carbides at the interdendritic or particle boundaries, grain growth, that might otherwise occur, is likely to be restricted. However, at temperatures considerably above the γ' solvus, in addition to γ', the carbides are also dissolved resulting in a coarse-grained structure. If the HIP temperature approaches solidus, which is possible particularly in the case of highly alloyed compositions having low solidus, precipitation of eutectic $\gamma + \gamma$' structure occurs [7]. Such a microstructure is detrimental to the tensile properties and creep ductility, although stress-rupture life is likely to improve on account of a coarse grain size. Hack and Eggar [98] and Symonds et al [99] observed that after an initial improvement with increase in HIP temperature, the impact strength of the P/M superalloy AP-1 dropped as the HIP temperature exceeded 1448 K. Creep ductility and fatigue life also showed a similar fall. This was attributed to the solutioning of

borides or boro-carbides and their subsequent reprecipitation
in the form of grain boundary films as a result of slow cooling
in the autoclave. In contrast, consolidation just below the γ'
solvus results in a bimodal distribution of γ' particles and
fine grain size leading to increased tensile strength. Fig.2.5
illustrates the effect of HIP temperature on the elevated tempera-
ture tensile and stress-rupture properties of low-carbon P/M
Astroloy [35]. Podob [97] also reports a similar behaviour.
HIP temperature much below the γ'-sulvus results in a micro-
structure dominated by residual dendrites of powder particles
[93]. Therefore, depending upon the type of alloy, consolidation
is carried out at a temperature below or above the γ' solvus.
Fig. 2.6 depicts the correlation between HIP temperature and
γ' solvus temperature for a few P/M superalloys [47].

Cooling rate in HIP after soaking is also an important
HIP parameter. As already discussed above, slow cooling through
boride solvus results in the formation of grain boundary films.
However, if the consolidation temperture is below the boride
solvus, formation of these boride films is likely to be avoided
irrespective of the change in cooling rate. Further,
controlled cooling from such a solutioning temperature develops
serrated grain boundaries which lead to improvement in intergranu-
lar strength and hence the elevated temperature properties
[100]. On the contrary, a slow cooling rate from HIP temperature
results in excessive precipitation of coarse intergranular
γ' leading to depleted availability of matrix Ti+Al for precipi-
tation during aging. Such microstructures are reported to
cause reduction in LCF life [98,99]. Solution treatment tempera-
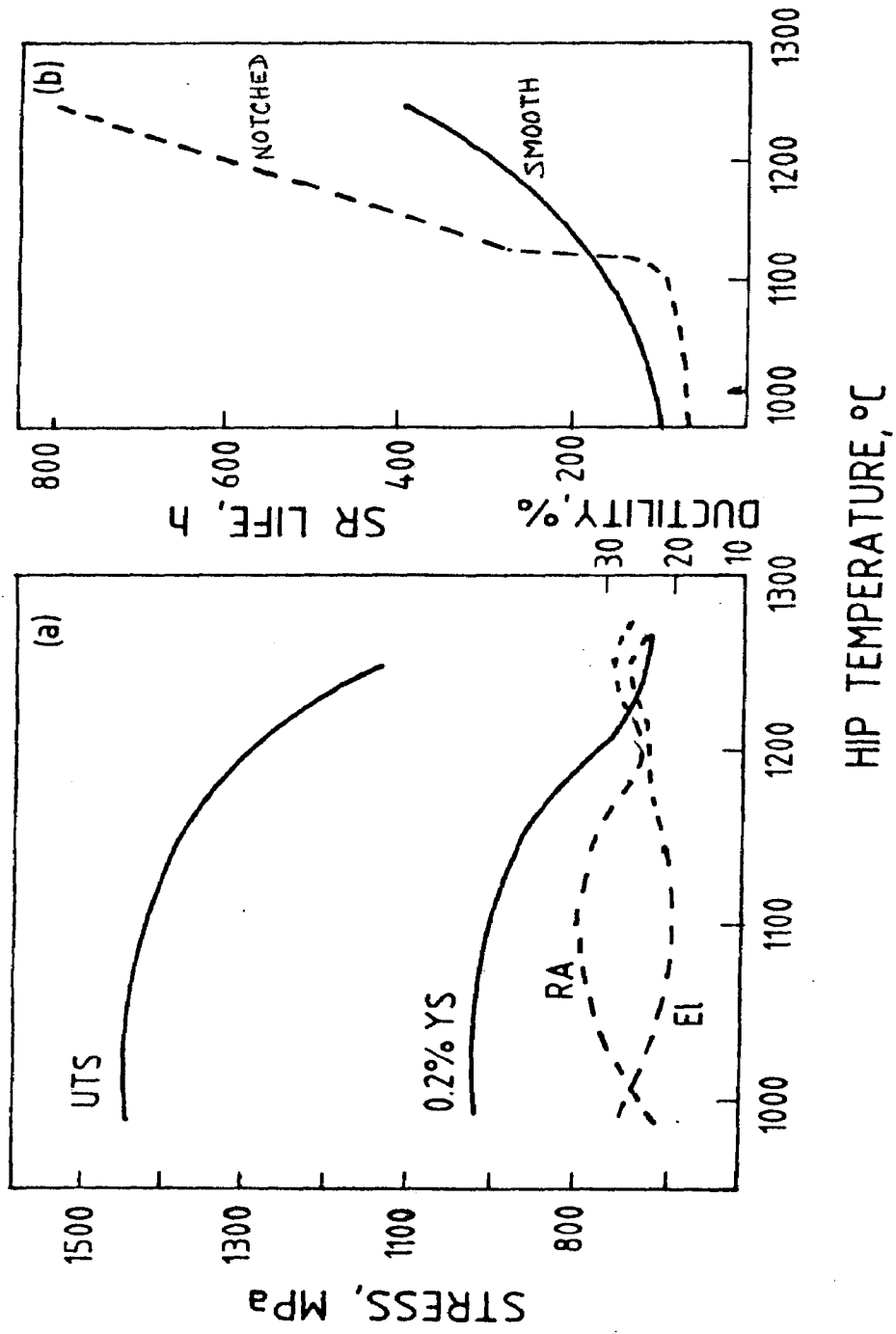
2.5 Variation of (a) 813 K tensile and (b) 1005 K/560 MPa stress rupture properties of low-C PM Astroloy with HIPing temperature[35].
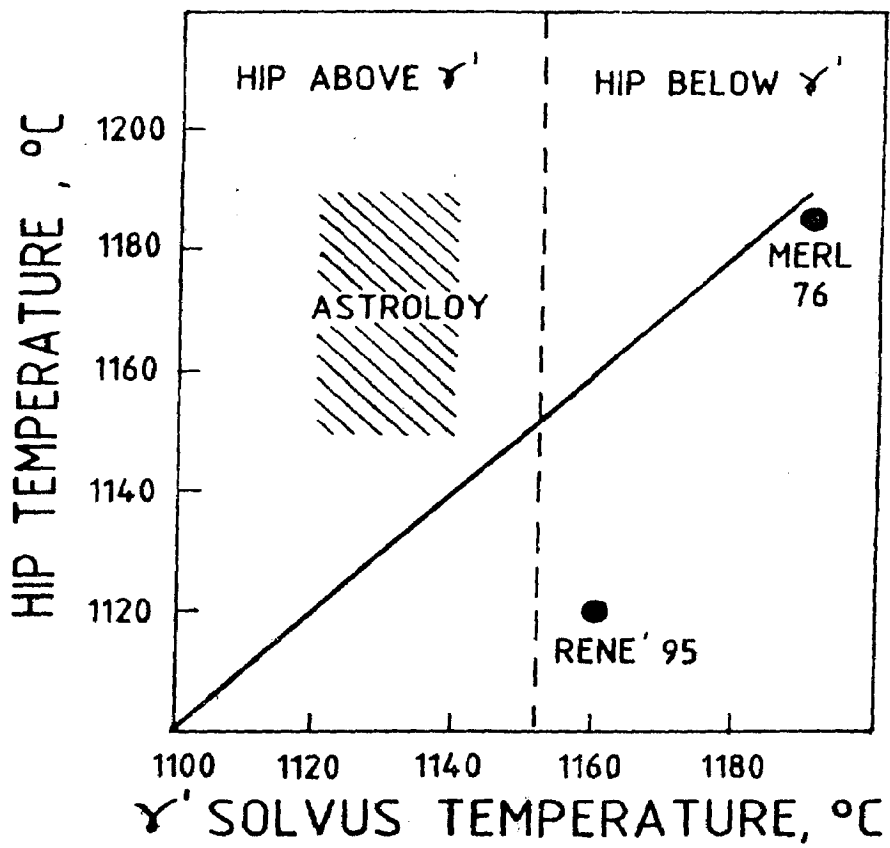
2.6 HIPing temperature versus γ' solvus for some PM superalloys [47].

tures required to dissolve such coarse γ' have to be very high. With modern hot isostatic presses, however, it is possible to achieve rapid cooling rates which not only help in avoiding the undesirable microstructural features of slow HIP cooling, but also increase the productivity of the HIP process [101].

2.7.2 Effects of Minor Chemistry Variations

Carbon:- Control of carbon has been found to be most critical in P/M superalloys. Cast nickel base superalloys contain a relatively high proportion of carbon (0.1 to 0.2%) to facilitate precipitation of intergranular carbides for increased resistance to grain boundary sliding at elevated temperatures. On the other hand, P/M superalloys contain less than 0.04% carbon to ward off the problem of undesirable PPB precipitation. Since the operating temperatures of P/M superalloys are moderate requiring moderate grain boundary strength, reduction in carbon to such low levels ($\cong$ 0.04%) is not likely to affect the desired mechanical properties. The early P/M superalloys did contain carbon upto 0.1% but the finding that carbon is partly responsible for the deleterious PPB precipitation provoked several studies to examine the effect of carbon on the mechanical properties of P/M superalloys [9,10,60,61,97]. Podob [97] observed that tensile and yield strengths increase but tensile ductility decreases with increase in carbon content in a low-carbon P/M Astroloy. In a study on the effect of carbon on both atomized and REP Astroloy powders, Aubin et al [88] found an improvement in tensile and creep ductility and impact strength when carbon was lowered. Reduction in carbon was also shown to reduce

the notch sensitivity, probably due to reduced PPB precipitation [60]. The work of Reichman and Smythe [10] also showed that if carbon is kept lower (below 100 ppm), desired grain size can be obtained by an appropriate selection of HIP and solution treatment temperatures. Larson [11] in an investigation on P/M IN-792 demonstrated that the room temperature and elevated tensile properties increased with increase in carbon; however, increase in carbon lowered the γ' solvus and decreased the grain size of the alloy.

Boron:- Another important element which is invariably present in most P/M superalloys is boron, although its concentration is usually below 250 ppm. Increase in boron with simultaneous decrease in carbon improves the elevated temperature mechanical properties and casting characteristics of cast superalloys [14,15,102]. This idea, generally known as B-C concept, has been successfully applied to several cast alloys but has not been investigated in relation to P/M superalloys to inhibit the tendency of PPB precipitation. However, in view of the observations made by Hack and Eggar [98] and Symonds et al [99] that HIPing of a low-carbon (less than 200 ppm) P/M Astroloy at a temperature above the γ' solvus causes the undesirable formation of boride films at the grain boundaries, application of B-C concept to P/M superalloys needs a careful examination.

Hafnium:- As already discussed in Section 2.2.1 hafnium is found to be beneficial in cast and wrought superalloys. However, its effect in decreasing the solidus is likely to influence the processing of wrought and P/M superalloys. Fig. 2.7 shows
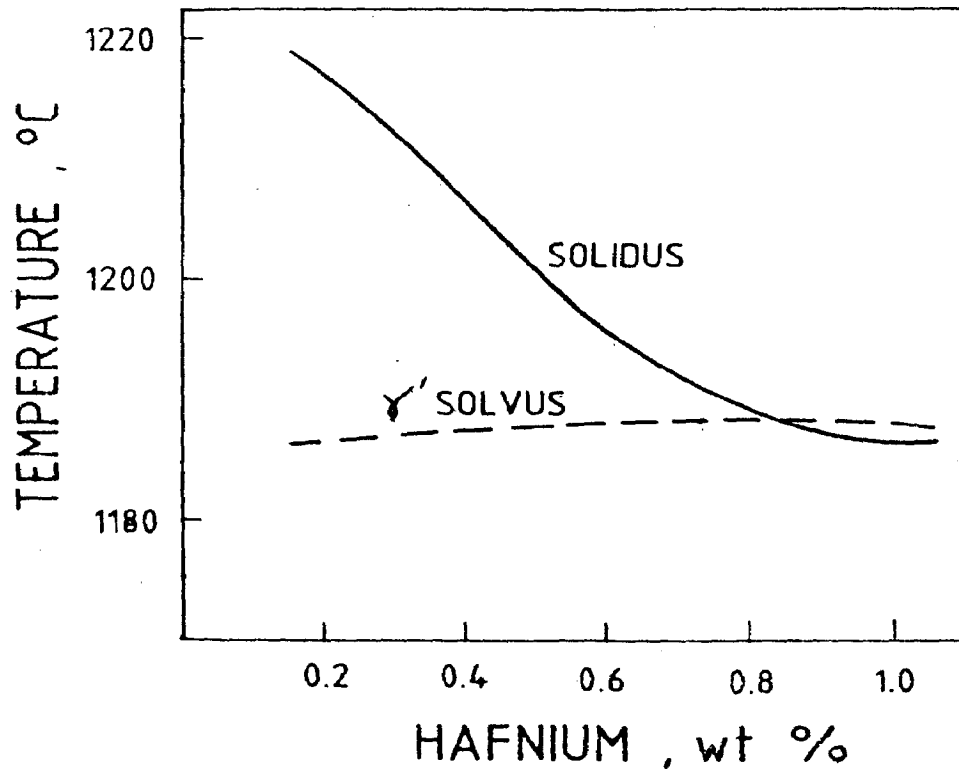
2.7   Effect of hafnium on γ' solvus and solidus temperatures in MERL-76 [103].

the effect of hafnium on the γ' solvus and incipient melting temperature of MERL-76 [103]. For 0.8% hafnium, the γ' solvus and incipient melting temperatures are almost identical. Chen [104] also reports that alloys containing large amounts of hafnium exhibit a tendency for coarsening and overaging of γ' which is definitely not desirable because of the attendent decrease in strength levels. Larson et al [105] also observed the precipitation of a large volume fraction of eutectic $\gamma + \gamma'$ structure (with Japanese fan-like morphology) in P/M Astroloy with increase in hafnium additions from 0.1 to 1.7%. They attribute the formation of this cellular structure to increase in difference between solvus temperatures of hetero-geneous γ' nucleating at the grain boundaries and homogeneous γ' nucleating within the grains. For the Hf-free Astroloy this temperature difference (Δ T) was estimated to be 8 K. With increase in hafnium, Δ T is likely to increase thereby enhancing the time during which this fan-like structure would form and before its growth is terminated by the nucleation of γ' within the grain. Larson et al, however, observed that PPB precipitation tends to be suppressed with increase in hafnium. Davidson and Aubin [86] recorded the formation of hafnium oxide precipitates in association with interdendritic carbides in REP Astroloy. They, however, suggest that the quantity of surface carbides is reduced by minor additions of hafnium or yttrium [86]. Warren et al [106] in a study involving the use of ESCA (electron spectroscopy for chemical analysis) and SAM (scanning Auger microscopy) on hafnium-modified P/M Astroloy, showed that hafnium does not necessarily reduce

the PPB precipitation because the formation of a more stable oxide at the particle surface offsets the advantage of greater affinity of hafnium towards carbon. It is further suggested by Warren et al [106] that the complex oxide of Al, Ti and Hf formed at the powder particle surface would rather attract more carbide forming elements to the boundary during HIP densification.

Niobium and Tantalum :— Wentzell [12] has shown that when niobium or tantalum are added in P/M superalloys they form stable MC carbides thereby restricting the rate for carbide redistribution during HIP consolidation and suppressing the tendency for PPB precipitation. The behaviour of these elements is, therefore, similar to that exhibited by hafnium, although their degree of carbide forming ability may vary. As has also been discussed in Section 2.2.2, Zheng and Cai [42] in a phase transformation study on hafnium bearing cast nickel base alloys showed that the stability of MC carbide follows the order:

(most stable) HfC →► NbC →► TaC →► TiC (least stable)
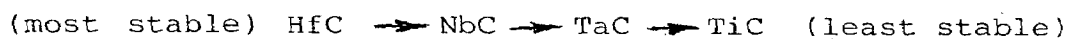
Their finding is based on the observations that a Hf-free alloy containing 3% Nb precipitates secondary NbC at high temperatures and a Hf-free alloy without Nb but with 2.4% tantalum does not precipitate secondary TaC. Bringegar et al [107] showed that Ta has a higher stabilizing effect on MC than Nb in the cast alloy IN 713 LC. However, addition of Ta was found to affect the microstructural stability of the alloy. When tantalum was raised from 0.1 to 1.75%, formation

of σ-phase was observed. However, Meng et al [108] in a study on tantalum-modified B-1900 observed that structural stability is not affected by the addition of tantalum. Both high temperature tensile strength and creep strength have been reported to improve with increase in the levels of tantalum. The same authors further report that additions of niobium influence the mechanical properties of the alloy in a similar fashion. In another study on the influence of niobium on steady-state creep behaviour of a wrought nickel base superalloy, Guo et al [109] report that niobium in γ' elevates the slip deformation resistance as a result of increase in its volume fraction, particle radius and long-range order parameter thereby increasing the creep resistance of the alloy. Unlike tantalum, niobium in moderate proportions has not been found to affect the alloy stability. P/M Rene' 95, a popular disc alloy containing about 3% Nb is not only found to offer an excellent combination of mechanical properties but also possesses a high structural stability [63,64,65].

2.8   CURRENT AREAS OF INVESTIGATION

From the foregoing literature survey it is clear that extensive work has been done to understand the role of minor elements such as hafnium, niobium and boron in cast nickel base superalloys and the metallurgical mechanisms underlying their mechanical behaviour are better understood. However, studies on the interactive role of such minor additions on microstructure and mechanical properties in P/M superalloy compositions seem to be very limited. Further, because of

the escalating prices of raw materials and strategic nature of some of the commonly used alloying elements, efforts are also being made to develop new P/M superalloy compositions with lowered levels of such strategic or expensive elements. Apparently, these new compositions need in-depth studies on their metallurgical behaviour. Additionally, processing of powder superalloys is very sensitive to compositional modifications and this aspect also deserves greater attention. A clear understanding of the effect of consolidation temperature and post-consolidation cooling rates is necessary to obtain desired microstructures and mechanical properties. Various problems such as powder cleanliness, freedom from inclusions in PPB precipitation, which have been the limiting factors for several years have now been partly overcome, yet the tolerance levels of defect size and especially with respect to NDT qualification are increasingly becoming important in current investigations on P/M superalloy hardware developments [110]. The emergence of some processing innovations such as rapid solidification processing (RSP) is offering new possibilities of alloy development [111]. It is, therefore, essential t effects of minor elements on the microstructure and mechan: properties of highly alloyed superalloy compositions be caref evaluated to exploit such potential to the fullest ext for greater performance levels combined with better production economics. This research is thus taken up with a view to contribute to a greater understanding of the metallurgical features of a novel P/M superalloy composition to enable its subsequent development for hardware applications.

CHAPTER 3

EXPERIMENTAL PROCEDURE

3.1 PREPARATION OF ALLOYS

The three compositions of DMP -1, DMP-2 and DMP -3 were prepared in the form of 100 mm diameter ingots weighing about 20 Kg and casting under a vacuum of $1x10^{-3}$ torr (0.13 Pa) in a GCA/VAC Vacuum Induction Melting (VIM) furnace. The base charge consisted of nickel, cobalt, chromium and master alloys of nickel-molybdenum and nickel-tungsten. After the initial melt down which took about 45 minutes, carbon was added to the melt through the addition charger. The molten metal was refined for a few minutes and as soon as the carbon boil subsided, additions of aluminium, titanium, ferro-niobium, nickel-zirconium, hafnium and boron were made successively followed by pouring at 1743-1763 K into 100mm dia x 400mm long cast iron moulds which were preheated at 773 K. 5 to 10 mm thick slices from top and bottom ends of the billet were cut off. Another disc of 10mm thickness was sliced off from the bottom end of each billet and further parted into small bars of approximately 10mm x 10mm x 10mm and 10mm x 10mm x 50mm sizes. The ingots were then machined and after the removal of 1mm deep top surface layers, turnings were collected for the purpose of chemical analysis. The compositions of the three as-cast alloys are given in Table 3.1.

3.2 POWDER PREPARATION

Argon atomization facility which has been described in Chapter-2 was used to produce the superalloy powders for

Table 3.1

Chemical Compositions of Alloys after Casting, wt%

Alloys	C	Cr	Co	Al	Ti	Mo	W	Nb	Hf	Zr	Bo	Fe	Ni
DMP-1	0.016	10.0	4.4	4.6	2.1	3.2	4.3	0.92	0.71	0.07	0.018	0.52	balance
DMP-2	0.018	9.9	4.6	4.5	1.95	3.4	4.2	0.90	0.72	0.08	0.085	0.50	balance
DMP-3	0.028	11.2	5.4	4.8	3.0	3.2	5.2	1.35	0.07	0.065	0.023	0.65	balance

the present work. The prealloyed ingot weighing around 16 kg was remelted under a vacuum of 5 x 10^{-3}torr (0.66 Pa) and atomized by a subsonic argon gas 'jet at a pressure of 1.0 to 1.5 MPa (10 to 15 atmospheres) using an atomizer nozzle of 6mm diameter. During induction melting of the ingots which took approximately one hour, 0.66 Pa (5x10^{-3}torr) vacuum was maintained. The argon gas used had a total impurity content of 15 ppm, oxygen being 6 ppm maximum. The powder was allowed to cool down to room temperature and transferred to a sealed container. The powders were subsequently sieved to obtain various size fractions and filled in sealed plastic covers, with all these operations performed under argon atmosphere in a glove box.

3.3 CHARACTERIZATION OF POWDERS

The powders sieved to obtain various size fractions ranging between -22 and -325 mesh were examined in a Leitz METALLUX optical microscope and an ISI-100A scanning electron microscope (SEM). Standard methods were used to measure physical properties such as flow rate [112], apparent density and tap density [113] of each powder of -100 mesh size. Powders were also analysed for their chemical composition and surface chemistry.

3.4 CONSOLIDATION OF POWDERS

The powders were filled into 10mm diameter, 2mm thick and 300mm long stainless steel tube capsules, one end of which has earlier been sealed by a welded stainless steel plug and the other end welded to mild steel evacuation tubes of 6mm internal diameter and 2mm wall thickness. The powder filled

TO VACCUM PUMP

MOLYBDENUM HEATER

HEATING

METALLIC CAPSULE WITH ALLOY POWDER

DEGASSING FOLLOWED BY SEALING

HOT ISOSTATIC PRESSING

HIP'ED COMPACT
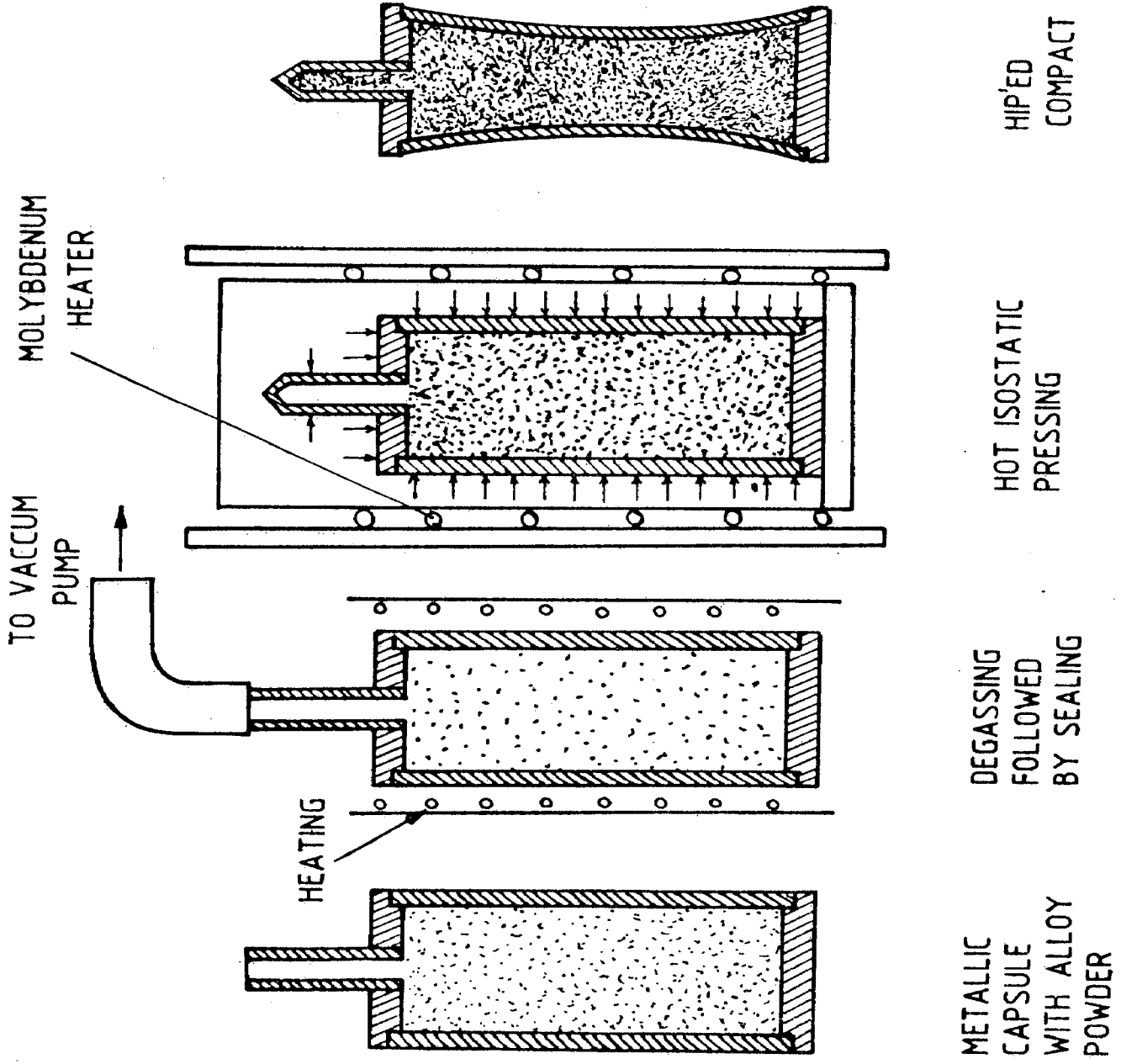
3.1 Procesing sequences showing encapsulation and hot isostatic pressing of powder.
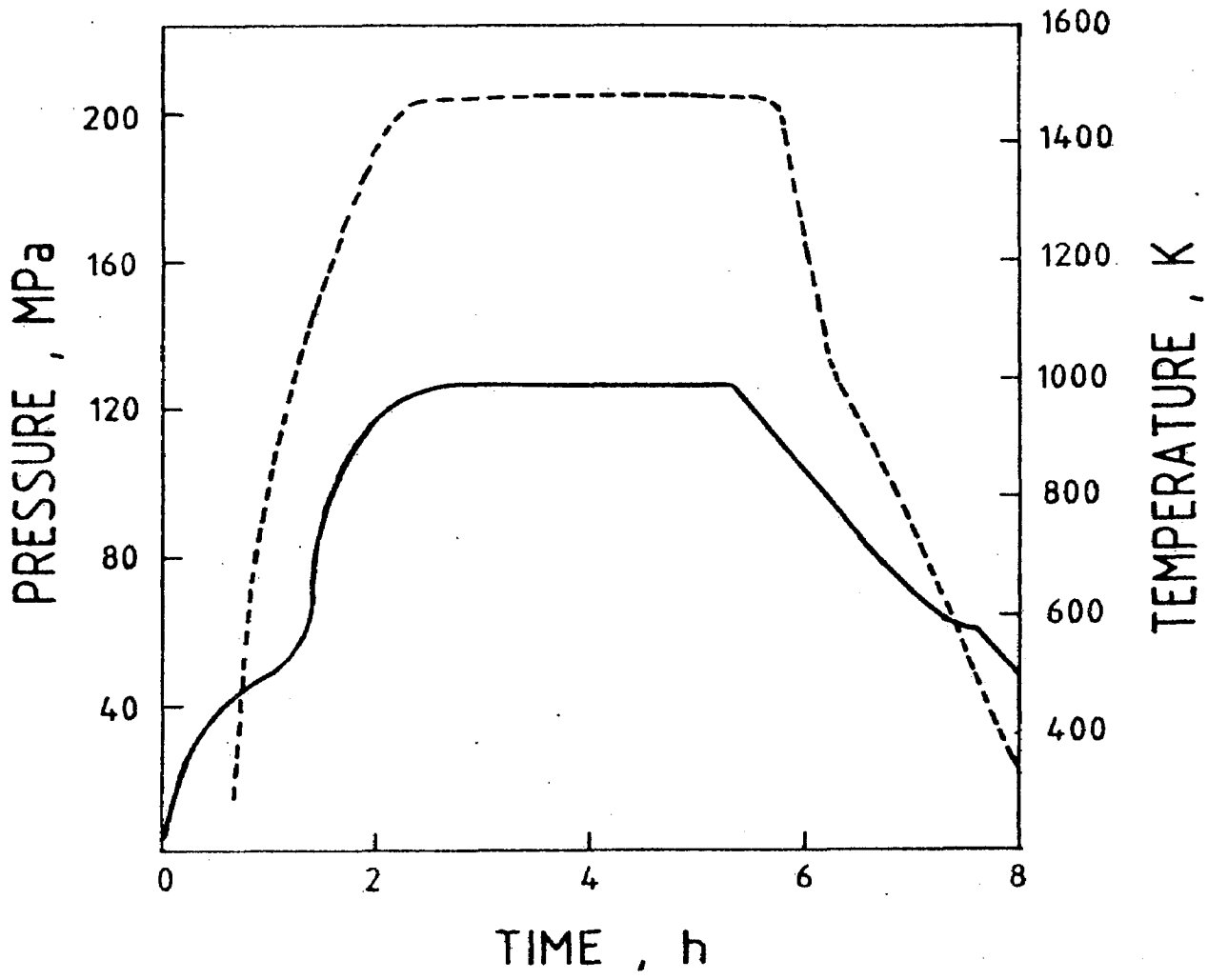
3.2   A typical HIP cycle.

capsules were evacuated to 1.33 x 10^{-3} Pa (1×10^{-5} torr) and outgassed at 1073 K for 12 hours followed by hot crimp-sealing of the evacuation tube a little above the welded joint. Fig.3.1 shows the sequence of operations involved in the preparation of capsules. The sealed capsules were consolidated in an ASEA QUINTUS Model QIH 32 hot isostatic press (HIP) at three different temperatures of 1448, 1473 and 1498 K, keeping the pressure and time constant at 120 MPa and 3 hours respectively. A typical HIP cycle showing temperature, pressure and time profiles is presented in Fig. 3.2. To facilitate the identification of each alloy and its HIP schedule, codes as given below would be used.

Alloy	Type	Consolidation Temperature	Code
DMP-1	(Low-C, Low-B, with Hf)	1448 K	AH1
DMP-1		1473 K	AH2
DMP-1		1498 K	AH3
DMP-2	(Low-C, High-B, with Hf)	1448 K	BH1
DMP-2		1473 K	BH2
DMP-2		1498 K	BH3
DMP-3	(Low-C, Low-B, Hf free)	1448 K	CH1
DMP-3		1473 K	CH2
DMP-3		1498 K	CH3

3.5   ISOTHERMAL FORGING OF HIPED ALLOY

30mm diameter and 60mm long compact of CH2 was compressively deformed at 1443 ± 5 K in a dynamic vacuum of 1.33×10^{-3} Pa using graphite dies in a 100 Ton, 60 KVA, GCA vacuum hot press. A ram speed of 1mm/min. was used to produce about **50%**

compressive deformation by upset forging. Fig.3.3 illustrates the schematic arrangement of the hot press and the positioning of compact with specially fabricated Nimonic-75 dies. The forged cake was cut into a number of bars of approximately 10mm x 10mm cross section in such a way that the test pieces machined from these bars would have their gauge lengths transverse to the forging direction.

3.6   BULK CHEMICAL ANALYSIS

While Cr, Co and W contents were determined by volumetric analysis method, Ti, Al, Mo and Fe contents were analysed using VARIAN AA6D Atomic Absorption Spectrometer. Emission Spectrometer was utilized to analyse Hf, Nb and B. Non-dispersive Infrared Spectroscopy using LECO 136 and LECO 12 instruments was employed to analyse carbon, sulphur and oxygen contents. For carbon and sulphur analysis, samples were burnt in a stream of oxygen to convert them into their oxides, which were subsequently analysed. For oxygen analysis, vacuum fusion technique was employed, wherein the samples were melted in a graphite crucible in high vacuum at a temperature of 2000 to 2400 K and high purity helium gas was used as a carrier gas.

3.7   MECHANICAL TESTING

Tensile and stress rupture specimens were machined from the three stages of as-cast, as-HIP and HIPed and heat treated alloys. For tensile testing, button headed specimens of 25.4 m m gauge length and 4.07 mm gauge diameter and for stress rupture testing, specimens having gauge diameter and length of 4.5mm and 20mm respectively were prepared. Tests were carried out

VACUUM CHAMBER

LAND OPTICAL PYROMETER

TOP MOVING RAM

GRAPHITE TOP PUNCH

GRAPHITE FELT INSULATION

GRAPHITE HEATER

Pt/Pt-Rh THERMOCOUPLE

NIMONIC 75 DIES

BOTTOM STATIONARY RAM

GROUND LEVEL
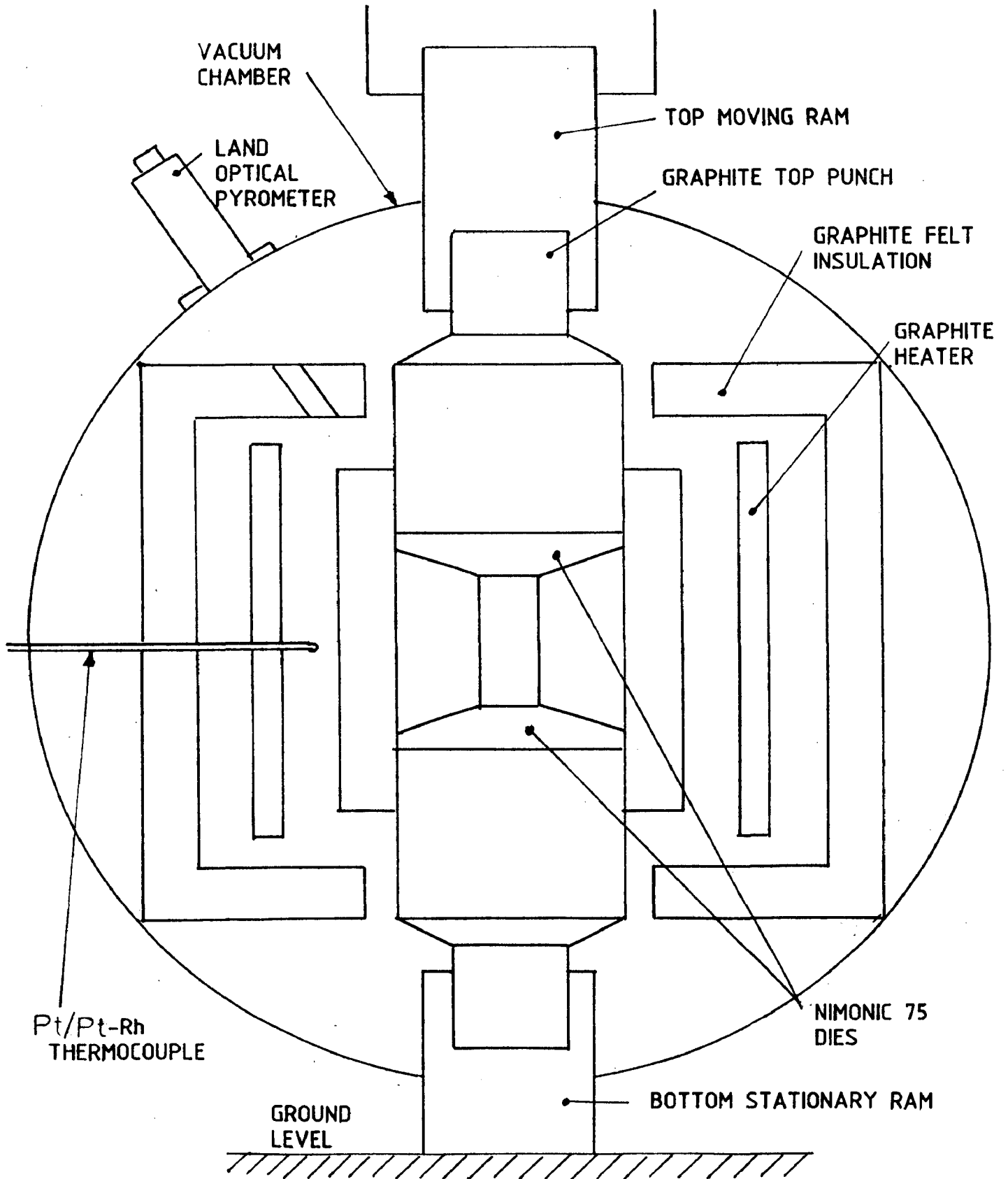
3.3   Schematic of vacuum hot press showing isothermal forging of HIPed compact.

according to the following schedules:

(a) As-cast alloys

    i) Tensile testing at room temperature and 1033 K in air

    ii) Stress rupture testing at 1033 K/590 MPa and 1173 K/330 MPa in air

(b) As-HIP alloys

Tensile testing at room temperature and 1033 K in vacuum

(c) Hiped' and Heat Treated Alloys

    i) Tensile testing at room temperature, 813 K, 923 K and 1033 K in air

    ii) Stress rupture testing at 978 K/760 MPa, 1005 K/640 MPa and 1033 K/590 MPa

(d) Hiped, Isothermally Forged and Heat Treated Alloy

    i) Tensile testing at room temperature and 1033 K

    ii) Stress rupture testing at 978 K/760 MPa, 1005 K/640 MPa and 1033 K/590 MPa.

All the tensile tests were carried out at a strain rate of 6.6×10^{-4}/s using a 10 ton screw driven INSTRON test machine. For stress rupture tests, EMEC creep machines were employed.

3.8 HEAT TREATMENT, METALLOGRAPHY AND FRACTOGRAPHY

In order to assess the microstructural stability of the alloys, specimens cut from the as-cast billets were heat treated at 1123 K for 300 hours. A number of specimens were also heat treated at different temperatures between 1433 K and 1493 K for two hours followed by water-quenching. Similar

heat treatments were performed on the P/M alloys also .Studies were also conducted to assess the effects of several solutionizing and aging temperatures on microstructure and to evolve suitable heat treatment cycles.

The P/M alloys were heat treated according to the following two schedules:

(i) Heat Treatment T_1:

1493 K/2 hours, rapid air cool

+

1323 K/8 hours, air cool

+

1123 K/16 hours, air cool

(ii) Heat Treatment T_2:

1353 K/8 hours, rapid air cool

+

923 K/24 hours, air cool

+

1033 K/16 hours, air cool

Specimens before and after the above heat treatments were metallographically examined. Both optical and electron microscopy were used. While the longitudinal sections of tensile and stress rupture tested specimens mounted paralled to the loading direction were examined by optical microscopy, the fractured surfaces were examined in the scanning electron microscope provided with energy dispersive X-ray spectrometry (EDAX)

attachment.   Thin foils prepared from the HIPed and heat treated alloys were examined in a PHILIPS EM 300 transmission electron microscope.

For optical microscopy, the samples were first ground on 600 grit emery paper and finally polished on Sylvet Cloth using 2 μm diamond paste followed by immersion etching in ferric chloride solution (for as-cast and powder specimens) or Kalling's solution (2g Cu Cl_2, 40 ml HCl and 80 ml CH_3OH). For electron microscopy, thin foils were prepared by jet electro polishing 3mm dia and 0.2mm thick discs with a solution of the following composition and conditions [114]:

Methanol	–	78%
H_2SO_4	–	7%
HF	–	2%
HNO_3	–	3%
Lactic acid	–	10%
Voltage	–	12V
Current	–	40 mA
Temperature	–	-243 K

A number of thin foils were also prepared using GATON Duel Ion Miller which makes use of argon beam to remove atom by atom. This operation was performed at 6 KV with a gun current of 0.5 mA, keeping the angle of incidence of argon beam at 12°. Two-stage carbon replica technique was employed to prepare replicas of forged and heat treated specimens to examine the morphology of γ' and grain boundary precipitates.

3.9   PHASE IDENTIFICATION AND MICROANALYSIS

Extraction of γ' and refractory phases such as carbides and borides was performed electrolytically according to the procedure described by Donachie and Kriege [115]. For extracting γ' phase, an electrolyte of 1% ammonium sulphate and 1% citric acid in distilled water was used at a current density of 100 to 150 mA/cm^2 for 3 hours. Carbides and borides were extracted by dissolving matrix and γ' in an electrolyte of 20 ml HCl, 1 g tartaric acid and 180 ml methanol at a current density of 150 mA to 200 mA/cm^2 for 4 to 5 hours.

The residue was allowed to set overnight, upper solution decanted, rinsed in methanol and the whole solution filtered off using Whatman ashless filter paper No.42. The residue collected on the filter paper was dried with the help of an infra-red lamp. The phases present in the residue were identified by X-ray diffraction in a PHILIPS diffractometer with Debye-Scherer camera. Electron diffraction patterns were also used to identify the minor phases.

CAMECA electron probe microanalyser (EPMA) was used to analyse the phases present in the three HIPed P/M superalloys before and after heat treatments. Scanning Auger electron spectroscopy was carried out on the atomized powders as well as in-situ fractured specimens using a Physical Electronics-545 scanning Auger microprobe (SAM). The powders or fractured surfaces were analysed before and after argon ion sputtering upto a surface of 80 nm, and Auger spectra obtained after every 10 nm sputtering intervals[8].The experimental conditions

of X-ray diffraction, EPMA and SAM are briefly listed below:

X-ray Diffraction

Radiation	–	Fe K_{α} (filtered)
Voltage	–	30 KV
Current	–	20 mA
Camera Dia	–	11.46 cm
Time of exposure	–	8 hours

EPMA

Beam Voltage	–	20 KV
Beam Current	–	30 mA

SAM

Primary beam voltage	–	3 KV
Primary beam current	–	3 μA

Etching gun voltage:

i)	for fixed depth analysis	–	1 KV
ii)	for continuous depth analysis	–	30 KV

Etching gun current:

i)	for fixed depth analysis	–	10 mA
ii)	for continuous depth analysis	–	30 mA
	Etching rate	–	20 A°/min (2 nm/min)

CHAPTER 4

MATERIAL CHARACTERIZATION AND EVALUATION

4.1 INTRODUCTION

In this chapter, studies carried out to characterize the microstructure and to assess the microstructural stability of as-cast alloys have been described. Mechanical properties at room temperature and high temperature have been evaluated to examine the potential of each alloy. Atomized powders as starting materials have also been characterized and evidence has been presented to show the effects of minor chemistry variations on the solidification behaviour of alloy powders.

4.2 AS-CAST ALLOYS

4.2.1 Analytical and Microstructural Observations

Examination of the chemical compositions of the alloys listed in Table 3.1 shows that carbon in DMP-1 and DMP-2 is considerably below the aimed level of 0.025%. This is because no extra carbon was added during the vacuum induction melting of alloys considering the fact that the basic raw materials such as nickel, chromium and cobalt contained 0.02% of carbon and masteralloys of tungsten, molybdenum, niobium etc., contained 0.03 to 0.04% carbon. Since chemical analysis of DMP-1 and DMP-2 indicated more than the expected loss of carbon due to deoxidation during vacuum induction melting and refining of the alloys, an extra amount of carbon (graphite granules) equivalent to 0.01% was added during the preparation of DMP-3.

Table 4.1

Electron Hole Numbers and Densities of Experimental Alloys

Alloy	$\overline{Nv}$	Density, g/cc (Theoretical)
DMP - 1	2.32	8.9
DMP - 2	2.26	8.9
DMP - 3	2.74	8.8

Table 4.1 lists the densities and electron vacancy numbers of the as-cast alloys DMP-1, DMP-2 and DMP-3. The $\overline{Nv}$ values of these alloys have been measured in accordance with the standard procedure described by Mihilsin et al [35]. However, since the chemical compositions being investigated here are different from the conventional ones, certain assumptions were made in respect of the compositions of minor phases such as carbides and borides. These are described in Appendix I. A comparison of the $\overline{Nv}$ values (Table 4.1) shows that whereas the alloy DMP-3 is likely to form TCP phases, alloys DMP-1 and DMP-2, by virtue of their $\overline{Nv}$ values being lower than the critical value of 2.5 [36], are not prone to the formation of such deleterious phases.

Figs. 4.1a and b show the optical micrographs of as-cast DMP-1 and DMP-2, which show similar microstructures except that the alloy DMP-2 contains relatively larger amount of eutectic structure (Fig. 4.1b) as compared to DMP-1a). Fig. 4.1c shows the SEM microstructure of as-cast DMP-1 illustrating the precipitation of intergranular and intragranular blocky particles, which are believed to be carbides and/or borides. The high boron alloy DMP-2 shows the additional precipitation of elongated particles at the grain boundaries or interdendritic boundaries (Fig. 4.1d). In the case of DMP-3, the microstructure is similar to that of DMP-1 but the volume fraction of carbide or boride precipitates is approximately 50% more.

Fig. 4.2 shows the microstructures of DMP-1, DMP-2 and DMP-3 specimens after a heat treatment of 1453 K for 2 hours
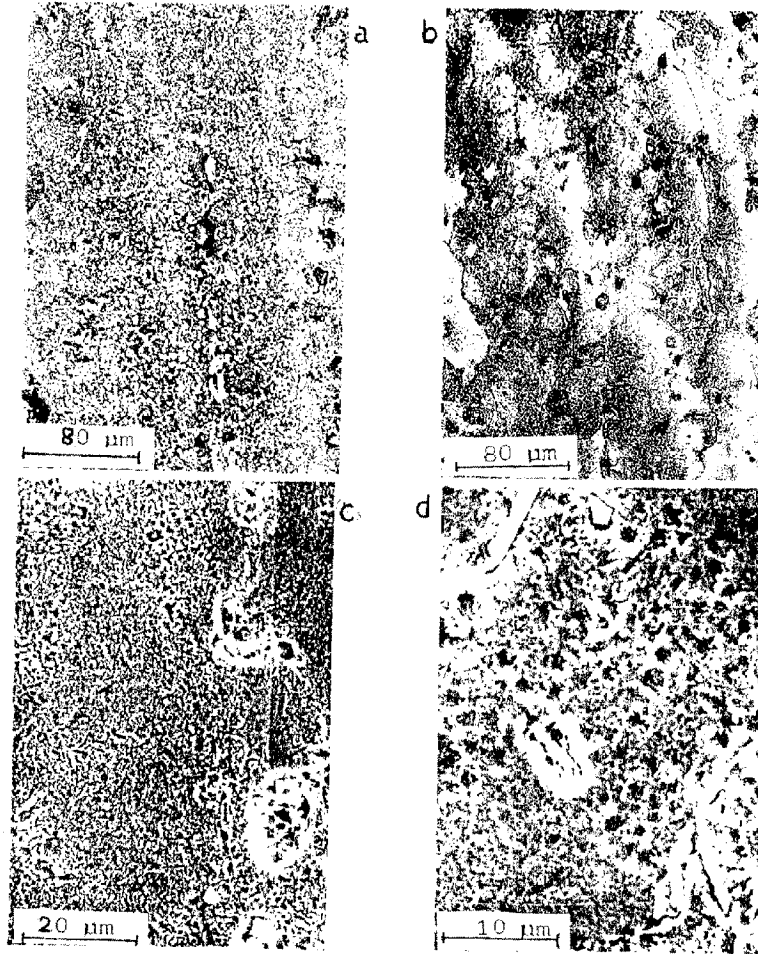
4.1   Microstructures of as-cast alloys (a) & (c) DMP-1, (b) & (d)DMP-2
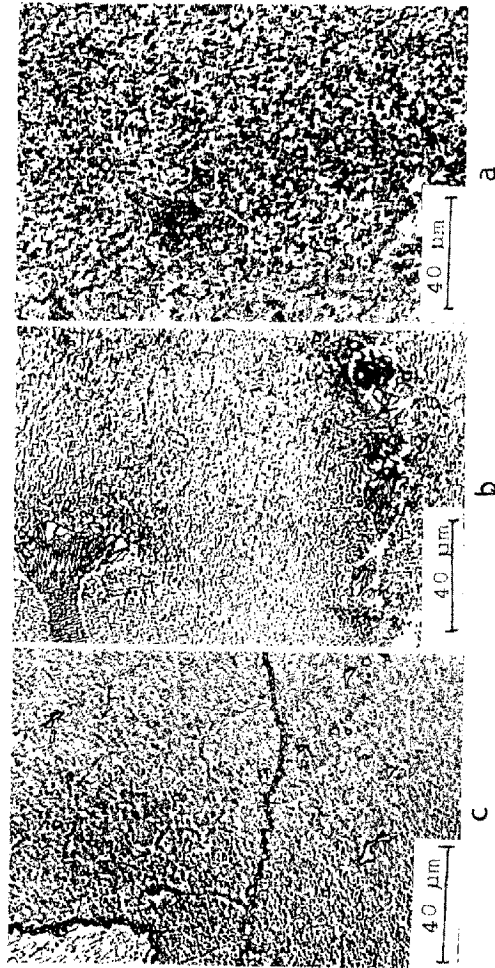
4.2 Microstructures of as-cast alloys after solutioning at 1453 K/ 2 hrs
(a) DMP -1 (b) DMP-2 and (c) DMP-3.
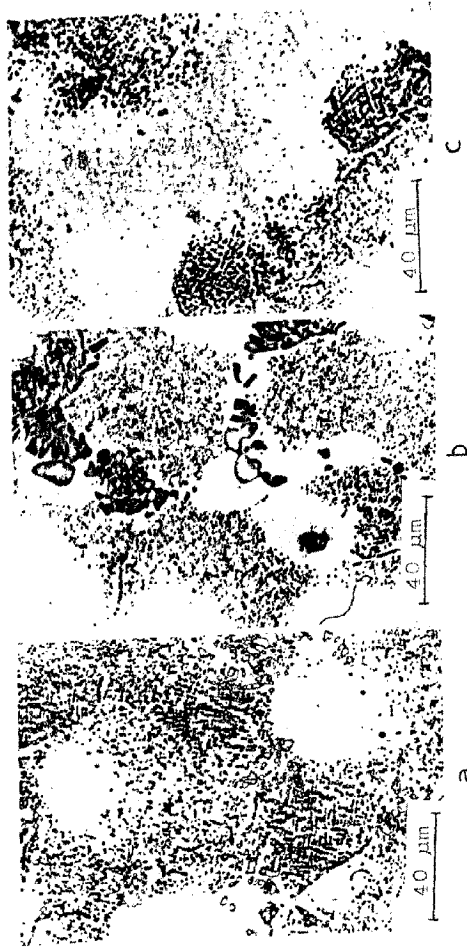
4.3   Microstructures of as-cast alloys after solutioning at 1473 K/2 hrs
(a) DMP-1 (b) DMP-2 (c) DMP-3.
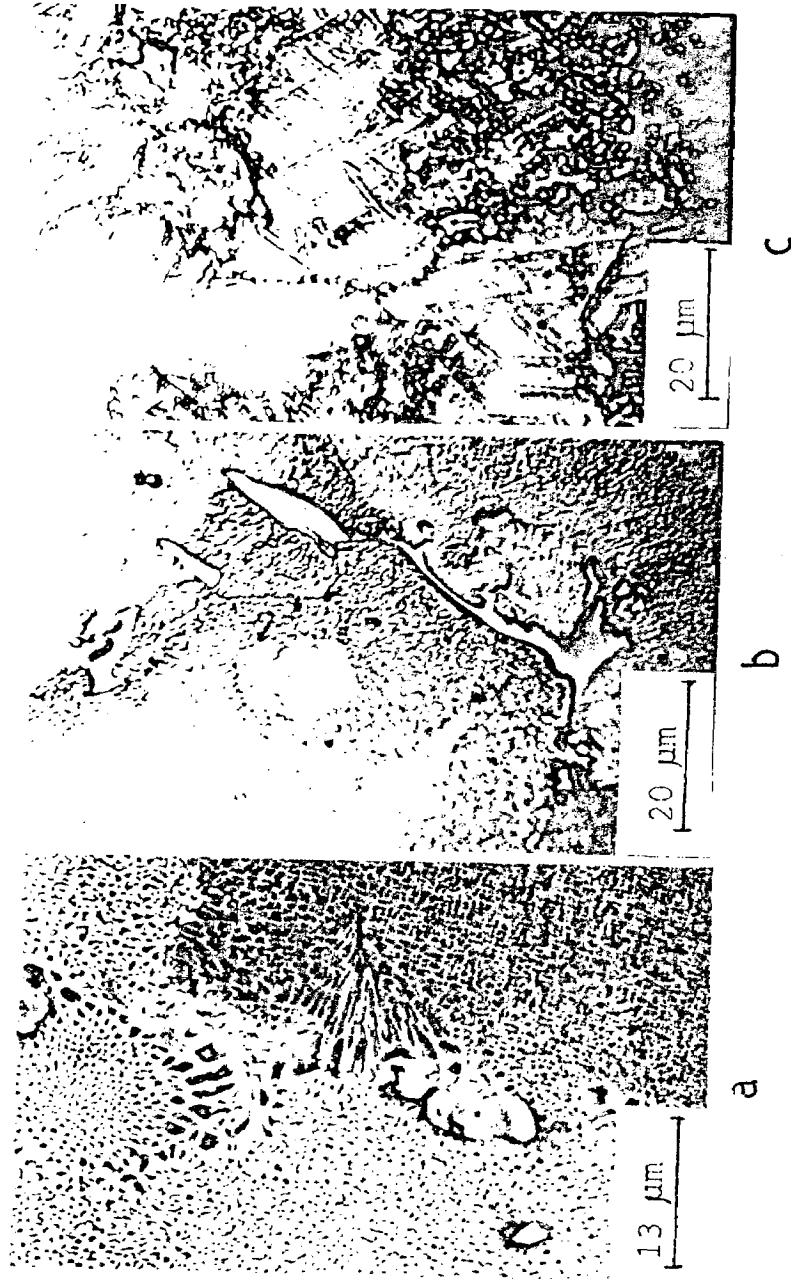
4.4 Microstructures of as-cast alloys after heat treatment at 1123 K/ 300 hours.
(a) DMP-1 (b) DMP-2 and (c) DMP-3 showing the precipitation of sigma phase.

followed by water quenching. Partial solutioning of γ' particles appears to have occurred particularly in DMP-1 and DMP-2. Microstructures of these alloys after solutioning at 1473 K are shown in Fig. 4.3. Although DMP-1 and DMP-3 show the dissolution of majority of γ' particles, a few γ' nodules are still left undissolved in DMP-2. From these microstructural observations γ' solvus for each alloy is deduced to be about 1473 K.

Fig. 4.4 shows the microstructures of the three as-cast alloys after an aging treatment of 1123 K for 300 hours. Whereas DMP-1 and DMP-2 did not show any optically visible microstructural changes after such a prolonged temperature exposure, DMP-3 developed a Widmanstatten type of structure (Fig. 4.4c). DMP-3 can, therefore, be considered to be a sigma prone alloy.

4.2.2 Mechanical Properties

The tensile properties of the three alloys tested at RT and 1033 K are given in Table 4.2. The yield strength and UTS of DMP-3 are marginally higher and tensile ductility appreciably lower than those of DMP-1 and DMP-2 at ambient. The tensile properties at 1033 K also show almost similar trend. Since some scatter in the mechanical properties of as-cast alloys is expected, the overall effect of chemistry variations on the tensile properties of these alloys cannot be considered to be of much significance. However, in respect of the stress rupture properties (Table 4.3), the high boron alloy DMP-2 shows a marked improvement over DMP-1 as well as DMP-3. This is in agreement with the observations of Kotval et al [30].

Table 4.2

Room Temperature and 1033 K Tensile Properties of
As-Cast Alloys

	298 K				1033 K			
0.2%YS	UTS	El*	RA		YS	UTS	El*	RA
MPa	MPa	%	%		MPa	MPa	%	%
DMP-1 816	1036	14	15		815	907	4	6
					768	923	8	12
DMP-2 807	951	13	15		758	941	9	14
					772	888	6	10
DMP-3 862	1042	7	8		845	934	5	7

* for a gauge length of 25.4 mm

Table 4.3

Stress Rupture Properties of As-Cast Alloys

Temperature/Stress (K) (MPa)	Stress Rupture Life (Hours)		
	DMP-1	DMP-2	DMP-3
1033 / 590	38	133	53
1173 / 325	31	66	36

who demonstrated that increase in boron improves S-R properties of cast superalloys.

4.3   LOOSE POWDERS

4.3.1 Particle Shape and Size Distribution

SEM examination of the DMP-1 powder revealed that most powder particles have acquired a spherical shape with several of them having smaller satellite particles attached to them. Some of the particles also showed either encrustment of their surfaces or pores within them (Figs. 4.5a,b&c). These pores are generally attributed to the gas-entrapment or microshrinkage. It was, however, observed that frequency of powder particles having such pores was a function of their particle size, the coarser fraction having higher percentage of porous particles. High magnification view (Fig. 4.5d) of the powder particles confirmed that these pores were only on the surface suggesting the effect of micro shrinkage rather than argon-entrapment. DMP-2 and DMP-3 powders also showed identical features.

Table 4.4 gives some of the important powder characteristics of the -100 mesh powder used in the present work. Apparent density and tap density have been shown as percentage values of the theoretical density for each alloy and are comparable with the P/M superalloy IN-100 [94]. The Size distribution of -22 mesh atomised powders illustrated in Fig. 4.6 is a manifestation of the various processing parameters of atomization such as melt superheat, argon gas pressure, nozzle diameter and free fall height of the atomizer column [69,70]. Out of the
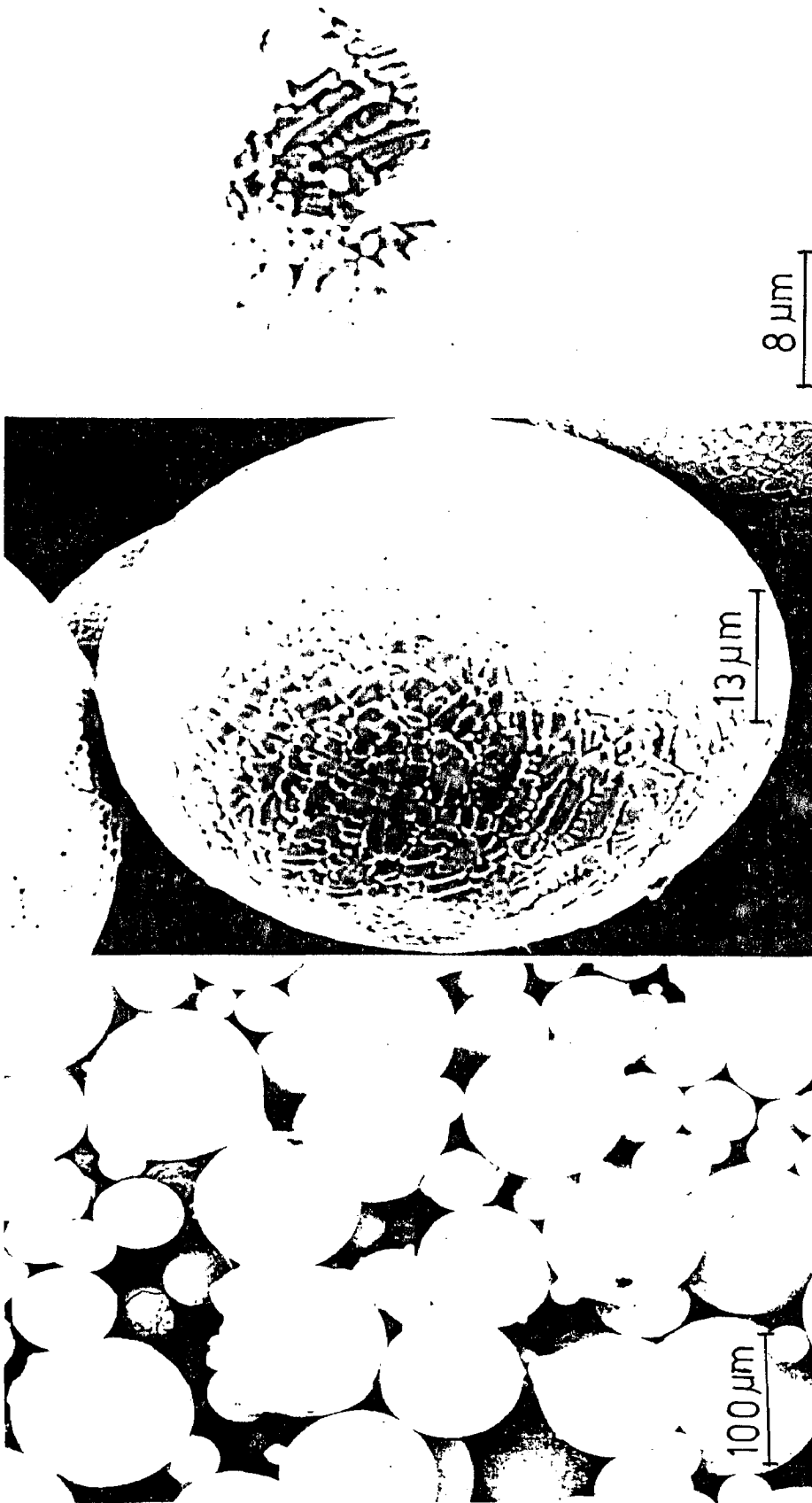
4.5   Scanning electron micrographs of DMP-2 powder showing (a) the presence of pores in coarse particles and satellite particles (b) dendritic morphology and (c) the presence of microstrinkage in a coarser particle.

Table 4.4

Characteristics of -100 Mesh (< 150 μm)

Argon Atomized Superalloy Powders

Alloy	Mesh Size Distribution		Apparent Density* (Percentage Theoretical	Tap Density* (Percentage Theoretical)	Flow Rate*
	Mesh size	Weight %			
DMP-1	-100 + 150	45.1			
	-150 + 325	33.2	50.6	57.5	3.54
	-325	22.7			
DMP-2	-100 + 150	41.9			
	-150 + 325	33.4	51.7	58.4	3.70
	-325	24.7			
DMP-3	-100 + 150	42.8			
	-150 + 325	32.0	53.4	60.7	3.72
	-325	25.2			

*   For -100 Mesh Powder
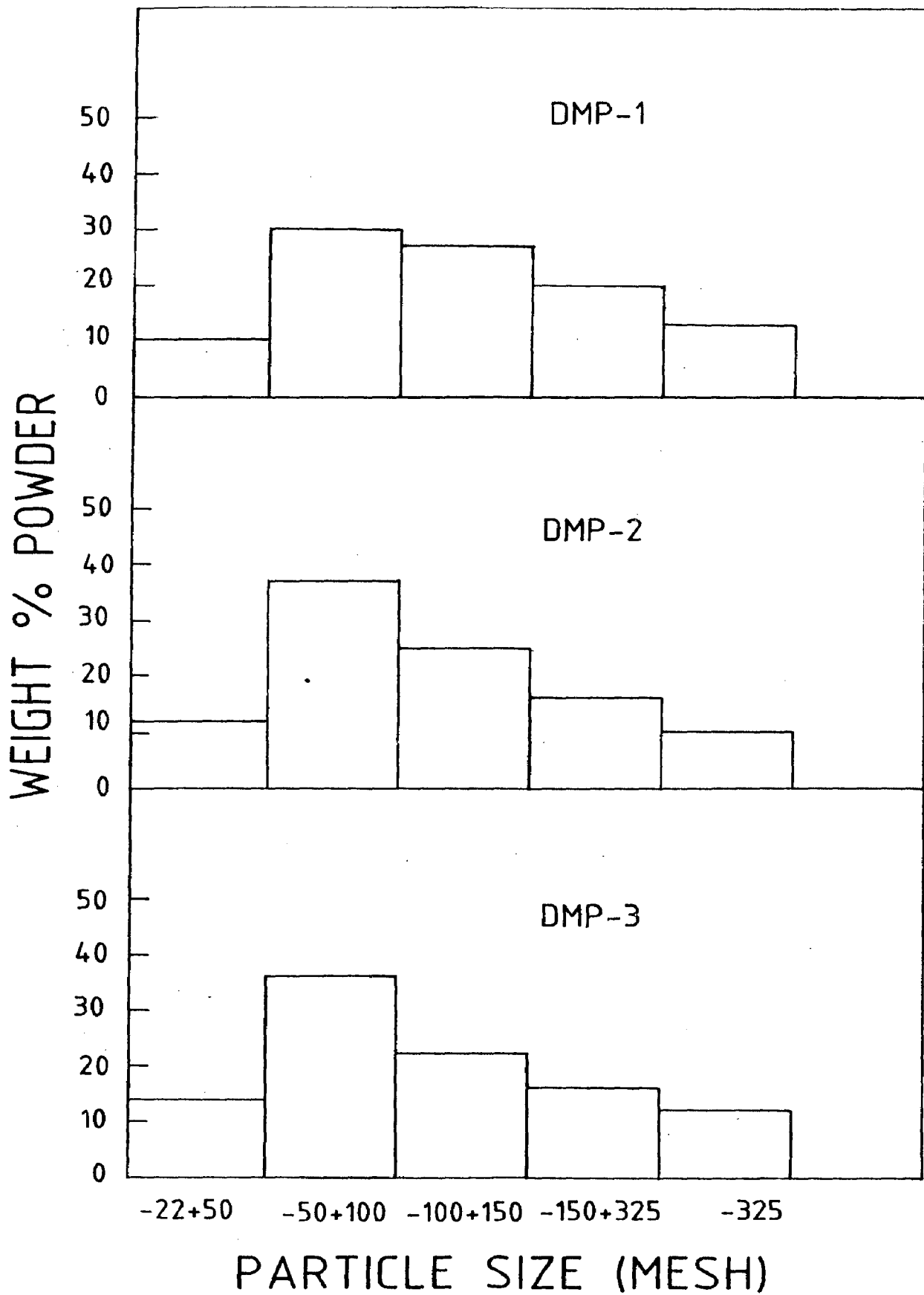
4.6   Mesh size distribution of   -22 mesh argon atomized superalloy
       powders.

total quantity of 12 kg of -22 mesh powder collected at the end of atomization experiment, 45 to 55% had a mesh size of -100 and was utilised for further investigation.

4.3.2 Effect of Cooling Rate on Secondary Dendrite Arm Spacings

Secondary dendrite arm spacings of the powders of different size fractions i.e., -22+36, -50+60, -85+100, -120+150, -200+240 and -325+400 were optically examined and measured (Table 4.5) These spacings are plotted in Fig. 4.7 against the average particle diameter for each alloy. The high-B alloy DMP-2 appears to have marginally coarser secondary dendrite arm spacings than the low boron alloy DMP-1 for all powder sizes.   DMP-3

has slightly larger inter-dendrite spacings for finer particles and smaller dendrite spacings for coarser particles than those given by the other two alloys.   The observation that small dendrite spacings are due to increased carbon content is in agreement with the finding of Patterson et al [59]. Utilising the known secondary dendrite arm spacing versus cooling rate data available for similar superalloys [116], the cooling rates for the three alloys of 100 μm powder size were found to be between 2000 and 3000 K/s as shown in Fig. 4.8 .   It is also manifest from Fig. 4.7 that minor chemistry variations in the alloys investigated do not have an appreciable effect on the secondary dendrite arm spacings.

4.3.3 Chemical Analysis

Chemical compositions of the powders including their gas analyses are given in Table 4.6   Oxygen and argon contents

Table 4.5

Secondary Dendrite Arm Spacings in Atomized Superalloy Powders for Different Powder Fractions

Particle size (ASTM Mesh size)	DMP - 1 (μm)	DMP -2 (μm)	DMP -3 (μm)
-30 + 36	5.2	5.5	5.1
- 50 + 60	4.0	4.2	3.7
- 85 + 100	3.2	3.4	3.3
-120 + 150	2.7	2.8	2.6
-200 + 240	1.9	2.1	2.0
-325 + 400	1.2	1.25	1.3
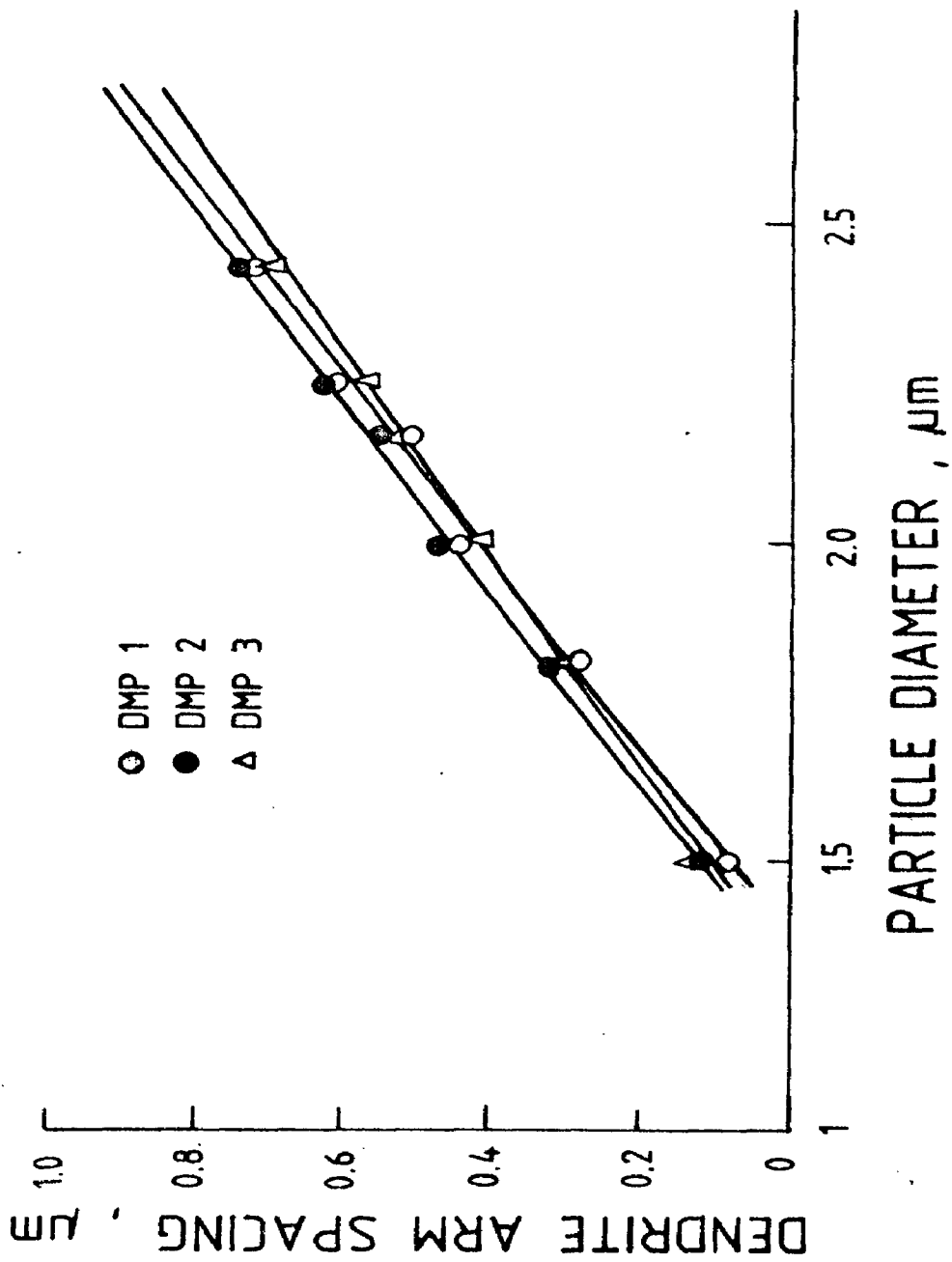
4.7   Secondary dendrite arm spacing as a function of particle diameter
       of the experimental superalloy powders.
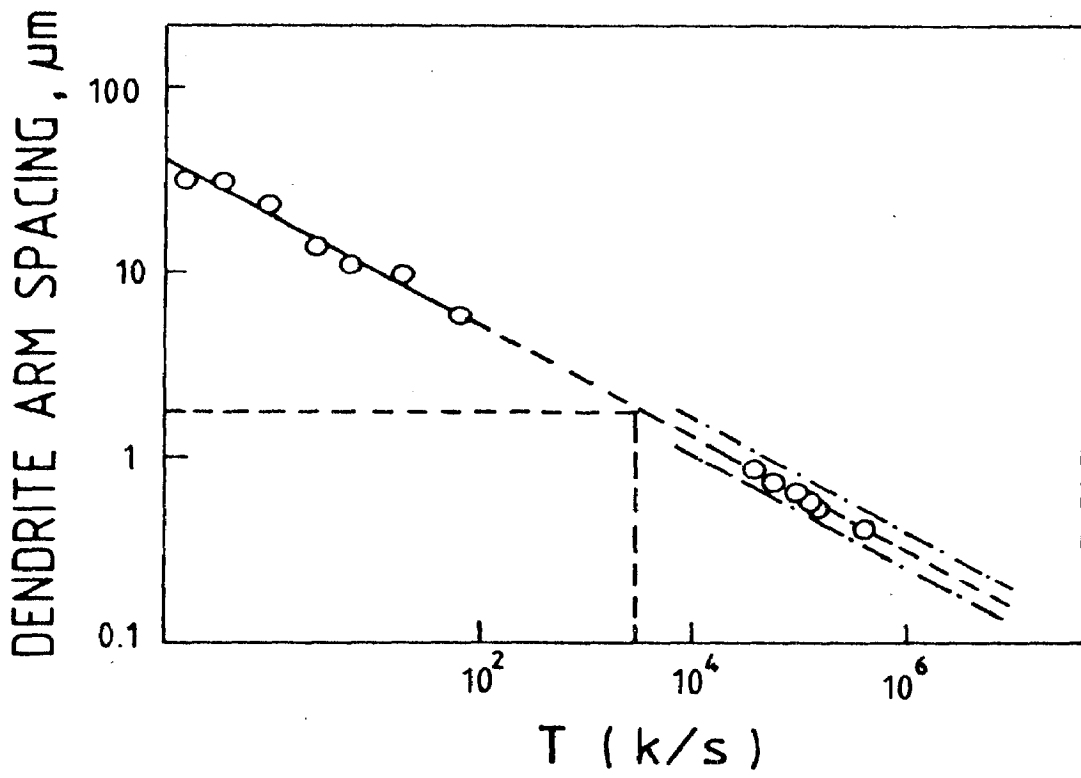
4.8   Secondary dendrite arm spacings versus cooling rate for the super-alloy powders.

Table 4.6

Chemical Compositions of -100 Mesh Superalloy Powders

Element	DMP - 1	DMP - 2	DMP - 3
Nickel	Balance	Balance	Balance
Carbon	0.018	0.018	0.030
Chromium	9.92	9.86	11.10
Cobalt	4.45	4.58	5.40
Tungsten	4.32	4.21	5.15
Molybdenum	3.20	3.35	3.22
Titanium	2.05	1.95	2.90
Aluminium	4.52	4.40	4.75
Niobium	0.92	0.91	1.32
Hafnium	0.69	0.70	0.07
Zirconium	0.060	0.075	0.062
Boron	0.018	0.084	0.023
Iron	0.52	0.51	0.67
Sulphur	0.003	0.002	0.006
Oxygen (ppm)	95	73	81
Nitrogen (ppm)	22	21	18
Argon (ppm)	1.7	1.4	1.6

in all the three superalloy powders are within the acceptable limits, i.e., below 100 ppm and 2 ppm respectively. The relatively high oxygen content in DMP-1 (95 ppm) is attributed to the starting material itself having higher oxygen (Table 3.1) than the other alloys.

4.3.4 Surface Chemistry of Powder

Fig. 4.9 shows an Auger electron spectrum from a powder particle of alloy DMP-1. The powder surface is covered with a layer of oxygen and carbon. Considerable amounts of titanium, sulphur, chromium and aluminium are also observed, although the concentrations of these elements are independent of their nominal contents. Similar spectra were obtained after 10 nm regular intervals of argon-ion sputtering in order to obtain information in regard to the chemistry of the powder particle below the surface. Peak-to-peak height ratios of the elements of interest with respect to nickel were measured and plotted as a function of sputtered depth. Sputtering rates were calibrated in terms of tantalum oxide (Ta_2O_5) film of known thickness. Similar procedure was adopted for the data pertaining to alloys DMP-2 and DMP-3. The sputtering profiles of DMP-1, DMP-2 and DMP-3 are presented in Figs. 4.10 , 4.11 and 4.12 . Observations made from the examination of these profiles are discussed below:

1. The unsputtered surface of the powder particles in each of these alloys indicates the maximum concentration of oxygen and carbon followed by sulphur, titanium and other elements. All these elements are in excess of their bulk composition. With progressive sputtering, peak-to-peak height ratios of
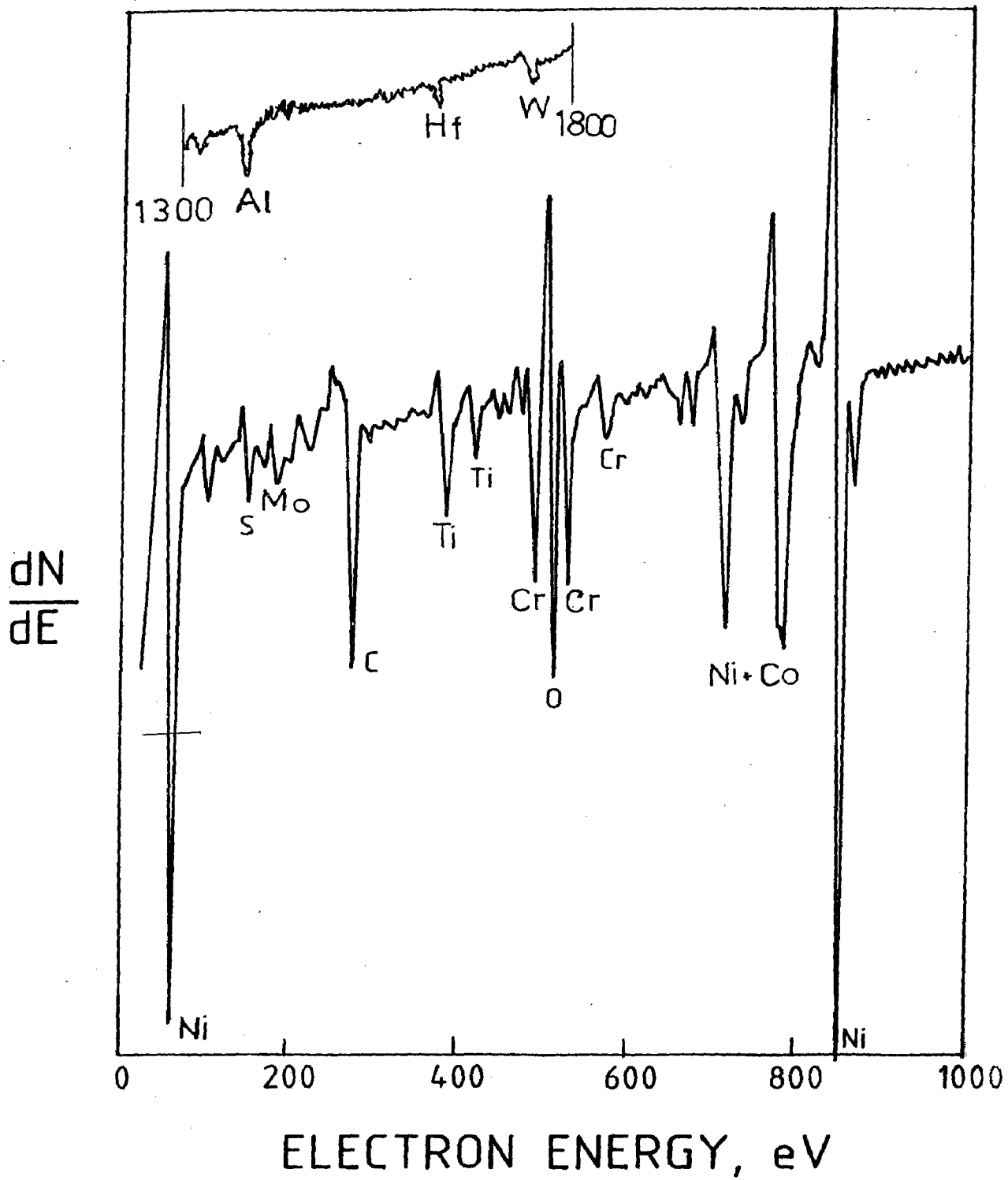
4.9   Auger spectra of various elements in DMP-1 powder.
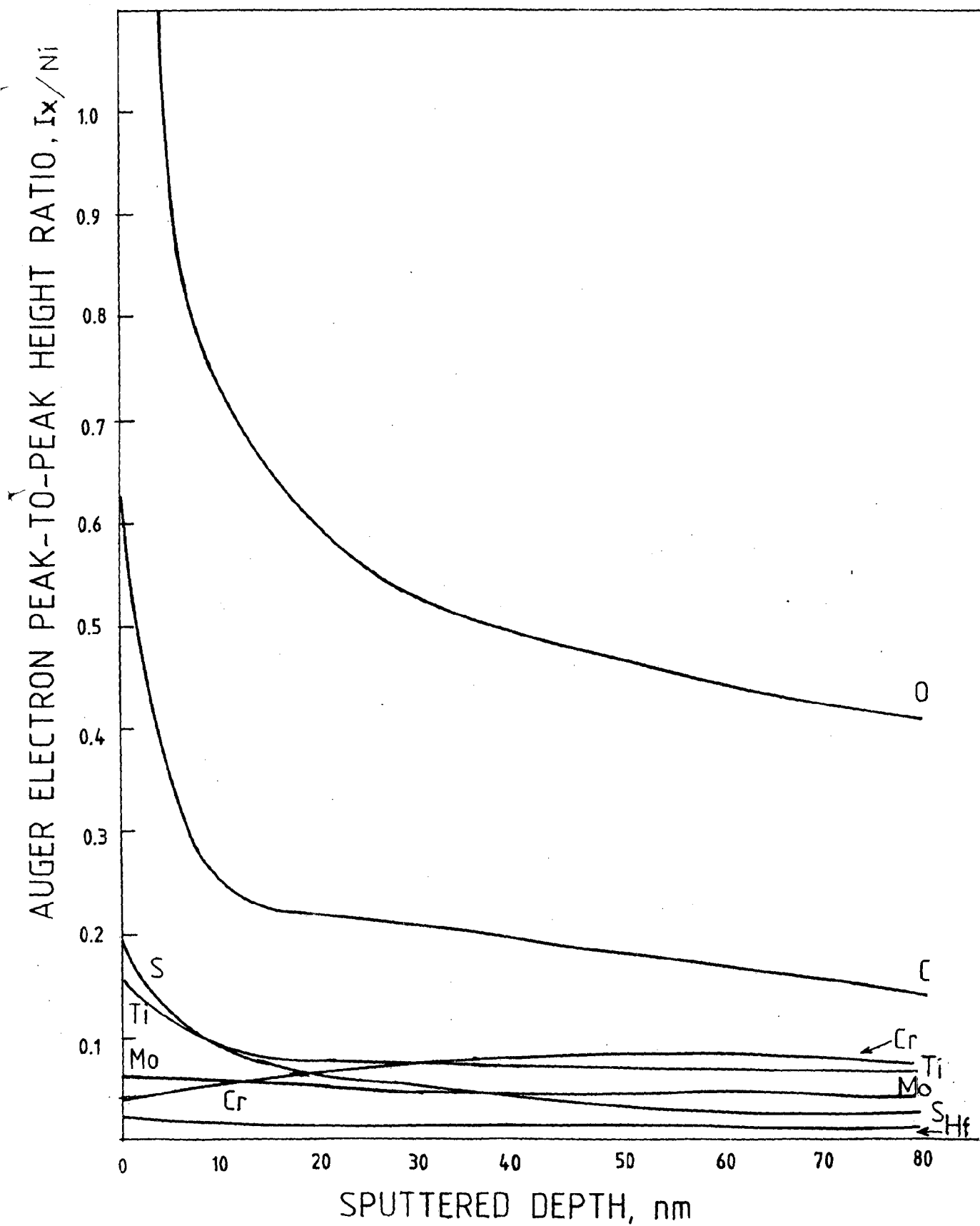
4.10   Auger electron peak-to-peak height ratio as a function of sputtered depth in DMP-I powder.
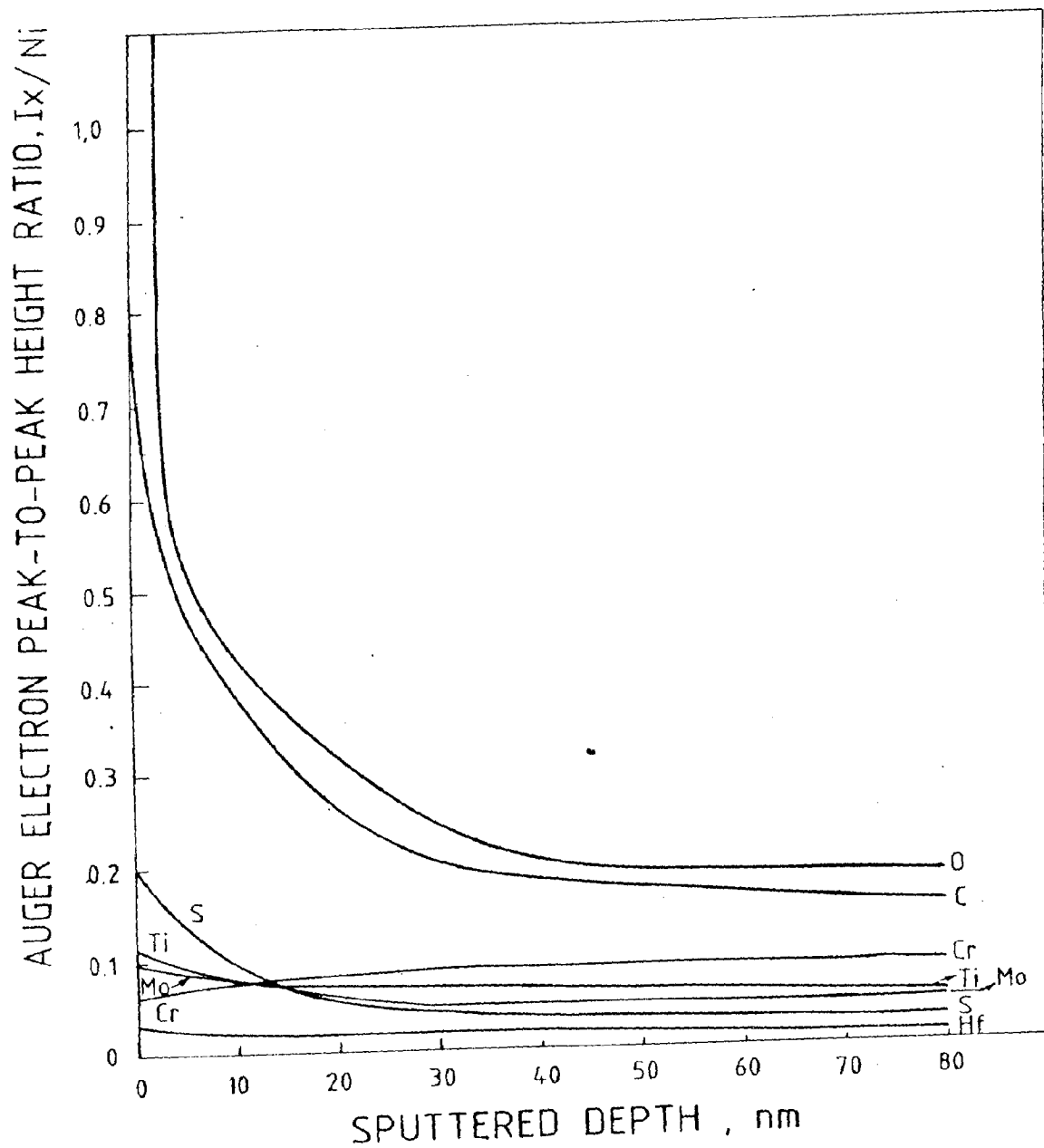
4.11 Auger electron peak-to-peak height ratio as a function of sputtered depth in DMP-2 powder.
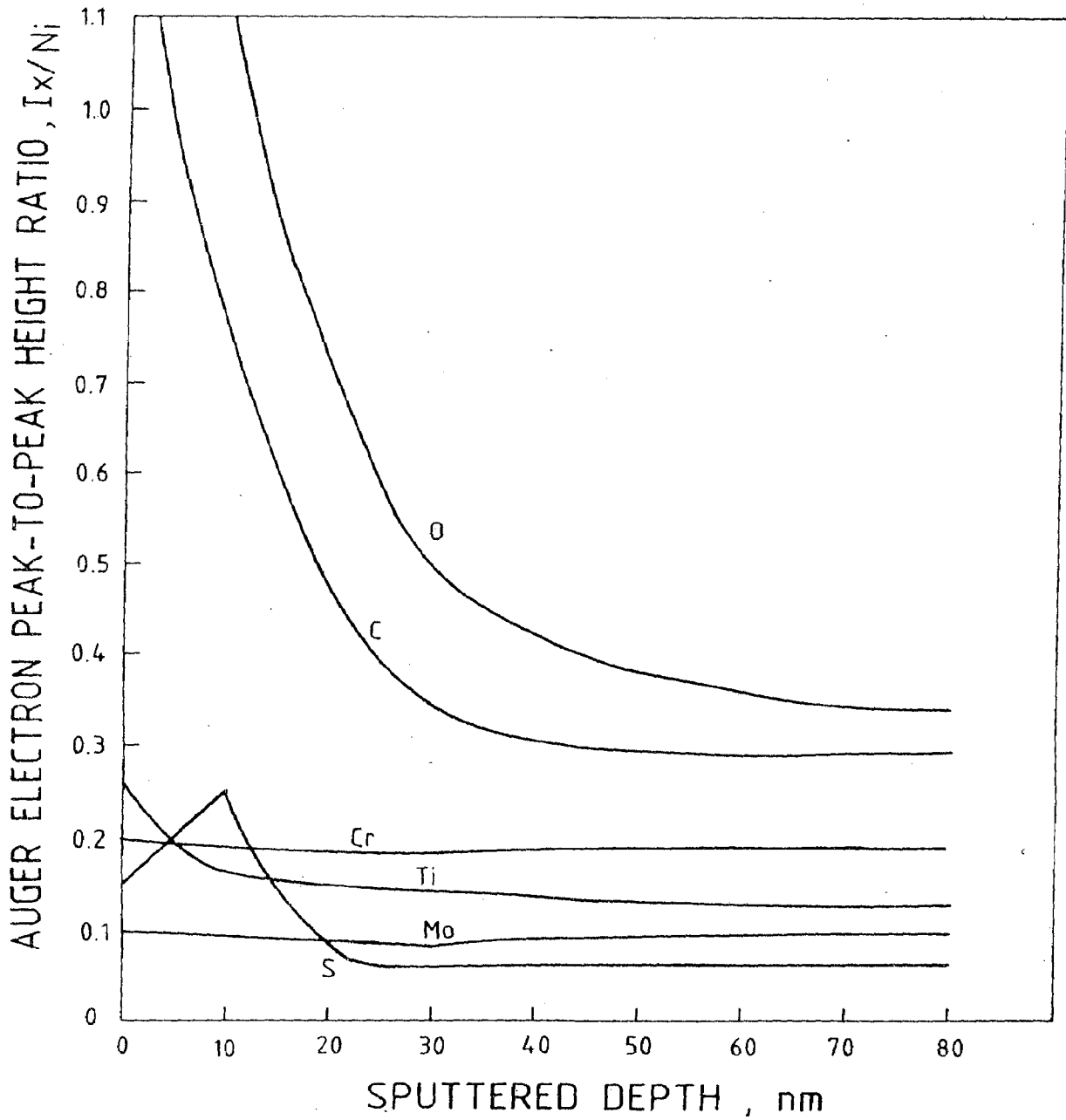
4.12   Auger electron peak-to-peak height ratio as a function of sputtered depth in DMP-3 powder.

these elements steadily decrease, with oxygen and carbon showing steep fall. This is a manifestation of the presence of about 10 nm amorphous layer of carbon and oxygen on the powder surface beneath which carbon is believed to be in the form of titanium carbides [88]. Carbides of tungsten, molybdenum and oxygen are also likely to be associated with these MC carbides. In the case of DMP-3, the powder surface had an extremely high concentration of titanium, carbon and oxygen. Peak-to-peak height ratios of these elements are high even after sputtering to a depth of 30 nm (Fig. 4.12). This is believed to be the effect of relatively higher carbon content in the alloy. Oxygen retained at the powder surface has presumably favoured the migration of titanium and carbon towards the surface, thereby leading to the formation of stable oxy-carbides of titanium. This argument is in agreement with the observations of Aubin et al [88]. In contrast, although DMP-1 and DMP-2 showed a high concentration of Ti, C and O at the powder surface, peak-to-peak height ratios of Ti/Ni, C/Ni and O/Ni are considerably low after 30 nm sputtering. In spite of high oxygen content in DMP-1, formation of oxy-carbides of titanium appears to be suppressed. This is possibly due to a very low carbon content (< 0.02%) in the alloy.

2. Effect of boron on the surface chemistry of powder particle is evident from the sharp decrease of O/Ni and C/Ni ratios (Fig. 4.14). Whereas O/Ti ratios are aproximately 8 and 7.5 after sputtering to a depth of 10 nm and 30 nm in DMP-1 (Fig. 4.10), these ratios are 6 and 4 in the case of DMP-2 (Fig. 4.11). Lower O/Ti ratio in the high-B alloy DMP-2 is thought

to be due to the decrease in the concentration of oxygen on the powder surface.

3.   Mo/Ni ratio on the powder surface is found higher but on subsequent etching, it first indicates a decreasing trend but again shows a slight increase.   Higher initial molybdenum content is indicative of the possibility of the presence of a volatile MoO_3 on the powder surface which was also observed by Water et al [8]

4.   The sputtering profiles of all the three alloys show the presence of sulphur at the powder particle surface.   This is believed to be due to either the formation of carbosulphide of titanium or segregation of sulphur at the surface.   Recent Auger and X-ray diffraction studies have convincingly proved the occurrence of Ti_2CS in maraging steels [117,118].   It has been suggested that in an alloy containing minor amounts of Ti, C and S, titanium carbide will not form without the formation of titanium carbosulphide.   Like maraging steels, superalloys contain low carbon contents ($\cong 0.02\%$) but their titanium contents are much higher and, therefore, probability for the formation of titanium carbosuphide is much higher in superalloys.   The initial increase of S/Ni ratio in DMP-3 is believed to be related to the carbon level in the alloy.   Aubin et al [88] have also observed the increase in sulphur concentration during the first few minutes of sputtering and attribute it to the disappearance of carbon and oxygen.   Ross and Kear [89] also observed that when carbon, oxygen and sulphur are concentrated at the surface

of a solidifying powder particle, the C + O $\rightleftharpoons$ CO reaction should

reduce the oxygen content for high carbon levels, thereby favour-

ing the formation of sulphides rather than oxy-sulphides.

Continuous decrease of S/Ni ratios in alloys DMP-1 (Fig. 4.10)

and DMP-2 (Fig. 4.11), which have extremely low levels of carbon

(< 0.02%) supports this hypothesis. The formation *of* oxy-sulphides

rather than sulphides or carbosulphides may, therefore, occur

in DMP-1 and DMP-2 ; and with etching, segregation of oxysulphide

may decrease.

5. Enrichment of hafnium at the powder particle surface

indicates the presence of hafnium oxide film or a hafnium rich

phase in alloys DMP-1 and DMP-2. This is likely to be responsi-

ble for the lower initial chromium concentration in these alloys.

Al/Ni ratio (not shown here) was also found to be low at the

powder surface. In contrast, DMP-3 showed the presence of

chromium at the powder surface (Fig. 4.12). Al was also found

to be high in DMP-3. Apparently, oxides of Al and Cr may be

low at the powder surface in Hf-modified alloys. Another reason

for the low concentration of chromium oxide in the alloys DMP-1

and DMP-2 is a relatively lower proportion of chromium and

aluminium in these alloys.

6. Presence of boron peak was not detected at the unsputtered

surface of alloys DMP-1 and DMP-3 but DMP-2 which has a high

boron content (0.085%) indicated the presence of a boron peak

(Fig. 4.13). However, this peak disappeared on subsequent

etching. A possible explanation for this interesting behaviour

could be the presence of an amorphous layer of boron and oxygen
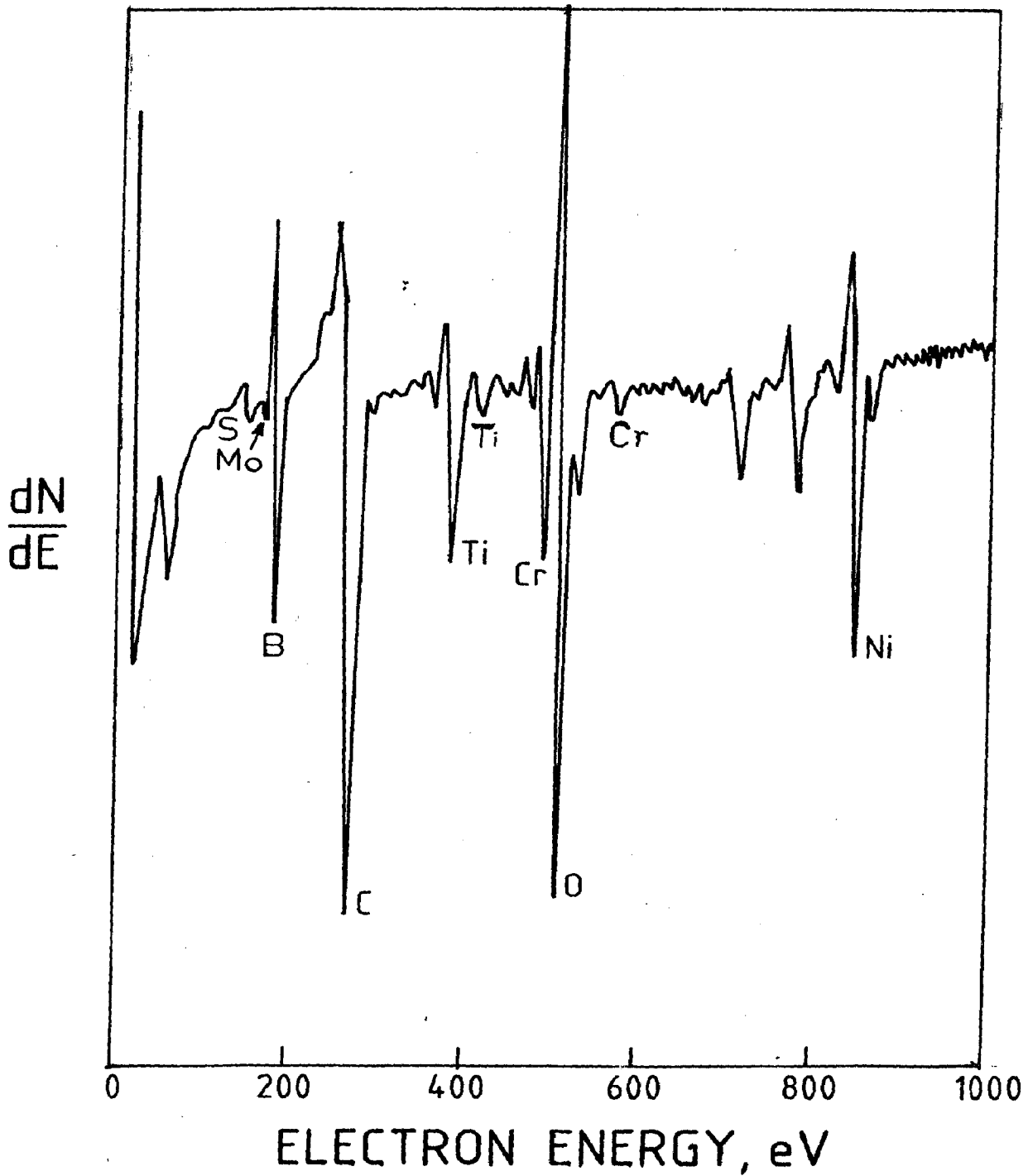
4.13 Auger electron spectrum for unsputtered DMP-2 powder showing the presence of boron on the powder particle surface.

similar to the layer of carbon and oxygen as suggested by Aubin et al [88]. Since Auger electron spectra of DMP-2 obtained after subsequent sputterings did not reveal the presence of boron peaks, boron is believed to be present in elemental form instead of forming borides or oxyborides and is likely to be preferentially etched out during sputtering.

4.4   CONCLUDING REMARKS

Evaluation of the as-cast alloys has shown that the alloy DMP-2 having 0.085% boron has much better microstructural stability and higher elevated temperature strength than DMP-1 or DMP-3. Investigation into its powder solidification behaviour shows that boron tends to suppress the concentration of oxygen on the powder surface in the high boron alloy DMP-2, in contrast to the enrichment of oxygen on the powder surface of DMP-1 and DMP-3. Moderate addition of hafnium has a retarding influence on the activity of sulphur, but results in the formation of an oxide film which is likely to affect the consolidation of the powder. Activities of chromium and titanium towards carbon or oxygen, however, tend to decrease in the presence of hafnium.

CHAPTER 5

INFLUENCE OF HIPING TEMPERATURE AND MINOR CHEMISTRY

VARIATIONS ON CONSOLIDATION BEHAVIOUR

5.1 INTRODUCTION

Hot isostatic pressing is the most commonly used technique to consolidate P/M superalloys. Among the various processing variables such as temperature, pressure, time and cooling rate, the HIPing temperature has been recognised to be the most critical parameter, provided that the pressure is maintained above a minimum level (usually 1 Kbar) and some minimum time (between 1 and 3 hrs) is allowed to achieve 100% densification. As already discussed in Section 2.7.1 (Chapter 2), a fairly wide consolidation temperature range from 25 K below to 50K above the γ' solvus exists for most P/M superalloys, although the higher temperature limit is also dictated by the solidus of the alloy. Depending on the fact whether the consolidation temperature is below or above the γ' solvus, microstructure of the alloy -- and hence its mechanical properties -- would considerably vary. The present chapter describes the effects of changes in the HIPing temperature on the structural and mechanical behaviour of alloys DMP-1, DMP-2 and DMP-3. Effects of minor chemistry variations on the morphological changes of γ', carbides and borides have also been discussed. The influence of Hf and B on the solidus of these alloys and their consolidation temperatures is shown by means of microstructural studies.

5.2   MICROSTRUCTURAL OBSERVATIONS ON AS-HIP MATERIAL

As seen in Section 4.2 (Chapter 4), γ'-solvus is 1473±10K for each of these alloys. It was, therefore, decided to consolidate the alloys at 1448 K (25 K below the γ'-solvus), and 1498 K (25 K above the γ'-solvus).

5.2.1 Hot Isostatic Pressing at 1448 K

Microstructures of DMP-1, DMP-2 and DMP-3 consolidated at 1448 K are shown in Figs. 5.1, 5.2 and 5.3 respectively and their important metallurgical features have been summarized in Table 5.1. Whereas the γ' particles have a cuboidal morphology (Fig. 5.1d) in the low-boron alloy (AH1 material), they have assumed a typical rosette-shaped (akin to dendritic) morphology (Fig. 5.2d) in the high-boron alloy (BH1 material). Further the primary γ' particles in the BH1 material are smaller in size but more widely spaced than those in the AH1 material. In the case of sigma prone alloy (CH1 material), the γ' particles are relatively much larger and cuboidal having an aspect ratio of 2 to 3 (Figs. 5.3c and d). Retention of original dendritic structure in most powder particles in the AH1 and BH1 materials (Figs. 5.1a and 5.2a) and the occasional presence of PPBs and pores in the CH1 material (Fig. 5.3a) indicate that the consolidation temperature of 1448 K is inadequate to achieve full densification.

5.2.2 Hot Isostatic Pressing at 1498 K

Figs. 5.4, 5.5 and 5.6 show the microstructures of the alloys consolidated at 1498 K. Compared to the microstructural
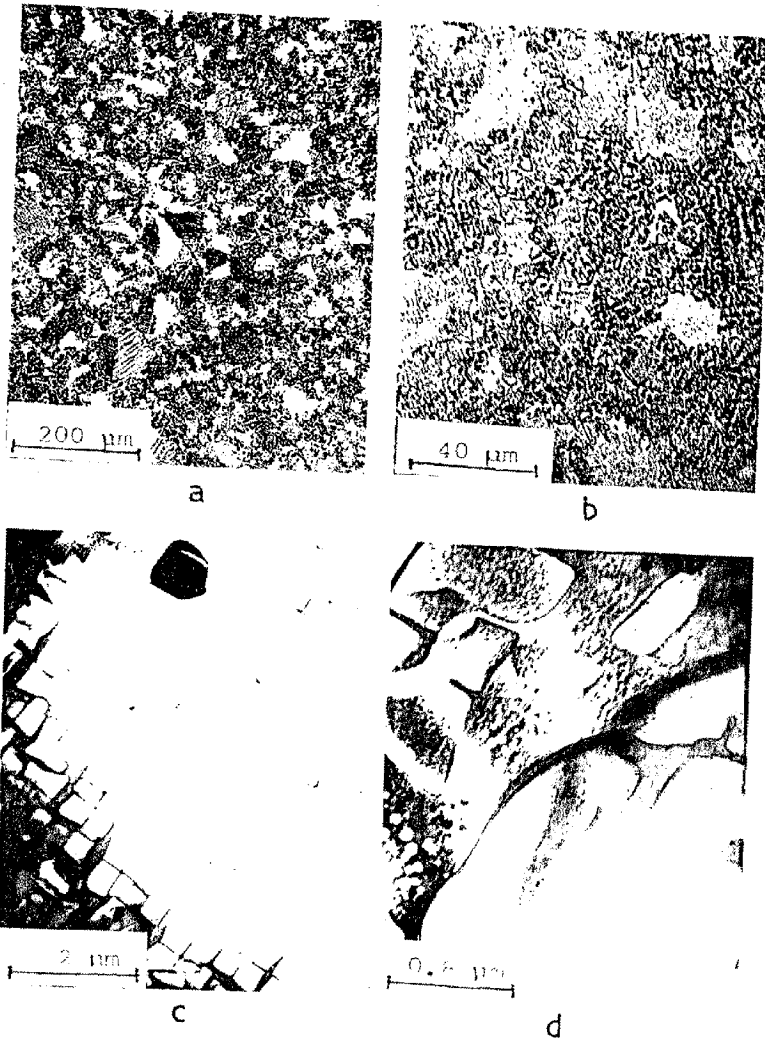
5.1   Microstructures of 1448 K HIPed DMP-1 showing (a) residual powder dendrite structure (b) absence of PPBs (c) morphology of γ' precipitates and carbides and (d) fine and coarse γ' particles at grain boundaries.
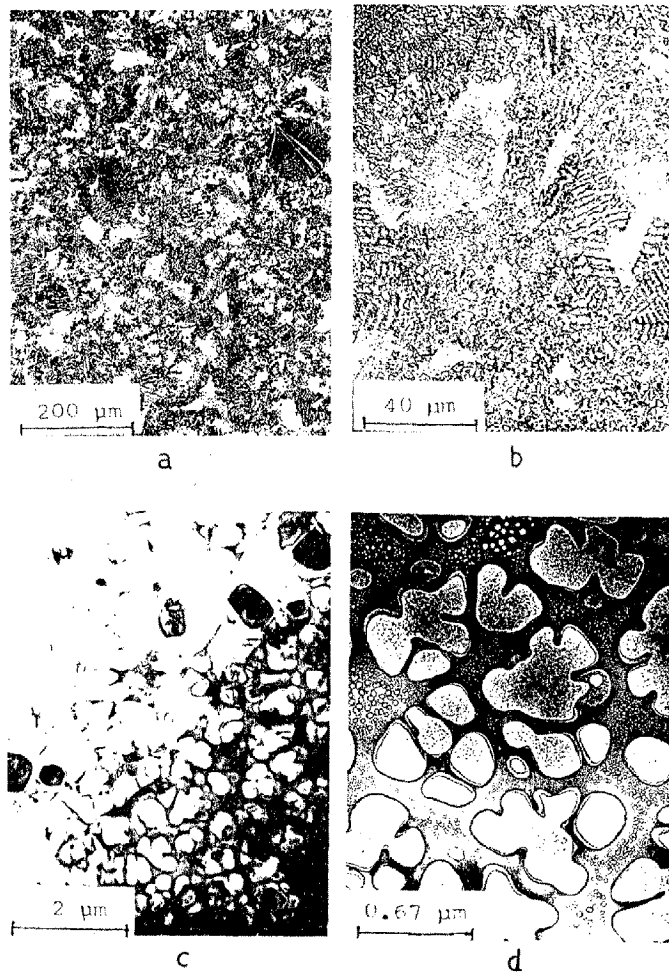
5.2   Microstructures of 1448 K HIPed DMP-2 showing (a) residual
powder dendrite structure (b) absence of PPBs, (c) distribution
of γ' and carbide/boride precipitates (d) dendrite morphology
of γ' precipitates.
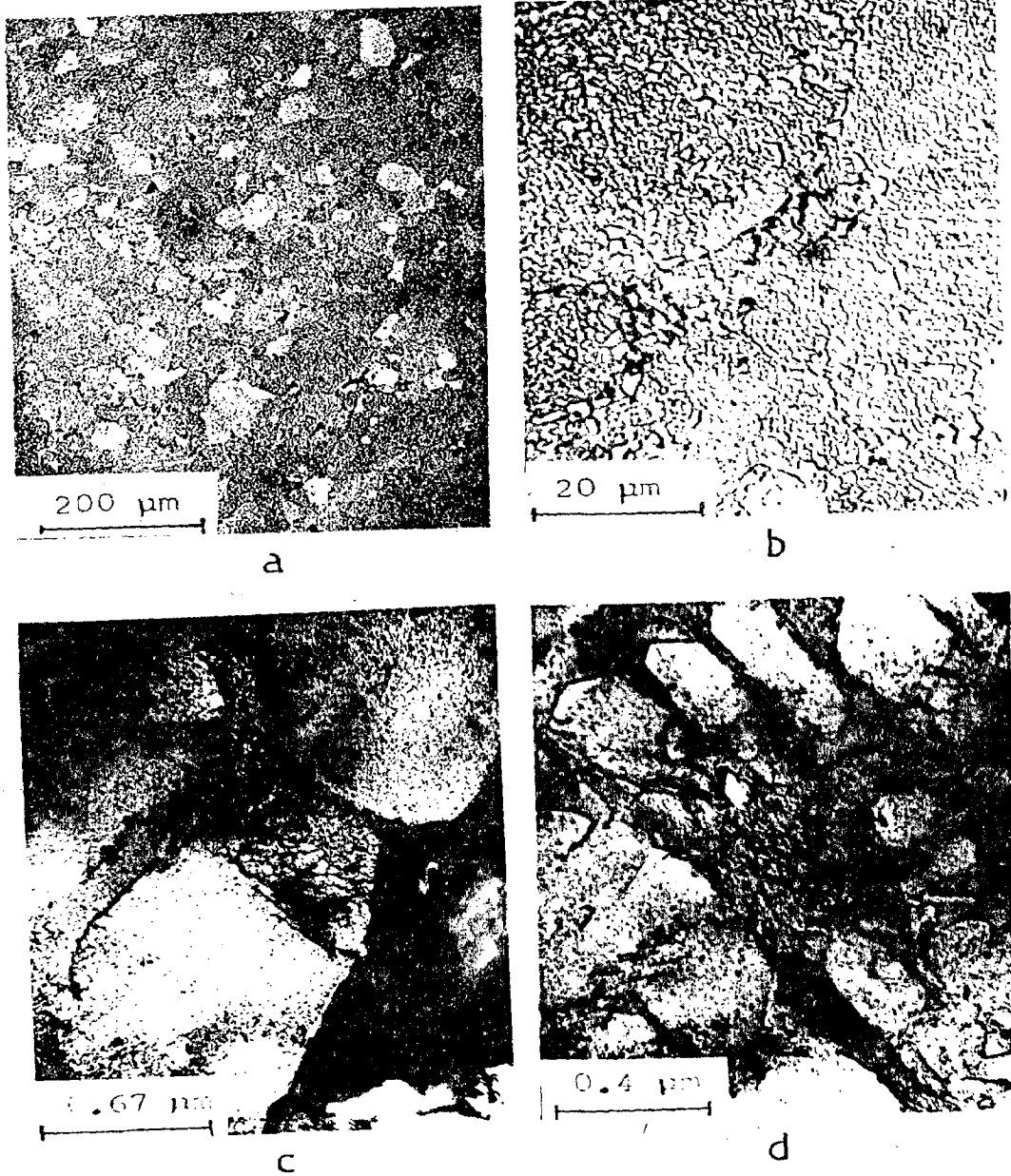
5.3 Microstructures of 1448 K HIPed DMP-3 showing (a) interparticle pores and occasional PPBs (b) coarse intergranular γ' particles engloving carbides (c) coarse intergranular γ' and carbide particles and (d) cuboidal intragranular γ' particles.

Table 5.1 Microstructural Characterization of P/M Superalloys HIPed at 1448 K

	DMP-1	DMP-2	DMP-3
1. General Features	Retention of original dendritic structure by most powder particles but reprecipitation at the PPBs	Predominantly dendritic but no precipitation at the PPBs	Partially dendritic with some precipitation at the PPBs. Fine pores randomly observed at the triple point boundaries
2. Average grain size	≃ 40 μm	≃ 40 μm	≃ 40 μm
3. Characterization of γ'			
(i) Volume fraction	50% approximately	50% approximately	50 to 60%
(ii) Distribution	Intergranular as well as intragranular distribution of primary γ' particles varying in size from 0.5 to 1 μm & ultra fine (0.02 to 0.4 μm) secondary γ' particles interspersed between larger γ' particles	Intergranular and intragranular distribution of primary γ' particles in size of 0.5 to 1 μm alongwith dispersion of ultrafine (0.02 to 0.1 μm) secondary γ' particles	Intergranular & intragranular primary γ' particles (1 to 2 μm) with secondary γ' particles (0.02 to 0.1 μm) interspersed between larger γ' particles
(iii) Morphology	Cuboidal or rosette-shaped particles with a halo around the edges	Spherical particles tending to coalesce together to give flower like appearance	Cuboidal as well as plate-shaped particles with aspect ratio between 2 and 3

Table 5.1 (Contd)

2

	DMP 1	DMP 2	DMP 3
4. Minor phases	Fine distribution of inter-grannular and intragrannular globular or cuboidal particles of 0.5 to 1 um size throughout the microstructure. Grain boundaries virtually free from carbides	Increased amount of inter-granular or intragranular cuboidal and hexagonal particles of 0.5 to 1 um size	Cuboidal or hexagonal particles enveloped by coarser particles mainly at the grain boundaries
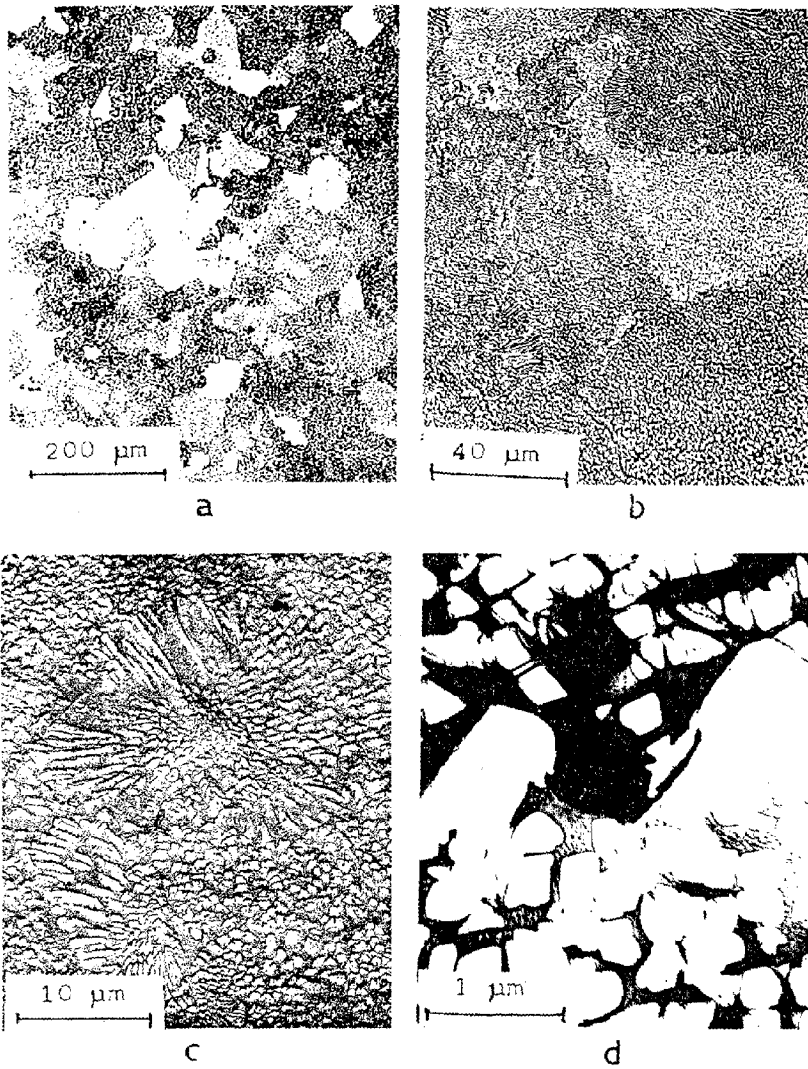
5.4   Microstructures of 1498 K HIPed DMP-1 showing (a) increase in grain size (b) absence of PPBs (c) the presence of eutectic $\gamma + \gamma'$ islands (d) morphology of γ' particles.
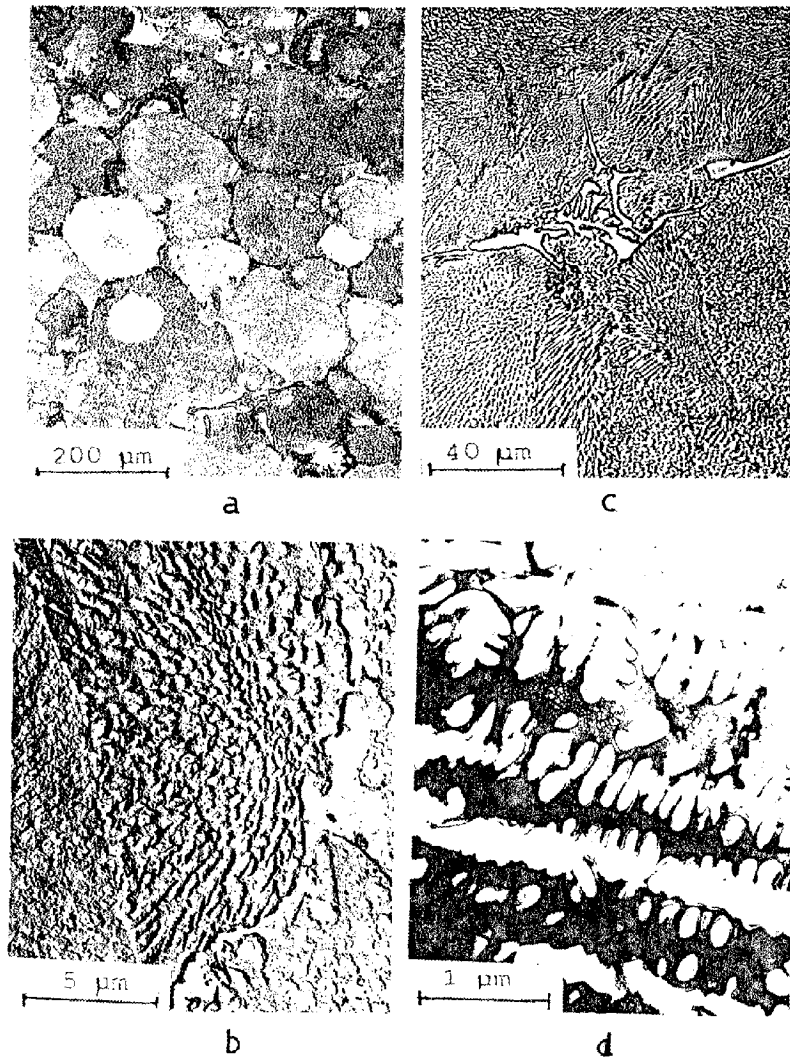
5.5 Microstructures of 1498 K HIPed DMP-2 showing (a) increase in grain size (b) the presence of grain boundary boride films and eutectic $\gamma + \gamma'$ structure (c) the higher magnification SEM view of the boride film and (d) morphology and distribution of fine and coarse dendrite γ' particles.
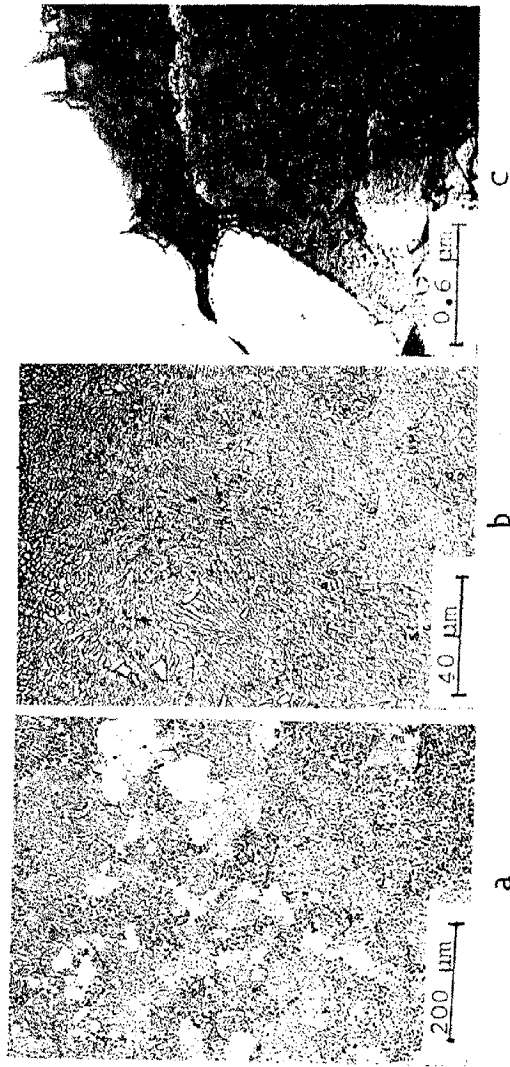
5.6 Microstructures of 1498 K HIPed DMP-3 showing (a) limited increase in grain size (b) the presence of eutectic $\gamma + \gamma'$ structure (c) distribution and morphology of coarse γ' and carbide particles at grain boundaries.

Table 5.2 Microstructural Characterization of P/M Superalloys HIPed at 1498 K

Microstructural details	DMP 1	DMP 2	DMP 3
1. General features	No precipitation at the PPBs, 30 to 40% of the microstructure has eutectic morphology	Large elongated particles delineating the grain boundaries, 50 to 60% of the structure has eutectic morphology, no PPBs	About 30% of the microstructure has eutectic morphology, no PPBs
2. Average grain size	$\simeq 80$ μm	$\simeq 120$ μm	$\simeq 60$ μm
3. Characteristics of γ'			
(i) Volume fraction	$\simeq 50\%$	$\simeq 50\%$	$\simeq 50\%$
(ii) Distribution	Intergranular as well as intragranular γ' particles, the former being of about 1 μm size & the later of 0.2 to 0.5 μm size. Secondary cooling γ' also seen	A wide distribution of inter-granular and intragranular γ' particles varying in size from 0.02 um to 1 μm	Intergranular γ' particles are of 1 μm size & mostly at the grain boundaries. Intra-granular γ' precipitates of 0.1 to 0.5 μm also dispersed uniformly with 0.02 to 0.1 μm secondary γ' particles
4. Minor phases	Virtually absent	Large intergranular boride films	virtually absent
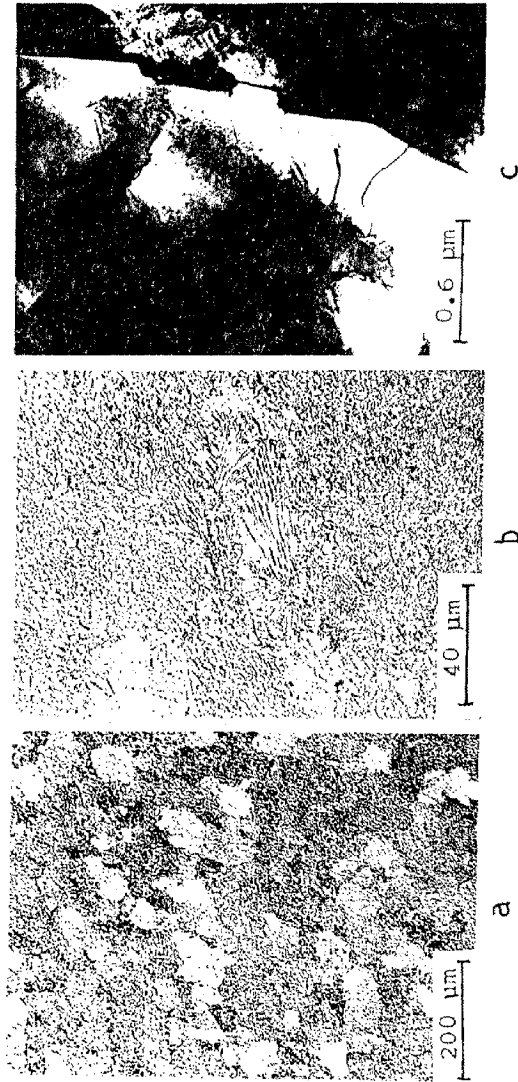
5.7 Microstructures of 1473 K HIPed DMP-1 showing (a) the absence of PPBs and grain size (b) the presence of occasionally dispersed eutectic $\gamma + \gamma'$ islands and (c) distribution and morphology of γ' and carbide particles at grain boundaries.
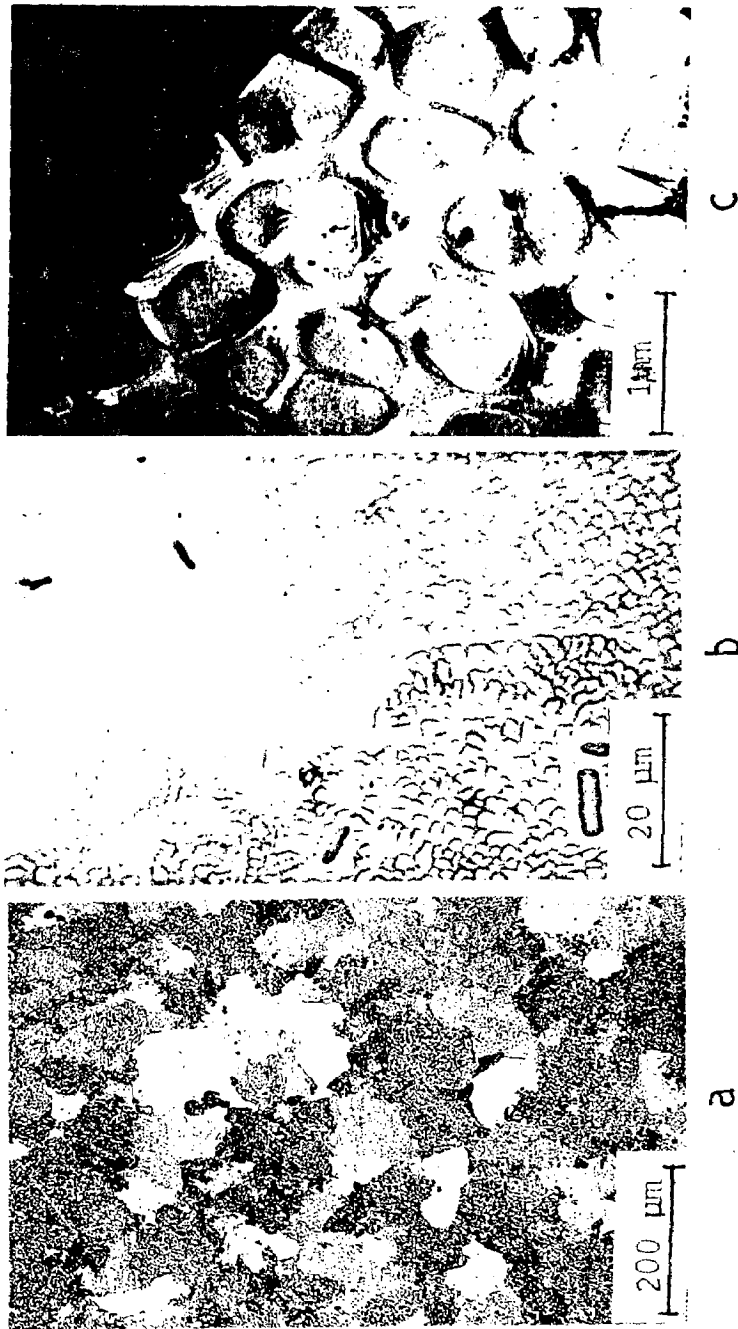
5.8 Microstructures of 1473 K HIPed DMP-2 showing (a) limited increase in grain size (b) distribution of cuboid-shaped carbide/boride particles interspersed with occasional eutectic $\gamma + \gamma''$ islands (c) spheroidal γ' particles tending to coalesce.
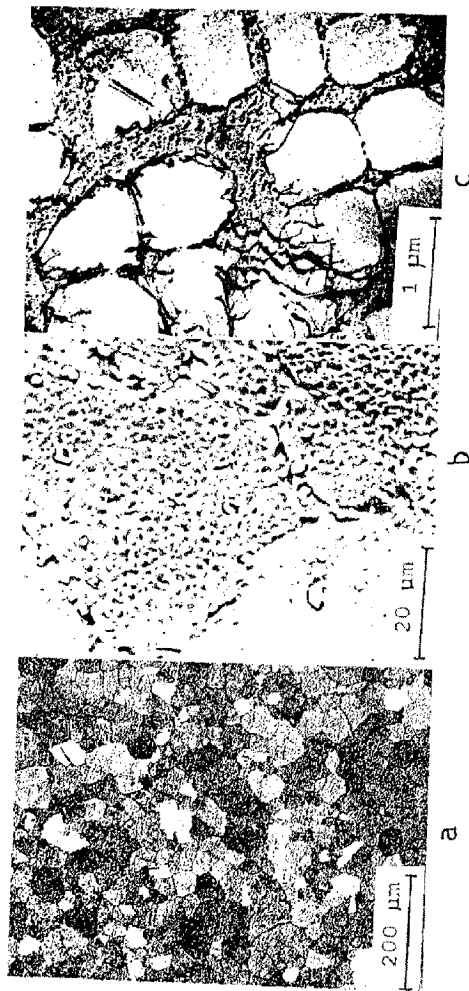
5.9   Microstructures of 1473 K HIPed DMP-3 showing (a) fine grain size (b) decoration of grain boundaries by carbides but without any trace of PPBs and (c) the morphology of γ'.

changes observed in 1448 K consolidated alloys, microstructural changes due to minor variations in alloy chemistry were more perceptible in 1498 K consolidated alloys and are listed in Table 5.2. As expected, each alloy registered a significant increase in grain size but the BH3 material showed an unusually large grain growth accompanied with the precipitation of massive elongated particles delineating the grain boundaries as shown in Figs. 5.5b and c. Film-like morphology of these particles suggests that these could be borides having reprecipitated during slow cooling in the HIP autoclave from the consolidation temperature, which apparently, is above the boride solvus Similar behaviour has been observed in AP-1 by Symonds et al[99]. Further, formation of a large volume fraction of eutectic $\gamma + \gamma'$ structure in AH3 and BH3 indicates that the consolidation temperature is not only above the γ' solvus but is also above the solidus. CH3 also reveals (Fig. 5.6) the presence of randomly dispersed eutectic $\gamma + \gamma'$ islands, although their volume fraction is much less in comparison with the other two alloys. However, grain growth in this alloy appears to be restricted. This is to be expected because the alloy has comparatively higher carbon contet [10,11].

From the above consolidation studies, it is apparent that while a temperature below the γ' solvus (i.e., 1448K) is not sufficient to produce full densification, a temperature 25 K above the γ' solvus (i.e. 1498 K) results in undesirable microstructures which are likely to adversely affect the mechanical properties, particularly for the high boron alloy. It

was, therefore, decided to consolidate the alloys at 1473K, an intermediate temperature between 1448 and 1498 K.

5.2.3 Hot Isostatic Pressing at 1473 K

Microstructures of the 1473 K consolidated alloys are given in Figs. 5.7, 5.8 and 5.9 showing some identical features such as grain size between 60 and 80 μm and uniformly distributed primary γ' particles of approximately 1 μm size. Whereas, AH2 and BH2 show the occasional presence of eutectic $\gamma + \gamma'$ colonies, the CH2 material does not show such a structure. Further, there is a wide variation among the three alloys in respect of the grain boundary precipitation of minor phases. In AH2, the grain boundaries are virtually devoid of carbides or borides (Fig. 5.7b). In BH2 also, the grain boundaries do not appear to be well defined because of the absence of carbides or borides, but fine to coarse (2 to 5 μm) cuboidal or plate-shaped precipitates are uniformly distributed throughout the structure (Fig. 5.8b). In contrast, the CH2 material, because of a higher proportion of carbon and refractory elements, exhibits well defined grain boundaries with spheroidal precipitates of 1 to 2 μm in size. These precipitates are believed to be carbides or borides.

5.3 INFLUENCE OF CONSOLIDATION TEMPERATURE ON PROPERTIES

5.3.1 Room Temperature Tensile Properties

Table 5.3 presents the room temperature (RT) tensile properties of the as-HIP alloys consolidated at 1448, 1473 and 1498 K. Low UTS and ductility of AH1 and BH1 are attributed

Table 5.3   Room Temperature Tensile Properties of As-HIP P/M
Superalloys

Alloy	Code	HIP temp-erature (K)	0.2% off-set yield strength (MPa)	Ultimate tensile stregnth (MPa)	Elonga-tion* (%)	RA%
	AH1	1448	791	1065	7	8
DMP 1	AH2	1473	844	1325	14	16
	AH3	1498	825	1054	8	9
	BH1	1448	855	963	4.5	6
DMP 2	BH2	1473	846	1138	15	16
	BH3	1498	858	1038	5	7
	CH1	1448	844	1159	8	10
DMP 3	CH2	1473	952	1349	15	16
	CH3	1498	974	1200	7.5	10

*   For gauge length of 25.4 mm

to the presence of residual dendrite structure. CH1 also exhibits the lowest RT tensile properties in comparison with the CH2 and CH3 materials. This is to be expected because the observed presence of pores and PPBs (Fig. 5.3a) can have adverse effect on the tensile behaviour in the CH1 material. Thus, HIPing temperature below the γ' solvus appears to be inadequate to achieve 100% densification for all the three alloys.

Consolidation above the γ' solvus, i.e., 1498 K, is observed to adversely affect the RT tensile properties for DMP-1 and DMP-2. This may be attributed to two factors, viz., grain growth that has occured during HIPing itself, and inhomogeneous microstructure due to the precipitation of a large amount of eutectic $\gamma + \gamma'$ phase.

A sharp decrease in the tensile ductility of the BH3 material is probably caused by the presence of nearly continuous boride films at the grain boundaries (Fig. 5.5c). It is, however, interesting to note that in spite of grain growth, the YS is not significantly affected presumably because of the increased hardening effect of borides both within the grains and at the grain boundaries. These borides, which are hard and brittle in nature, block the movements of dislocations, thereby producing a high work hardening rate. However, with the increase in deformation and the consequent increase in the stress concentration at the locations of these borides, cracks are likely to occur leading to premature failure. This was in fact confirmed during the fractographic examination (discussed in Section 5.4).

In contrast, the same consolidation temperature of 1498K did not affect the YS of CH3 material, probably because the grain growth during consolidation was restricted by the presence of finely distributed intergranular as well as intragranular carbide precipitates, which have a larger volume fraction in this alloy by virtue of comparatively higher carbon content. Reduction in ductility with corresponding decrease in UTS is attributed to the precipitation of eutectic γ + γ' structure.

It can thus be deduced from the comparison of RT tensile properties (Table 5.3) that consolidation performed at the intermediate temperature of 1473 K, which is very close to the γ' solvus of all these alloys, offers an optimal combination of properties.

5.3.2 Elevated Temperature Tensile Properties

Table 5.4 shows a comparison of the 1033 K tensile properties of the three alloys consolidated at 1448, 1473 and 1498K. In the case of DMP-1, both YS and UTS appear to remain relatively unaffected by the increase in HIPing temperature but the tensile ductility of the AH2 material is much higher than that of the AH1 or AH3 materials. BH2 has the best combination of YS, UTS and ductility as compared to BH1 or BH3. Severe drop in the YS and ductility of BH3 is possibly due to an inhomogeneous microstructure consisting of a large volume fraction of eutectic γ + γ' phase and continuous boride films at the grain boundaries. Low ductility in BH3 should have been accompanied by low UTS as well, but the UTS observed is rather high. Reason for this high rate of work hardening is not

Table 5.4   Tensile   properties of As-HIP P/ M superalloys
at 1033 K in vacuum

Alloy	Code	HIP tempera- ture (K)	0.2% Off- set yield strength (MPa)	Ultimate tensile strength (MPa)	Elonga- tion* (%)	R A (%)
	AH1	1448	822	942	6	6
			815	985	7	7
DMP 1	AH2	1473	802	976	15	18
			830	984	12	16
	AH3	1498	768	889	6	8
			785	897	6	8
	BH1	1448	908	953	7	8
			856	914	6	8
DMP 2	BH2	1473	789	986	15	10
			834	997	10	12
	BH3	1498	749	959	3.5	5
			765	932	4	5
	CH1	1448	878	963	6	6
			898	981	5	5
DMP 3	CH2	1473	975	1019	7	10
			989	1025	10	12
	CH3	1498	950	1000	4	4
			962	1032	6	7

*   For gauge length of 25.4mm

clearly understood. In contrast, the mechanical properties of DMP-3 do not appear to be significantly affected by changes in its consolidation temperature from 1473 to 1498 K, although tensile ductility of the 1498 K HIPed material (CH3) is lower than that of the 1473 K HIPed material (CH2).

From the mechanical behaviour of these alloys it can be inferred that the alloy DMP-3 offers the best combination of room temperature and elevated temperature mechanical properties in comparison with DMP-1 and DMP-2. Further, the optimum consolidation temperature for all the three alloys is considered to be 1473 ± 10 K.

5.4 FRACTURE BEHAVIOUR OF AS-HIP ALLOYS

Fig. 5.10a shows the SEM fractographs of CH1 specimens tensile tested at RT revealing the presence of voids at the interparticle boundaries and prior particle boundaries and thus confirms that the HIPing temperature of 1448 K is not adequate to achieve full densification. Both AH1 and BH1 specimens tested at RT and 1033 K also showed interparticle failure but voids were not seen. Examination of the longitudinal gauge section of the 1033 K tensile tested specimens under optical microscope revealed the presence of residual dendritic structure (Fig. 5.10b) further confirming that the HIP temperature of 1448 K is insufficient. In contrast, the alloys consolidated at 1473 K exhibited complete densification as is evident from the SEM fractographs of CH2 material tested at RT (Fig.5.11). Formation of shear lip (Fig. 5.11a) and presence of dimples
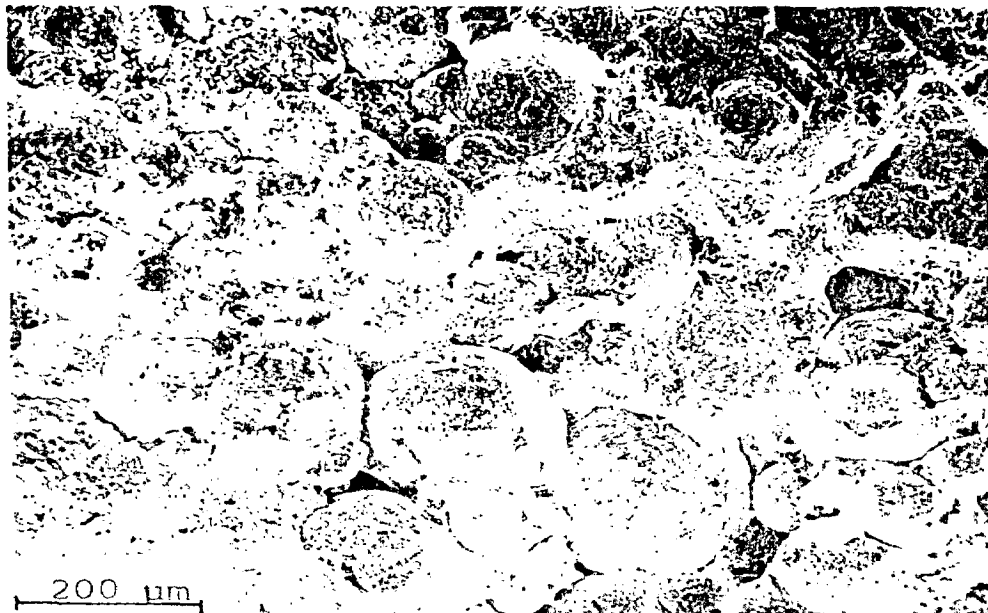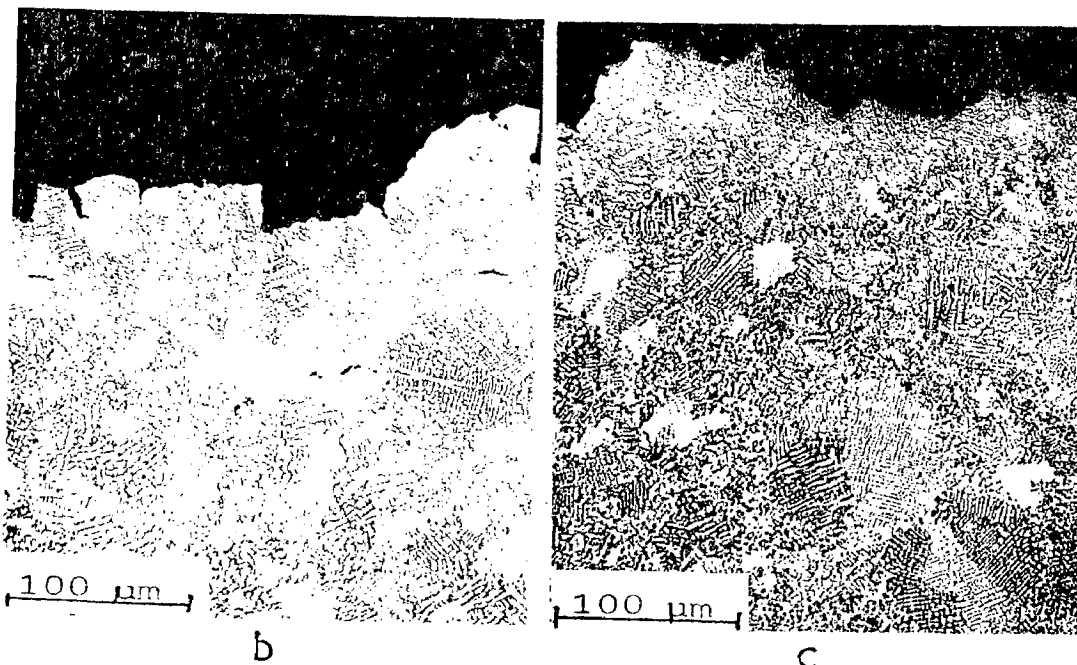
5.10   Fracture behaviour of 1448 K HIPed alloys: (a) SEM fractograph
of DMP-3 (CH I specimen) tensile tested at RT showing interparticle
failure and presence of pores; (b) and (c) optical micrographs
of the AH1 and BH1 specimens respectively tensile tested at
1033 K illustrating the occurrence of failure at interdendritic
or interparticle boundaries.

a

b

5.11   SEM fractographs of RT tensile tested CH2 specimen (1473 K HIPed DMP-3) showing (a) formation of shear lip and (b) high magnification view of region 'A' illustrating the presence of dimples and a mixed (ductile-cum-brittle) failure.
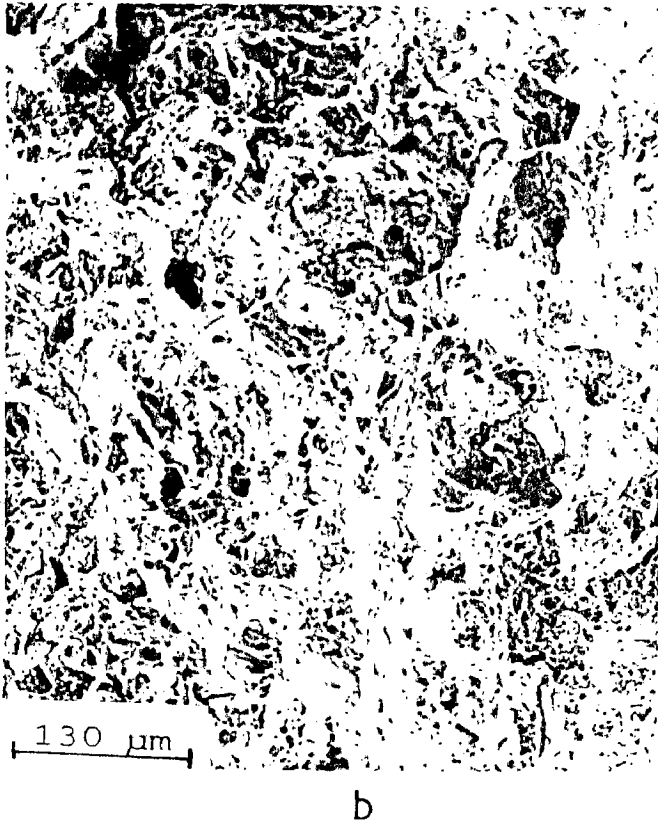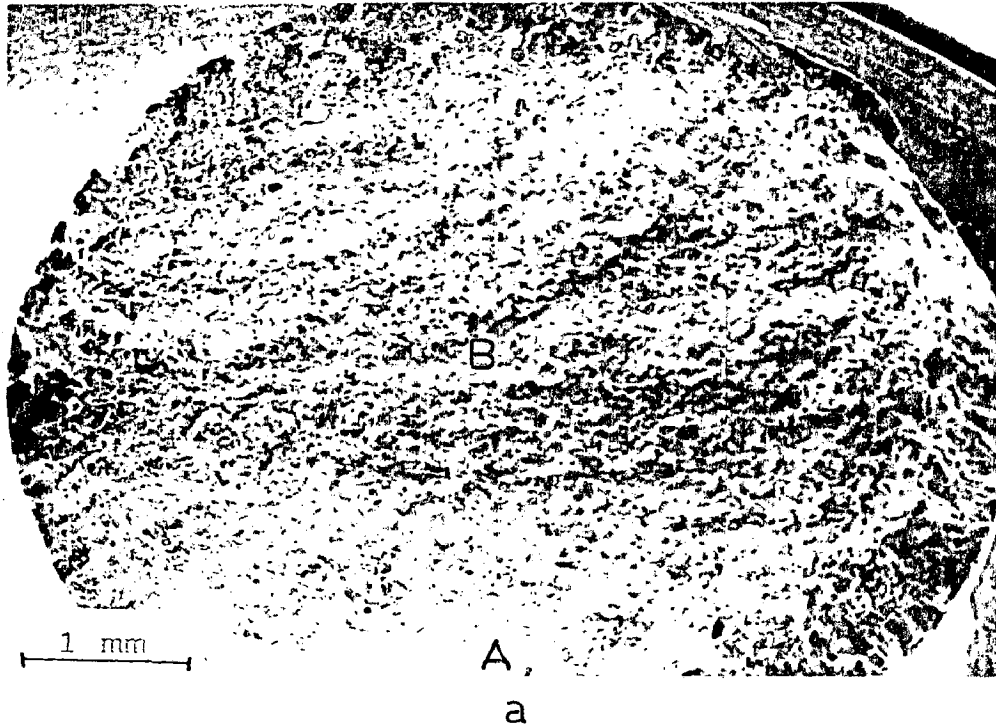
5.12   SEM fractographs of 1033 K tensile tested AH2 specimen (1473K HIPed DMP-1) showing (a) formation of shear lip and (b) deformation dimples and considerable ductility in region 'A' (c) partly ductile and partly brittle fracture mode evident in the central region 'B'.
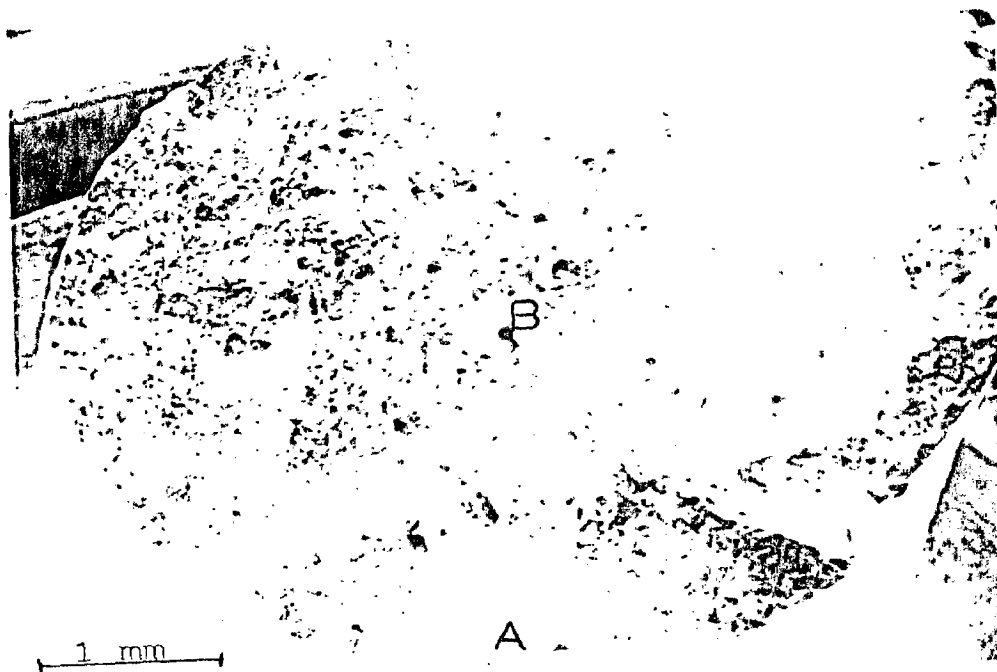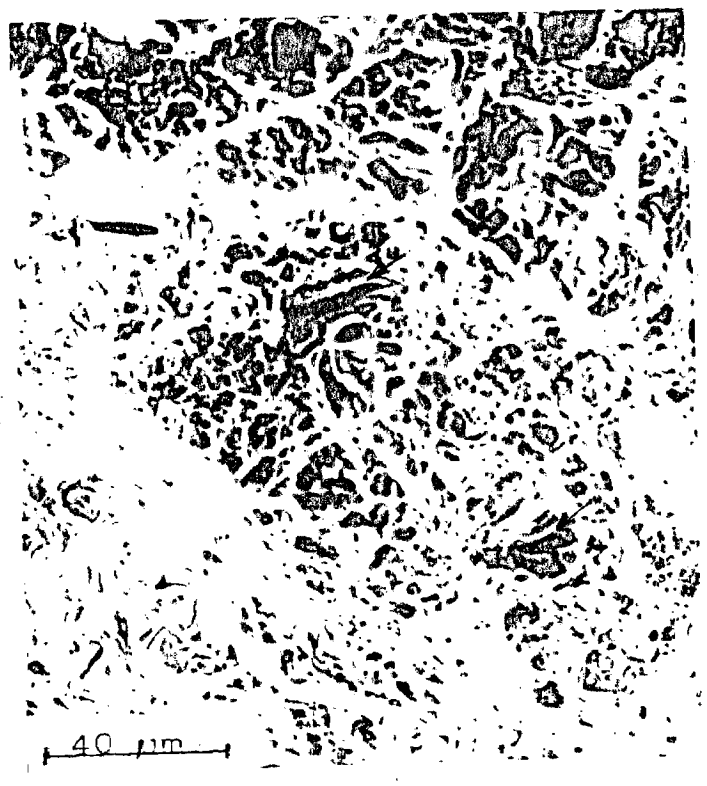
5.13   SEM fractographs of 1033 K tensile tested BH 2 specimen (1473K
        HIPed DMP-2) showing (a) macroview (b) intergranular features
        accompanied with considerable ductility in the peripheral region
        marked 'A' and (c) high magnification view of the central region 'B'
        revealing the fragmentation of boride particles (marked by arrows).
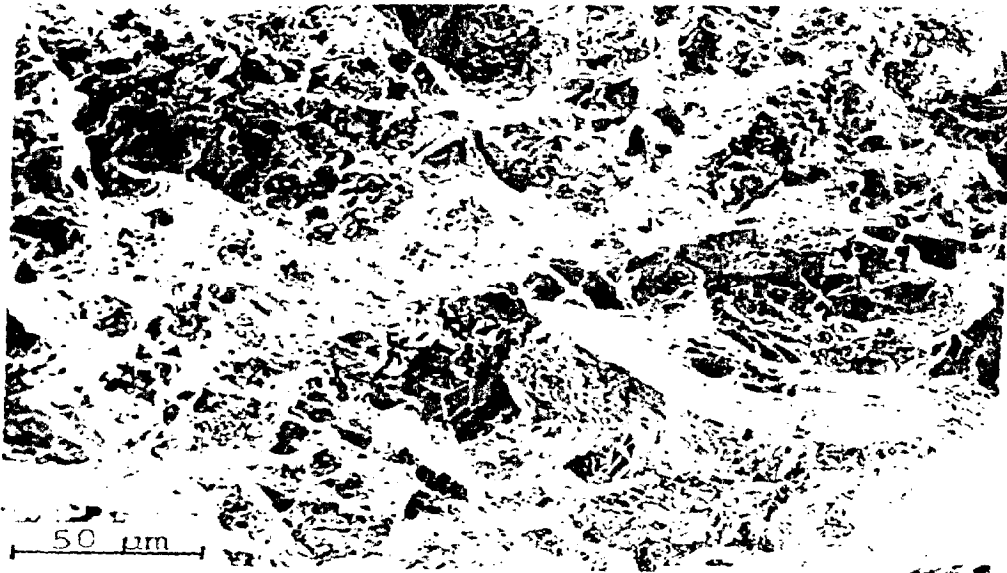
5.14   SEM fractographs of 1033 K tensile tested CH2 specimen (1473K HIPed DMP-3) showing (a) macroview (b) both intergranular and transgranular features with considerable ductility.
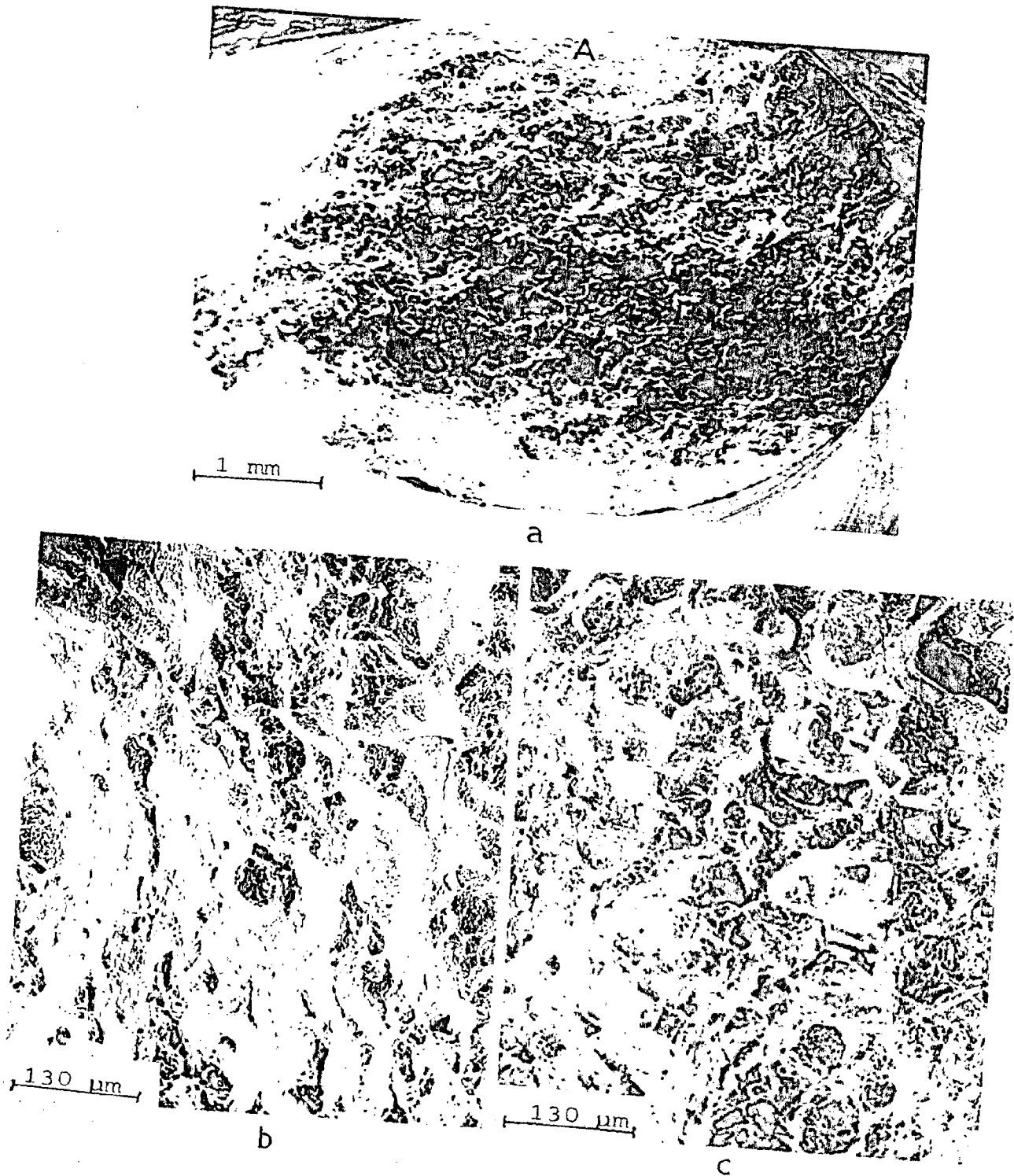
5.15   SEM fractographs of the 1033 K tensile tested AH 3 specimen
(1498 K HIPed DMP-1) showing (a) the formation of shear lip
(b) extensive slip deformation in the peripheral portion 'A' in
(a) and (c) occasional presence of powder particle facets suggesting
an interparticle failure.
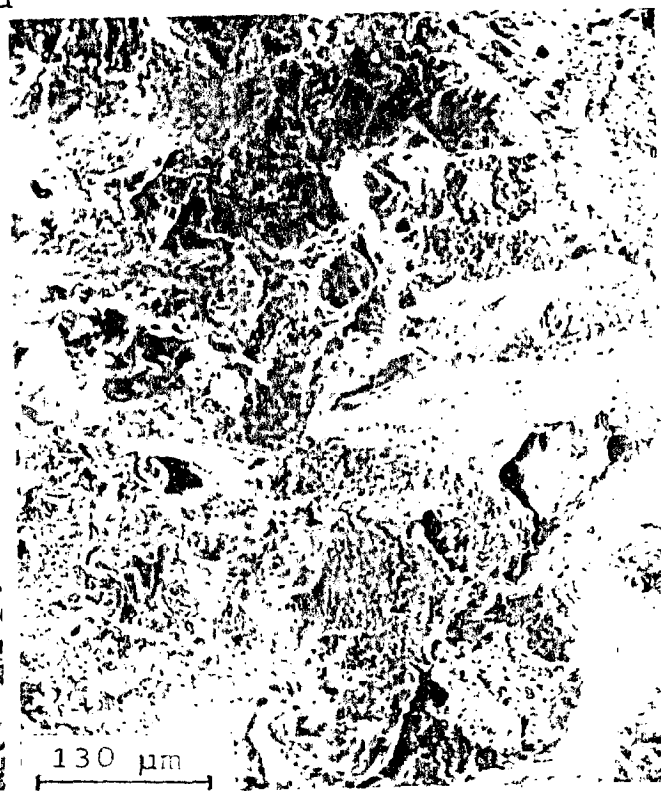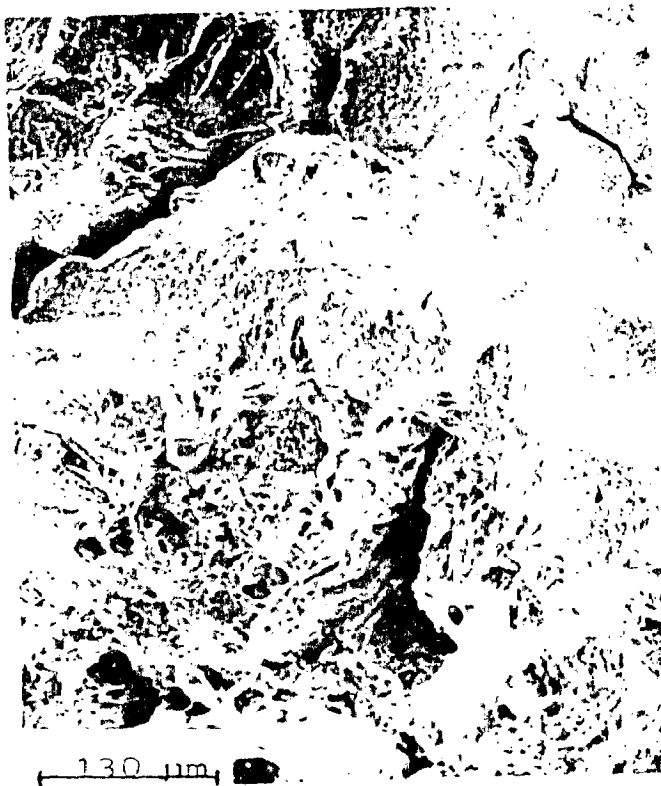
5.16   SEM fractographs of 1033 K tensile tested BH3 specimen showing
        extensive cracking accompanied with cleavage both at the edges
        (b) and the centre (c).

indicate a fair amount of ductility thereby suggesting that the material has yielded to a mixed (ductile-cum-brittle) failure. AH2 and BH2 specimens also showed similar behaviour.

Figs. 5.12, 5.13 and 5.14 show the SEM micrographs of the fractured surfaces of AH2, BH2 and CH2 specimens respectively after these were tensile tested at 1033 K. Each of these specimens exhibited a limited amount of ductility (Table 5.4) before yielding to an intergranular failure, as manifested by the presence of numerous deformatioin dimples in the fracture surfaces of these specimens. The BH2 specimen (high-boron alloy) also showed some fragmented particles (Fig.5.13c). On microanalysis with the help of EDAX attachment to SEM these particles (marked by arrows) were found to be rich in tungsten, molybdenum, niobium and chromium and are believed to be their borides or borocarbides. Such fragmented particles were not seen in the AH2 or CH2 material.

The AH3 specimen tensile tested at 1033 K showed the formation of shear lip covering approximately 60% of the peripherial area (Fig. 5.15a). This shear lip portion reveals extensive slip deformation (Fig. 5.15b), whereas the central portion shows the occasional presence of powder particle facets (Fig. 5.15c) suggesting the initiation of failure at PPBs. In the case of BH3 specimen tensile tested at 1033 K, presence of PPBs was not detected but the fracture surface showed extensive cracking accompanied with cleavage facets (Fig. 5.16). These cracks are believed to be the result of large stress

40 µm
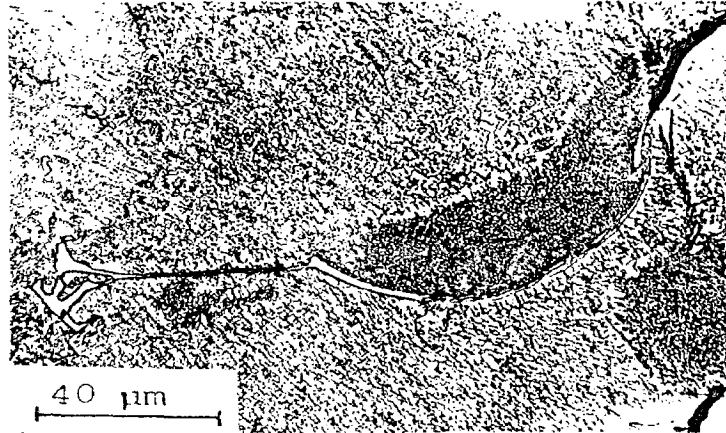
5.17   Microstructure of the 1033 K tensile tested BH3 specimen showing the propagation of cracks along the boride films.

1 mm

a

130 µm

b

5.18   SEM fractographs of 1033 K tensile tested CH3 specimen (1498K HIPed DMP-3) showing (a) macroview (b) surface defect l~ ⁻¹⁻⁻ to a premature failure.

concentration at the locations of boride particles which are hard and brittle in nature. This was also confirmed by the microstructural examination of the other half of the specimen longitudinally mounted, as shown in Fig. 5.17. Being of a film-like morphology and mostly delineating the grain boundaries, these boride precipitates induce initiation as well as propagation of cracks along their lengths thus adversely affecting the ductility and the UTS. In the case of CH3, the fracture surface showed the formation of shear lip (Fig. 5.18a), indicating some ductility. High magnification view of peripheral area marked as A in Fig. 5.18a, however, showed that the specimen had some surface defects (Fig. 5.18b). This appears to be the cause of lower ductility of the CH3 material (Table 5.4).

5.5   AUGER ANALYSIS OF IN-SITU FRACTURE

Fig. 5.19 shows the results of scanning Auger electron microprobe analysis on the AH2 specimen fractured in-situ. Occasionally dispersed particles rich in sulphur and oxygen were detected and are shown in Figs. 5.19b and c. X-ray image for carbon was found to be very faint in the oxygen-rich area This area was argon sputtered to a depth of 50 nm. The peak-to-peak height ratios for oxygen, carbon, sulphur and titanium with respect to nickel were plotted against the sputtered depth and are shown in Fig. 5.19d. Both O/Ni and S/Ni ratios show marked decrease after 10nm sputtering, thereby suggesting sulphur enrichment of the powder particle surface. This is indicative of the segregation of a $Ni-Ni_2S$ eutectic phase
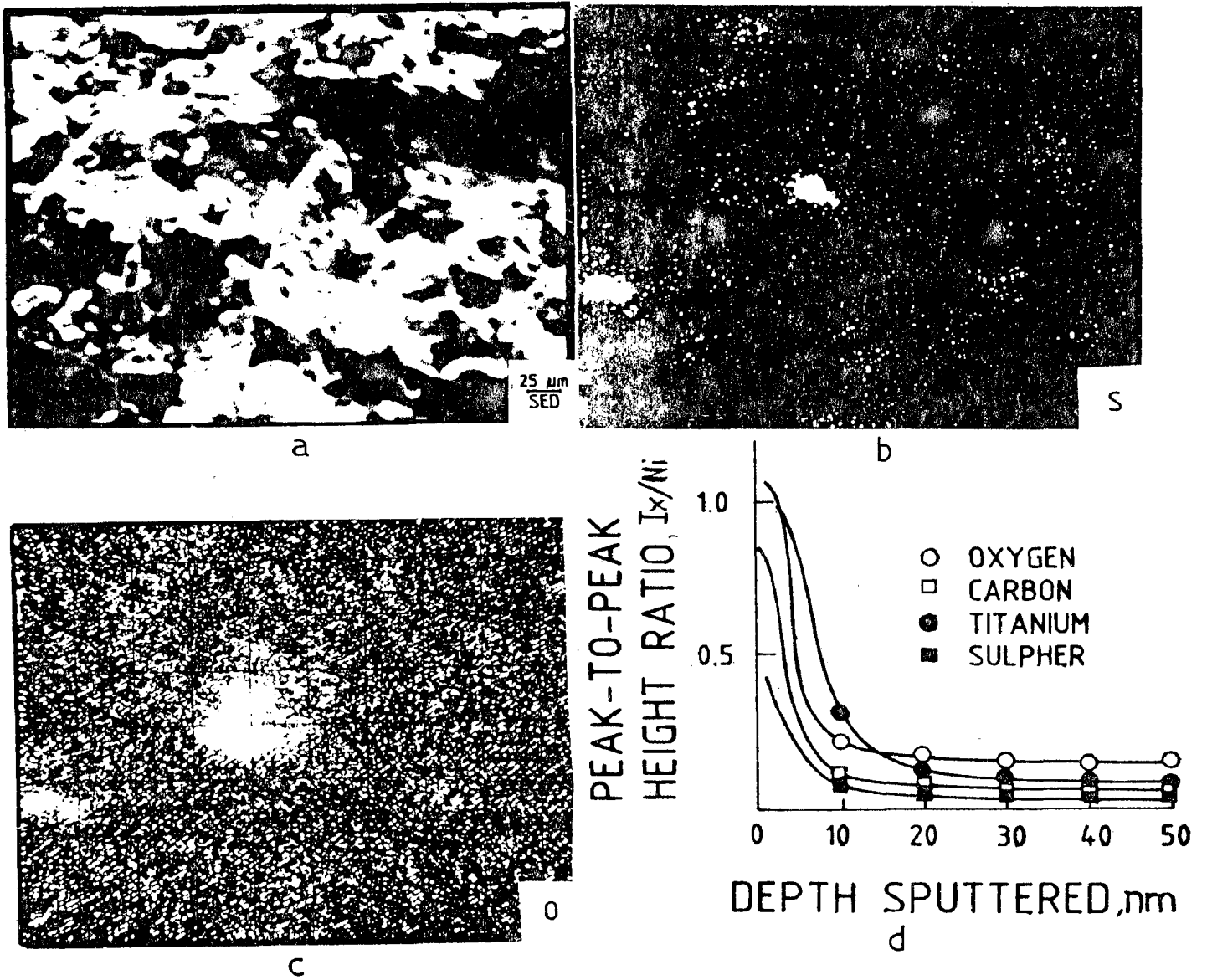
5.19   Auger analysis of AH2 specimen (low- β alloy) fractured in situ showing (a) Auger fractograph (b) Augergraph for sulphur (c) Auger-graph for oxygen and (d) sputtering profiles for carbon, sulphur, oxygen and titanium.
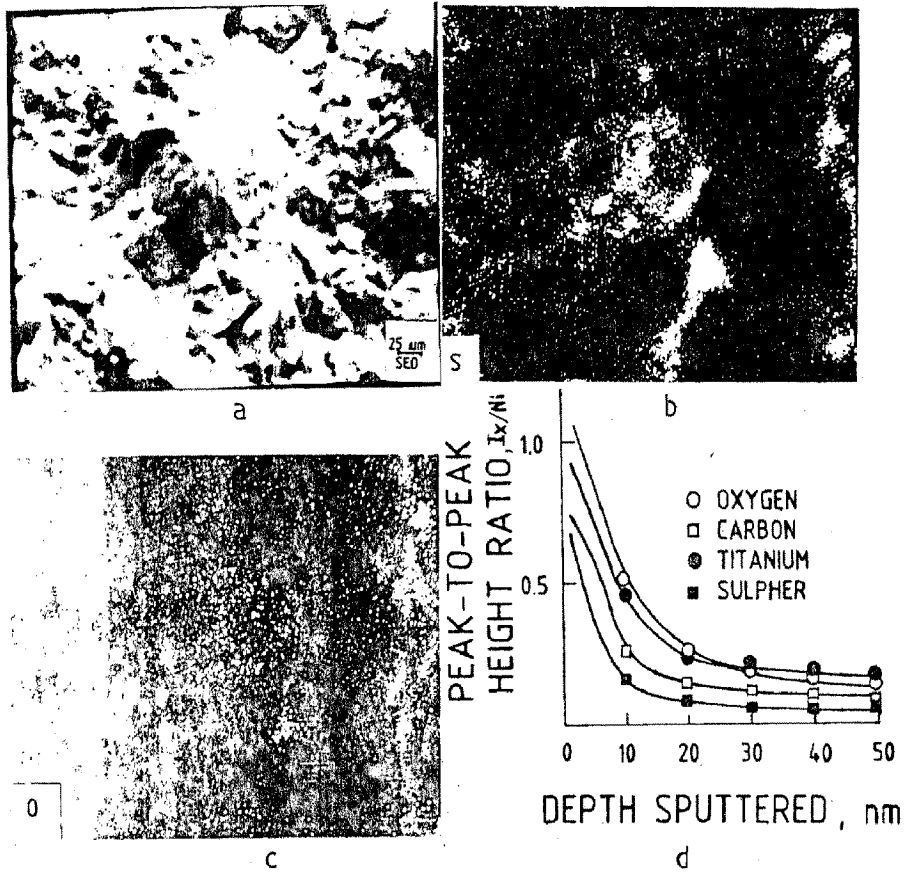
5.20 Auger analysis of BH2 specimen (high- B alloy) fractured in situ
showing (a) Auger fractograph (b)Augergraph for sulphur, (c) Auger-
graph for oxygen & (d) sputtering profiles for carbon, sulphur,
oxygen and titanium.
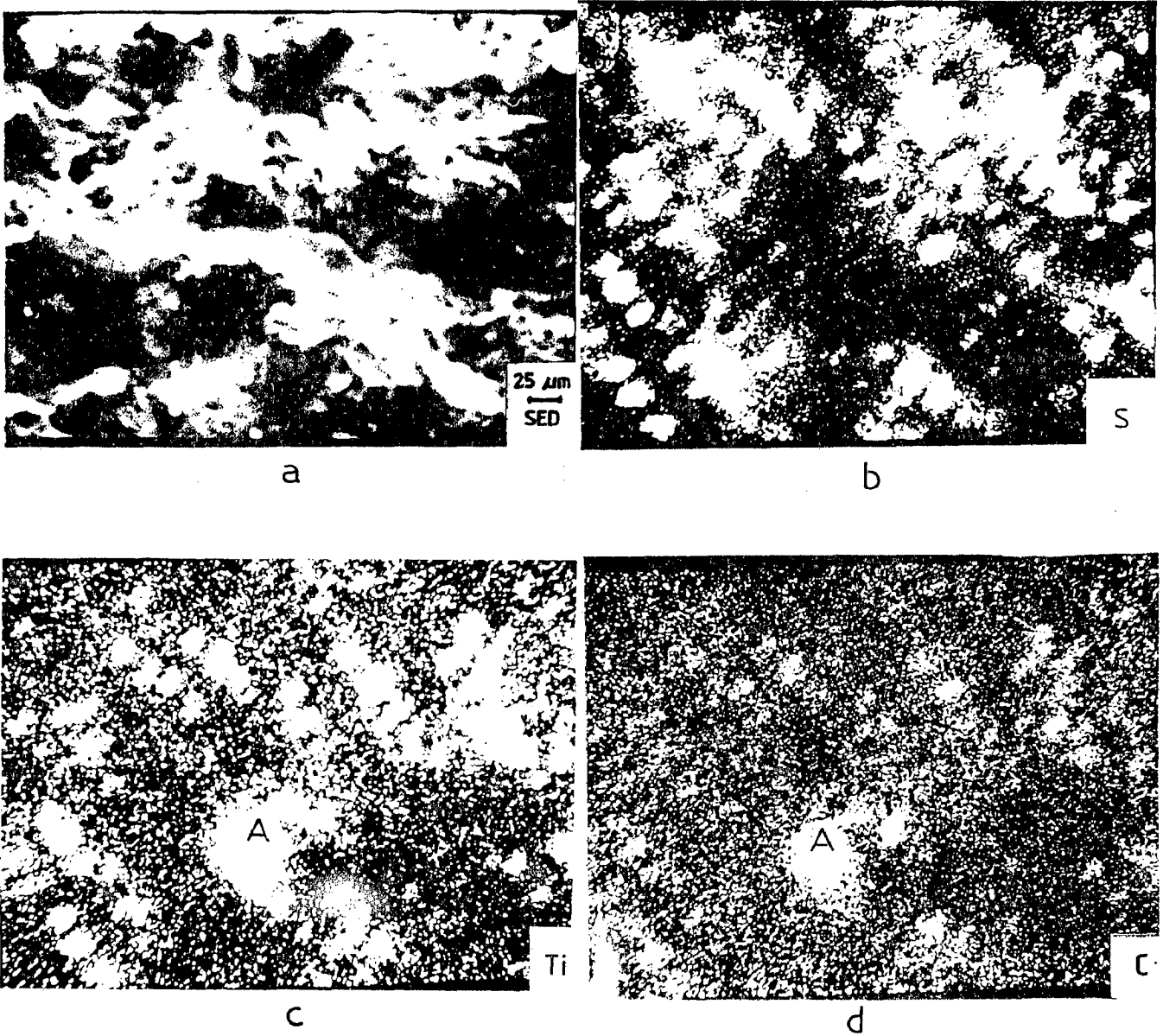
5.21 Auger analysis of CH2 specimen (sigma-prone alloy) fractured in situ showing (a) Auger fractograph and Augergraphs for (b)sulphur (c) titanium and (d) oxygen.
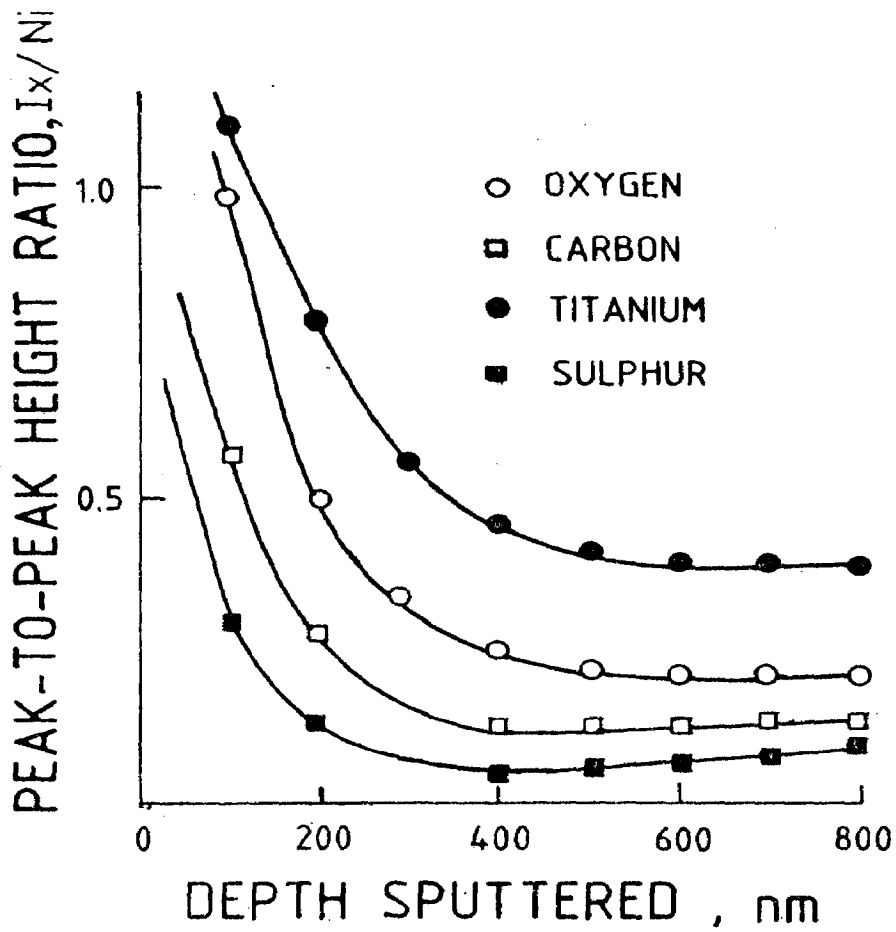
5.22 Auger electron peak-to-peak height ratio for carbon, oxygen, titanium and sulphur as a function of sputtered depth. Rise in S/Ni and C/Ni ratios indicates the presence of carbosulphides.

at the powder surface and is in compliance with the observations of Ross and Kear [89]. A similar behaviour has been noticed during the Auger analysis of loose powders (Section 4.3.4, Chapter 4).

The BH2 specimen (the high-B alloy), showed a slightly higher concentration of sulphur but a lower concentration of oxygen on the fractured surface as is evident from the Auger graphs of sulphur and oxygen (Fig. 5.20). This obviously is due to a low concentration of oxygen in the starting material itself. The sulphur-rich region was argon sputtered as before and Auger electron spectra were recorded both before and after regular intervals of 10nm etching. Peak-height ratios vs sputtered depth determined for some important elements are shown in Fig. 5.20d. Boron was not detected in the Auger graphs nor in the spectra probably because of its suppression by molybdenum peaks. This is also in agreement with the observations of Davidson and Aubin [86].

Fig. 5.21 shows the Augergraphs for carbon, titanium and sulphur in the CH2 material fractured in-situ. The area marked "A" in the Augergraphs for C and Ti is apparently a TiC type of precipitate without any sulphur content. However, a large area of fractured surface is also found to be rich in Ti, C and S. Oxygen is found to be uniformly but lightly distributed throughout the surface similar to that observed in Fig. 5.19c. As usual, Auger electron spectra were recorded

at regular intervals of 10nm after argon sputtering upto an etched depth of 80nm. Sputtering profiles for C H 3 are shown in Fig. 5.22. It is interesting to note that after initial reduction upto a depth of 40nm, sulphur and carbon showed a slightly upward trend with further etching. This is possibly an indication of the formation of M_2CS type of precipitates [116] and also illustrates the role of hafnium in suppressing the activity of sulphur and oxygen in the P/M superalloys.

5.6   IDENTIFICATION AND ANALYSIS OF PHASES

5.6.1 X-ray Diffraction of Electrolytically Extracted Phases

The lattice parameters of the electrolytic extracts of γ' phase as determined from the interplanar spacings ("d" spacings) listed in Table 5.5 are given below:

Alloy	Lattice Parameter
DMP-1	3.594
DMP-2	3.588
DMP-3	3.597

A strongly intense line having a "d" spacing of 2.28 to 2.29 A° was found in each alloy. Some other lines of weak intensities which do not conform to the γ' phase were also observed suggesting the extraction of some unknown phase along-with γ'. An attempt to precisely index this phase proved futile, although an extensive search of ASTM cards of various intermetallic compounds, oxides, borides or carbides etc. which are likely to form in nickel base superalloys was made.

Table 5.5 "d" spacings of γ' in P/M superalloys

Observed values of "d" spacings in A°			ASTM Card No. 9-97 for Ni$_3$Al		
DMP 1	DMP 2	DMP 3	d, A°	I/I_o	h, k, l
3.591 (W)	3.581 (W)	3.599 (W)	3.600	40	100
2.546 (W)	2.541 (W)	2.548 (W)	2.547	40	110
2.283 (S)	2.293 (S)	2.286 (S)	-	-	-
2.075 (VS)	2.072 (VS)	2.077 (VS)	2.074	100	111
1.986 (W)	1.996 (W)	1.9800 (W)	-	-	-
1.797 (VS)	1.789 (VS)	1.802 (VS)	1.799	70	200
-	1.762	-	-	-	-
-	1.686	-	-	-	-
1.610	-	1.619	1.603	40	210
-	-	-	1.524	-	-
1.428		-	1.461	20	211
-	1.358	-	1.265	60	220
			1.078	60	311
			1.032	40	222

(S), (VS) and (W) denote strong, very strong and weak intensities of lines observed in the Debye-Scherer films

Table 5.6 "d" spacings, A° obtained on electrolytic extracts of minor phases for the three alloys

DMP 1	DMP 2	DMP 3	MC	M_6C	T_3B_4	M_5B_3	CrB	HfO_2
3.139 W	3.139 W	3.147 S						111
-	2.889 VW	-						
2.834 W@	2.821 S	2.838 S		400		200	101	111
2.536 W*	2/553 S	2.555 W	111		031	200	103	200
2.486 VW	2/482 W	2.524 W				211		
2.280 VW	2.271 VW	2.301 VW		422	060	114		012
2.192 S*@	2.203 S	2.216 S	200	511	102			211
-	-	2.191 W						
2.137 W	2.127 W	2.126 W			121		105	
2.069 VW	2.071 S	2.070 W			150	213`		
-	2.048 VW	2.05 W						
2.009 W@	1.996 W	1.996 W		440			112	112
1.982 VW								211
1.907 W								202
	1.834 VW	1.837 VW						
	1.793 VW	1.799 VW						
1.694 VW@	1.689 VW	1.712 VW						
1.607 VW	1.609 VW							
1.551 W*@	1.560 W	1.564 S	220	551				
-	1.548							

Table 5.6 lists the "d" spacings of the electrolytic extracts of minor phases such as carbides and borides in the three alloys. The presence of MC type of cubic phase was detected and its lattice parameters are given below:

Alloy	Lattice Parameter	
DMP-1	4.384	for "d" spacings
DMP-2	4.406	of * marked lines
DMP-3	4.432	in Table 5.6.

The presence of a M_6C type of cubic phase having a lattice parameter between 11.20 and 11.40 was also confirmed from the "d" spacings marked @ in Table 5.6. Except for these phases, identification of other phases proved to be extremely difficult probably because the compositions of the phases in the present alloys are different from the existing systems. However, several of the "d" spacings measured for the minor phases were found to match with the "d" spacings of some secondary phases such as cubic NbC (ASTM Card No.9-368) or tetragonal CrB (Card No. 26-420) or tetragonal M_5B_3 (Card No.21-150) or orthorhombic Ti_3B_4 (Card No.19-1368) or orthorhombic M_3B_2 (Card No. 25-1082). Selected area electron diffraction patterns (SADPs) were also utilized to identify some of these phases.

5.6.2 Indexing of Electron Diffraction Patterns

Low-Boron Alloy :- Figs. 5.23, 5.24 and 5.25 show the TEM micrographs of some commonly observed precipitates having different morphologies in the AH1 material. The SADPs along-
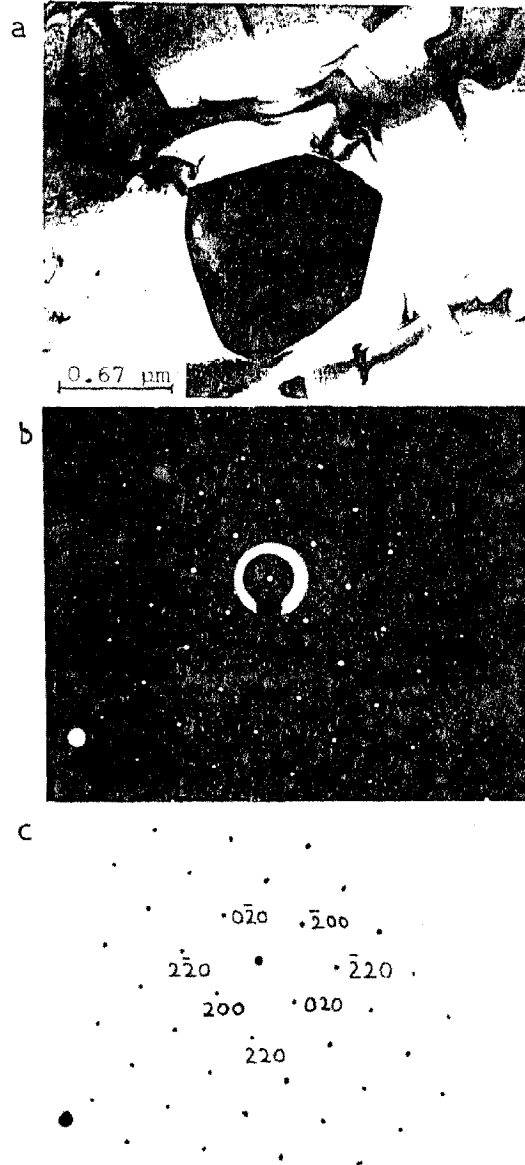
5.23   Transmission electron micrograph of DMP-1 (low- B alloy) showing
(a) blocky precipitate engloved by a coarse γ' particle (b) the
SADP of the precipitate and (c) the key to the SADP.

a

0.67 μm

b

c

. ĪI2

● OO2

● ĪĪ2

● ĪI0

● ●
ooo

● ĪI2   IĪo

● ●OOĪ
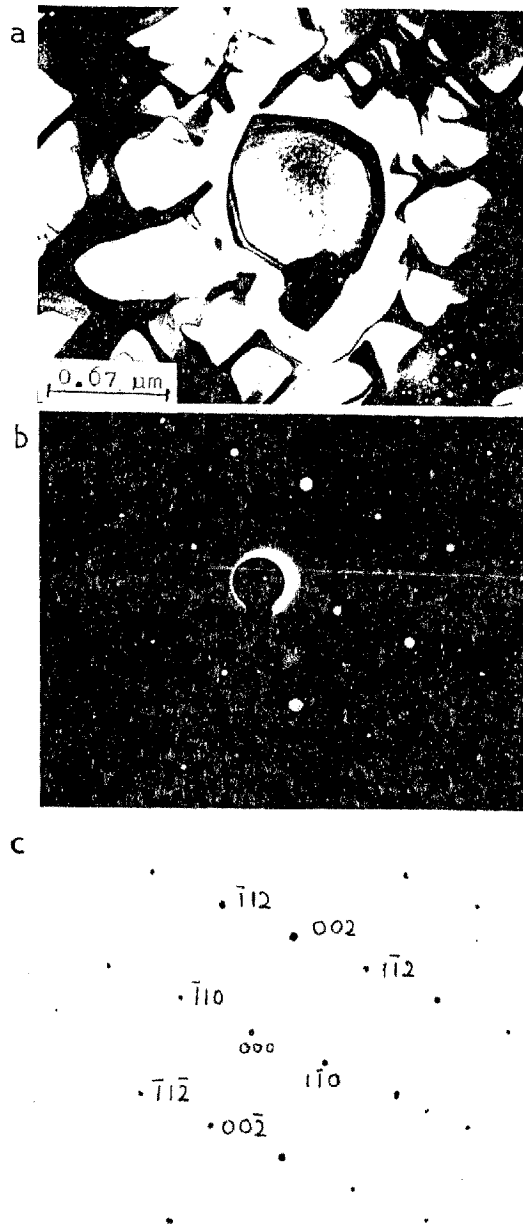
5.24   Transmission electron micrograph of the low- β alloy DMP-1
showing (a) the precipitation of a carbide/boride particle enveloped
by a coarse γ′ particle (b) the SADP and (c) the key to the
SADP.

5.25   Transmission electron micrograph of the low- B alloy DMP-1 showing a needle shaped precipitate and (b) the SADP.

with their keys are also presented. The SADP in Fig. 5.23 shows that the intragranular particle possessing an ogodoidal morphology and fcc structure is a carbide of M_6C type having a lattice parameter of approximately 11.7 A^o. The SADP of a cuboidal particle shown in Fig. 5.24, however, appeared to closely coincide with a pattern for bcc structure and lattice parameter was found to vary between 5.8 and 6.2 A^o depending upon the values of "d" spacings measured from this SADP. The SADP of a needle-shaped particle shown in Fig. 5.25 was also not found to coincide with any standard pattern and therefore could not be indexed. However, several of the "d" spacings measured from these SADPs comply with the X-ray diffraction results.

High-Boron Alloy :- Fig. 5.26 shows the TEM micrograph of a grain boundary precipitate and its SADP. As is evident from the key to the SADP, this particle has a fcc structure and a lattice parameter of about 11.48^o A. A small cuboidal particle engloved by a coarser γ' particle (Fig. 5.27) also showed a similar fcc structure with a lattice parameter of approximately 11.5 A^o. These particles are, therefore, M_6C carbides, where M is likely to have chromium, tungsten and molybdenum. The precipitates with octahedral cross section were found to be frequently dispersed in the alloy. A typical particle is shown in Fig. 5.28 along with its SADP. This pattern, however, could not be indexed. The precipitates with hexagonal cross section were also observed in the high-boron alloy (Fig. 5.29). These too have been found to have fcc structure and lattice parameter measuring approximately 11.5^o A. The presence of a fine rectangular particle can also be seen from the TEM micrograph in Fig.5.29 a. Such particles were seen widely dispersed but their SADP could not be properly recorded.

a

0.8 μm

b

c

$\bar{4}00$ $\bar{4}20$ $\bar{4}40$

$\bar{2}\bar{4}0$ $\bar{2}20$ $\bar{2}00$ $\bar{2}20$ $\bar{2}40$

$0\bar{4}0$ $0\bar{2}0$ 020 040

$2\bar{4}0$ $2\bar{2}0$ 220 240
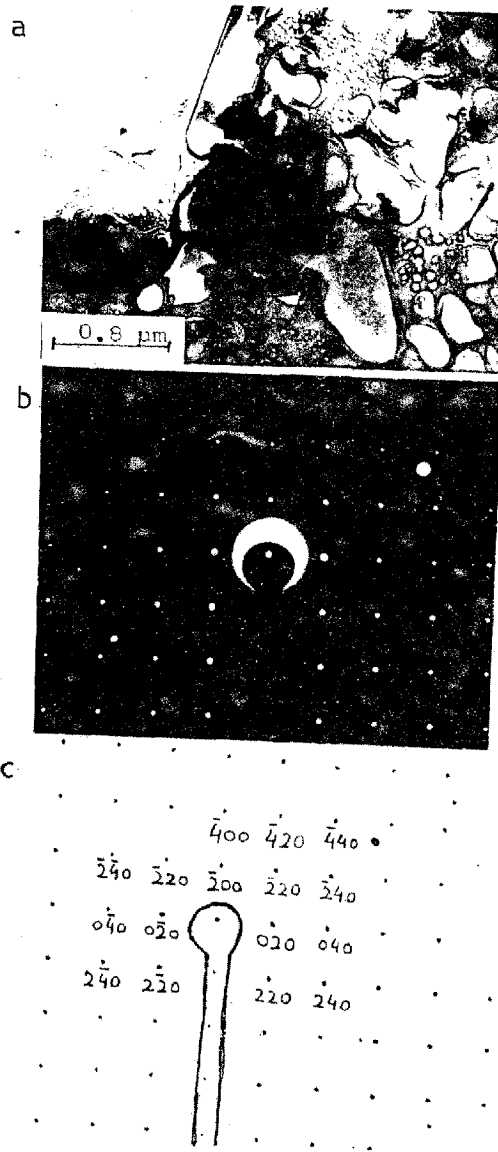
5.26 Transmission electron micrograph of the high- B alloy DMP-2 showing (a) grain boundary precipitates (b) the SADP and (c)the key to the SADP .
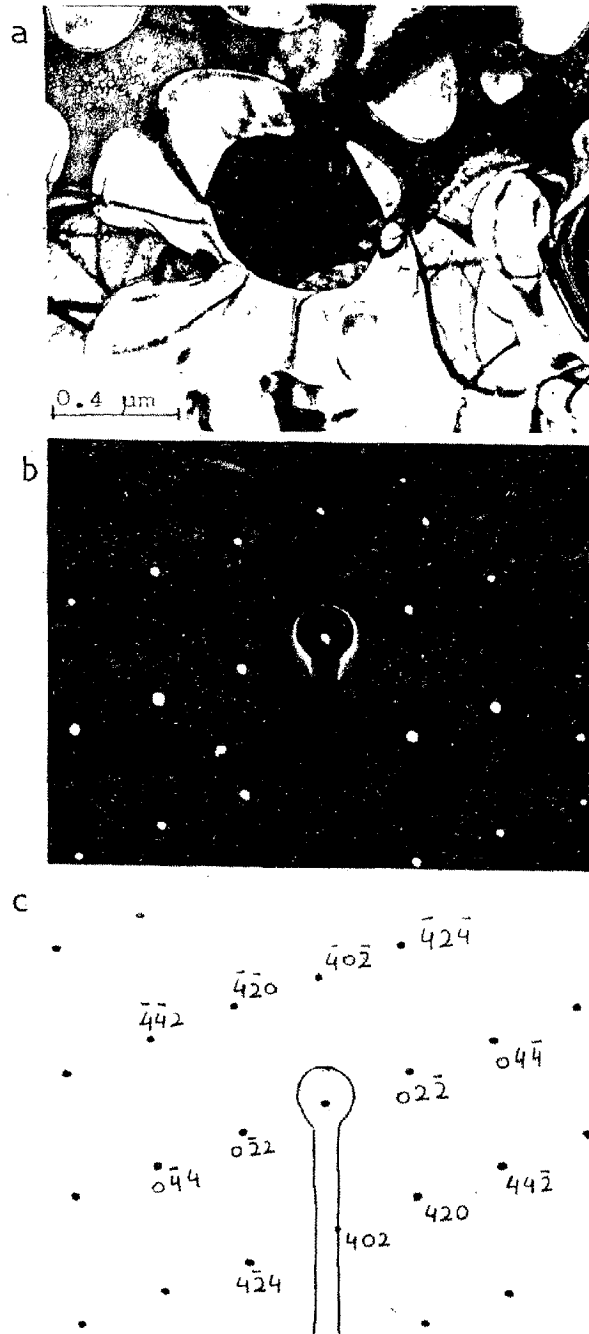
5.27   Transmission electron micrograph of the high- ß   alloy DMP-2
        showing (a) an octahedral   carbide/ boride precipitate eveloped
        by a large γ' particle (b) the SADP of the precipitate and (c)the
        key to the SADP.

a

0·4 µm

b

c

. $\bar{2}20$ • 311

•

• 131

$\overset{\bullet}{131}$

• 220   •

$\overset{\bullet}{311}$

•
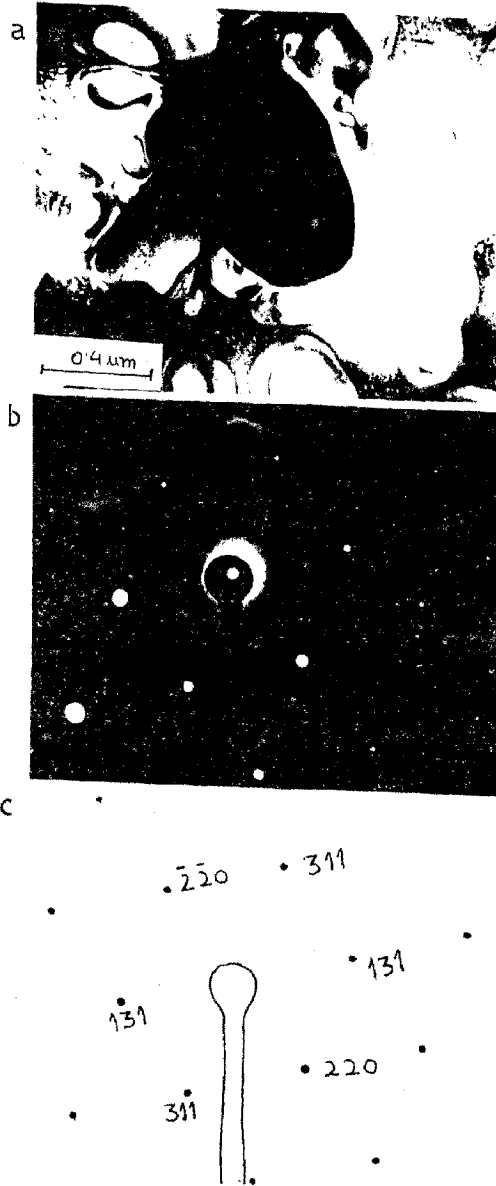
5.28   Transmission electron micrograph of the high- β alloy DMP-2 showing (a) a blocky precipitate on a coarse γ' particle (b) the SADP of the precipitate and (c) the key to the SADP.
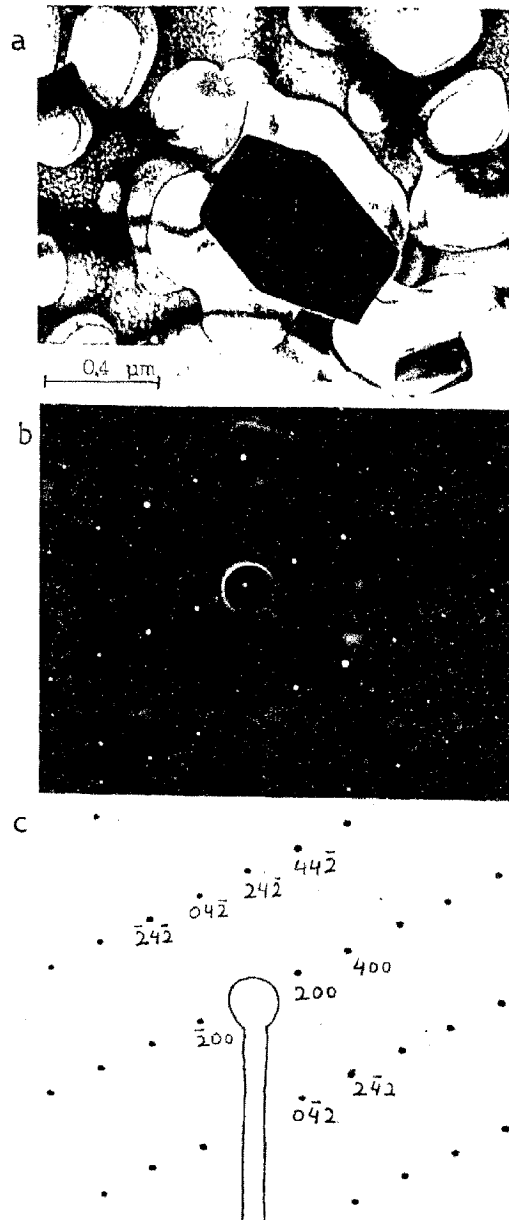
5.29   Transmission electron micrograph of the high- B alloy DMP-2
        showing (a) the presence of hexagonal and cuboidal precipitates
        (b) the SADP of the hexagonal particle   and (c) the key to the SADP.

Certain needle-shaped particles having an aspect ratio of 5 were also found to be randomly distributed but their electron diffraction pattern did not exactly match with the standard patterns.

Sigma Prone Alloy :- A cuboidal intragranular particle possessing fcc structure and having a lattice parameter of approximately 4.5 $\overset{o}{A}$ is shown in Fig. 5.30. This is believed to be a carbide of MC type, possibly NbC which has a lattice parameter of $\simeq 4.47$ (ASTM Card No.10-181). The TEM micrograph of a grain boundary precipitate alongwith its SADP and key to the diffraction pattern is shown in Fig. 5.31. The grain boundary precipitate appears to have fcc structure with a lattice parameter of approximately 8.2 A. However, the "d" spacings measured from this SADP were not in compliance with the X-ray diffraction results (Table 5.6)

Fig. 5.32 shows the dark field image of a needle-shaped particle having an aspect ratio of approximately 10. The occurrence of such particles of varying lengths was, however, occasional i.e. less than 1% by volume fraction. As seen from the SADP and key to the SADP, this particle possesses a fcc structure having a lattice parameter of approximately 11.5 A, and is believed to be a carbide of M_6C type. Such particles were found to be both within the grains and also at the grain boundaries.

5.6.3 **Chemical Analysis of γ'**

The chemical compositions of the electrolytic extracts of γ' phase in the three alloys are listed in Table 5.7. Presence of boron was not detected even in the phase extract of the high boron alloy. The presence of hafnium in γ' is
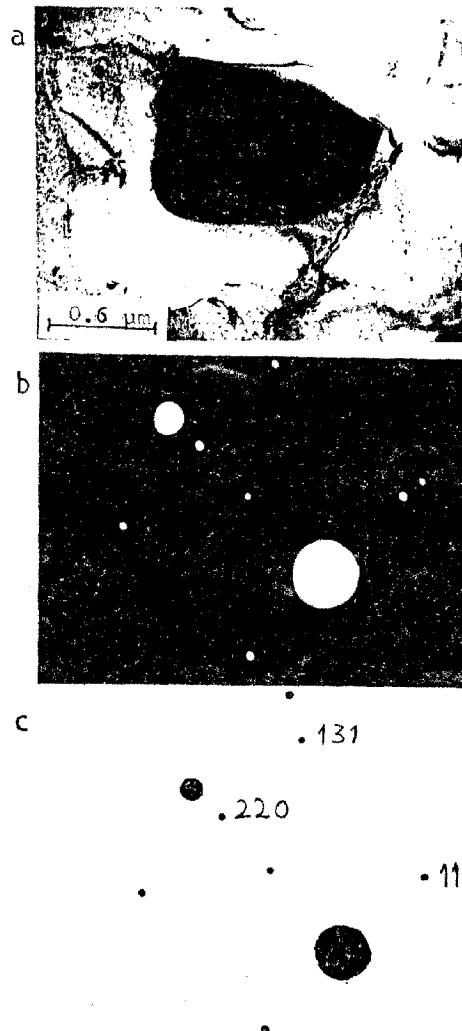
5.30 Transmission electron micrograph of the sigma-prone alloy DMP-3
showing (a) the precipitation of a blocky irregularly shaped intra-
granular precipitate (b) the SADP of the precipitate and (c) the
key to the SADP.
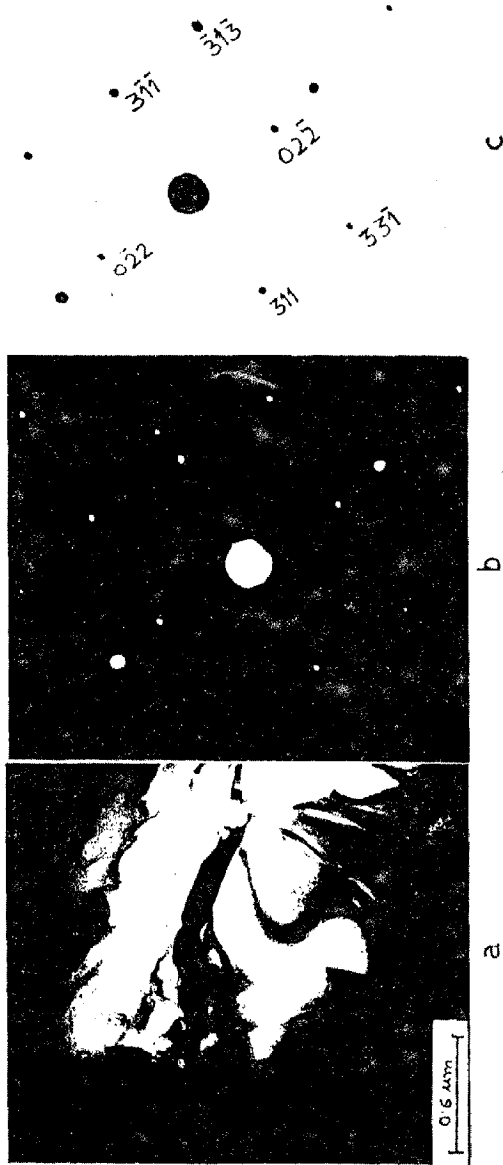
5.31 Transmission electron micrograph of the sigma-prone alloy DMP-3
      showing (a) intergranular plate-shaped precipitates (b) the SADP
      of one of the precipitate and (c) the key to the SADP.

a

0.6 μm

b

c · · · • • • • • • • • • • • • • · •

· · · · · · · • • • • · · · ·
2̄00   2̄00

· · · · • • • • • • • · · · ·

2̄8̄2̄ o8̄2̄ 2̄ 82
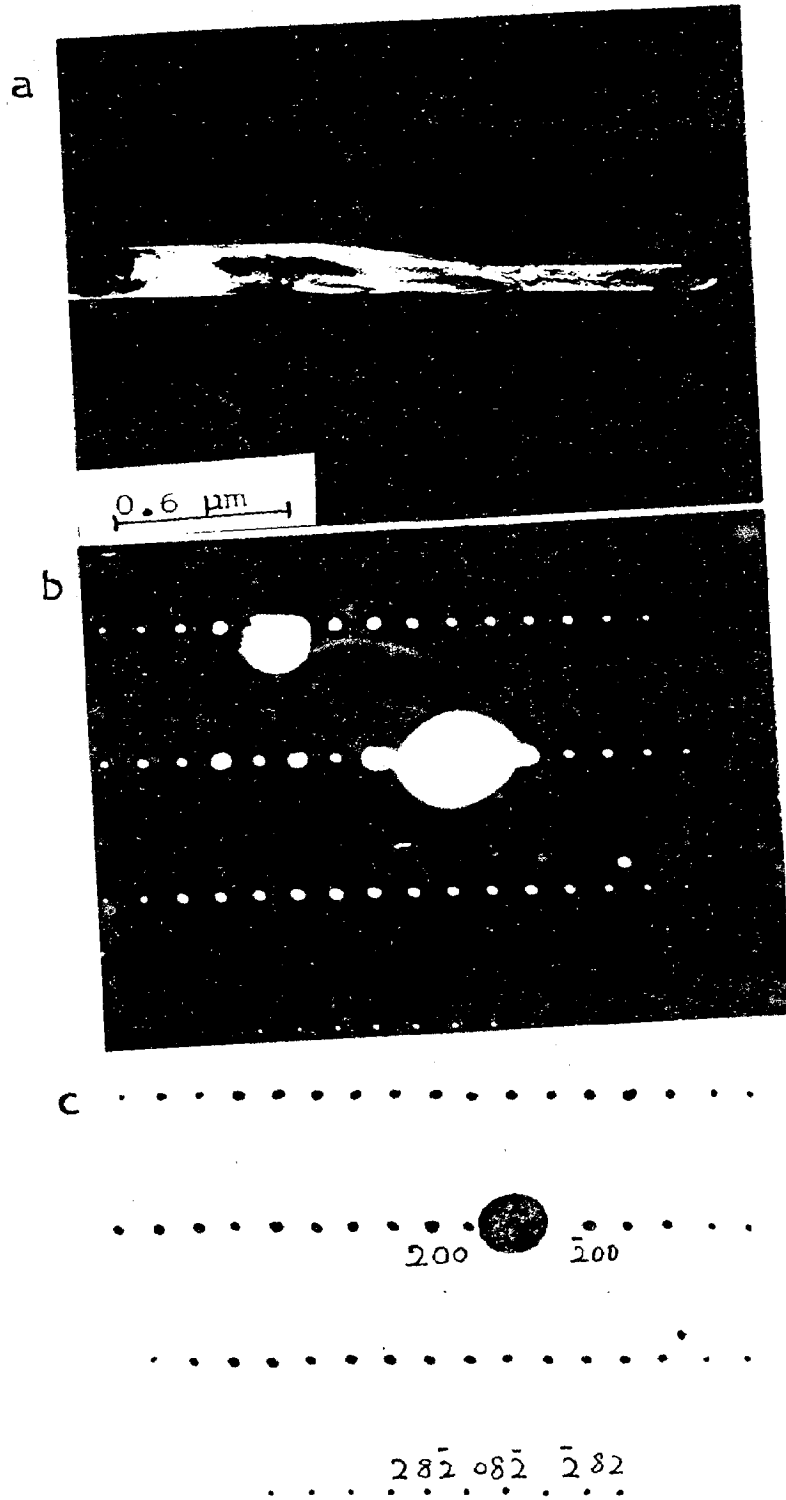
5.32   Transmission electron micrograph of the sigma-prone alloy DMP-3 showing (a) the dark field image of a needle-shaped intragranular particle (b) the SADP of the particle and (c) the key to the SADP.

Table 5.7 Chemical composition of γ' phase in P/M superalloys, atomic %

Alloy Code	Ni	Al	Ti	W	Cr	Mo	Nb	Hf
D M P - 1	*74.457	13.881	5.760	0.646	3.356	0.876	0.623	0.401
D M P - 2	*75.593	13.386	5.891	0.560	2.870	0.641	0.577	0.482
D M P - 3	*74.821	13.726	6.032	0.688	3.278	0.712	0.743	-

* By difference

in compliance with the earlier finding that hafnium has 7% solubility in γ' as compared to 1% solubility in γ [31,32]. Tungsten is also found to be present in γ', although its concentration is much less in comparison with Mo or Nb.

5.6.4 Electron Probe Microanalysis of Minor Phases

Both DMP-1 and DMP-2 consolidated at 1473 K were found to have occasionally dispersed hafnium-rich phase or inclusions as is evident from the X-ray images for DMP-1 in Fig. 5.33. Although the size of these agglomerates was very large, the frequency of their occurrence was very less i.e. not more than 1% of the total area scanned. This agglomerate also contained traces of oxygen but carbon and sulphur were not present. The occurrence of this phase was, however, not detected in the 1448 K consolidated alloys. This is indicative of the formation of a hafnium-rich phase which has an incipient melting temperature between 1448 K and 1473 K and is in agreement with the observations of Zheng and Cai [42] who have reported the occurrence of Ni_5Hf in Hf modified nickel base alloys.

Fig. 5.34 shows the microanalysis of a cuboidal particle in the AH2 material (low-boron alloy). Such particles were generally found to have precipitated intragranularly. The presence of Nb, Ti and C in these particles indicates that these are MC carbides. Hafnium was not detected in these carbide particles. In contrast, the BH2 material showed particles of varying shapes and sizes and were confirmed to be complex borides or borocarbides of W, Mo, Nb and Cr (Fig.5.35). An interesting observation was that these borides did not contain
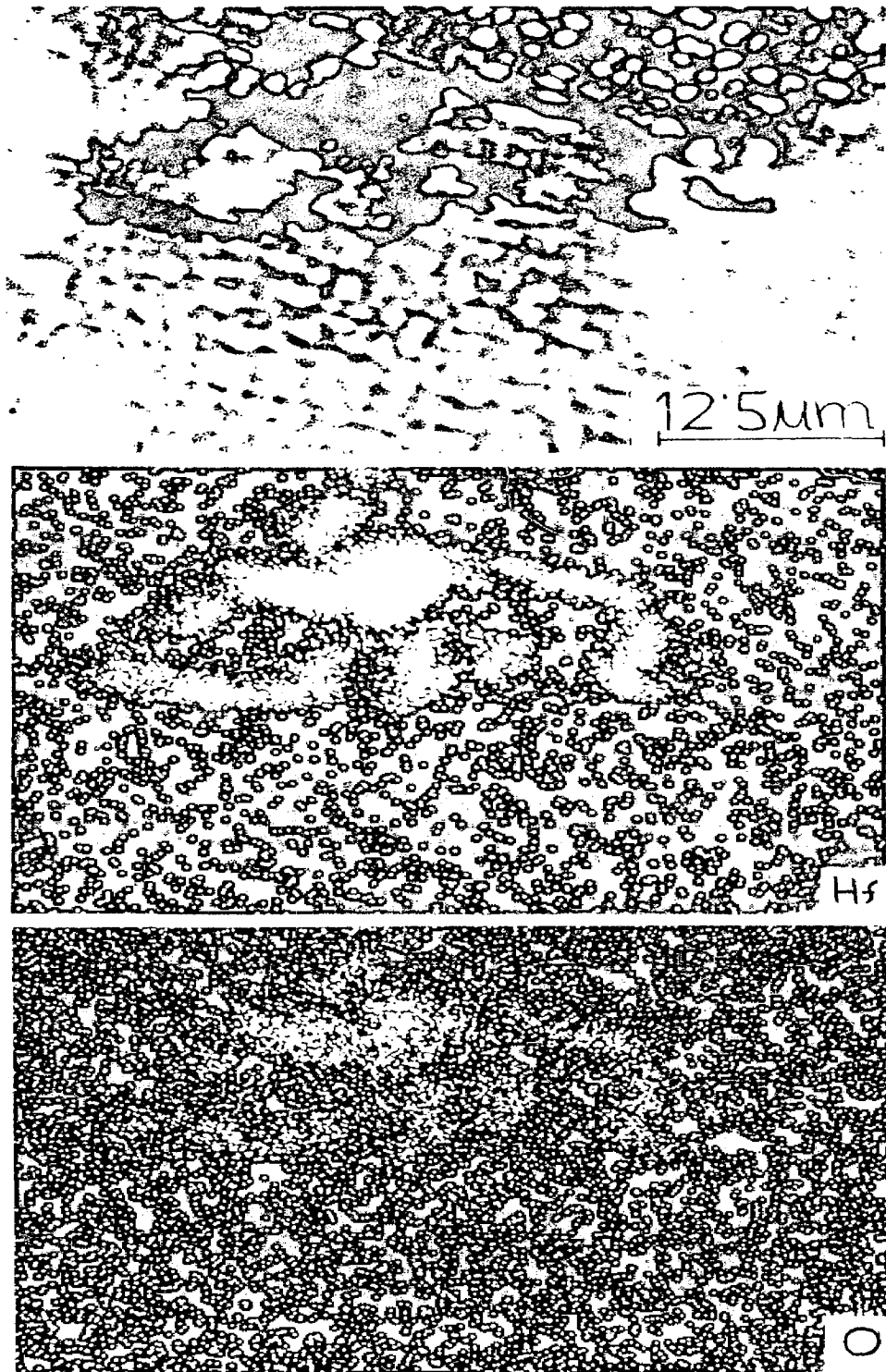
5.33 Electron probe microanalysis of the low- B alloy DMP-1 confirming the occurrence of a hafnium-rich segregation.
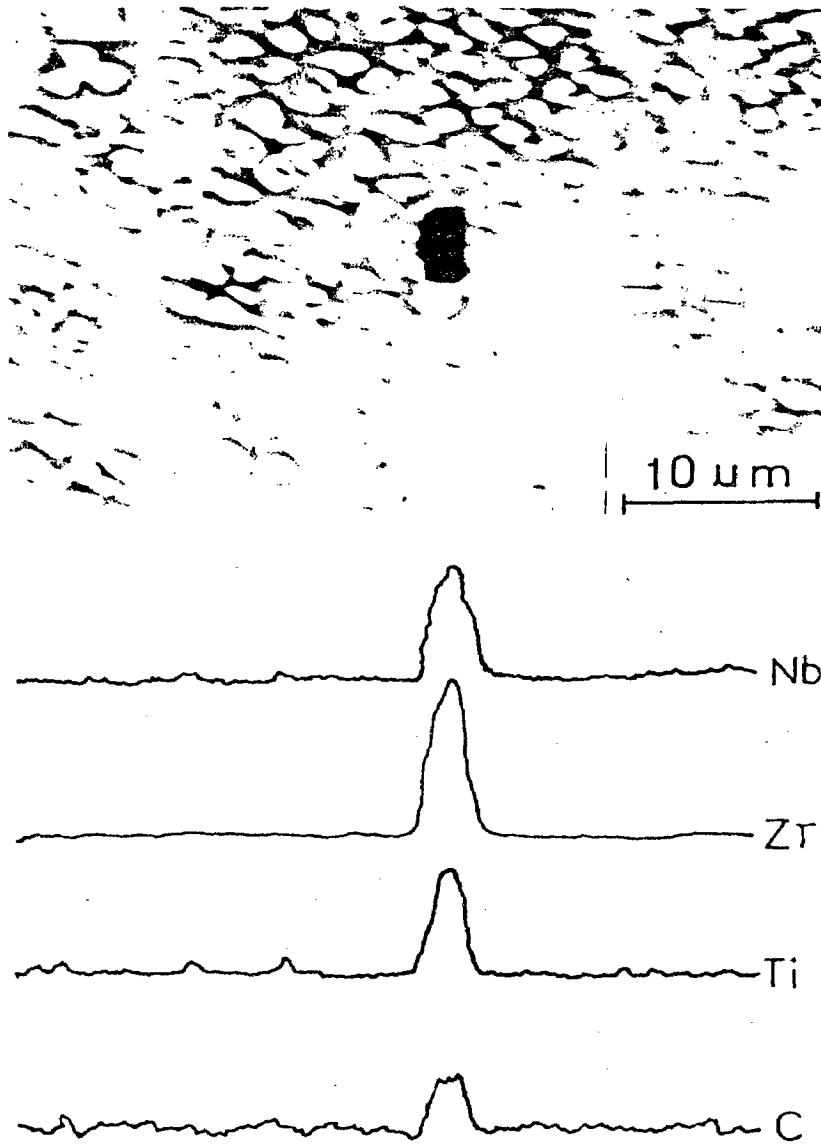
5.34   Electron probe microanalysis of 1498 K HIPed low- B alloy showing the occurrence of intragranular cuboidal precipitates of MC type.
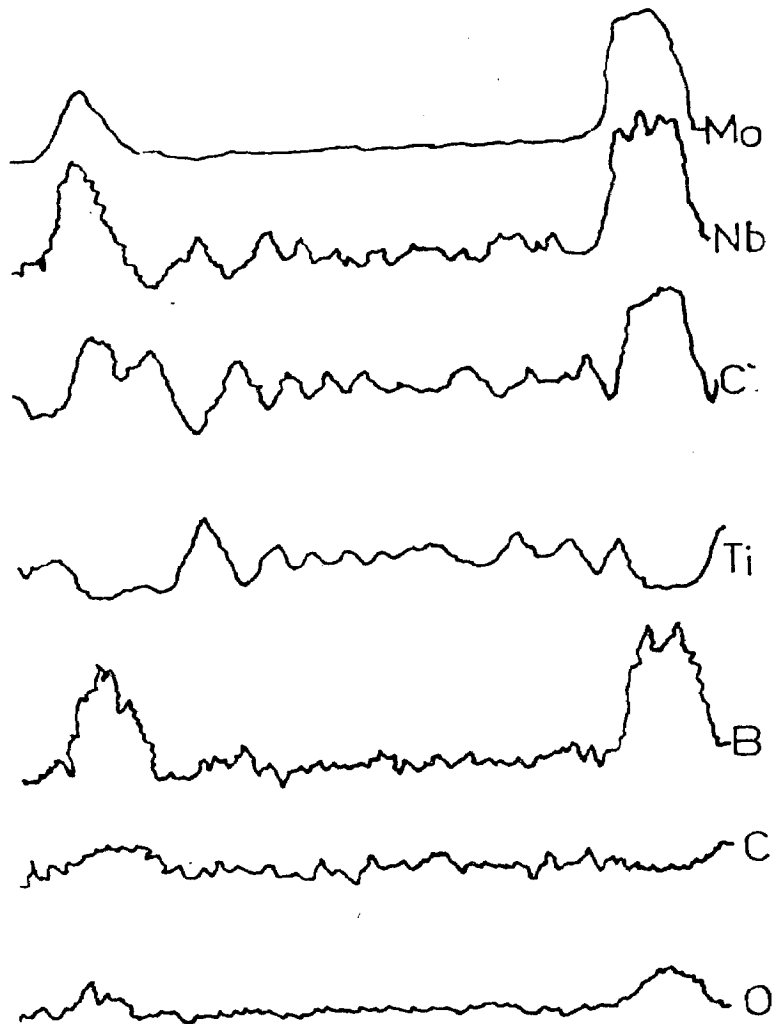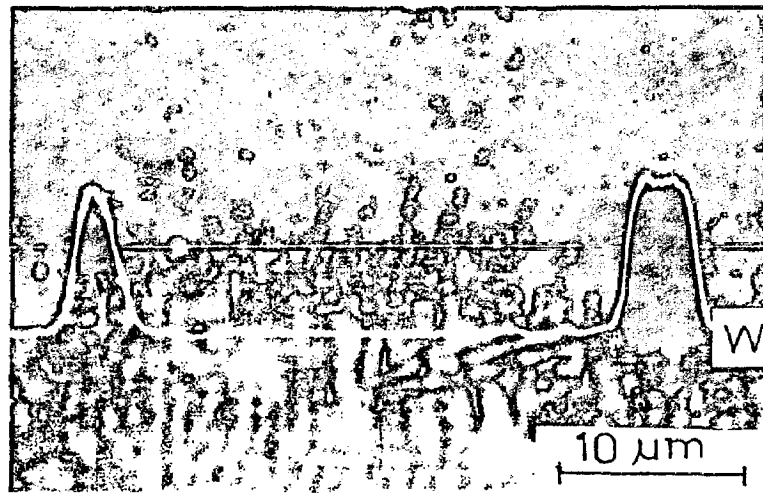
5.35 Electron probe microanalysis of cuboidal/spheroidal precipitates in the 1473 K HIPed high- B alloy.
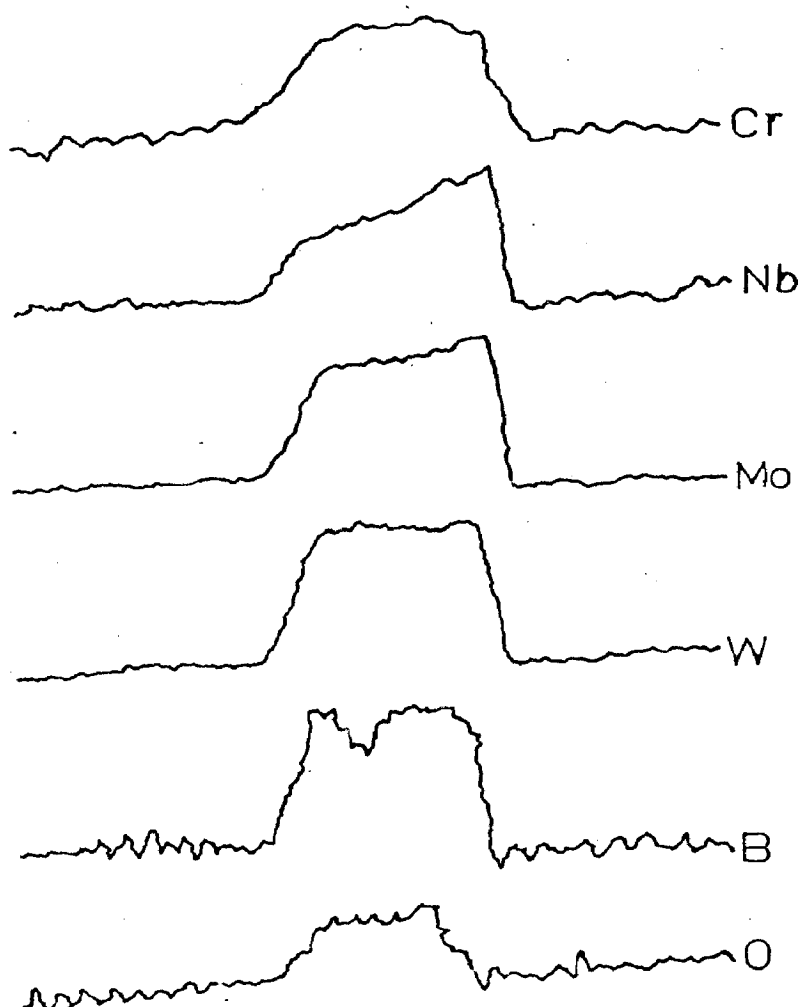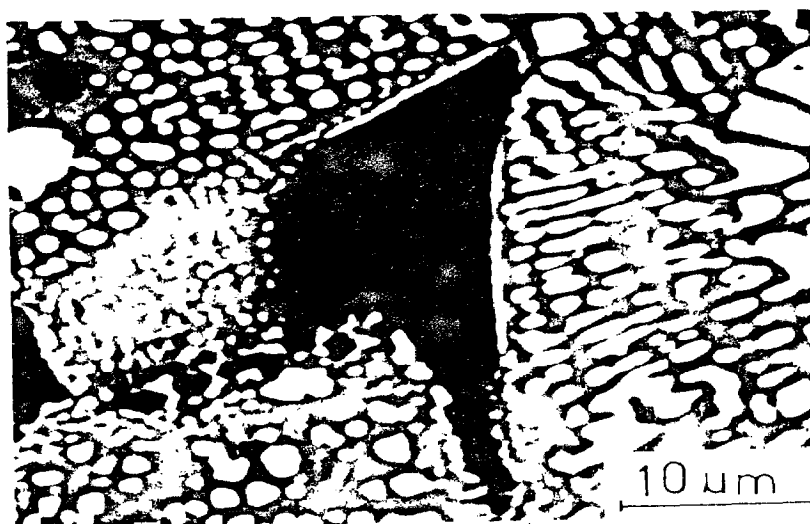
5.36   Electron probe microanalysis of an intergranular massive precipitate in the 1498 K HIPed high- B alloy.
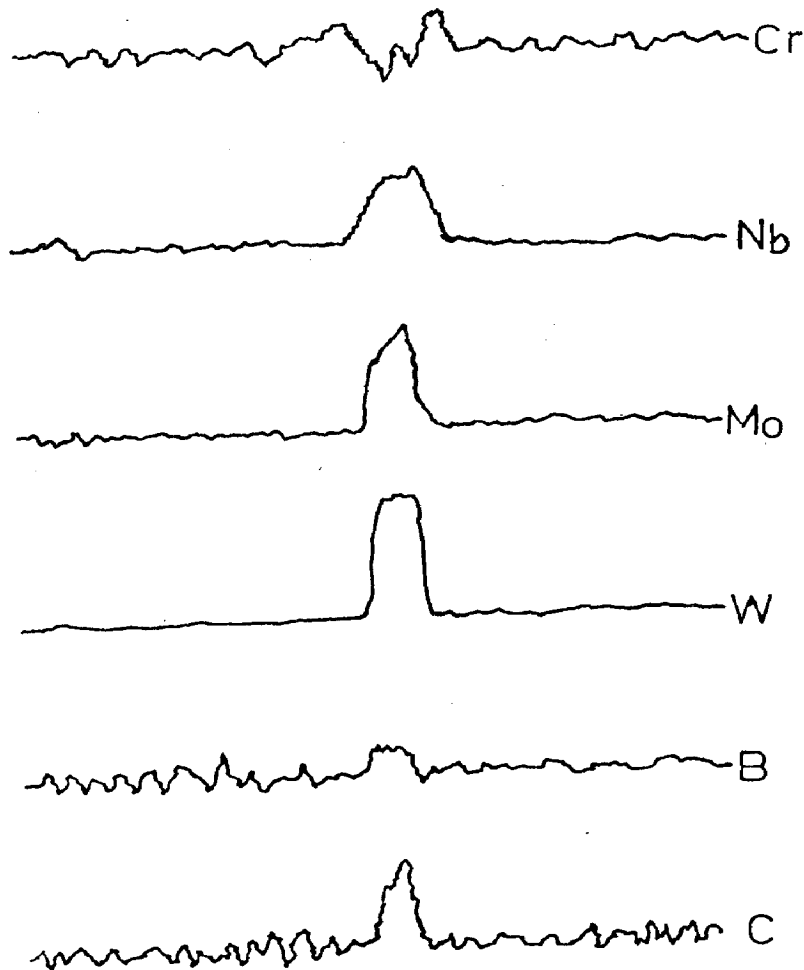
5.37   Electron probe microanalysis of an intergranular precipitate in
        the 1473 K HIPed sigma prone alloy.
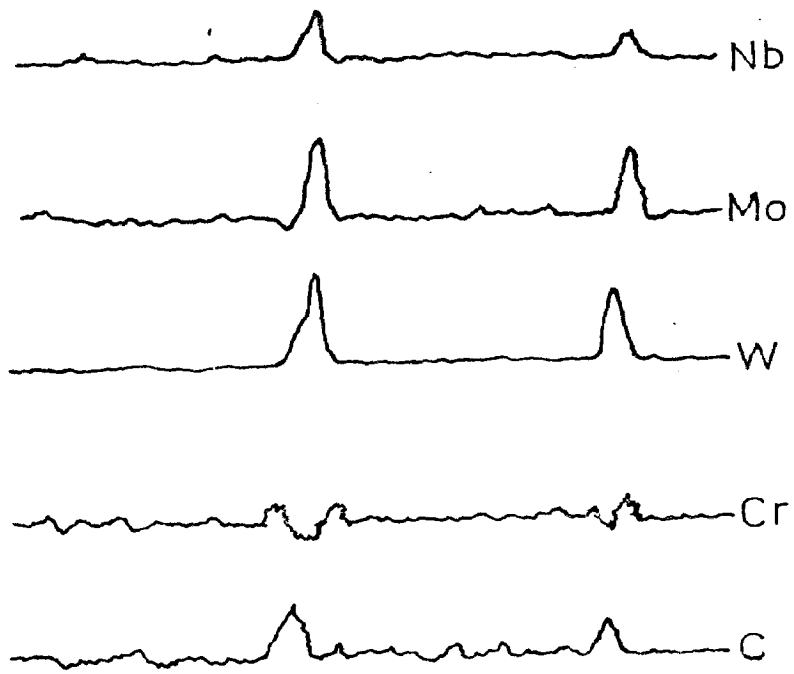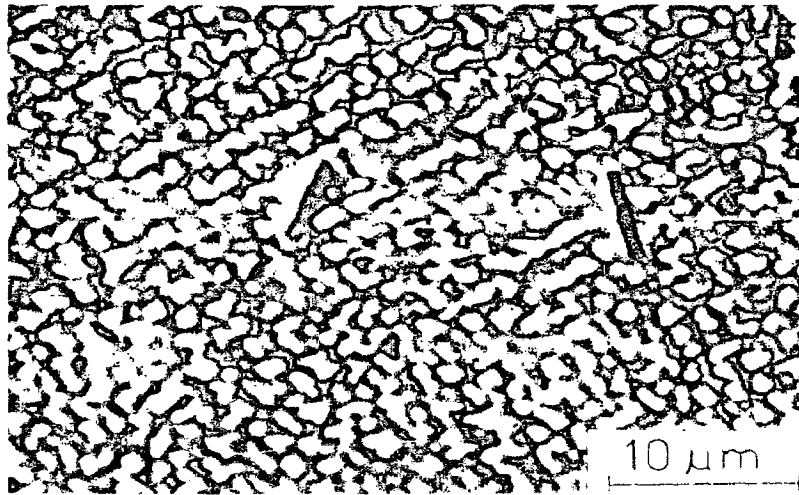
5.38   Electron probe microanalysis of intragranular plate-shaped precipitates in the 1473 K HIPed sigma prone alloy.

titanium but had traces of oxygen. The presence of hafnium was also not detected in these borides or borocarbides.

Fig. 5.36 illustrates the microanalysis of a large grain boundary boride precipitate in the BH3 material, (high-boron alloy consolidated at 1498 K). Titanium -- as well as carbon were again found to be absent in these particles. The presence of oxygen was, however, detected in these borides.

X-ray images alongwith the microanalyses of a grain boundary precipitate and intragranular needle-shaped precipitates in the CH2 material (sigma prone alloy consolidted at 1473K) are shown in Figs. 5.37 and 5.38. It is obvious from Fig.5.37 that the grain boundary precipitates are borocarbides and being absent in titanium can be considered to be of M_6CB type. Needle-shape precipitates in Fig. 5.38 are believed to be M_6C carbides.

5.7   EFFECT OF BORON ON γ'-MORPHOLOGY

The difference in the morphology of γ' particles in nickel base superalloys have been attributed to the differences in the lattice mismatch between the matrix and the hardening phase γ' [37-41]. The cuboidal morphology of γ' precipitates in DMP-1 (Fig. 5.1d) is indicative of a positive mismatch between γ and γ' which agrees with the observations of Rick et al [117], who have also shown that negative or near-zero lattice misfits between γ and γ' lead to the development of a dendritic morphology of γ'. Based on the observations on several alloy systems including nickel base superalloys, Doherty [118] has

also suggested that the solute precipitates are likely to acquire a dendritic morphology if they are widely spaced and if there is also a low lattice mismatch between the matrix and the precipitating phase. The lattice mismatch depends on the local compositional variations at the interface between γ and γ' particles. These compositional variations in turn produce substantial effect on the interfacial energy and consequently on the morphology of γ'. Obviously, boron has brought about local compositional variations at the interfaces between γ and γ' either due to its dispersion at the interface in the elemental form or due to its effect on the partioning of tungsten, molybdenum, niobium and chromium to γ or γ'. It is seen from the TEM micrographs of DMP-2 (Fig. 5.2d) that the γ' particles are basically spheroids which have coalesced to give the appearance of a dendritic morphology. Interparticle spacing between the coalesced γ' particles of DMP-2 (Fig. 5.2d) also appears to be more as compared to the spacing in DMP-1 (Fig. 5.1d). The dendritic morphology of γ' particles in DMP-2 is further confirmed by the examination of TEM micrograph of the 1498 K HIPed high-B alloy (Fig. 5.5d), which also shows a wider spacing between γ' dendrites as against the closely spaced cuboidal γ' particles in the 1498 K HIPed low-B alloy. The conjecture that the γ' particles in the high-B alloy are basically of a spheroidal morphology is supported by the TEM micrograph of the 1473 K HIPed DMP-2 (Fig.5.8d). The changes in γ' morphology with changes in the HIPing temperature clearly suggest that the consolidation temperature does exert some effect on the misfit parameter and this effect is more pronounced in the case of high-B alloy.

In the absence of accurate lattice parameter data of γ as well as γ', effect of boron on the partitioning of various elements cannot be ascertained. It can, however, be inferred that the formation of borides is likely to deplete the matrix of tungsten and molybdenum and γ' of niobium mainly. Thus lattice parameters of both γ and γ' are likely to be lowered. Amounts by which these decrease will be a measure of the mismatch. It is, however, evident that $\gamma - \gamma'$ mismatch is either negative or very low in the high boron alloy DMP-2.

5.8 EFFECT OF ALLOY CHEMISTRY ON CONSOLIDATION BEHAVIOUR

Reduced amounts of oxygen and carbon [87] and minor additions of hafnium [84] and niobium [12] are reported to be largely responsible in minimizing the formation of PPBs, which are considered to be mainly decorated by titanium oxy-carbides [86]. Absence of PPBs in DMP-1 is evidently due to a very low carbon concentration and additions of hafnium and niobium also appear to contribute to the suppression of the precipitation of oxycarbides of titanium at the PPBs. High proportions of refractory elements having low diffusivities such as W and Mo in the alloy chemistry are probably responsible for the residual dendritic structure although the consolidation has been performed at a reasonably high temperature of 1448K which is of course, marginally below the γ'-solvus. HIPing at a temperature very close to the γ'-solvus, i.e. at 1473K results in a homogeneous structure (except for the random distribution of eutectic $\gamma + \gamma'$ islands) as is shown in Fig. 5.7.

Further increase in the HIPing temperature to 1498 K, appears to result in incipient melting reflected by the increase in eutectic $\gamma + \gamma'$ structure (Fig. 5.4). These microstructural observations suggest that the solidus and boride solvus temperatures are fairly close to the HIPing temperature of 1498 K. Apparently, certain elements present in the alloy have lowered its solidus.

Like DMP-1, PPBs were not observed in DMP-2 thereby suggesting that unlike carbon, boron does not promote the formation of stable oxyborides at the PPBs. However, boron does narrow down the consolidation temperature range by decreasing the solidus. The effect of boron on the lowering of solidus is well known [15,16]. Formation of massive boride precipitates along the grain boundaries and precipitation of a large volume fraction of eutectic $\gamma + \gamma'$ structure are pointers towards the fact that addition of boron in P/M nickel base superalloys demands a precise control on the consolidation temperature particularly for the alloys which have high γ' solvus. For DMP-2, a consolidation temperature of 1473 K, which is very close to its γ' solvus has been found to be optimum.

Irrespective of the boron content, the formation of eutectic $\gamma + \gamma'$ structure in the 1473 K consolidated DMP-1 is a manifestation of the fact that the solidus for DMP-1 is very close to 1473 K. Such an unusually low solidus can be attributed to the additional effect of Hf in lowering the alloy solidus as has also been shown by Burton [15], Kotval et al [30] and Eng and Evans [103] in cast nickel base alloys. The formation

of a Ni_5Hf phase in nickel base superalloys having more than 0.4 wt% Hf has also been reported by Zheng and Cai [42], who have observed that Ni_5Hf phase is generally dispersed around eutectic $\gamma + \gamma'$ structure and its incipient melting temperature is around 1463 K. The present microstructural observations are in agreement with this finding.

The effect of hafnium on the solidus of the nickel base superalloys can further be explained by comparing the consolidation behaviour of the Hf-modified alloys DMP-1 and DMP-2 with that of the Hf-free alloy DMP-3. HIPing of DMP-3 at 1473 K does not produce any eutectic structure (Fig. 5.9). However, further increase in the HIPing temperature to 1498 K induces the precipitation of eutectic $\gamma + \gamma'$ structure, although its volume fraction is much less (Fig. 5.6). The formation of this eutectic structure is attributed to the lowering of alloy solidus by boron addition.

From chemistry and consolidation temperature range considerations, DMP-3 appears to be more attractive. Unlike DMP-1 and DMP-2, the Hf-free alloy DMP-3 has a higher consolidation temperature range and is not susceptible to the formation of inhomogeneous structures such as eutectic $\gamma + \gamma'$ islands and boride films.

5.9 ARE Hf AND B ESSENTIAL IN P/M SUPERALLOYS ?

The preceding discussion shows that although hafnium and boron appear to be effective in minimizing the tendency

for PPB precipitation in the P/M nickel base superalloys, they reduce solidus and produce undesirable phases which adversely affect the mechanical properties of the alloys. The absence of PPB precipitation in the Hf-modified low-B alloy DMP-1 is, however, believed to be mainly due to a very low carbon level. In contrast, hafnium has been found to suppress the formation of carbosulphides.

The alloy DMP-3 which has virtually no hafnium is also not prone to the precipitation of carbides at the PPBs although carbon content in this alloy is relatively higher than in DMP-1 or DMP-2. This is attributed to the presence of niobium. However, formation of carbosulphides has been observed in DMP-3 after consolidation. These carbosulphides are believed to adversely affect the elevated temperature properties. The low ductility observed in this alloy is possibly due to the presence of carbosulphides. Low fraction of eutectic $\gamma + \gamma'$ structure in DMP-3 is, however, an evidence of the fact that the solidus of Hf-free DMP-3 is higher than the Hf-modified alloys DMP-1 and DMP-2. It can, therefore, be inferred that moderate additions of hafnium, which do not appreciably lower the alloy solidus, can be made in P/M nickel base superalloys.

Boron has a definite influence on the formation of PPB networks although the high-B alloy DMP-2 is low in carbon. Apparently, an increase in the carbon level (equivalent to the boron level) would have certainly made the alloy susceptible to the precipitation of carbides at the PPBs. However, the addition of boron results in the formation of undesirable boride

films at the grain boundaries and eutectic $\gamma + \gamma'$ structure when the high-B alloy is HIPed at temperatures above the γ' solvus. Large size of blocky intergranular boride precipitates in the 1473 K HIPed alloy have been found to be the sites for stress concentration leading to a reduction in the elevated temperature strength and the ductility. It is, therefore, evident that unlike cast superalloys, boron additions in the P/M nickel base superalloys should be kept to low levels.

CHAPTER 6

HEAT TREATMENT OF HIP-CONSOLIDATED ALLOYS

6.1   INTRODUCTION

The availability of various precipitating phases in the nickel base alloys make them extremely versatile in respect of property capability. Earlier, all wrought superalloys were solution treated at temperatures above the γ' solvus to anneal the matrix and completely dissolve γ' but this also resulted in some grain growth. As the gas turbine engine technology advanced requiring superalloys with fine-grained structure for turbine disc applications, modified heat treatments involving lower solutioning temperatures were developed. As already discussed in Section 2.2.1 (Chapter 2), advanced wrought superalloys have very complex compositions whose properties are greatly influenced by microstructural changes. The present chapter records and discusses the effects of two heat treatments on the microstructure and properties of the three as-HIP alloys separately. For all the three alloys, the material consolidated at the optimum temperature of 1473 K has been investigated. Results of limited forging experiments done on the 1448 K HIPed DMP-3 have also been presented.

6.2   SELECTION OF HEAT TREATMENT

As already discussed in Section 2.2.2 (Chapter 2), in addition to the effects of compositional variations, a judicious selection of solutioning and aging temperatures is essential

to obtain a microstructure which would result in optimum proper-
ties. The main microstructural variables in nickel base super-
alloys are:

(i)   grain size,

(ii)   volume fraction and morphology of γ' precipitate and

(iii)   precipitation of carbides.

P/M superalloys are inherently fine-grained because the starting
powder material has an average particle size of 60 to 80 μm. Although,
the consolidation of the powder material above the γ' solvus tempera-
ture is likely to cause some grain growth, the carbides precipitated
at PPBs act as barriers to grain growth. Nevertheless, the grain
growth is not likely to exceed the particle size of the powder material.

In the present investigation, all the three alloys consolidated
at 1473 K were found to be virutally free from PPB-precipitation.
Some grain growth was observed in DMP-1 and DMP-2 suggesting
that the consolidation has been carried out at a temperature above
the γ' solvus. The absence of grain growth in DMP-3, as already
discussed in Section 5.2 (Chapter 5) is attributed to higher carbon
content in the alloy. As also confirmed by the solvus determina-
tion studies on the alloys (to be discussed later) the γ' solvus
for all the three alloys is 1473 ± 10 K. Therefore, the following
two heat treatments were selected.

T_1 :   1493 K/2h, rapid air cooling (RAC)
                +
            1323 K/8h, air cooling (AC)
                +
            1123 K/16h, AC

T_2 :   1353 K/8h, RAC
+
923 K/24h, AC
+
1033 K/16h, AC

The heat treatment T_1, mainly aimed at causing some grain growth is a slight modification of a heat treatment applied to EI-929, an advanced wrought Soviet superalloys [21, 23]. The solutioning temperature of 1493 K, being well above the γ' solvus for DMP-1, DMP-2 or DMP-3 is likely to completely dissolve the γ' precipitate. Rapid air cooling, i.e., cooling of the samples by air blower, was considered adequate to restrict the reprecipitation of γ' and keep the matrix in a semi-supersaturated state as the samples handled were small. Another reason for choosing rapid air cooling was the development of quench cracks in the samples when they were quenched in water during the γ' solvus determination study. The first aging treatment of 1323 K is believed to cause precipitation and growth of intergranular and intragranular γ' precipitates besides precipitating M_6C carbides at the grain boundaries, which essentially require high temperature exposure for their precipitation [26]. Pigrova and Levin [43] have also shown that as aging temperature increases from 1000 to 1300 K the reaction, $MC \rightarrow M_{23}C_6 \rightarrow M_6C$ is favoured. The final aging temperature of 1123 K is required to stabilize the microstructure and precipitate additional fine γ' between the γ' particles precipitated earlier. It is also likely to cause some coarsening of γ' besides promoting additional precipitation of the M_6C type of carbide.

The heat treatment T_2 is primarily aimed at developing a fine-grained bimodal microstructure, i.e., a structure consisting of coarse and fine intergranular and intragranular γ' precipitates. The partial solutioning treatment of 1353 K is expected to dissolve the finer fraction of the γ' particles and further coarsen the larger γ' particles (Ostwald ripening). In addition, this treatment helps stabilize the formation of the M_6C carbides [26,43]. The first aging temperature of 923 K is expected to nucleate fine γ' and the second aging treatment of 1033 K is likely to coarsen this newly precipitated γ' particles besides nucleation and growth of additional γ' particles.

6.3   LOW-BORON ALLOY, DMP-1

6.3.1 Microstructural Observations

Fig. 6.1 shows the result of γ' solvus determination study conducted on the AH3 material. Dissolution of γ' appears to be complete at 1473 K and, therefore, the γ' solvus of the low-B alloy DMP-1 is definitely below 1473 and above 1453K. This is obviously the reason for grain growth observed in the alloy after consolidation at 1473 K (Fig. 5.7, Chapter 5).

Fig. 6.2 shows the microstructures of AH2 material after the heat treatment T_1. In comparison with the as-HIP material which had a grain size of approximately 60 μm (Fig. 5.7,Chapter 5), the grain size of the heat treated material, i.e., AH2/T_1 is approximately 100 μm. Coarse γ' particles of irregular shape are seen at the grain boundaries, which otherwise appear
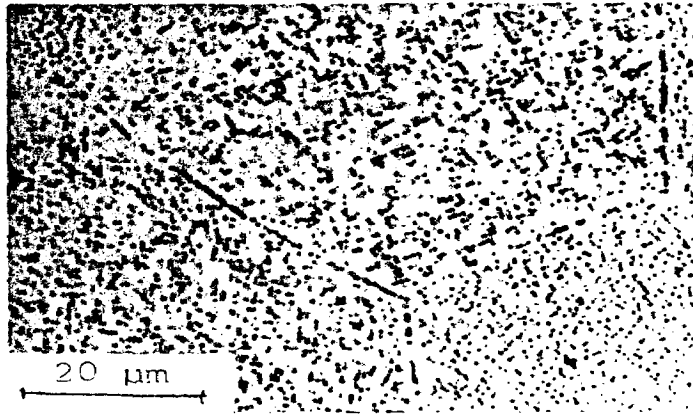
a
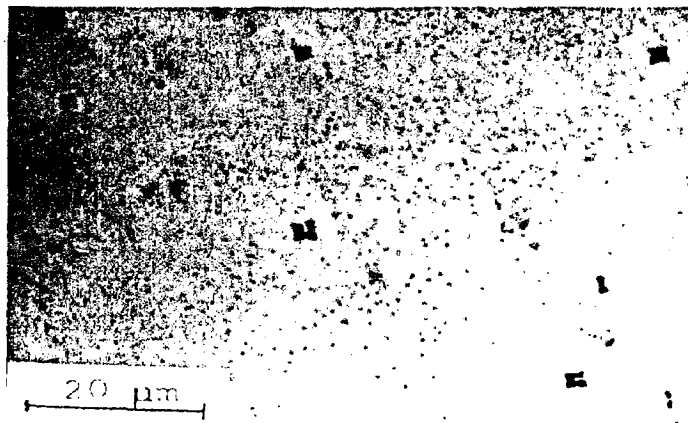
b
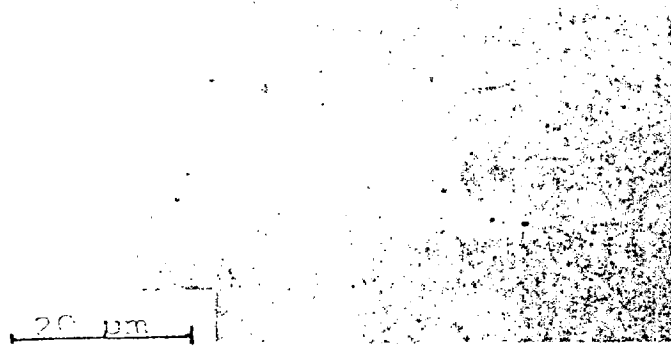
c

6.1   Determination of γ' solvus for the PM superalloy DMP-1 (a)1453K/
2 h, WQ (b) 1473 K/ 2 h, WQ and (c) 1493 K/ 2h, WQ.
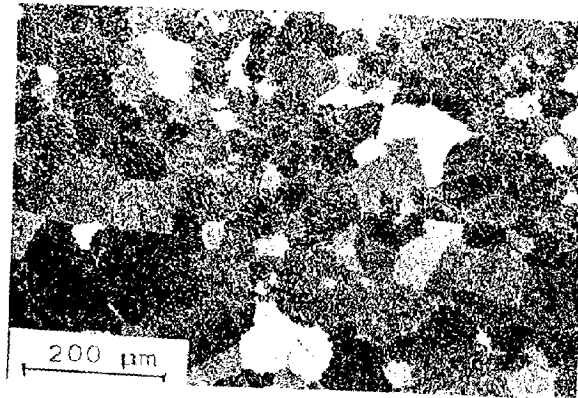
a
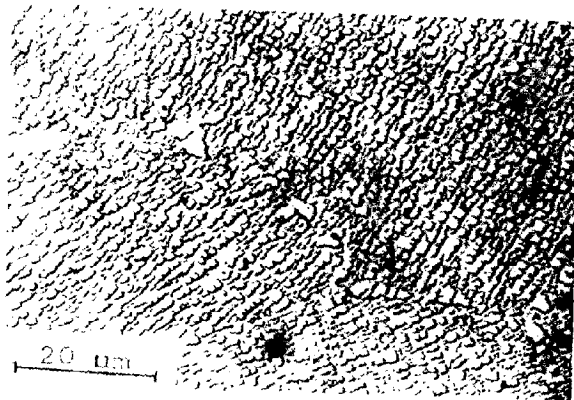
b

6.2   Microstructures of 1473 K HIPed DMP-1 after heat treatment
       T_1 showing (a) increase in grain size and (b) absence of carbides
       precipitation at the grain boundaries.
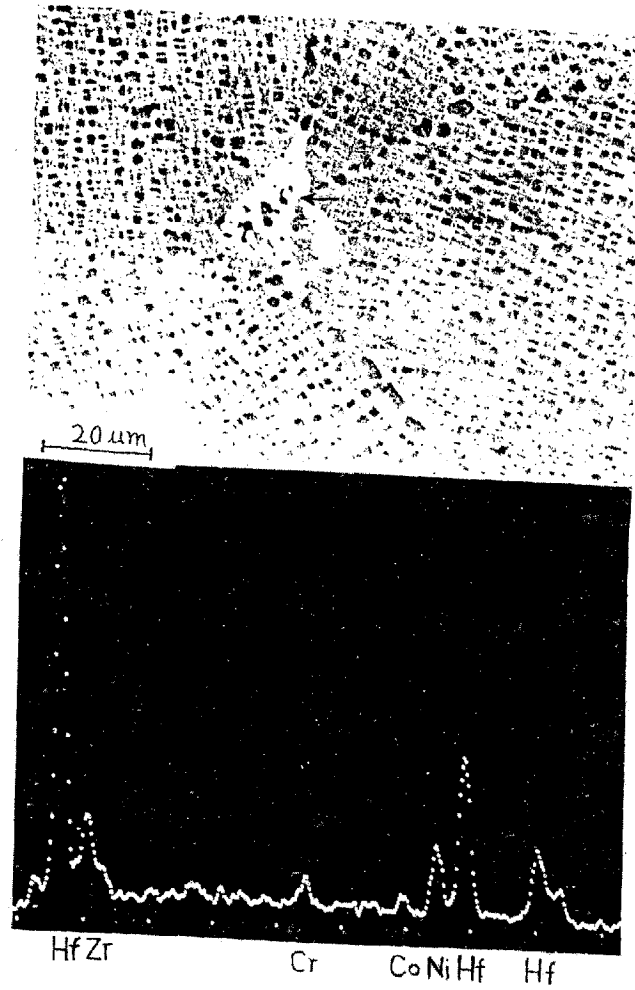
6.3   Microstructures of 1473 K HIPed DMP-1 after heat treatment
       T_1 demonstrating the evidence of a hafnium-rich phase at the
       triple point boundaries.
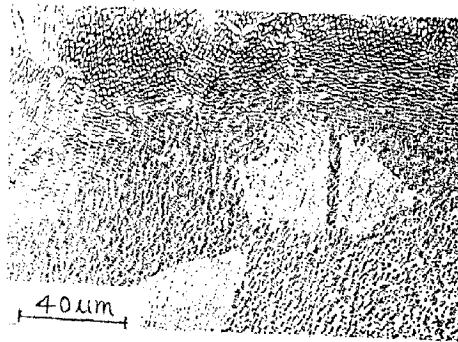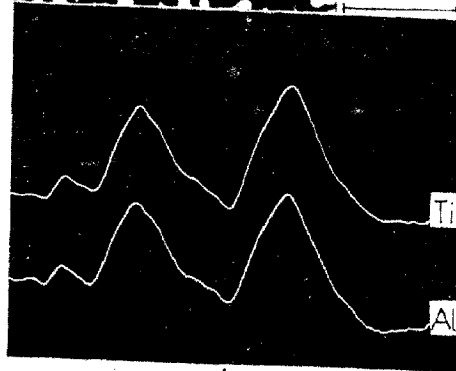
6.4   Microstructures of 1473 K HIPed DMP-1 after heat treatment T_2 showing (a) an optical micrograph (b) X-ray image of grain boundary precipitates alongwith the line scans for titanium and aluminium.

to be devoid of any carbide precipitation (Fig. 6.2b). Examination under SEM also did not show the precipitation of carbides (Fig. 6.3). This figure, however, shows a white coloured phase at the triple point boundaries. On microanalysis with EDAX attachment, this phase was found to be rich in hafnium. Similar kind of phase rich in hafnium and oxygen was also observed in the as-HIP alloy (Fig. 5.33, Chapter 5). However, in the present case, zirconium, nickel cobalt and chromium are also seen to be present (Fig. 6.3b). The mechanisms underlying the formation of this phase at the triple point boundaries is not clearly understood but based on the observations of Zheng and Cai [42] that formation of eutectic Ni_5Hf occurs in Hf-bearing nickel base alloys, a mechanism for the precipitation of this phase at the triple point boundaries has been proposed in Section 6.6.

Fig. 6.4 shows the microstructure of the AH2 material after the heat treatment T_2. Similar to what has been observed in the $AH2/T_1$ material, the grain boundaries in the $AH2/T_2$ material are also devoid of carbides precipitation which is confirmed by EPMA of coarse intergranular precipitates (Fig.6.4b) Being rich in Ti and Al, these precipitates are expected to be γ'. This material also showed randomly dispersed hafnium rich particles.

6.3.2 Mechanical Properties

The tensile properties of the $AH2/T_1$ and $AH2/T_2$ materials are compared in Table 6.1. Since the heat treatment T_2 restricts

Table 6.1

Tensile and Stress – Rupture Properties of 1473 K HIP DMP-1

After Heat Treatment T_1^*

Tensile Properties					Stress – Rupture Properties			
Test Temperature	0.2% YS	UTS	El**		Temperature/Stress		S-R Life	RA
(K)	MPa	MPa	%		(K)	MPa	(Hours)	%
298	890	1122	8		978 / 760		16	4
813	912	1105	7		1005 / 640		10	2
1033	1009	1075	4		1033 / 590		3	-

T_1^* 1493 K/2 h, Rapid Aircool (RAC) + 1323 K/8 h, AC + 1123 K/16 h, AC

**   For gauge length of 25.4 mm

Table 6.2

Tensile and Stress - Rupture Properties of 1473 K HIP DMP-1

After Heat Treatment, T_2^*

Tensile Properties				Strress - Rupture Properties		
Test Temperature (K)	0.2% YS MPa	UTS MPa	El** %	Temperature/Stress (K) / MPa	S-R Life (Hours)	RA %
298	970	1272	12	978 / 760	23	4
813	957	1234	10	1005 / 640	18	4
923	982	1218	7.5			
1033	923	1032	5	1033 / 590	8	2

T_2^* 1353 K/8 h, RAC + 923 K/24 h, AC + 1033 K/16 h, AC

**   For gauge length of 25.4 mm
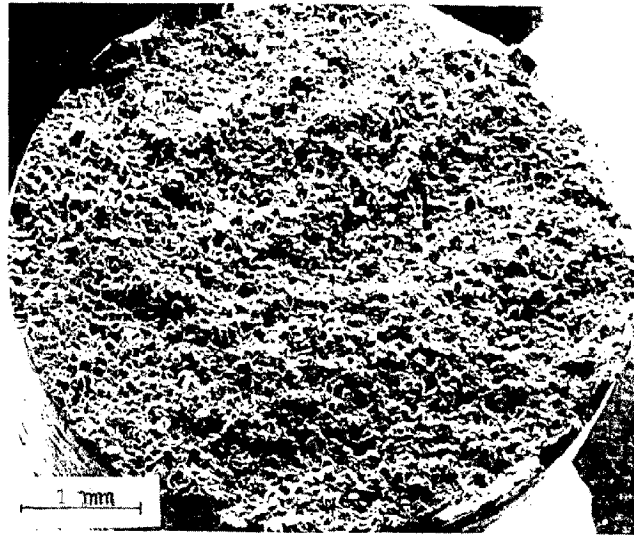
a
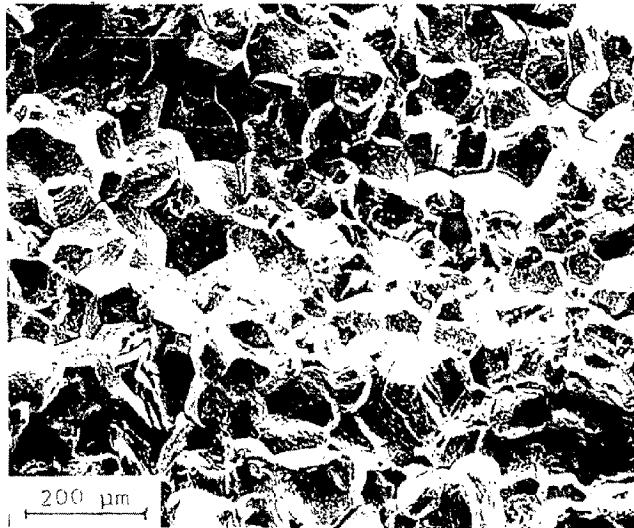
b

6.5 SEM fractograph of AH2/ T_2 specimen (1473 K HIPed and heat treated DMP-1) after stress rupture testing at 1033K/760 MPa showing (a) macroview (b) magnified view illustrating intergranular type of fracture.

grain growth, the tensile properties of the AH2/T_2 material at RT, 813K, and 923K are better than those of the AH2/T_1 material, which had higher grain size. However, at 1033K, where grain boundary sliding is likely to be more prominent, the YS and the UTS of the AH2/T_1 material are higher than those of the AH2/T_2 material.

Table 6.2 lists the stress-rupture properties of the AH2 material after the heat treatments T_1 and T_2. In general, these properties do not show any distinct improvement due to change in the heat treatment. Apparently, the alloy is inherently poor in its grain boundary strength on account of a low carbon content. This was also confirmed during the fractographic examination of the tensile and the stress-rupture specimens. Fig. 6.5 shows the SEM fractographs of the AH2/T_2 specimen stress-rupture tested at 1033 K/760 MPa illustrating an intergranular fracture without any noticeable evidence of ductility.

6.4 HIGH-BORON ALLOY, DMP-2

6.4.1 Microstructural Observations

The microstructures of the BH3 specimens solution treated at 1453, 1473 and 1493 K followed by water quenching are shown in Fig. 6.6. At 1473 K, solutioning of γ' is observed to be virtually complete except for the occasional presence of coarse eutectic γ' particles. Since the starting microstructure of the BH3 specimen had a fairly large volume fraction of
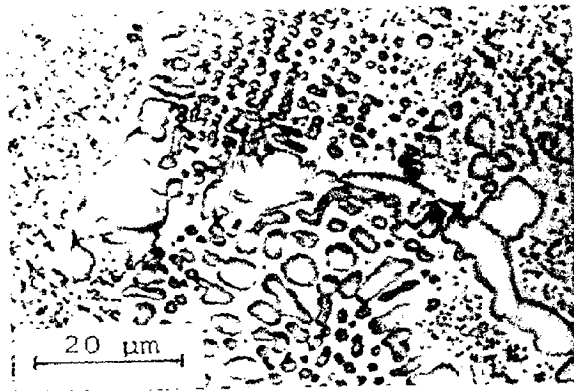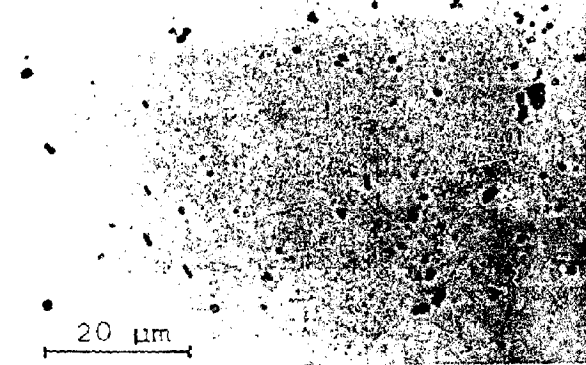
6.6 γ' solvus study on PM alloy DMP-2 (a) 1453 K/ 2h, WQ (b)1473K/ 2h, WQ and (c) 1493 K/ 2h, WQ.

coarse eutectic γ' particles, its complete dissolution may require somewhat higher temperature. On the other hand, a structure having reduced amount of eutectic γ' particles will exhibit solutioning of γ' at slightly lower temperature. Therefore, the γ' solvus of the alloy DMP-2 can be considered to be approximately 1473 K.

The heat treatment of BH2 at high temperatures followed by rapid air cooling resulted in an abnormal grain growth and formation of film-like precipitates at the grain boundaries. The microstructure of such a specimen after the two-step aging is shown in Fig. 6.7. The analysis of this grain boundary phase with the EDAX attachment to SEM showed these grain boundary precipitates to be high in tungsten, molybdenum and chromium. These are believed to be either borides or borocarbides. The grains have almost acquired the configuration of prior particles giving the appearance of PPBS. This behaviour closely resembles the effect of supersolidus sintering of Astroloy powder observed by Jeandin et al [121], who proposed that quenched molybdenum- and chromium-rich carbides form fine networks in zones of high carbon liquid prior to quenching. In the present case, as the alloy contains high boron, these acicular or spheroidal white particles marked "A" in Fig. 6.7a) are considered to be the borides or the borocarbides of tungsten molybdenum and chromium.

Fig. 6.8 shows the microstructure of the BH2 material after the heat treatment T_2. The cuboidal or blocky particles
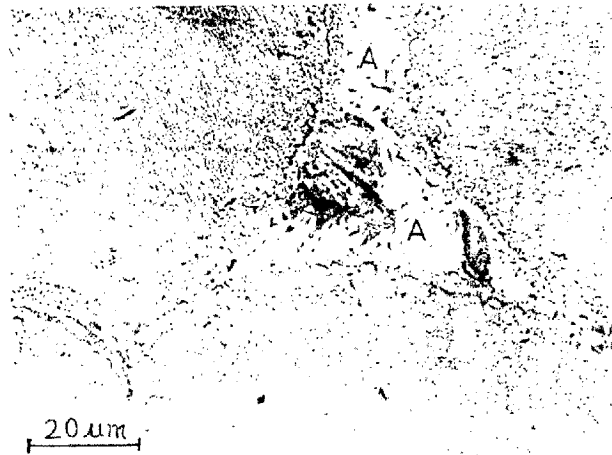
a
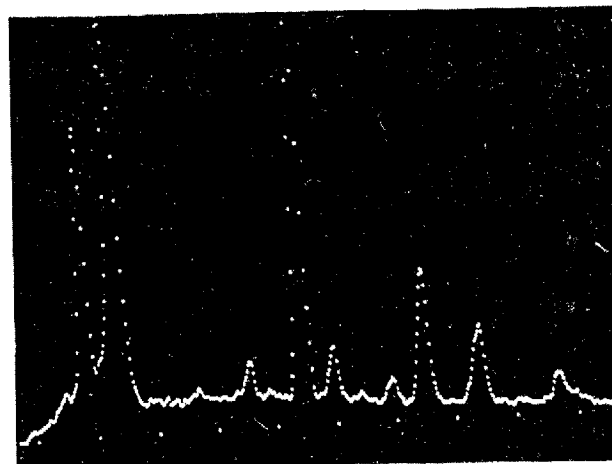
W Mo   Ti Cr   Ni Ni   W

b

6.7   Microstructures of 1473 K HIPed DMP-2 after heat treatment T_1 showing (a) incipient melting at the triple point boundaries (b) microanalysis of precipitates marked as 'A' in Fig.(a).

a
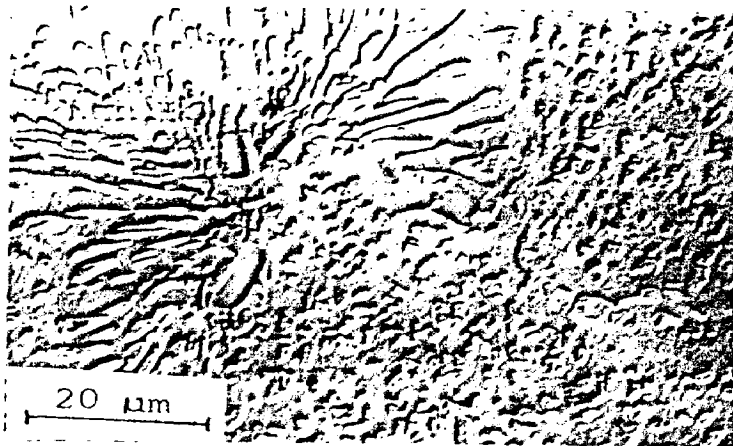
b

6.8   Microstructures of 1473 K HIPed DMP-2 after heat treatment T_2 illustrating (a) limited increase in grain size and (b) the precipitation of cuboidal carbides/borides precipitates iterspersed with eutectic $\gamma + \gamma'$ colonies.
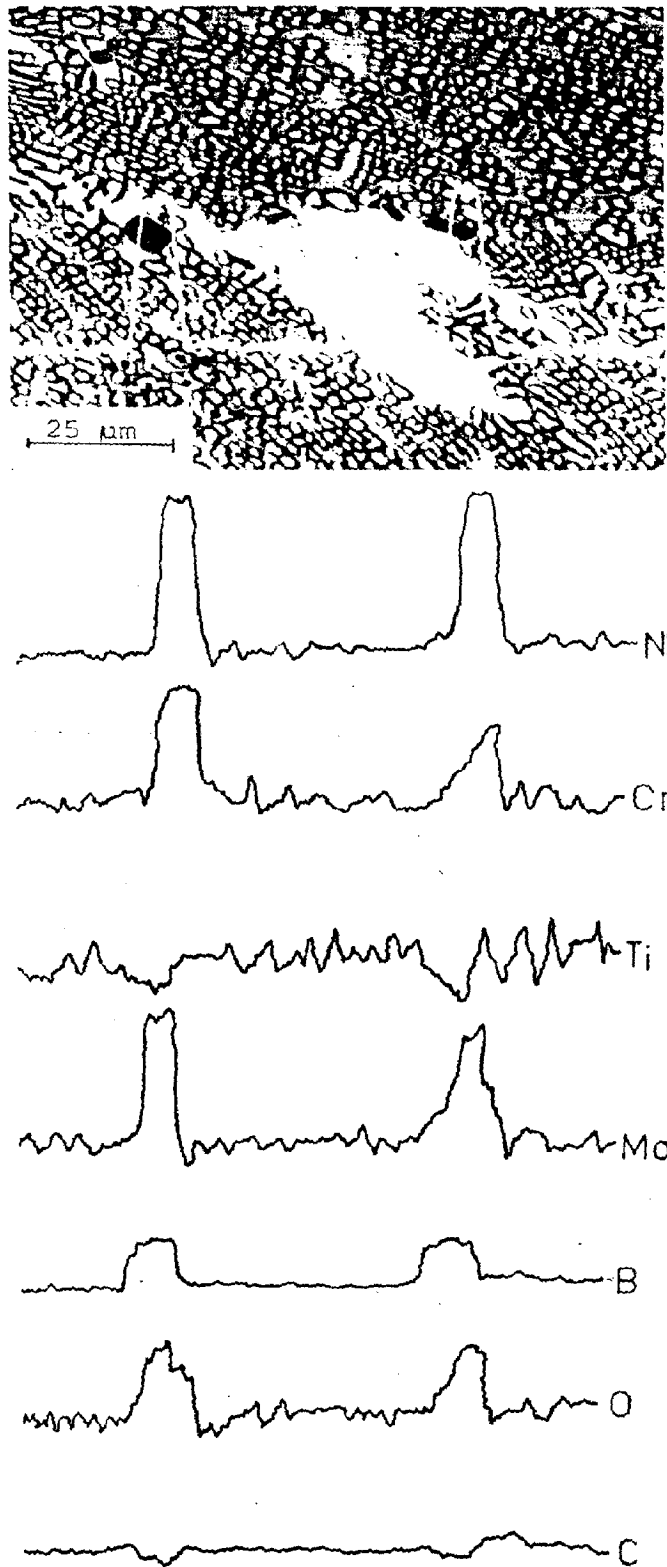
6.9   Electron probe microanalysis of intergranular cuboidal pre
in the 1473 K HIPed DMP-2 after heat treatment T_2.

are randomly distributed in a microstructure dominated by coarse γ' particles. These particles were confirmed to be the borides of W, Mo, Nb and Cr (Fig. 6.9). Oxygen is also found to be present in these borides but C is absent. Similar type of particles but of much finer size are also seen engloved by γ' particles (marked by arrows) throughout the structure. It is also obvious from this microstructure that the intergranular γ' particles possess a coarse cellular morphology (eutectic or nodular γ') and the intragranular particles are of irregular shape with corners rounded.

6.4.2 Mechanical Properties

The tensile and stress rupture properties of the BH2/T$_1$ material are likely to suffer because of the occurrence of incipient melting and abnormally large grain size. Specimens tested under different conditions (Table 6.3) in fact confirmed this aspect. It is interesting to note that the RT specimen exhibits low ductility in spite of fairly large difference between the YS and the UTS. As earlier conjectured for the BH3 material (Section 5.3.1 Chapter 5), this work hardening is due to the reprecipitation of intergranular brittle bo ˙ ˉ films which make the alloy highly strong. Initially, 1 grain boundary films may serve as sinks accommodating the pi: of dislocations but as the deformation continues, the pi: may become so high that abrupt failure occurs. Severe. of stress rupture properties is also attributed to the pres· of brittle boride films at the grain boundaries.

Table 6.3

Tensile and Stress - Rupture Properties of 1473 K HIP. DMP-2

After Heat Treatment, T_1^*

Test Temperature (K)	Tensile Properties			Stress - Rupture Properties		
	0.2% YS MPa	UTS MPa	El** %	Temperature/Stress (K) MPa	S-R Life (Hours)	RA %
298	870	1055	5	978 / 760	2.5	-
				1055 / 640	3.0	-
1033	866	907	2	1033 / 760	0.5	-

T_1^* 1493 K/2 h, RAC + 1323 K/8 h, AC + 1123 K/16 h, AC

**   For gauge length of 25.4 mm

Table 6.4 lists the tensile and stress rupture properties of BH2 material after heat treatment T_2. Increased YS and UTS accompanied with moderate ductility are evidently due to the material having a fine grained homogeneous structure without any film like phase. An interesting observation is the consistently high yield strength of the material upto 1033 K, which is comparable with the yield strength of several current P/M superalloys (Table 2.2 Chapter 2). The SEM examination of the fracture surface of the RT tensile specimen showed that the material has failed intergranularly after producing a moderate deformation (Fig. 6.10). The presence of numerous cracks suggests that preceded by a high stress concentration at the locations of boride particles, the fracture has propagated through the grain boundaries.

The stress rupture properties of the BH2/T_2 material (Table 6.4) are also found to be comparable with many current P/M superalloys (Table 2.3 Chapter 2). The SEM fractographs of the BH2/T_2 specimen tested at 978 K/760 MPa are given in Fig. 6.11. The fracture is of mixed type, mostly transgranular and with reasonably good ductility (9%). Numerous cracks seen at several places are probably due to the excessive stress concentration at the sites of borides. It is, therefore, conjectured that had these borides been of finer size, the stress rupture properties would have been far better. The elevated temperature tensile properties would have also shown further improvement under that situation.

Table 6.4

Tensile and Stress - Rupture Properties of 1473 K HIP DMP-2

After Heat Treatment T_2^*

	Tensile Properties				Stress - Rupture Properties		
Test Temperature (K)	0.2% YS MPa	UTS MPa	El** %	Temperature/Stress (K) MPa	S-R Life (Hours)	RA %
298	978	1092	9	978 / 760	56	9
813	919	1099	8			
923	939	1105	8	1005 / 640	51	9
1033	925	1044	6	1033 / 590	36	8

T_2^* 1353 K/8 h, RAC + 923 K/24 h, AC + 1033 K/16 h, AC

**   For gauge length of 25.4 mm
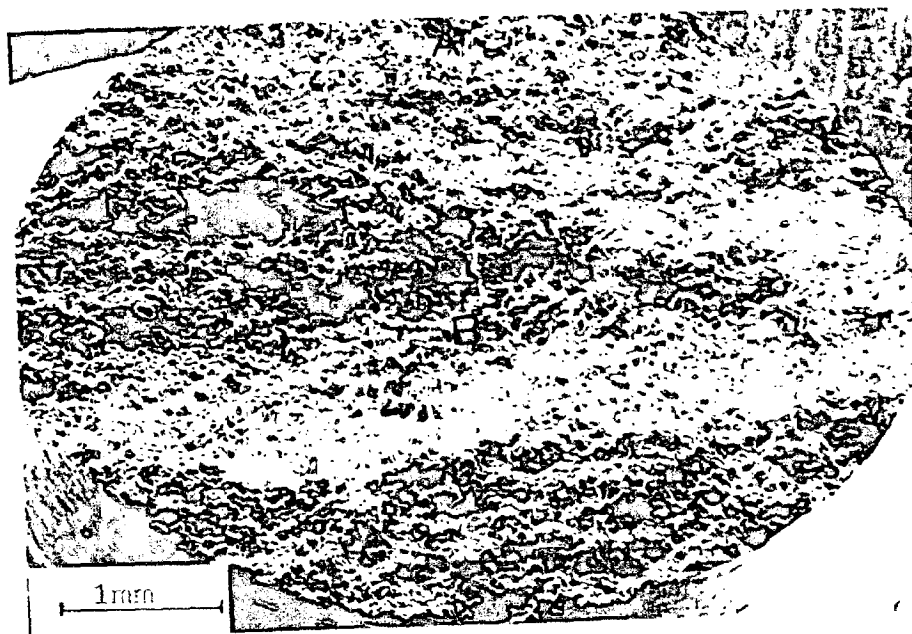
6.10   SEM fractographs of BH2/ T_2 specimen (1473 K HIPed DMP-2 subjected to heat treatment T_2) after tensile testing at RT showing intergranular type of failure and considerable deformation.
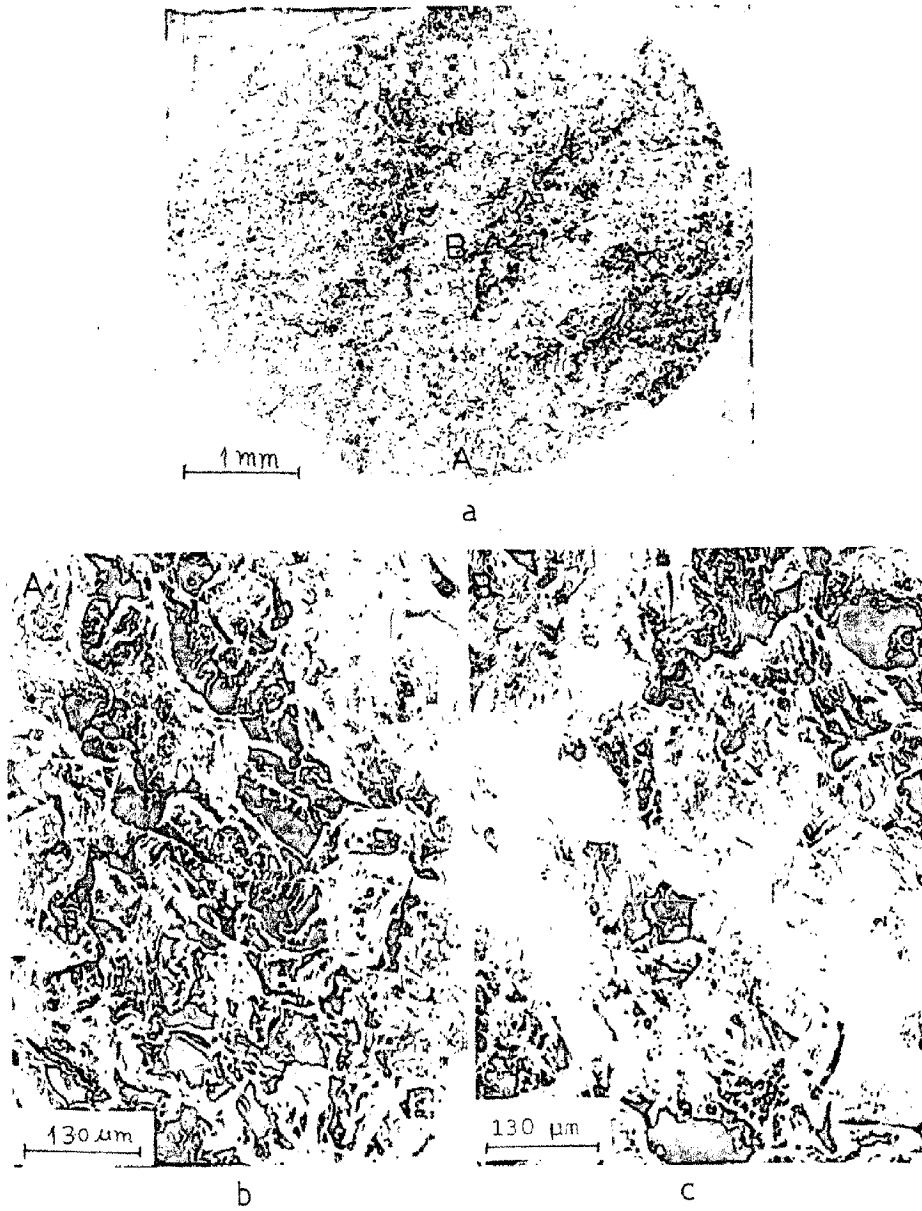
6.11   SEM fractograph of BH2/T_2 specimen stress-rupture tested at 978 K/760 MPa showing numerous cracks leading to a ductile-cum-brittle fracture.

6.5   SIGMA PRONE ALLOY, DMP-3

6. .1   Microstructural Observations

Fig. 6.12 shows the results of γ'-solvus determination study on the CH1 material. At 1473 K, dissolution of γ' is virtually complete. Therefore, the γ'-solvus of the alloy DMP-3 is considered to be 1473 ± 10 K.

The microstructure of CH2 after heat treatment T_1 is shown in Fig. 6.13. As compared with the 1473 K HIPed material (CH2), the grain size of the $CH2/T_1$ material has slightly increased. The volume fraction of γ' appears to be extremely large, possibly more than 60% with γ' particles having adopted a raft like or lamellar appearance. The grain boundaries are heavily decorated with fine-to-coarse precipitates, which were found to be the carbides rich in tungsten, molybdenum and also niobium as is evident from their microanalyses in Fig. 6.14. Since titanium is absent in these carbides, they are believed to be of M_6C type. This was infact confirmed by the analysis of the SADP of grain boundary carbides observed during transmission electron microscopy (Figs. 6.15b and c). These carbides have a lattice parameter of approximately 11.65 $\overset{\circ}{A}$. An interesting feature of this microstructure is the absence of any precipitate-free zone (PFZ) around the grain boundary carbides (Fig. 6.15a). The γ' particles have cuboidal morphology, uniform size and are also fully coherent with the matrix.

Fig. 6.16 shows the microstructure of CH2 after heat treatment T_2. In comparison with the $CH2/T_1$ material, the $CH2/T_2$ material does not show any grain growth and has a bimodal
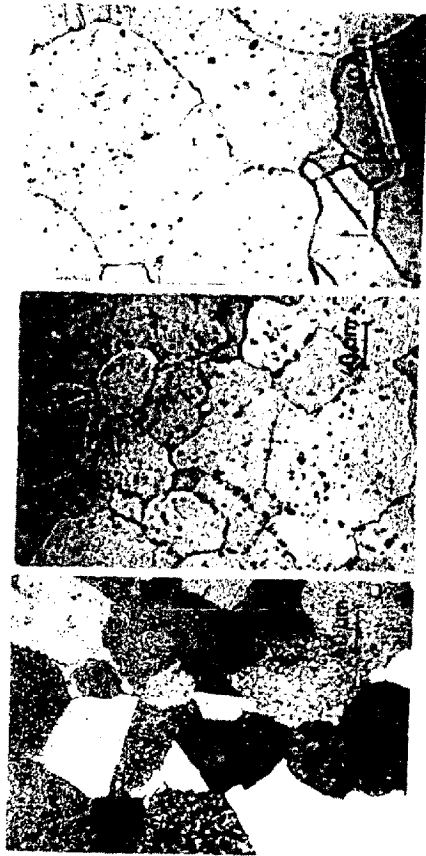
6.12 γ' solvus study on the sigma-prone PM alloy DMP-3 (a) 1453K/ 2h, WQ, 1473 K/ 2h, WQ and 1493 K/ 2h, WQ.

a

b

c
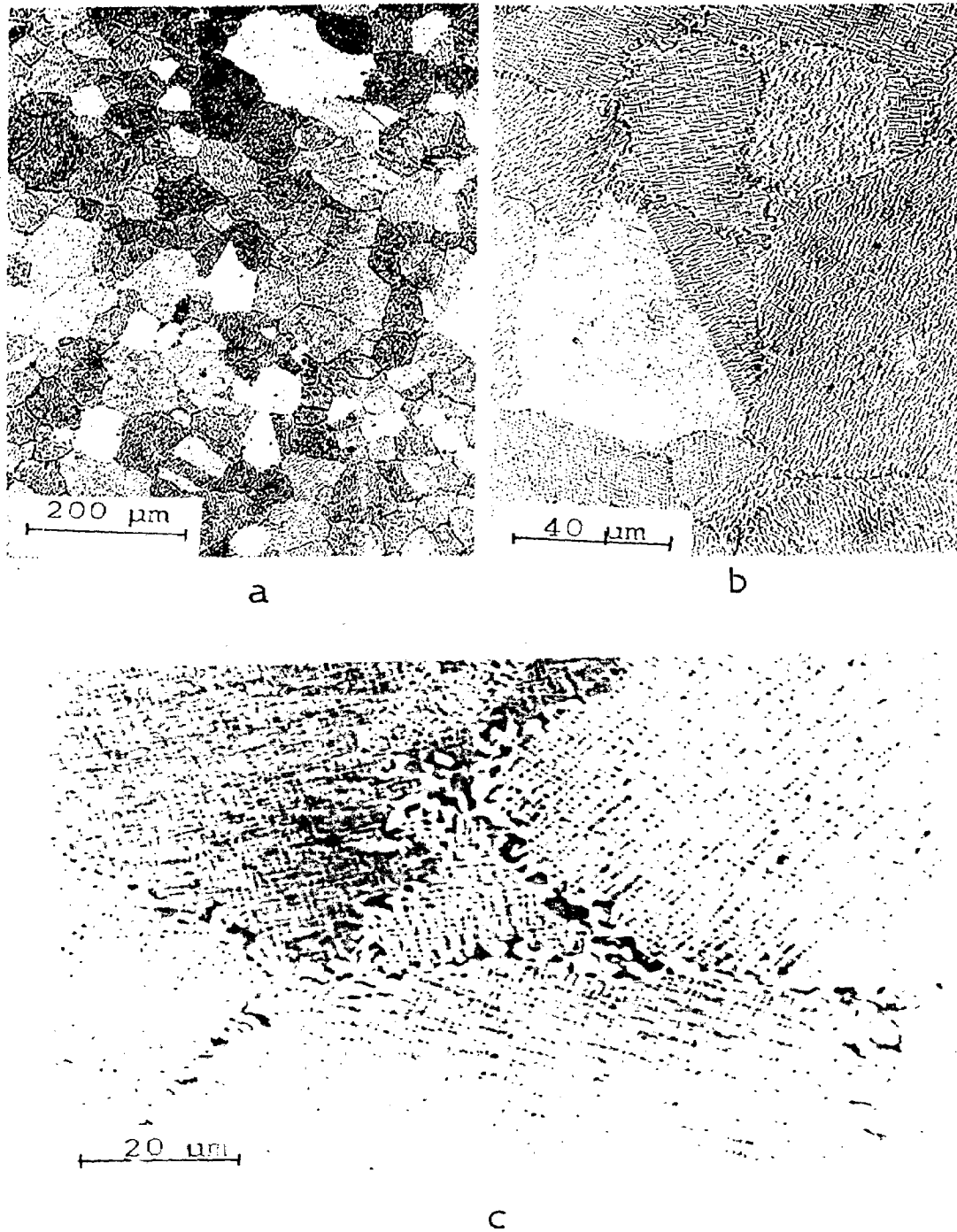
6.13 Microstructure of CH2/T$_I$ specimen (1498 K HIPed DMP-3 after heat-treatment T$_I$) showing (a) increase in grain size (b) raft-like γ' structure (c) precipitation of carbides and coarse γ' at grain boundaries.
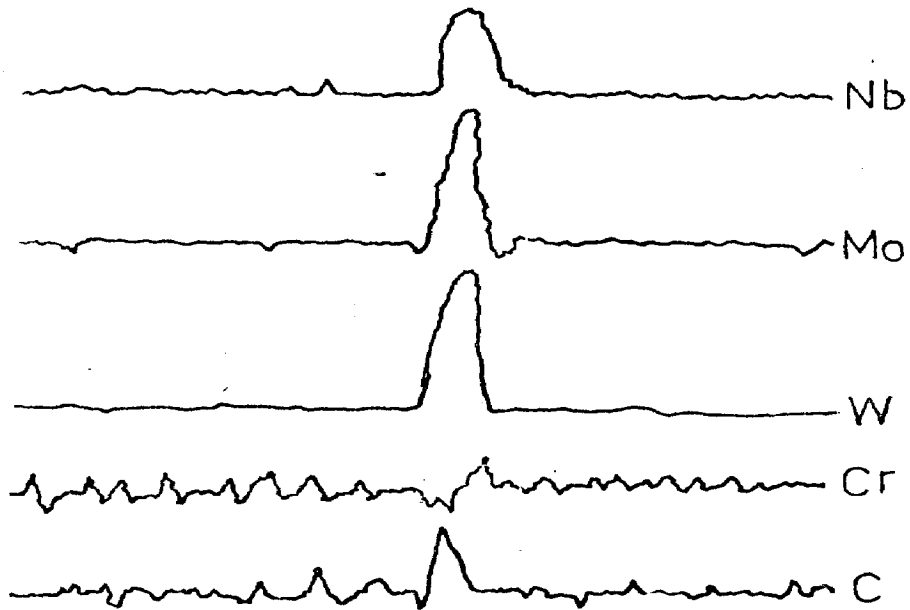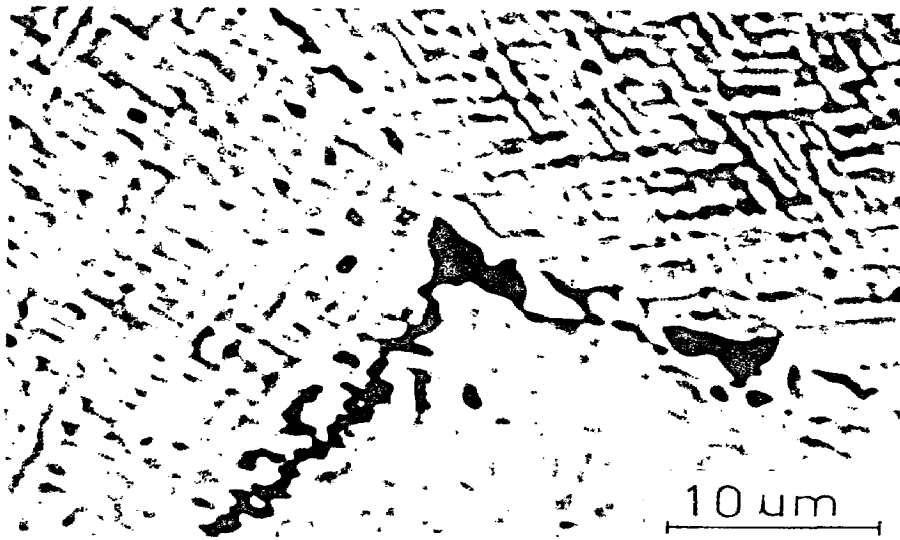
6.14   Electron probe microanalysis of intergranular carbide precipitates in 1473 K HIPed, DMP-3 after heat treatment T_1.

189

6.15   Transmission electron micrograph of 1473 K HIPed DMP-3 after
       heat treatment T_1 showing (a) grain boundary carbide precipitates
       and morphology of γ' (b) the SADP of a grain boundary precipitate
       and (c) the key to the SADP.

distribution of γ', i.e. coarse particles at the grain boundaries and medium-to-coarse particles in the grains (Fig. 6.16b). The TEM examination further confirmed the evidence of bimodal structure (Fig. 6.16c). The volume fraction of γ' appears to be less than 50% but it is presumed that ultrafine particles of secondary γ' are spaced between the medium-sized cuboidal γ' particles. This figure (Fig. 6.16) also shows the presence of a needle-shaped precipitate in the corase primary γ' particle. These needle-shaped precipitates were identified to be M_6C and are believed to be similar to the grain boundary carbides. The microanalysis of a grain boundary carbide particle in the $CH2/T_2$ material is shown in Fig. 6.17. Like the carbides observed in the $CH2/T_1$ material, these carbides are also rich in tungsten, molybdenum and also niobium but do not contain titanium. However, a distinctive microstructural feature of $CH2/T_2$ is the presence of an envelope around the grain boundary precipitates which seems to give an appearance of serrated grain boundaries in the optical micrograph (Fig. 6.16b). On TEM examination, this envelope was confirmed to be due to the precipitation of irregularly shaped primary coarse γ' particles (Fig. 6.18a). As is evident from Figs. 6.17b and 6.18a, intergranular precipitation of carbides is discrete in the $CH2/T_2$ material as compared to a continuous precipitation in the case of $CH2/T_1$ material (Fig. 6.15). These carbides were identified as M_6C having a lattice parameter of approximately 11.48° A by indexing the SADP (Figs. 6.18b and c).
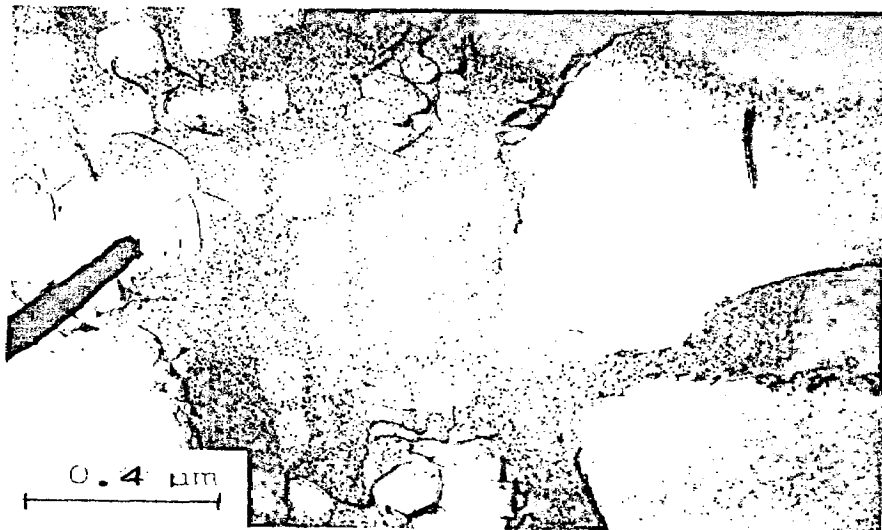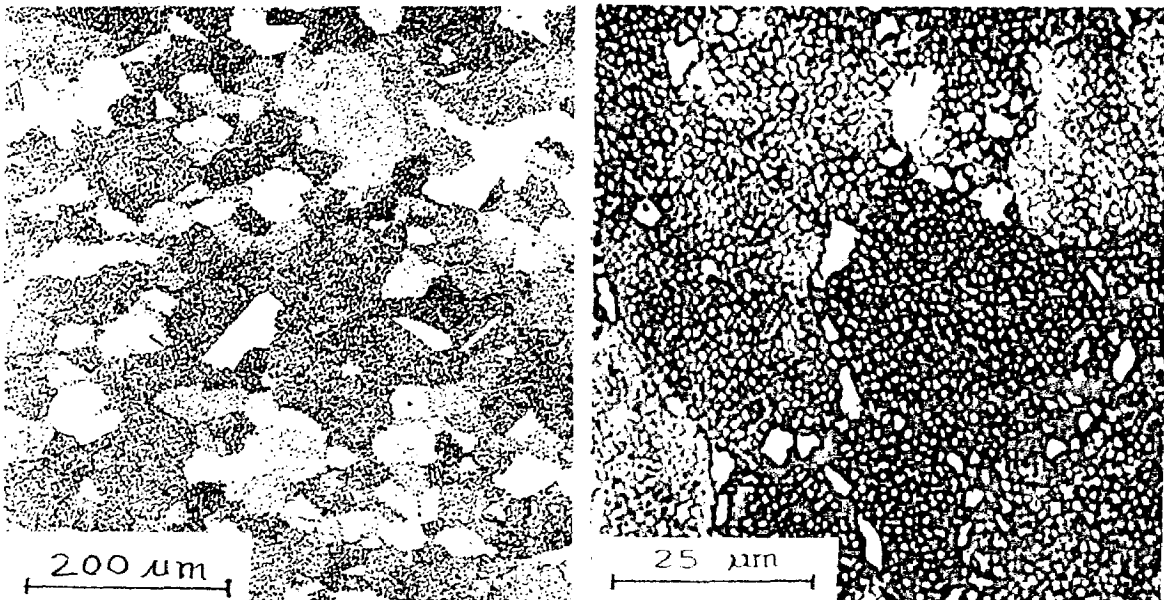
6.16   Microstructures of 1473 K HIPed DMP-3 after heat treatment
        T_2 showing (b) grain boundary configuration and (c) morphology
        of γ' precipitates.
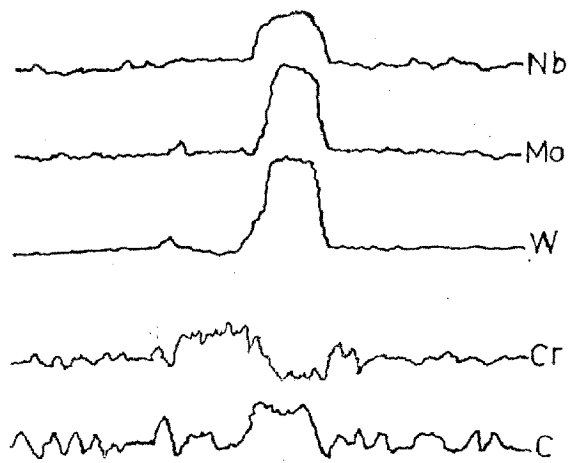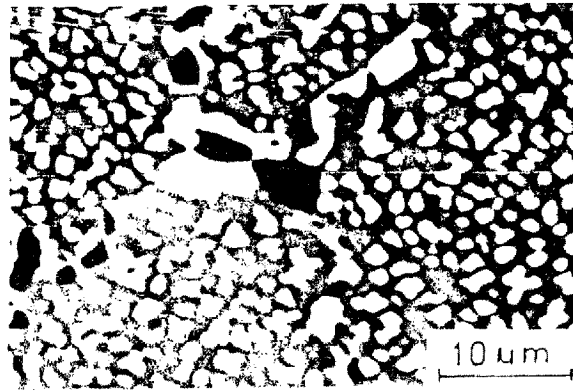
6.17 Electron probe microanalysis of 1473 K HIPed DMP-3 after heat treatment T_2.

282
082
282
482
200
200

c

b

a

0.67 μm
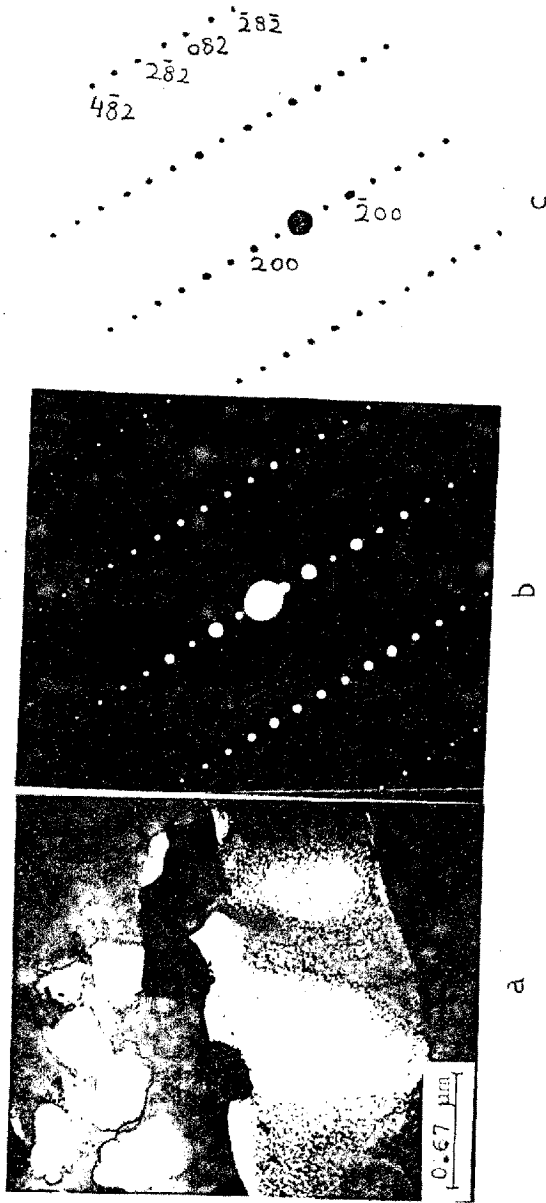
6.18 Transmission electron micrograph of 1473 K HIPed DMP-3 after heat treatment T_2 showing (a) distribution of carbide particles at grain boundaries (b) the SADP of a grain boundary carbide particle and (c) the key to the SADP.

6.5.2 Mechanical Properties

Table 6.5 presents a comparison of the tensile properties of the $CH2/T_1$ and $CH2/T_2$ materials. At 298, 813 and 923 K, the tensile properties of the $CH2/T_2$ specimens are much higher than those of the $CH2/T_1$ specimens. This is attributed to a relatively finer grain size of the $CH2/T_2$ material (Figs. 6.13 and 6.16). However, at 1033 K, where the grain boundary sliding effect is likely to be more prominent, the coarse-grained $CH2/T_1$ material should have shown some property improvement over the $CH2/T_2$ material but a reverse trend is observed. The stress rupture properties of $CH2/T_2$ also show significant improvement over $CH2/T_1$ (Table 6.6).

Since fractographic examination of the $CH2/T_1$ and $CH2/T_2$ specimens did not show any noticeable change in their fracture behaviour the beneficial effect of heat treatment T_2 on the alloy strength is explained on the basis of certain important microstructural differences caused by the two heat treatments and these are discussed as follows:

During deformation, dislocations caused by high tensile stresses form large pile-ups at the grain boundaries and other obstacles to their motion. A continuous network of carbides at the grain boundaries would, therefore, result in an excessive stress concentration and as superalloys with high volume fraction of fine γ' are susceptible to environmental embrittlement at temperatures in the viscinity of 1033 K [122], the probability of reduced tensile strength and rupture life is high. In the

Table 6.5

Effect of Heat Treatment on the Tensile Properties of 1473 K HIP DMP-3

Test Tempera-ture (K)	0.2%YS (MPa)		UTS (MPa)		El* (%)		RA (%)	
	T_1	T_2	T_1	T_2	T_1	T_2	T_1	T_2
298	830	1104	980	1293	9	10	8	10
813	857	990	1220	1334	9	7	10	10
923	896	1093	1240	1462	10	8	12	12
1033	950	1000	1050	1111	5	8	6	10

* For gauge length of 25.4 mm

T_1 1493 K/2 h, RAC + 1323 K/8 h, AC + 1123 K/16 h, AC

T_2 1353 K/8 h, RAC + 923 K/24 h, AC + 1033 K/16 h, AC

Table 6.6

Effect of Heat Treatment on the Stress - Rupture Properties
of 1473 K HIP DMP-3

Temperature / Stress (K) . MPa		Stress - Rupture Life (HOURS)		Reduction in Area (%)	
		T_1	T_2	T_1	T_2
978	/ 760	40	92	5	6
1005	/ 640	29	136	5	8
1033	/ 590	25,48	35,59	3,3	5,8

T_1 1493 K/2 h, RAC + 1323 K/8 h, AC + 1123 K/16 h, AC

T_2 1353 K/8 h, RAC + 923 K/24 h, AC + 1033 K/16 h, AC

case of CH2/T$_1$ material, these conditions do exist and, therefore, in spite of a coarse grain size, both the tensile and the stress rupture properties suffer when the material is tested at 1033K. In contrast, the formation of serrated grain boundaries in the CH2/T$_2$ -material is believed to provide increased resistance to grain boundary sliding at 1033 K. It is also well known that the mechanical properties of a fine-grained material are superior to a coarse-grained material at temperatures below 0.6 Tm, where Tm is the melting point of the material concerned. The highest test temperature used here is 1033 K, which is definitely below 0.6 Tm. At 1033 K, the tensile and the stress rupture properties of CH2/T$_2$ are not much superior to CH2/T$_1$ but at temperatures below 1033 K, CH2/T$_2$ possesses higher strength than CH2/T$_1$. It can, therefore, be deduced that the superior tensile and stress rupture properties of CH2/T$_2$ material at temperatures upto 1033 K are due to the cumulative effects of fine grain size, bimodal distribution of γ', discrete precipitation of carbides at the grain boundaries and grain boundary serrations.

6.6 MECHANISM UNDERLYING THE FORMATION OF Hf-RICH PHASE AT TRIPLE POINT BOUNDARIES

Hafnium has a very high affinity for oxygen, which was also confirmed by the electron probe microanalysis of the as-HIP material and has been discussed in Section 5.6.4 (Chapter 5). During atomization, a powder particle is likely to develop some sites which are more enriched with hafnium oxide in comparison to the remaining surface. Ni$_5$Hf phase may also form and concen-

trate at some areas in a powder particle surface. As proposed by Zheng and Cai [42], the eutectic Ni_5Hf phase has an incipient melting temperature of 1463 K. Therefore, during HIP consolidation or solution treatment, which have been carried out at temperatures above 1463 K, melting of this Ni_5Hf phase has occurred. Wherever the surfaces of powder particles enriched with Ni_5Hf and hafnium oxide come into contact, incipient melting leading to the formation of segregation would occur. The triple point boundaries are the preferential sites for the formation of such segregation which is also likely to attract oxygen from the adjoining areas of the powder particle surface. Such a situation would also make the alloy susceptible to the formation of PPB networks. That this has not happened in the case of DMP-1 and DMP-2 is because these alloys have very low carbon contents. If carbon content is high, tendency of PPB precipitation would increase. The Ni_5Hf phase which is unstable is also likely to transform into stable MC carbides. The transformation of Ni_5Hf to MC carbides on thermal exposure in cast nickel base superalloys has been reported by Zheng and Cai [42].

6.7   ISOTHERMAL FORGING OF DMP-3

Examination of the mechanical properties of the as-HIP and HIPed + heat treated DMP-3 has shown that the alloy possesses strength comparable to several existing P/M nickel base superalloys. However, as the ductility of DMP-3 has been found to be considerably low, it was thought that on account of a high proportion of refractory elements, the alloy is likely to have poor forgeability. It was, therefore, decided to carry out forging experiments

on the HIPed alloy. In order to have an inherently fine-grained structure, DMP-3 consolidated at 1448 K was used for the forging study in a vacuum hot press. Another important reason for choosing this HIPing temperature was to investigate the effect of forging on a HIPed compact with pores. Forging was done on a 30mm dia x 60mm long billet at 1448 ± 5 K to prevent grain growth. Before forging the HIPed compact was machined to partly remove the stainless steel casing and to make it perfectly cylindrical in shape.

Fig. 6.19 shows the HIPed compact before and after iso-thermal forging, which produced a deformation of about 50%. The material after forging was found to be completely free from any cracks. Rectangular blanks (8mmx8mmx40mm) transverse to forging direction (i.e. perpendicular to the axis of forged piece) were cut. The bars were heat treated according to the heat treatment T_2. Specimens with reduced dimensions were machined and tested under different conditions. Table 6.7 presents the tensile and the stress rupture properties of the HIPed + forged + heat treated DMP-3. Examination of these properties shows that the forging has not produced any appreciable improvement in the mechanical properties of the alloy. The microstructural examination of the forged and heat treated alloy showed the occasional presence of pores at the triple point boundaries (Fig.6.20), suggesting that either the deformation of 50% is not adequate to close the pores present in the HIPed compact or the 1448 K HIPed material by virtue of the presence of pores is not suitable for forging. Shortage of

Table 6.7 Tensile and stress-rupture properties of HIPed*, forged and heat treated** DMP-3

Tensile Properties					Stress-rupture properties			
Test tempera-ture (K)	0.2% YS MPa	UTS MPa	El %	RA %	Temperature / stress (K)	MPa	SR Life (Hours)	RA %
298	1097	1275	8	10	978 /	760	57	6
923	1084	1320	10	12	1033 /	590	32	6
1033	962	1094	7	10				

* HIPed at 1448 K

** Heat treated 1353 K/8h, RAC + 923 K/24h, AC + 1033 K/10h, AC
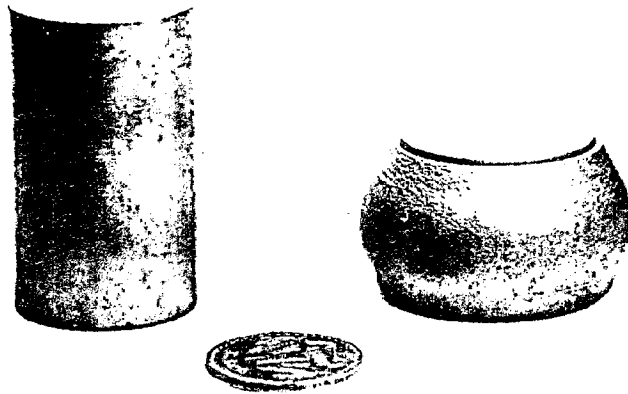
6.19   A macroview of HIPed DMP-3 compact before and after forging.
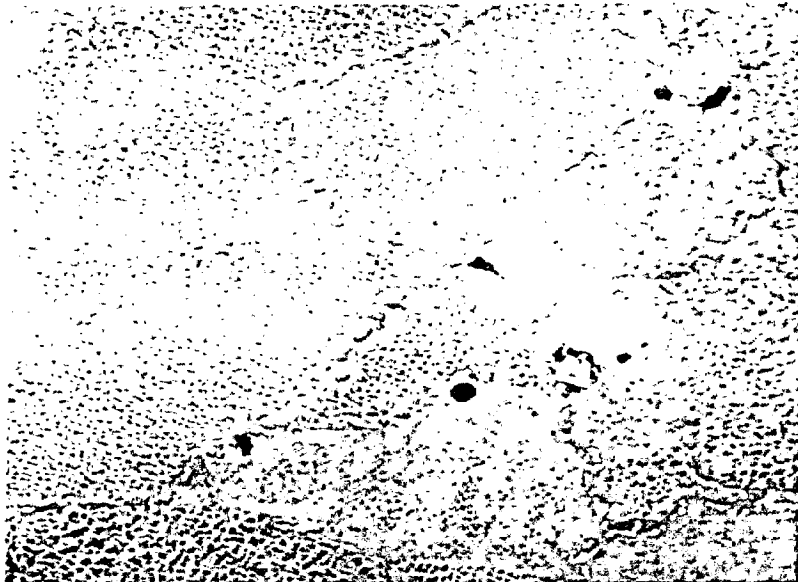
6.20   Microstructure of HIPed, forged and heat treated DMP-3.

powder material, however, prevented further forging experiments but this forging study suggests that the alloy does possess a good forgeability.

6.8   OPTIMUM HEAT TREATMENT FOR Hf-and B-MODIFIED
P/M SUPERALLOYS

From the foregoing observations, it is clear that the heat treatments involving solutioning temperatures above the γ ' solvus are not suitable for P/M nickel base superalloys which are modified by the additions of boron and hafnium. Both boron and hafnium have been found to sharply decrease the solidus of the alloys leading to incipient melting and segregation of undesirable phases at the grain boundaries. Although water quenching has been found to suppress the precipitation of such undesirable phases but quench cracks noticed on the specimen prohibit the use of such rapid cooling methods. The alternate heat treatment T_2 which includes a low solution treatment temperature has been found to be optimum as it produces a homogeneous fine-grained microstructure and a good combination of mechanical properties.

This study convincingly shows that either both these elements should not be simultaneously added in a P/M superalloy or their total content should be low so that the overall effect on the decrease of alloy solidus is minimized.

CHAPTER 7

SUMMARY AND CONCLUSIONS

7.1 SUMMARY

Detailed investigations have been undertaken on the PM processing of a high performance cast nickel-base superalloy ZhS6-K (Ni-10Cr-5W-5Al-4.5Co-4Mo-2.5Ti-0.15C-0.02 B). Minor compositional modifications were done by reducing carbon to 0.02%, titanium to 2.2% and aluminium to 4.5%. Niobium and hafnium were also added in minor proportions mainly to minimize the formation of carbides at the prior particle boundaries. Three chemistry variants of the P/M alloys designated as DMP-1 (with 0.7% Hf and 0.02% B), DMP-2 (with 0.7% Hf and 0.085% B) and DMP-3 (sigma-prone composition with marginal increases in Cr, Co, W, Ti, Al and Nb but without Hf) have been examined with a view to evaluate the effects of boron and hafnium on the consolidation behaviour, microstructure and mechanical properties. The alloys have been prepared by vacuum induction melting and, powder by argon atomization process. Important powder characteristics including the composition and structure of the powder particle surfaces have been evaluated. The powders have been HIP consolidated at different temperatures below and above, the γ' solvus to optimize the consolidation temperature. With the help of EPMA, X-ray diffraction and TEM techniques, minor phases present in the three alloys have been identified. The observed microstructural effects due to changes in the consolidation temperature have been related with the mechanical properties and fracture behaviour of the three P/M alloys. An optimum heat treatment schedule which brings about significant improvement in the tensile and stress rupture properties of each of the three alloys has been established.

An important aspect investigated in the present work is the question whether addition of hafnium or boron is essential in nickel base P/M superalloys in reducing the precipitation of carbides at the prior particle boundaries. Based on the microstructural observations and information available in the literature, the most likely mechanisms explaining the phase changes due to additions of hafnium and boron have been proposed. Limited forging experiments have been conducted to assess the forgeability of these superalloys containing high proportions of refractory elements.

7.2 CONCLUSIONS

Following conclusions have been drawn from the present investigation :

1. Additions of both niobium and hafnium aided by reduction in carbon have been shown to suppress the precipitation at PPBs in DMP-1 and DMP-2. The same effect has been observed in DMP-3 by niobium addition alone in spite of the fact that the alloy has relatively higher carbon content.

2. Unlike carbon - although an interstitial element - boron does not promote the formation of PPB networks.

3. Increase in boron reduces the activity of oxygen at the powder particle surface thereby lowering the tendency for the precipitation of oxycarbides at the PPBs.

4. Hot Isostatic pressing of high boron alloy at a temperature marginally above the γ' solvus results in the formation

of massive boride films at the grain boundaries and a large volume fraction of eutectic $\gamma + \gamma$ ' structure implying that increase in boron narrows down the consolidation temperature range.

5. Grain boundary boride films, when present, makes the alloy highly sensitive to rapid cooling from high solutioning temperatures inducing quench cracks even in small specimens.

6. Hot isostatic pressing of high-boron superalloys, when carried out at temperatures just below or very close to the γ' solvus, prevents the formation of boride films and also restricts the precipitation of eutectic $\gamma + \gamma$' structure.

7. The very low levels of titanium in the carbides and borides in these alloys indicate that titanium is mostly partitioning to γ' phase.

8. On account of its decreasing effect on the alloy solidus, hafnium narrows down the consolidation temperature range of superalloys.

9. Hafnium has a tendency to form hafnium oxide or eutectic Ni_5Hf phase, but does not partition to carbides in the alloys which are low in carbon.

10. The hafnium rich phase identified to be Ni_5Hf and segregating at the triple point boundaries appears to occur only at higher consolidation or solution treatment temperatures.

This may be attributed to the incipient melting of Ni_5Hf. As Ni_5Hf melts, it attracts oxygen from the adjoining powder particle surface. Grain boundaries or triple point boundaries which have high free energies are apparently the preferential sites for the segregation of this phase.

11.   As confirmed by Auger Electron Spectroscopy studies on the loose powders and the consolidated material, the presence of hafnium in a superalloy is beneficial in minimizing the activity of sulphur at the powder particle surface thereby reducing the tendency for the formation of carbosulphides.

12. M_6C carbides formed at the grain boundaries in these alloys are rich in W and Mo and do not degenerate even after high temperature exposures. Since solvus of the M_6C carbides is generalloy lower than the MC carbides and also the γ', these alloys are capable to develop grain boundary serrations by suitably modifying the heat treatment schedules. Absence of depleted zone around carbides and precipitation of coarse γ' at the grain boundaries further contribute to the high elevated temperature strength of such P/M superalloys.

13.   As in several wrought superalloys which have γ'-solvus above carbide solvus, the modified P/M superalloys studied in the present investigation have also responded to slow cooling from HIPing temperature by way of the appearance of serrated grain boundaries. These serrations are retained during the solution treatment step, particularly when the

solutioning temperature is below the γ' solvus. The formation of grain boundary serrations is seen to improve the elevated temperature strength of the alloys.

14. Reduction of cobalt does not produce any adverse effects on the elevated temperature properties of the present super-alloys which contain high proportions of refractory elements.

15. DMP-3, inspite of a sigma prone composition, possesses good forgeability and offers a good combination of tensile and stress rupture properties as compared with several existing P/M superalloys.

7.3 SUGGESTIONS FOR FURTHER WORK

It is hoped that this work has provided some answers to the problems arising with the development of new superalloy composi-tions which are specifically tailored to powder metallurgical applica-tions such as turbine discs. However, there is considerable scope for further work in this area. The effects of variations in hafnium levels in a boron-free P/M superalloy can be studied to have further understanding on the effect of hafnium on microstructure and mechanical properties of the alloy. It would also be of interest to study the partioning behaviour of various elements such as W, Mo, Nb and Cr towards carbides or γ or γ' as a function of boron level. Although the present investigation has convincingly shown that the low-cobalt sigma-prone P/M composition of DMP-3, possesses good forgeability

and high strength capabilities, more detailed investigations on consolidation between deformation and microstructure would be desirable. Studies on the effect of isothermal forging of the consolidated billet or direct extrusion of the powder on the mechanical properties of the optimized composition is also desirable to examine the full potential of this alloy as a prospective turbine disc material.

REFERENCES

1. C.T. Sims and W.C. Hagel, "The Superalloys", J. Wiley & Sons, New York, 1972

2. R.F. Decker in "Steel Strengthening Mechanisms", Climax Molybdenum Co. Greenwich, CT, 1970, 147

3. C.T. Sims, Superalloys 1984, Ed. M.Gell, C.S. Kortorich, R.H. Bricknell, W.B. Kent, J.E. Radavich, The Metall Soc. of AIME, Pa, USA, 1984, 401

4. G.H. Gessinger and M.J. Bomford, Inter . Metall. Rev. 1974, 19, 51

5. R.L. Dreshfield and H.R. Gray, Met. Powder Rep., 1985

6. P. Wildgoose, N.G. Turner, H.F. Davies, B.J. Helliwell, R. Ubank and H. Harrison, Powder Metallurgy, 1981, No.2, 75

7. R.D. Eng and D.J. Evans, in "Superalloys 1980, ed. J.K. Tien,S.T.Wlodek H. Morrow III, M Gell and G.E. Maurer, ASM Press, Metals Park, Ohio, USA, 1980, 491

8. R.E. Waters, J.A. Charles and C. Lea, Met.Tech., 1981, 8, 194

9. R. Thamburaj, W. Wallace, Y.N. Chari and T.L. Prakash, Powder Metallurgy, 1984, 7(3), 169

10. S.H. Reichman and J.W. Smythe, in "Mod. Dev. in Powder Metallurgy" ed. H. Hausner, Plenum, New York, 1971, Vol.5, 73

11. J.M. Larson, Metall. Trans., 1976, 7A, 1497

12. J.M. Wentzell, Met. Engg. Quarterly, 1974, 14(4), 47

13. R.V. Miner Jr., Metall. Trans, 1977, 8A, 259

14. C.A. Hammersley, Metallurgia, 1978, 487

15. C.J. Burton in "Superalloys: Metallurgy and Manufacture",Claitors Publishing Division, USA, 1976, 147

16. R.T. Holt and W. Wallace, Inter.Met.Reviews., 1976, 21, 1

17. J.K. Tien, T.E. Howson, G.L. Chen and X.S.Xie, Jour. of Met. 1980, 32(10), 12

18. J. Heslop, Cobalt, Sept. 1964, 24, 128

19. G.E. Maurer, L.A. Jackman and J. Domingue, in "Superalloys 1980", ASM, Metals Park, Ohio, USA, 1980, 43

20. A.M. Borzd'ika, Met.Sc. and Heat Treatment (transl. from Russian), 1977, 19, 937

21. R.N. Jarett and J.K. Tien, Metall. Trans. 1982, 13A, 1021

22. F.F. Khimushin, "High Temperature Steels and Alloys, Part-II", Foreign Technology Division, WP-AFB, Ohio, USA, April, 1971

23. K.K. Sharma and S.N. Tewari, Jour. of Mat. Sc. 1983, 18, 1021

24. S.N. Tewari, Jour. of Mat. Sc. 1981, 16, 2193

25. R.L. Dreshfield, Trans. ASM Quarterly, 1968, 61, 352

26. H.E. Collins and R.J. Quigg, Trans. ASM Quarterly, 1968, 61, 139

27. C.T. Sims, High Temp. Technology, 1984, 2(4), 185

28. E.C. Guo and F.J.Ma in "Superalloys 1980", ed. J.K. Tien, S-T Wlodek, H. Morrow III, M.Gell and G.E. Maurer, ASM Press,Metals Park, OH, 1980, 345

29. J.M. Dahl, F.W. Danesi and R.G. Dunn, Metall. Trans. 1973, 4A,1087

30. P.S. Kotval, J.D. Venables and R.W. Calder, Metall. Trans. 1972, 3A, 453

31. V. Ya Markiv and V.V. Burnashova, Izvestia Akademi Nauk SSSR Metally. 1969, No.6, 1356

32. R.P. Elliot in "Constitution of Binary Alloys, Suppl. I, Mc Graw Hill, 1965

33. G.L.R. Durber in "High Temp. Alloys for Gas Turbines", Appl. Science Publishers, Essex, UK, 1978, 459

34. L.R. Woodyatt, C.T. Sims and H.J. Beattie Jr., Trans. AIME, 1966, 236, 519

35. J.R. Mihilsin, C.G. Bieber and R.T. Grant, Trans. AIME, 1968, 242, 2399

36. H.J. Murphy, C.T. Sims and A.M. Beltran,Jour. of Met., November,1968, 46

37. S.M. Copley and B.H. Kear, Trans. AIME, 1967, 239, 977

38. S.M. Copley and B.H. Kear,Trans. AIME, 1967,239, 984

39. P.H. Thornton, R.G. Davies and T.L. Johston, Metall. Trans. 1970, 1(1), 207

40. J.M. Oblak and B.H. Kear in Electron Microscopy and the Structure of Material, ed. G. Thomas, R.M. Fulrath and R.M. Fisher, University of Calif. Press, Berkeley, 1972, 565

41. R.F. Decker and J.R. Mihilsin, ASM Trans. Quarterly, 1969, 62,481

42. Y.R. Zheng and Y.L. Cai, in "Superalloy 1980", ed. J.K. Tien et al , ASM Press, Oh, 1980, 565

43. G.D. Pigrova and Ye Ye Levin, Physics of Met. and Metallo., 1972, 33(6), 166

44. B.J. Piercey and R.W. Smashey, Trans. AIME, 1967, 239, 451

45. M.J. Donachie Jr. in "Metals Hand Book", 9th Edition, Vol.3, ASM Metals Park, OH, 1980, 220

46. F.Schubert in "Superalloys Source Book" ed. M.J. Donachie,Jr. ASM, Metals Park, OH, 1984, 71

47. G.H. Gessinger, Powder Met. Inter. 1981, 13(2), 93

48. D.J. Evans, D.N. Duhl and R.B. Slack, Mod. Dev. in Powder Metallurgy, ed. H.H. Hausner and G.D. Smith, MPIF, New Jersey, 1974, 8, 473

49. H.A. Johnson,in"Prog. in Powder Metallurgy," Ed. G.D. Smith, MPIF, Princeton, New Jersey, Vol.31, 223

50. B.H. Kear, P.R. Holiday and A.R. Cox,Metall. Trans. 1976, 10A, 191

51. J.S. Benjamin, Metall. Trans. 1970, 1, 2943

52. R.K. Hotzler and T.K.Glasgow in"Superalloys 1980," Ed. J.K.Tien, S.T. Wlodak, H. Morrow III, M. Gell and G.E. Maurer, ASM, Metals Park, OH, 1980, 455

53. W.H. Wiegert and R.J. Henrick, ibid, 575

54. H.D. Hanes, D.A. Siefert and C.R. Watts in Hot Isostatic Pressing" MCIC-77-34, Metals & Ceramics Information Center, Battelle Labs, Columbus, OH, 1977

55. C.H. Symonds and F.A. Thompson,"Nickel Superalloy Powder Production and Fabrication to Turbine Discs", paper presented at AGARD Meeting, Toronto, March, 1976

56. R.L. Athey and J.B. Moore in"Powder Metallurgy for High Performance Applications", ed. J.J. Burke and V. Weiss, Syracuse University Press, New York, 1972, 281

57. R. Johnasson and S.E. Isakson, Powder Metall. Inter. 1970, 2, 49

58. J.D. Buzzanol and L.W. Lherbier, in "Superalloys 1980" ed. J.K. Tien, S.T. Wlodek, H. Morrow III, M. Gell, G.E. Maurer, ASM Press, Metals Park, OH, 1980, 149

59. B.R. Patterson, E.C. Bates and W.V. Knopp, Progress in Powder Metall. 1981, 32, 67

60. M.M. Allen, R.L. Athey and J.B. Moore, Metals Engg. Quarterly, 1970, 10, 20

61. M.J. Blackburn and R.A. Sprague in " Superalloys Source Book," ASM, Metals Park, OH, 1984, 269

62. L.N. Moscowitz, R.M. Pelloux and N.J. Grant, in "Superalloys Processing" MCIC-72-10, Battelle Memorial Labs., Columbus, OH, 1972, Z-1

63. J.L. Bartos and P.S. Mathur, in "Superalloys: Metallurgy and Manufacture", Claitors Publishing Div., USA, 1976, 495

64. J.F. Barker and E.H. Van-Der Molen, in "Superalloys Processing", MCIC-72-10, Battelle Memorial Labs, Columbus, OH, 1972, AA-1

65. J.E. Coyne, W.H. Couts, C.C. Chen and R.P. Roehn, in "P/M Superalloys and Aerospace Materials for the 1980s", Zurich Inter. Conf. MPR, 1980, 1, 11.1

66. D.M. Carlson, in "Superalloys 1980", ed. J.K. Tien, S.T. Wlodek, H. Morrow III, M. Gell, G.E. Maurer, ASM, Metals Park, OH, 1980, 501

67. H.Y. Xiu and T.Y. Hon in"Modern Dev. in Powder Metallurgy," ed. H.H. Hausner, H.W. Antes and G.D. Smith, MPIF, Princeton, New Jersey, 1981, Vol. 12, 141

68. P. Loewenstein, in "Progress in Powder Metallurgy", ed. J.M. Campus and D.L.Dyke, MPIF, Princeton, N.J., 1981, 9

69. A. Lawley, Jour. of Metals, 1981, 33(1), 13

70. S.B. Ekbote, M. Kumar and V.S. Arunachalam, Paper presented at the National Symposium on Vacuum Technology and Metallurgical Applications, Hyderabad, India, 21-23, Jan. 1981

71. G.J. Lewis,D.M. Parkins and F.A. Thompson, in "Adv. Processing Techniques for the Manufacture of Nickel-Base Alloy Discs from Powder, Proc. of Metals Soc. Conf. Leeds, UK, 5-7, Jan. 1978

72. F. Thummler and W. Thomma, Metals and Materials, 1967, 1(6),197

73. A. Rozner and G.C. Kuczyanski, Jour. of Amer. Ceramic Soc. 1962, 45, 92

74. J.E. Harris, Met. Sci. Journal, 1978, 7, 1

75. R.L. Hewitt, W. Wallace and M.C. De Malherbe, Powder Metall. 1973, 16, 88

76. R.L. Coble, Jour of Apl. Phys., 1970, 41, 4796

77. D.S. Wilkinson and M.F. Ashby, Acta Met. 1978, 23, 1277

78. T.B. Bhat, Ph.D. Thesis, IIT, Madras, India, 1981

79. T.B. Bhat, N.Ramakrishnan and V.S. Arunachalam,Scripta Met., 1981, 15, 339

80. J.M. Larson in "Superalloys 1980", Ed. J.K. Tien et al., ASM, Metals Park, OH, USA

81. W. Track and W. Betz, Powder Metallurgy Superalloys, Zurich, Inter. Conf. Vol.2, MPR, Shresbury

82. C.C. Law and M.J. Blackburn in "Mod. Dev. in Powder Metallurgy", ed, H.H. Hausner, H.W. Antes and G.D. Smith, MPIF, Princeton, N.J. 1981, Vol. 14, 93

83. D.R. Chang,D.D. Krueger and R.A. Sprague in "Superalloys 1984", ed. MauriceGell, C.S. Kortovich, R.H. Bricknell, W.B. Kent and J.F. Radavich, Metallurgical Soc. of AIME, Pa, USA, 1984, 245

84. R.V. Miner and R.L. Dreshfield Metall. Trans. 1981, 12A,261

85. R.L. Dreshfield and R.V. Miner Jr. Powder Met. Inter. 1980, 12, 83

86. J.H. Davidson and C. Aubin in "High Temperature Alloys for Gas Turbines", ed. R. Brunetand, D. Coutsouradis, T.B. Gibbons, Y. Lindblom, D.B. Meadowcroft and R. Stickler, Reidel Publishing Co., Dordrecht, Holland, 1982, 853

87. N.G. Ingesten, R. Warren and L. Winberg, ibid, 1013

88. C. Aubin, J.H. Davidson, J.P. Trottier in"Superalloys 1980", ed. J.K. Tien et al., ASM, Metal Park, Ohio, 1980, 345

89. P.N. Ross and B.H. Kear in "Rapid Solidification Processing, Principles and Technologies, ed. R. Mehrabian, B.H. Kear and M.Cohen, Claitors Publishing Division, Baton Rouge, USA, 1978, 278

90. P.L. Antona and A. Bennani, Proc. of AGARD Conf. on Advanced Fabrication Processes, Neuilly-sur-Seine, France, 1978, 18

91. D.L. Williams, Powder Metall. 1977, 84

92. M. Dahlen, N. Ingesten and H. Fischmeister, in "Mod. Dev. in Powder Metallurgy",ed. H.H. Hausner, H.W. Antes and G.D. Smith, MPIF, Princeton, N.J. 1981, Vol. 14, 3

93. T.L. Prakash, Y.N. Chari, E.S. Bhagiradha Rao and R. Thamburaj, Metall. Trans., 1983, 14A, 733

94. J.H. Larson,F.A. Thompson and R.C. Gibson in "Superalloys: Metallurgy and Manufacture", Claitors Publishing Division, 1976, 483

95. M. Dahlen and L. Winberg, Met.Sci. 1979, 13, 163

96. P.E. Price, R. Widmer and J.C. Runkle in Mod. Dev. in Powder Metallurgy, ed. H.H. Hausner and P.W. Taubenblat, MPIF, Princeton, N.J., 1977, Vol. 11, 45

97. M.T. Podob in "Mod. Dev. in Powder Metallurgy," ed. H.H. Hausner and P.W. Taubenblat, MPIF, Princeton, N.J., 1977, Vol. 11, 25

98. G.A.J. Hack and J.W. Eggar, Powder Metallurgy Superalloys, Zurich Inter. Conf., MPR, Shresbury, 1980, Vol. 2, 20-1

99. C.H. Symonds, J.W. Eggar, G.J. Lewis and R.J. Siddal, Powder Metall. Inter., 1983, 15(1), 30

100. A.K. Koul and R. Thamburaj, Metall. Trans. 1985, 16A, 17

101. U. Odebo, Powder Metall. Inter. 1985, 17(6), 292

102. G.L.R. Durber in "High Temperature Alloys for Gas Turbines, Applied Science Publishers, Essex, UK, 1978, 459

103. R.D. Eng and D.J. Evans in "Mod. Dev. in Powder Metallurgy," ed. H.H. Hausner, H.W. Antes and G.D. Smith, MPIF, Princeton, 1981, Vol. 14, 51

104. Y.O. Chen, D.J. Evans and M.J. Blackburn, "Some Effects of Processing and Composition Variations on Microstructure of a High Strength P/M Superalloy - MERL 76", paper presented at the 1979 Fall Meeting, TMS/AIME, Milwauke, Wisconsin, Sept., 1979

105. J.M. Larson, T.E. Volin and F.G. Larson in "Microstructural Science", ed. J.D. Braun, H.W. Arrowsmith and J.L. Mc Call, Elsevier North-Holland Inc., New York, 1977, Vol.5, 209

106. R. Warren, N.G. Ingeston, L. Wingberg and T. Ronnhult, Powder Metall, 1984, 27 (3), 141

107. J.R. Brinegar, J.R. Mihilsin and J. Vandersluis, Superalloys 1984, ed. M. Gell, C. Kortovich, R.H. Bricknell, W.B. Kent, J.F. Radavich, The Metall. Society of AIME, Pa, USA, 1984, 53

108. Z. Meng. G. Sun, M. Li and X. Xie, ibid, 565

109. E. Guo, Z. Han and S. Yu, ibid, 583

110. M.J. Weaver, Powder Metall., 1984, 27(3), 135

111. J.P. Immarigeon and W. Wallace, Metal Powder Report, Oct. 1983, 540

112. ASTM Standard B 213-77

113. ASTM Standard B 212-76

114. J.M. Oblak and W.A. Owezarski, TMS-AIME, 1968, 242, 1563

115. M.J. Donachie and O.H. Kriege, Jour. of Materials, Sept.1972, 7(3), 269

116. R. Mehrabian "Rapid Solidification Processing, Principles and Technologies, ed. R. Mehrabian, B.H. Kear and M. Cohen, Claitors Publishing Division, Baton Rouge, USA, 1978, 9

117. C.J. Ball, Met. Sci. 1984, 18, 577

118. R.D.K. Misra, T.V. Balasubramaniam and P. Rama Rao, unpublished results obtained in the authors' laboratories (DMRL)

119. R.A. Ricks, A.J. Porter and R.C. Ecob, Acta Metall. 31,1983,43

120. R.D.Doherty, Met. Sci., 1982, 16 (1),1

121. M. Jeandin, S. Rupp, J. Massol and Y. Bienvenu, Mat.Sci. and Engg., 77, 1986, 139

122. M. Prager and G. Sines, Jour. of Basic Engg. 1971, 93(2),225

DETERMINATION OF ELECTRON HOLE NUMBERS

Basically, the procedure described below is the same as proposed by Mihilsin et al [35]. Alloy DMP-1 is first considered and atomic percentage of each element is calculated as follows:

(i) Atomic Percentage of each Element

$$C \quad - \quad 0.016 \div 12.0 \quad = \quad 0.0013 \quad \longrightarrow \quad \frac{0.0013}{1.7358} \times 100 \quad = \quad 0.075$$

$$B \quad - \quad 0.018 \div 10.8 \quad = \quad 0.0017 \quad \longrightarrow \quad \frac{0.0017}{1.7358} \times 100 \quad = \quad 0.098$$

$$Cr \quad - \quad 10.0 \div 52.0 \quad = \quad 0.1923 \quad \longrightarrow \quad \frac{0.1923}{1.7358} \times 100 \quad = \quad 11.078$$

$$Co \quad - \quad 4.4 \div 58.9 \quad = \quad 0.0747 \quad \longrightarrow \quad \frac{0.0747}{1.7358} \times 100 \quad = \quad 4.303$$

$$W \quad - \quad 4.35 \div 184.0 \quad = \quad 0.0236 \quad \longrightarrow \quad \frac{0.0236}{1.7358} \times 100 \quad = \quad 1.359$$

$$Mo \quad - \quad 3.23 \div 96.0 \quad = \quad 0.0336 \quad \longrightarrow \quad \frac{0.0336}{1.7358} \times 100 \quad = \quad 1.936$$

$$Ti \quad - \quad 2.10 \div 48.0 \quad = \quad 0.0437 \quad \longrightarrow \quad \frac{0.0437}{1.7358} \times 100 \quad = \quad 2.517$$

$$Al \quad - \quad 4.60 \div 27.0 \quad = \quad 0.1704 \quad \longrightarrow \quad \frac{0.1704}{1.7358} \times 100 \quad = \quad 9.816$$

$$Hf \quad - \quad 0.71 \div 178.5 \quad = \quad 0.0039 \quad \longrightarrow \quad \frac{0.0039}{1.7358} \times 100 \quad = \quad 0.225$$

$$Nb \quad - \quad 0.92 \div 93.0 \quad = \quad 0.0099 \quad \longrightarrow \quad \frac{0.0099}{1.7358} \times 100 \quad = \quad 0.570$$

$$Zr \quad - \quad 0.06 \div 91.0 \quad = \quad 0.0006 \quad \longrightarrow \quad \frac{0.0006}{1.7358} \times 100 \quad = \quad 0.034$$

$$Fe \quad - \quad 0.52 \div 55.8 \quad = \quad 0.0093 \quad \longrightarrow \quad \frac{0.0093}{1.7358} \times 100 \quad = \quad 0.536$$

$$Ni \quad - \quad 69.076 \div 59.0 \quad = \quad \underline{1.1707} \quad \longrightarrow \quad \frac{1.1707}{1.7358} \times 100 \quad = \quad 67.444$$

$$1.7358$$

(ii)   Boride Precipitation

It is assumed that the boride formed is of M_3B_2 type. Since the boride is likely to contain the elements Mo, W, Cr and Ti and assuming that these elements are present in equal proportions, the stoichiometric formula of the boride may be ,

$$(Mo_{0.25}W_{0.25}Nb_{0.25}Ti_{0.25})_3 \; B_2$$
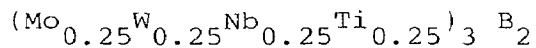
Now we proceed to substract the atomic percentage of each element consumed in forming these borides from the total content of each element i.e.,

Cr = Cr - Cr in boride = 11.078 - $0.25 \times 3 \times \dfrac{0.098}{2}$ = 11.041

Mo = Mo - Mo in boride = 1.936 - $0.25 \times 3 \times \dfrac{0.098}{2}$ = 1.899

W = W - W in boride = 1.359 - $0.25 \times 3 \times \dfrac{0.098}{2}$ = 1.322

Ti = Ti - Ti in boride = 2.517 - $0.25 \times 3 \times \dfrac{0.098}{2}$ = 2.480

(iii)   Carbide Precipitation

Carbides of the type (Nb, Ti)C and $(Mo_4W_2)C$ are assumed to be formed. Partitioning of Hf to carbides is ignored and as the alloy has a high proportion of W and Mo, formation of M_6C type of carbide rather than $M_{23}C_6$ is more likely. It is further assumed that carbon is equally shared by both MC and M_6C carbides. Amount of each element consumed in forming these carbides is sub.tracted as usual.

$$Ti = Ti - Ti \text{ in carbide} = 2.480 - \frac{0.075}{2 \times 2} = 2.461$$

$$Nb = Nb - Nb \text{ in carbide} = 0.570 - \frac{0.075}{2 \times 2} = 0.551$$

$$Mo = Mo - Mo \text{ in carbide} = 1.936 - \frac{0.075 \times 4}{2 \times 2} = 1.861$$

$$W = W - W \text{ in carbide} = 1.359 - \frac{0.075 \times 2}{2 \times 2} = 1.321$$

(iv) γ' Precipitation

It is assumed that γ' has a formula $Ni_3(Al\ Ti)$. Partitioning of other elements such as Cr, Co, Nb, Mo and W to γ' has been ignored for simplicity sake.

Thus,

$$Ni = Ni \quad - Ni \text{ in } \gamma'$$
$$= 67.444 - 3(9.816 + 2.461)$$
$$= 67.444 - 36.831$$
$$= 30.613$$

Now residual amounts of each elements will be:

Ni	Co	Fe	Cr	Zr	Nb	Mo	W	Total
30.613	4.303	0.536	11.041	0.034	0.551	1.861	1.321	50.26

Their percentage will be:

Ni	Co	Fe	Cr	Zr	Nb	Mo	W
60.90	8.56	1.07	21.97	0.067	1.097	3.70	2.63

Now we shall apply the formula to calculate the electron hole number, $\overline{N}v$

$$\overline{Nv} = 1/100 \ [\ 0.66Ni + 1.71Co + 2.66Fe + 4.66Cr + 6.66(Zr+Nb)$$
$$+ 9.66 \ (Mo+W) \ ]$$

$$= 1/100 \ [\ 0.66 \times 60.9 + 1.61 \times 8.56 + 2.66 \times 1.07 + 4.66 \times 21.97$$
$$+ 6.66 \ (1.164) + 9.66 \ (6.33) \ ]$$

$$= 1/100 \times 232.13$$

$$= 2.32$$

Following the similar procedure for the alloys DMP-2 and DMP-3, $\overline{Nv}$ values were found to be 2.26 and 2.74.

The actual values of $\overline{Nv}$ are believed to be slightly different because of various reasons. First, the partitioning of niobium to γ ' has been ignored. Secondly, hafnium is supposed to marginally affect the $\overline{Nv}$ value because of its low concentration, although it has 7% solubility in γ ' as compared to 1% in γ (Section 2.2.1 and references 31 and 32). Further, the stoichiometric formulae of borides, carbides and γ ' assumed here may vary in actual practice. However, by comparison of these $\overline{Nv}$ values it is evident that the alloy most likely to form sigma phase is DMP-3.